Institut für Physik und Astronomie

Universität Potsdam

und

Max-Planck-Institut für Gravitationsphysik

(Albert-Einstein-Institut) Potsdam

Worldtube Excision Method for Intermediate Mass Ratio Inspirals

Dissertation

zur Erlangung des akademischen Grades

Doktor der Naturwissenschaften (Dr. rer. nat.)

von

Nikolas A. Wittek

betreut durch

Prof. Dr. Harald Pfeiffer

Potsdam 2024

Published online on the
Publication Server of the University of Potsdam:
https://doi.org/10.25932/publishup-66639
https://nbn-resolving.org/urn:nbn:de:kobv:517-opus4-666398

An meinen Großvater, *Prof. Dr. Dr. h.c. Klaus Kühn*

Allgemeinverständliche Zusammenfassung

Gravitationswellen entstehen durch beschleunigte Massen, die Energie in das Raum-Zeit-Kontinuum abstrahlen. Diese Wellen komprimieren und dehnen alles in ihrem Weg um einen winzige Distanz, während sie sich durch das Universum ausbreiten. Nur extrem kompakte Objekte, wie etwa Schwarze Löcher und Neutronensterne, können genug Energie emittieren, um messbare Gravitationswellen zu erzeugen. Die erste Detektion eines solchen Signals erfolgte am 14. September 2015 durch das LIGO Interferometer. Es wurde von zwei verschmelzenden schwarzen Löchern erzeugt, die über eine Milliarden Lichtjahre von unserem Sonnensystem entfernt sind.

Die korrekte Auswertung solcher Messungen setzt voraus, dass die möglichen Signale, auf die der Detektor empfindlich ist, berechnet werden können. Die Dynamik von binären schwarzen Löchern und die emittierte Gravitationswellensignatur sind durch die Einsteingleichungen bestimmt. In der Numerischen Relativitätstheorie (NR) wird die Wellenform eines Systems erzeugt, indem diese Gleichungen auf einem Gitter diskretisiert und dann auf Supercomputern gelöst werden. Diese Berechnungen sind ein wichtiger Beitrag zur aktuellen Bestimmung und Analyse von Gravitationswellen.

Zukünftige Detektoren, wie etwa das Einstein-Teleskop oder LISA, werden in der Lage sein Gravitationswellen von Binärsystemen zu detektieren, die aus zwei schwarzen Löchern von weit unterschiedlichen Massen bestehen. Der Rechenaufwand von NR Simulationen nimmt jedoch stark mit diesem Massenverhältnis zu, sodass derzeitige Methoden nicht in der Lage sind, effizient Wellenformen für solche Systeme zu erstellen. In dieser Dissertation beschreibe ich eine neuen Ansatz, der solche Berechnungen stark beschleunigen soll. Die grundlegende Idee besteht darin, eine Region um das kleinere schwarze Loch aus der Simulation auszuschneiden. In diesem Bereich ist das Gravitationsfeld sehr genau durch die Präsenz des kleinen schwarzen Lochs bestimmt, wohingegen das große schwarze Loch nur sehr geringen Einfluss hat. Eine solche Konfiguration ist mathematisch durch eine *perturbative* Lösung beschrieben. Ich erkläre, wie eine solche Lösung in die ausgeschnittene Region der Simulation eingesetzt werden kann und wie dies den Rechenaufwand reduziert.

Abstract

Future gravitational wave detectors will be sensitive to signals emitted from binary black hole systems with small mass ratios $q = m_2/m_1 \lesssim 10^{-2}$. The generation of accurate waveforms for these systems has proven to be a challenging task. In numerical relativity, the computational cost of a simulation grows inversely proportional to the square of the mass ratio which quickly becomes unfeasible. In this thesis, I present a novel approach for the simulation of small mass ratio binary black hole systems that aims to partially alleviate this problem. A spherical region around the smaller black hole is excised from the computational domain and replaced with a perturbative solution of a tidally deformed black hole. This removes the tight grid spacing near the small black hole and thereby the limitations imposed on the time step by the Courant-Friedrich-Lewy condition.

The scheme is tested on the example of a scalar toy model consisting of a point charge orbiting a Schwarzschild black hole. An initial study of this problem was carried out by Dhesi *et al.* [1] in 1+1 dimensions. I generalize their method to 3+1 dimensions and present an implementation using the SpECTRE numerical relativity code. The accuracy and efficiency of the simulations are demonstrated for circular geodesic orbits. As a second step, I include the effect of the scalar self-force and present the first implementation of a fully self-consistent evolution for a scalar charge model. By dynamically adjusting the size of the excision region, the simulations are able to model the inspiral, plunge, merger and ringdown of the orbit. I present a series of quasi-circular inspirals and compare the results to an adiabatic approximation, demonstrating that post-adiabatic effects are accurately resolved. Finally, I show how the code can be extended to simulate highly eccentric orbits as well as hyperbolic encounters including direct captures.

Contents

1 Introduction

On the 14th of September 2015, the 4 km long arms of the LIGO observatory in Livingston, Louisiana were compressed and stretched by a distance less than 1000 times the diameter of an atomic nucleus [2]. About seven milliseconds later, a detector in Hanford, Washington experienced a very similar oscillation. This signal was caused by a gravitational wave emitted by two merging black holes with 36 and 29 solar masses, respectively. They formed a larger black hole of 62 solar masses; the remaining 3 solar masses were radiated away in the form of gravitational waves. During the last few milliseconds of their merger, the system emitted more power than all the stars of the visible universe combined [3].

[2]: LIGO/VIRGO (2016), *Observation of Gravitational Waves from a Binary Black Hole Merger*

[3]: Abbott et al. (2016), *Observation of Gravitational Waves from a Binary Black Hole Merger*

The signal had been traversing the universe for over a billion years. At the time it started its journey[1], Earth was dominated by prokaryotic cyanobacteria that colored its oceans black, while its most complex lifeforms, multi-celled eukaryotes, just started to form their first organelles [4]. If we re-scale the estimated travel time into a single year so that the waves were emitted at midnight on January 1st, the first major changes to life on Earth occurred in about May, when increased oxygen levels in the atmosphere allowed for more complex life such as mosses and ferns to form. Soon after, the first fish-like vertebrates started to occupy the oceans in June and July. In August, some decided to leave the oceans and go for a walk on land. By October, they had evolved into the first dinosaurs roaming the plains of Pangaea. Then, on December 7th, a 15 km wide asteroid struck the Gulf of Mexico, killing all non-avian dinosaurs almost instantly. This proved an opportunity in particular for mammals which started to massively diversify. On December 29th, the first apes walked on two legs; the first modern humans arrived at around 9 pm on December 31st. The earliest societies formed at 11:56 pm that day and 3 seconds before the signal reached earth, a German physicist first published a theory that could explain the oscillations about to shake the planet. The observatories used for the detections were built in the 0.3 seconds before they made the measurement.

1: The stringent physicist may forgive my liberal usage of simultaneity for dramatization purposes.

[4]: Gee (2021), *A (Very) Short History of Life on Earth: 4.6 Billion Years in 12 Pithy Chapters*

In this thesis, I try and explain the efforts of my PhD to contribute to our understanding and measurement capabilities of these signals. In Section 1.1, I explain how General Relativity (GR) predicts gravitational waves and summarize the most important astrophysical results from their measurements. I give a brief overview of how

binary black hole (BBH) systems are modeled with a particular focus on numerical relativity in Section 1.2. A selection of numerical techniques to solve partial differential equations is reviewed in Section 1.3 and I present the code used for the simulations of this thesis in Section 1.4. Finally, I give an introduction to the numerical evolution of intermediate mass ratio binary black holes system and what my work has been trying to accomplish in Section 1.5. The Einstein summation convention is used throughout the thesis, where Greek letters indicate spacetime indices and Latin letters correspond to spatial components.

1.1 Gravitational waves

1.1.1 General relativity

Sources and Further Reading

In this section, I give a very brief overview of the theory gravitational waves, as well as some important astrophysical results from current detectors. For a more in-depth description, consult your favorite textbook such as e.g. [5] or [6].

For centuries, the most successful description of gravity was given by Newton's laws. One central postulate is that two masses M and m exert an instantaneous, equal and opposite force onto each other that is proportional to the inverse square of the distance $r = \sqrt{\delta_{ij} x^i x^j}$ between them. The acceleration of the body with mass m is then given by this force divided by its mass

$$\cancel{m}\frac{d^2 x^i}{dt^2} = -\frac{GM\cancel{m}x^i}{r^3}, \tag{1.1}$$

where G is the gravitational constant. Here, I have carelessly canceled out the mass m on both sides without asking the important question:

Why is a body's inertial mass (lhs), which determines its acceleration in response to an applied force, equal to its gravitational mass (rhs), which dictates the strength of the gravitational force it experiences?

While Newton never found an adequate answer to this question, known as the (weak) equivalence principle, Einstein formulated the theory of general relativity without the concept of inertial mass altogether [7]. Rather, any gravitational mass or energy curves

[7]: Einstein (1911), *Über den Einfluß der Schwerkraft auf die Ausbreitung des Lichtes*

the spacetime around it and bodies simply follow this curvature independent of their mass [8].

[8]: Einstein (1916), *The foundation of the general theory of relativity.*

Central to describing the curvature of spacetime is the metric $g_{\mu\nu}$. Given a coordinate system x^α, one can define the spacetime interval which serves as a fundamental invariant encapsulating the geometric properties of the four-dimensional spacetime manifold. It is defined as

$$ds^2 = g_{\mu\nu} dx^\mu dx^\nu. \tag{1.2}$$

The Einstein field equations then connect this metric to the matter content of the universe [9]:

[9]: Einstein (1915), *Die Feldgleichungen der Gravitation*

$$R_{\mu\nu} - \frac{1}{2} R g_{\mu\nu} = \frac{8\pi G}{c^4} T_{\mu\nu} \tag{1.3}$$

This simple-looking equation relates the geometry of spacetime on the left, described by the Ricci tensor $R_{\mu\nu}$ and Ricci scalar R, to the energy content of the universe on the right, described by the energy-momentum tensor $T_{\mu\nu}$. However, hidden behind the notation is a system of 10 semi-linear partial differential equations which are highly difficult to solve in most cases.

Schwarzschild solution

Einstein did not believe that there existed any analytical solutions to his field equations at first and was most surprised when Karl Schwarzschild found the following solution just a month after he published his theory [10]

[10]: Schwarzschild (1916), *On the gravitational field of a mass point according to Einstein's theory*

$$ds^2 = -\left(1 - \frac{2GM}{c^2 r}\right) c^2 dt^2 + \left(1 - \frac{2GM}{c^2 r}\right)^{-1} dr^2 + r^2 d\Omega^2. \tag{1.4}$$

This solution describes exactly a static, spherically symmetric spacetime in a vacuum around a mass M as a function of radius r.

The metric has a particularly interesting feature at the so-called Schwarzschild radius at $r_s = 2M$. In the coordinates presented here, the metric blows up at this point and it was long unclear what physical significance this implied. It was later shown that the singularity can be removed with an appropriate coordinate transformation [11, 12].

[11]: Eddington (1924), *A Comparison of Whitehead's and Einstein's Formulæ*
[12]: Lemaitre (1933), *The expanding universe*

The region inside the event horizon $r < r_s$ is particularly interesting as the radial coordinate r becomes timelike and the time coordinate

t becomes spacelike - the light cone of a particle crossing this line will flip to its side as seen in Figure 1.1.

This implies that a worldline can not remain at a constant radius but must fall further inside, the same way any worldline has to go forward in time outside this region. This suggests the existence of an event horizon: any particle must fall into the true physical singularity at $r = 0$ once it crosses the event horizon at $r = r_s$. If a spherical body like a star collapses beyond this point, no physical force can prevent it from fully collapsing into the central singularity: a black hole is formed.

The Schwarzschild solution, Eq. (1.4), is particularly remarkable because the black hole is described exactly by a single parameter, the mass M. A few decades later, another solution to the field equations was found describing a black hole with angular momentum. Such a spacetime is described by the Kerr metric [14] and has three additional parameters[2] given by the spin vector χ.

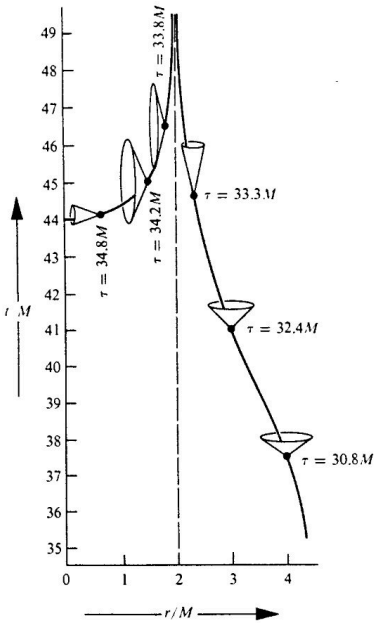

Figure 1.1: A diagram demonstrating the apparent singularity at $r = 2M$ in Schwarzschild coordinates and the flipping of the light cones inside the region. Source: [13]

[14]: Kerr (1963), *Gravitational field of a spinning mass as an example of algebraically special metrics*

2: In addition, black holes are able to hold an electromagnetic charge, however there are no known astrophysical formation channels for such objects and they are not expected to exist in nature.

[15]: Einstein (1918), *Über Gravitationswellen*

Gravitational waves

The Einstein field equations can also be solved approximately through linearization. Here, one considers the evolution of perturbations $h_{\mu\nu}$ on flat spacetime described by the Minkowski metric $\eta_{\mu\nu}$ [15]

$$g_{\mu\nu} = \eta_{\mu\nu} + h_{\mu\nu}. \tag{1.5}$$

When this ansatz is inserted into the vacuum Einstein field equations (1.3), one obtains in the Lorenz gauge

$$\Box h_{\mu\nu} = -\frac{16\pi G}{c^4} T_{\mu\nu}. \tag{1.6}$$

Here, the D'Alembertian $\Box = \eta^{\alpha\beta}\nabla_\alpha\nabla_\beta$ is a differential operator that describes the evolution of a wave traversing across flat spacetime. In general, such gravitational waves are emitted by any system with an accelerating mass quadrupole as captured by the formula first conceived by Einstein in 1918 [15]

$$h_{ij} = \frac{2G}{c^4 r}\ddot{I}_{ij}. \tag{1.7}$$

The amplitude of a gravitational wave is sourced by the second time derivative of the system's quadrupole $\ddot{I}_{ij}$ divided by the distance to the observer r and multiplied by a constant with a value of $10^{-44}\frac{\mathrm{s}^2}{\mathrm{kg\,m}}$. The small value of this constant is the reason it was long doubted gravitational waves would ever be detected.

[15]: Einstein (1918), *Über Gravitationswellen*

Binary compact object systems

As of today, all detections of gravitational waves come from binary systems consisting of black holes and neutron stars, the densest known objects of the universe. A system of two such objects will, at sufficiently small separation, start to dissipate orbital potential energy in the form of gravitational waves at a rate that significantly accelerates its inspiral. This causes the separation to shrink which in turn increases the gravitational wave flux and thereby the inspiral rate [16]. At some small distance, the two objects will plunge onto each other and emit a final burst of gravitational radiation. Finally, they will merge to a single remnant. Any binary system involving a black hole will merge to a larger black hole, whereas a system of two neutron stars may either collapse to a black hole or form a more massive neutron star. A black hole remnant will relax to a Schwarzschild or Kerr black hole through the emission of gravitational waves known as quasi-normal modes. This part of the waveform is known as the ringdown signal.

[16]: Maggiore (2007), *Gravitational Waves. Vol. 1: Theory and Experiments*

Binary black hole systems, which are the focus of this thesis, are characterized by a set of intrinsic and extrinsic parameters. The intrinsic parameters include the black hole masses, m_1 and m_2, their respective spin vectors χ_1 and χ_2 with three components each and the orbital eccentricity e. The extrinsic parameters capture the system's location and orientation with respect to the detector, encompassing right ascension, declination, luminosity distance, coalescence time, inclination, orbital phase, and polarization.

The dimensionless mass ratio $q = m_1/m_2 \leq 1$ is usually introduced as a gravitational wave signal can easily be rescaled to different individual masses if the mass ratio remains the same. Gravitational wave signals from binary black holes are then categorized[3] into comparable mass binaries with $q \gtrsim 10^{-2}$, intermediate mass ratio inspirals (IMRIs) with $10^{-2} \gtrsim q \gtrsim 10^{-5}$ and extreme mass ratio inspirals (EMRIs) $q \lesssim 10^{-5}$.

3: There is no sharp boundary at which mass ratios q a BBH starts to become an IMRI or EMRI and other publications might use slightly different intervals for definitions.

1.1.2 The LIGO detectors

Sources and Further Reading

This section briefly summarizes how the LIGO/VIRGO detectors are able to detect gravitational waves. It is based largely on chapters 7 and 9 of the textbook [16] and the reviews [17, 18] which provide a much more detailed analysis of current detectors as well as data analysis techniques.

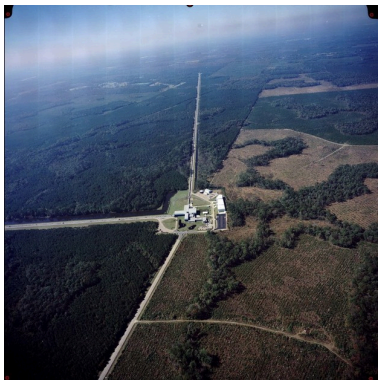

Figure 1.2: An aerial view of the LIGO detector in Livingston, Louisiana.
Source: LIGO/VIRGO

LIGO (Laser Interferometer Gravitational-Wave Observatory) consists of a giant laser interferometer with two arms extending 4 kilometers each. A high-powered laser is split into two beams that traverse each arm toward mirrors which reflect them back. Upon recombination at the beam splitter, the beams form an interference pattern which depends on their phase difference. This difference and any variation to it can be measured with extreme accuracy as light intensity variations at a photodetector. A gravitational wave passing through Earth will expand and contract the space(time) occupied by these arms which causes one of the laser beams to travel a slightly longer distance than the other one. The change in phase difference of the recombined laser beams is then used to re-construct the gravitational wave signal.

A typical detection of LIGO will distort the arms by 10^{-17} meters i.e. by less than 1000 times the size of a proton [16–18]. Measurements on such small scales are constantly contaminated by noise from different sources such as seismic movement, Brownian motion and quantum effects. We define the data stream of such a detector as the time series $s(t)$ consisting of the noise $n(t)$ and (perhaps) a signal $h(t)$

$$s(t) = n(t) + h(t). \tag{1.8}$$

The noise-weighted inner product between two time series $a(t)$ and $b(t)$ is given by

$$\langle a(t)|b(t)\rangle = 4\mathrm{Re}\int_0^\infty \frac{a(f)b^*(f)}{S_n(f)}df, \tag{1.9}$$

where $a^*(f)$ is the Fourier transform of $a(t)$ and $S_n(f)$ is the one-sided power spectral density (PSD) of the detector noise. The PSD quantifies the distribution of noise power as a function of frequency, characterizing the sensitivity of the detector across different frequency bands.

The extraction of a signal from this sea of noise is done through

[16]: Maggiore (2007), *Gravitational Waves. Vol. 1: Theory and Experiments*
[17]: Abbott et al. (2020), *A guide to LIGO–Virgo detector noise and extraction of transient gravitational-wave signals*
[18]: Cahillane et al. (2022), *Review of the Advanced LIGO Gravitational Wave Observatories Leading to Observing Run Four*

a technique known as matched filtering which involves cross-correlating the data stream $s(t)$ with a template waveform that represent the expected gravitational wave signal $h(t)$. The central metric capturing the correlation is the signal-to-noise ratio (SNR)

$$\rho = \frac{\langle s|h\rangle}{\sqrt{\langle h|h\rangle}}. \tag{1.10}$$

The SNR quantifies to what extent the signal of the detector $s(t)$ matches the theoretical prediction of a waveform $h(t)$. A high SNR means a very high probability that the signal was buried in the data whereas a low SNR suggests that the correlation to the template could merely be a result of random noise movement. Once the false alarm rate of a signal is sufficiently low and the astrophysical probability of detecting such a signal is sufficiently large, a detection is claimed. This typically happens around SNR ~ 8.

The detection of a gravitational wave signal through matched filtering therefore requires a template - a theoretical prediction of the waveform one is trying to detect. For this purpose, template banks are created which attempt to cover the parameter space of all gravitational wave signals in the sensitivity range of a detector.

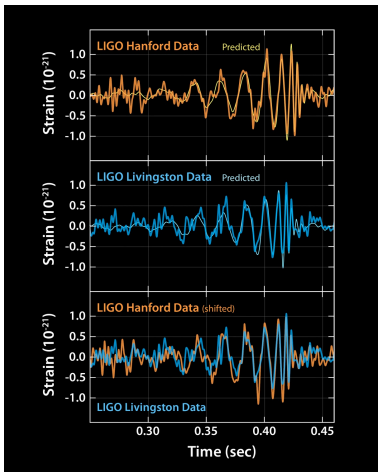

Figure 1.3: The gravitational wave strain h detected by LIGO in Hanford and Livingston. Overlayed with the measured signal is the theoretical prediction of the waveform used to justify the detection. Source: LIGO/VIRGO

1.1.3 Observational results

Today, all gravitational wave detections have been made by the two LIGO detectors in the US and the VIRGO detector in Italy. Figure 1.4 shows a visualization of signals with astrophysical probability $p_{\text{astro}} > 0.5$ detected within the first three observing runs up to March 2020. It contains 90 gravitational wave signals, including two originating from binary neutron star systems and at least three emitted by black hole-neutron star mergers [19, 20]. These detections represent a new way of probing the universe which have yielded many new findings. I will try and summarize the most important results in this section.

[19]: Abbott et al. (2021), *Observation of Gravitational Waves from Two Neutron Star–Black Hole Coalescences*
[20]: Abbott et al. (2023), *GWTC-3: Compact Binary Coalescences Observed by LIGO and Virgo during the Second Part of the Third Observing Run*

Binary black holes

First and foremost, the detections give the first direct evidence for the existence of binary black hole systems and gravitational waves. Until GW150914, gravitational waves had only been measured indirectly through pulsar timing [21]. The waveform and inferred

[21]: Hulse et al. (1975), *Discovery of a pulsar in a binary system*

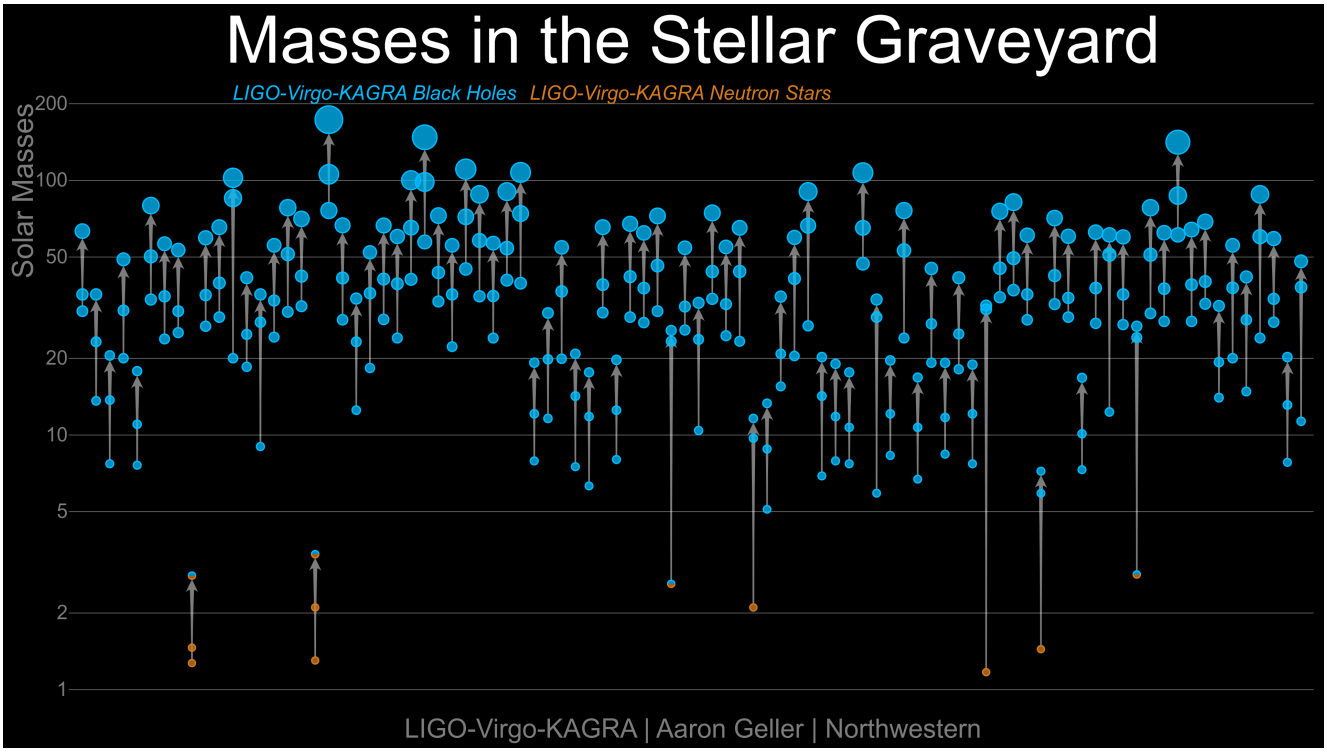

Figure 1.4: A visualization of the announced gravitational-wave detections up until the end of the third observing run. Source: LIGO/VIRGO/KAGRA & Aaron Geller

merging dynamics represent the strongest gravitational interaction ever recorded, providing a spectacular confirmation of General Relativity. As all theories in physics, it is expected that GR will eventually break down in some strong-field regime. The growing number of measurements give increasingly stringent upper bounds on deviations from GR and place constraints on alternative theories of gravity [22, 23].

The distribution of merger properties also provides information about black hole and neutron star populations as well as the formation channels of binary systems. For instance, Figure 1.4 also includes several signals originating from neutron stars with masses between 1.2 $M_\odot$ and 2 $M_\odot$, as well as black hole mergers with more than 5 $M_\odot$. However, the merger rate rapidly declines between those masses even though the detectors would be sensitive in this region. This discrepancy is known as the lower mass gap [24] and the astrophysical origin is a field of active research.

Gravitational wave detections allow the measurement of the binary system's component spins, which, among other things, allows analysis of the formation channel. While there are many proposed ways a binary black hole system can form, they can be roughly divided into two categories [25]: In the isolated, or in-field evolu-

[22]: Abbott et al. (2016), *Tests of general relativity with GW150914*
[23]: Krishnendu et al. (2021), *Testing General Relativity with Gravitational Waves: An Overview*

[24]: Abbott et al. (2023), *Population of Merging Compact Binaries Inferred Using Gravitational Waves through GWTC-3*

[25]: Rodriguez et al. (2016), *Illuminating Black Hole Binary Formation Channels with Spins in Advanced LIGO*

tion, compact binaries evolve from pairs of stars which eventually collapse to a black hole. Many astrophysical parameters influence the properties of the final binary, but it is generally expected that the spins of the individual black holes are aligned with the orbital angular momentum [26–28]. In the dynamical formation channel, the binary black hole system is formed through interactions with third bodies in dense globular clusters [27]; the spins and angular momenta are then expected to be randomly distributed. Measurements from BBH systems so far mostly show low effective spins with very poorly constrained individual black hole spins [20]. It has been suggested that this is consistent with in-field evolution as the primary formation channel [29]. However, several candidates show evidence of spins that are anti-aligned with the orbital angular momentum, likely resulting from dynamical formation [30].

[26]: Hurley et al. (2002), *Evolution of binary stars and the effect of tides on binary populations*
[27]: Mapelli (2021), *Formation Channels of Single and Binary Stellar-Mass Black Holes*
[28]: Bonino et al. (2023), *Inferring eccentricity evolution from observations of coalescing binary black holes*
[27]: Mapelli (2021), *Formation Channels of Single and Binary Stellar-Mass Black Holes*
[20]: Abbott et al. (2023), *GWTC-3: Compact Binary Coalescences Observed by LIGO and Virgo during the Second Part of the Third Observing Run*
[29]: Bavera et al. (2020), *The origin of spin in binary black holes: Predicting the distributions of the main observables of Advanced LIGO*
[30]: Antonelli et al. (2023), *Classifying the generation and formation channels of individual LIGO-Virgo-KAGRA observations from dynamically formed binaries*

Binary neutron stars

Gravitational wave signals from binary neutron stars give insight into the extreme states of matter found at the center of these objects. The pressure in the core of a neutron star is much larger than what is accessible by experiments on Earth. As a result, almost nothing is known about how matter behaves in these regimes. However, this unknown equation of state has a large effect on the tidal deformability of a neutron star which quantifies of how easily its shape is distorted by the tidal field of a companion object. This can significantly affect the tidal interactions of a binary system, creating measurable imprints in the waveform [31]. Neutron star waveforms detected so far have loosely constrained what equations of state are physically possible [32] and it is expected that future measurements will further reduce this uncertainty [33].

[31]: Takami et al. (2014), *Constraining the Equation of State of Neutron Stars from Binary Mergers*
[32]: Annala et al. (2018), *Gravitational-wave constraints on the neutron-star-matter Equation of State*
[33]: Hernandez Vivanco et al. (2019), *Measuring the neutron star equation of state with gravitational waves: The first forty binary neutron star merger observations*

Some of the most groundbreaking results in the field of gravitational waves come from multi-messenger events, where a counterpart to the gravitational signal is detected through electromagnetic radiation or neutrinos. The only example of this to date is GW170817 which was the first gravitational wave detection originating from a binary neutron star inspiral [34]. About $\approx 1.7s$ after the peak of the gravitational wave signal, the Fermi Gamma-ray Burst Monitor independently measured a gamma-ray burst GRB 170817A [35]. More than 70 telescopes then participated in the electromagnetic follow-up of the transient kilonova in the galaxy NGC 4993. It initially emitted ultraviolet radiation and traversed the electromagnetic spectrum down to infrared as it cooled off.

[34]: Abbott et al. (2017), *GW170817: Observation of Gravitational Waves from a Binary Neutron Star Inspiral*
[35]: Abbott et al. (2017), *Multi-messenger Observations of a Binary Neutron Star Merger*

The observation confirmed that merging binary neutron stars can emit gamma ray bursts, an idea which had long been postulated. The small delay between the signals constrained the relative difference between the speed of gravitational waves and light to less than $\sim 10^{-15}$, representing an extreme test of Lorentz invariance. In addition, the velocity of the system could be determined from the redshift of the host galaxy NGC 4993, while its distance was independently calculated from the gravitational wave signal. This allowed for a measurement of the Hubble constant as $70^{+12.0}_{-8.0}$ km s^{-1} Mpc^{-1} [36]. It is expected that future multi-messenger measurements may be precise enough to resolve the Hubble tension that currently exists between measurements from supernovae and the cosmic microwave background [37].

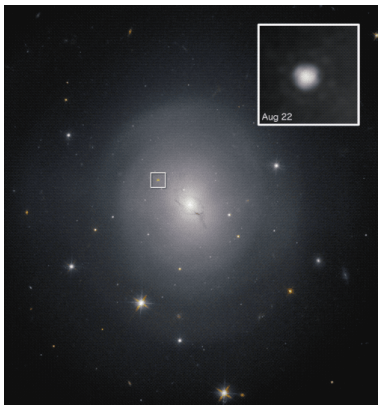

Figure 1.5: The kilonova transient in NGC 4993 associated with GW170817 as observed by the Hubble Space Telescope.
Source: ESA/NASA

[36]: Abbott et al. (2017), *A gravitational-wave standard siren measurement of the Hubble constant*

[37]: Feeney et al. (2021), *Prospects for Measuring the Hubble Constant with Neutron-Star–Black-Hole Mergers*

1.1.4 Future detectors

While gravitational waves have already contributed to many branches of astrophysics, future detectors will be sensitive to an even broader range of signals. Figure 1.6 shows the noise sensitivity curves of current and planned detectors as well as the expected frequencies and characteristic strains produced by different populations of binary black holes [38]. The signals that current detectors are sensitive to are shown by the green line denoted "LIGO-like binaries" and consist of stellar-mass black holes with a mass ratio q close to unity.

[38]: Jani et al. (2019), *Detectability of Intermediate-Mass Black Holes in Multiband Gravitational Wave Astronomy*

Einstein Telescope & Cosmic Explorer

Future Ground-based detectors such as the Einstein Telescope (ET) [39] and Cosmic Explorer (CE) [40] will be able to detect the same signals as LIGO with a much larger SNR, allowing for an improved analysis of black hole and neutron star populations as well as their formation channels. In addition, they will be sensitive to many signals that LIGO is currently missing, particularly those emitted at larger redshifts up to $z = 10$. Current estimates are e.g. between 10^5 and 10^6 binary black hole events per year for ET [39].

[39]: Maggiore et al. (2020), *Science Case for the Einstein Telescope*

[40]: Evans et al. (2021), *A Horizon Study for Cosmic Explorer: Science, Observatories, and Community*

This opens up a window into regions beyond the reionization epoch $z > 6$, where only metal-poor progenitor stars are expected to have formed. Measurements of gravitational waves from these distances then reveal how the formation of compact objects depends on

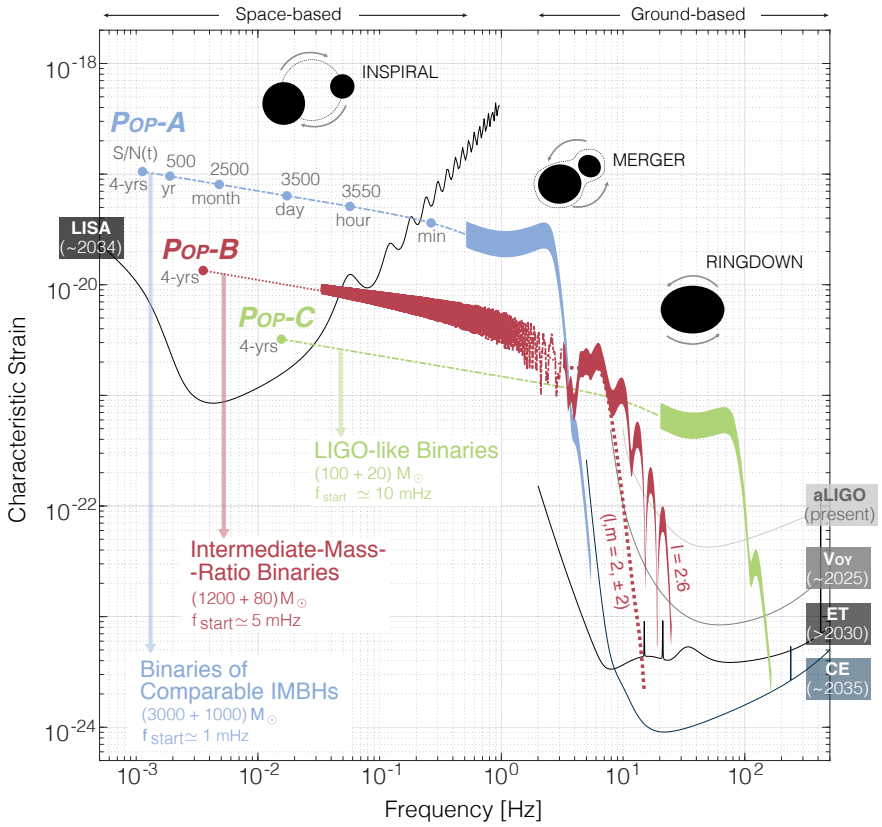

Figure 1.6: The noise sensitivity curves of current and future detectors along the frequency bands of gravitational wave signals generated by different populations of binary black hole systems. Source: [38]

the metallicity of stars. If stellar mass black holes are truly a result of collapsing stars, the rate of gravitational wave events will have a strong dependence on the stellar formation rate. If the number of gravitational waves from BBH sources is not correlated with the star formation rate through different epochs, this could indicate that these black holes are of primordial rather than stellar origin [39].

While the two binary neutron star signals detected so far have already started to constrain the equation of state, the tidal deformability parameter needs to be measured with an order of magnitude higher accuracy to distinguish between more realistic models and to provide evidence for phase transitions in the neutron star interior [41]. ET alone is expected to detect 7×10^4 binary neutron stars coalescences per year [39]. For multi-messenger signals, a network of detectors across the globe will greatly improve the sky localization of sources to allow for a follow-up search of a transient. A network of multiple third generation detectors will likely detect between 10^2 and 10^3 binary neutron star events with an electromagnetic counterpart [42].

Compared to LIGO, third generation detectors will be better insulated from seismic noise at lower frequencies of $\sim 5Hz$. Currently,

[41]: Tews et al. (2018), *Constraining the speed of sound inside neutron stars with chiral effective field theory interactions and observations*

[42]: Belgacem et al. (2019), *Cosmology and dark energy from joint gravitational wave-GRB observations*

the smallest mass ratios detected are GW190814 and GW200210_092254 with $q \equiv m_2/m_1 \sim 0.11$ [20, 43], and GW191219_163120 which is estimated to have $q \sim 0.04$ [20]. The CE and ET, however, will be sensitive to the final inspiral orbits of IMRIs with mass-ratios down to $q \sim 10^{-3}$, indicated by the red line in Fig. 1.6.

[20]: Abbott et al. (2023), *GWTC-3: Compact Binary Coalescences Observed by LIGO and Virgo during the Second Part of the Third Observing Run*

[43]: Abbott et al. (2020), *GW190814: Gravitational Waves from the Coalescence of a 23 Solar Mass Black Hole with a 2.6 Solar Mass Compact Object*

LISA

The LISA observatory [44, 45] is a space-based interferometer that will be sensitive to completely new populations of gravitational wave sources not accessible on earth. This includes, e.g. *Galactic* binary systems located inside the Milky Way. The proximity of these sources would allow for the detection of much fainter signals such as binaries involving white dwarfs [46].

[20]: Abbott et al. (2023), *GWTC-3: Compact Binary Coalescences Observed by LIGO and Virgo during the Second Part of the Third Observing Run*

[44]: Amaro-Seoane et al. (2017), *Laser Interferometer Space Antenna*

[45]: Colpi et al. (2024), *LISA Definition Study Report*

[46]: Postnov et al. (2014), *The Evolution of Compact Binary Star Systems*

Critically, LISA's low frequency band makes it sensitive to at least the partial inspiral of almost all possible types of black hole binaries. This includes higher mass systems such as binaries consisting of similar mass IMBHs shown by the blue line in Fig. 1.6 and massive black hole binaries expected to form during galaxy mergers [47]. The detection of these events could help shed light on the objects' formation channels. It is widely assumed that massive black holes grow either through a sequence of black hole mergers, a process known as a hierarchical merger model, or through rapid gas accretion. However, detections of quasars at large redshifts [48] have left open questions about the astrophysical processes that could maintain the required merger/accretion rates to form massive black holes within a few hundred million years of the Big Bang [49]. An alternative explanation are primordial black holes formed in the early universe which act as seeds for the massive black holes observed today [50]. LISA is expected to detect black holes in mass ranges between 10^2 and 10^8 $M_\odot$ with the majority of events occurring between redshifts $z \sim 2-4$ [51]. This presents a unique insight into the formation channels of the early universe.

[47]: Merritt (2013), *Dynamics and Evolution of Galactic Nuclei*

[48]: Fan et al. (2006), *A Survey of $z > 5.7$ Quasars in the Sloan Digital Sky Survey IV: Discovery of Seven Additional Quasars*

[49]: Latif et al. (2016), *Formation of supermassive black hole seeds*

[50]: Clesse et al. (2015), *Massive Primordial Black Holes from Hybrid Inflation as Dark Matter and the seeds of Galaxies*

[51]: Afshordi et al. (2023), *Waveform Modelling for the Laser Interferometer Space Antenna*

Finally, LISA will be sensitive to IMRIs and EMRIs up to mass ratios $q \sim 10^{-8}$. A typical IMRI consists of a stellar mass black hole inspiraling into an IMBH, for example in the center of a dwarf galaxy [52]; see the red curve in Fig. 1.6. Such an event provides a possible source of a *multiband* detection: the early inspiral is observable by LISA but the signal leaves the sensitivity band as the waveform frequency increases over the course of the inspiral. Before merger, the waveform will become detectable

[52]: Arca-Sedda et al. (2021), *Merging stellar and intermediate-mass black holes in dense clusters: implications for LIGO, LISA, and the next generation of gravitational wave detectors*

again by third generation detectors on Earth, enabling the study of the long-term evolutionary history of these binaries. In addition, the early LISA measurements should be able to constrain the sky location and merger time sufficiently to allow for a targeted search for electromagnetic counterparts immediately following the merger [53].

[53]: Sesana (2016), *Prospects for Multiband Gravitational-Wave Astronomy after GW150914*

A canonical EMRI source for LISA consists of a stellar mass compact object orbiting a massive black hole at the center of a galaxy. These binaries spend $10^4 - 10^5$ orbits in the sensitivity band of LISA which allows the signal to build up a very large SNR. With an EMRI, it is expected that all intrinsic parameters including the masses of the bodies, the spin magnitude of the MBH and the orbital eccentricity can be determined with a relative uncertainty of $10^{-4} - 10^{-6}$ [54]. The sky position and distance will be measured accurately enough to determine the host galaxy without the need for electromagnetic counterparts [55]. Measurements of such extreme precision will provide a stringent test of the Kerr metric and the associated no-hair theorem, further constraining modified gravity theories [56]. In addition, different growth mechanisms of massive galaxies predict significantly different mass and spin distributions of MBHs; a large number of accurate EMRI measurements will make it possible to identify the dominant channels [57]. The number of expected EMRI detections over the LISA mission duration is highly uncertain but ranges from a few to several thousands [54].

[54]: Babak et al. (2017), *Science with the space-based interferometer LISA. V: Extreme mass-ratio inspirals*

[55]: Pan et al. (2020), *Probing the Growth of Massive Black Holes with Black Hole-Host Galaxy Spin Correlations*

[56]: Barausse et al. (2020), *Prospects for Fundamental Physics with LISA*

[57]: Sesana et al. (2014), *Linking the spin evolution of massive black holes to galaxy kinematics*

The detection of all these signals relies on the availability of accurate waveform models covering the entire parameter space of expected sources. However, particularly for large mass ratios these are not yet available and their generation is an ongoing effort. In this thesis, I describe a new approach for modeling such IMRI and EMRI systems using numerical relativity. In the next section, I summarize the most common approaches of source modeling that try and solve the Einstein equations governing the interactions of these binary systems.

[54]: Babak et al. (2017), *Science with the space-based interferometer LISA. V: Extreme mass-ratio inspirals*

1.2 Source modeling

Sources and Further Reading

This section gives a brief summary of perturbative methods used to solve the two body problem in general relativity, as well as numerical relativity. The latter is mostly based on Chapter 2 of [58] and Chapters 2 through 4 of [59].

1.2.1 Perturbative approaches

While exact analytical solutions to the Einstein field equations exist for some systems with high levels of symmetry, there is little hope in finding these for dynamic systems such as binary black holes. Any analytical approaches to the relativistic two body problem are based on perturbation theory where the Einstein field equations are expanded in a small parameter.

The earliest such approach, used by Einstein himself [60], is *post-Newtonian* (PN) theory. Here, the equations of motions are described by Newtonian gravitation at zeroth order and relativistic effects are added as an expansion in the bodies' velocities v/c. This theory has been very successful in describing the early inspiral of binary black holes with high accuracy. However, during later stages of the inspiral (which are particularly important to achieve a high SNR for current detectors), the speed of the objects approach the relativistic regime and the theory becomes inaccurate [61].

In *post-Minkowskian* (PM) theory, the field equations are expanded in the gravitational constant G itself. This method is particularly effective in systems where the bodies move at relativistic speeds but the gravitational field remains weak such as scattering events. PM theory has seen rapid development in recent years as sophisticated and mature mathematical techniques describing scattering events in quantum field theory have started to be applied to binary black hole systems [62]. However, as of today, its use for gravitational wave detection and parameter estimation remains limited.

A third avenue is the *gravitational self-force* approach (GSF) which expands the equations of motions in the mass ratio q of the two black holes. Here, the larger black hole of the system is denoted the primary body and the smaller black hole the secondary. At zeroth order, the secondary body moves on a geodesic of the spacetime created by the primary. Higher order terms in the expansion then capture the effect of the secondary's presence onto its own motion

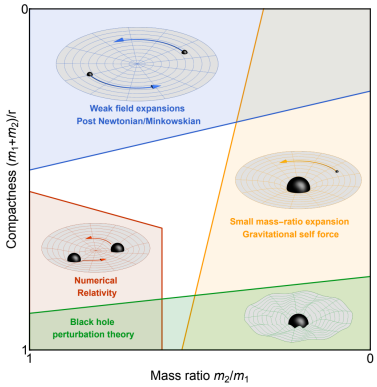

Figure 1.7: A diagram showing the domain of validity for different approaches to the relativistic two body problem. Source: [51]

[60]: Einstein (1915), *Explanation of the Perihelion Motion of Mercury from the General Theory of Relativity*

[61]: Blanchet (2014), *Gravitational Radiation from Post-Newtonian Sources and Inspiralling Compact Binaries*

[62]: Bjerrum-Bohr et al. (2022), *The SAGEX review on scattering amplitudes Chapter 13: Post-Minkowskian expansion from scattering amplitudes*

as its mass distorts the spacetime around it. This approach is particularly suitable for high mass ratio binaries such as IMRIs and EMRIs. Gravitational self-force theory has so far been developed up to first order for the full parameter space [63, 64] and up to second order for non-spinning black holes on quasi-circular orbits [65, 66]. Extending the second order terms to the full parameter space is currently considered the only promising approach to generate EMRI waveforms of sufficient accuracy for LISA [67].

Finally, the effective one body (EOB) formalism uses a Hamiltonian framework to transform the two-body problem into an equivalent one-body system where a test particle moves in an effective potential [68–70]. This allows it to include post-Newtonian expansion terms while exactly satisfying the geodesic test body limit. It is further improved by calibrating its terms to numerical relativity simulations and has even started to include results from post-Minkowskian [71] and gravitational self-force theory [72]. The waveforms it generates remain accurate until the late inspiral of binary black holes and have been employed both in detection templates as well as for parameter estimation.

Overall, all analytical approaches presented here remain accurate in limited regions of parameter space and none are able to accurately describe the dynamics of a BBH system in the highly relativistic regime near the plunge and merger. A plot indicating the regions of parameter space where different approximations are effective is shown in Fig. 1.7. At this stage, analytical perturbation theory inevitably breaks down and the full Einstein equations have to be solved.

[63]: Barack et al. (2019), *Self-force and radiation reaction in general relativity*

[64]: Pound et al. (2022), *Black Hole Perturbation Theory and Gravitational Self-Force*

[65]: Pound et al. (2020), *Second-Order Self-Force Calculation of Gravitational Binding Energy in Compact Binaries*

[66]: Wardell et al. (2021), *Gravitational waveforms for compact binaries from second-order self-force theory*

[67]: Burke et al. (2023), *Accuracy Requirements: Assessing the Importance of First Post-Adiabatic Terms for Small-Mass-Ratio Binaries*

[68]: Buonanno et al. (1999), *Effective one-body approach to general relativistic two-body dynamics*

[69]: Buonanno et al. (2000), *Transition from inspiral to plunge in binary black hole coalescences*

[70]: Damour et al. (2011), *The Effective One Body description of the Two-Body problem*

[71]: Khalil et al. (2022), *Energetics and scattering of gravitational two-body systems at fourth post-Minkowskian order*

[72]: Meent et al. (2023), *Enhancing the SEOBNRv5 effective-one-body waveform model with second-order gravitational self-force fluxes*

1.2.2 Numerical relativity

Numerical relativity solves the relativistic two body problem by discretizing the full non-linear Einstein field equations (1.3) over a grid and solving them numerically.

For this thesis, I will explain the steps to numerically solve the simpler but similar problem of the scalar wave equation in curved spacetime, also known as the massless Klein-Gordon equation. This is the same equations that will be solved in the main chapters. This hyperbolic partial differential equation describes the evolution of a scalar field Ψ on a (fixed) spacetime background

$$g^{\mu\nu}\nabla_\mu\nabla_\nu\Psi = 0. \tag{1.11}$$

Solving such an equation numerically requires formulating it as an initial value problem where a set of initial data is advanced through successive time steps. However, Eq. (1.11) (and the Einstein equations) are formulated on a four-dimensional spacetime manifold which first has to be decomposed into a structure that allows for such a prescription.

3+1D decomposition

In the 3+1 decomposition, the spacetime manifold is foliated into a sequence of three-dimensional spatial slices. A global time function t is used to define the slices Σ_t of constant time. This motivates the definition of the lapse [58]

$$\alpha = \left(-g^{\mu\nu}\nabla_\mu t \nabla_\nu t\right)^{-\frac{1}{2}}, \tag{1.12}$$

which measures how much proper time elapses between adjacent time slices and is used to normalize the timelike unit normal vector to the slice

$$n^\mu = -\alpha g^{\mu\nu}\nabla_\nu t. \tag{1.13}$$

The shift vector β^μ measures how much the spatial coordinates are shifted within a slice with respect to n^μ and is defined through [59]

$$t^\mu = \alpha n^\mu + \beta^\mu, \tag{1.14}$$

where $t^\mu = \delta^\mu_t$ connects points with the same spatial coordinates on adjacent time slices. The normal vector also allows us to construct the spatial metric $\gamma_{\mu\nu}$ that is induced on Σ_t as well the extrinsic curvature $K_{\mu\nu}$:

$$\gamma_{\mu\nu} = g_{\mu\nu} + n_\mu n_\nu, \tag{1.15}$$

$$K_{\mu\nu} = \gamma^\nu_\mu \gamma^\sigma_\rho \nabla_\mu n_\sigma. \tag{1.16}$$

The metric $\gamma_{\mu\nu}$ allows one to compute distances within a slice Σ_t. The extrinsic curvature $K_{\mu\nu}$ measures the gradient of the unit normal vector, i.e. how much its direction changes from one point on Σ_t to the next.

All the quantities introduced here are fully spatial $n^\mu\gamma_{\mu\nu} = n^\mu K_{\mu\nu} = n^\mu\beta_\mu = 0$. For contravariant(upper) indices, the time component vanishes when we choose the coordinate time t to foliate our spacetime. The full four-metric is then re-expressed in

[58]: Baumgarte et al. (2010), *Numerical Relativity: Solving Einstein's Equations on the Computer*

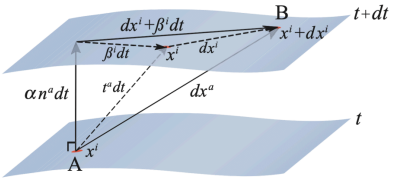

Figure 1.8: The 3+1D decomposition: the spacetime manifold is foliated into hypersurfaces of constant t.
Source: [58]

[59]: Gourgoulhon (2007), *3+1 formalism and bases of numerical relativity*

terms of these quantities as

$$g_{\mu\nu}dx^\mu dx^\nu = -\alpha^2 dt^2 + \gamma_{ij}(dx^i + \beta^i dt)(dx^j + \beta^j dt). \tag{1.17}$$

This decomposition is known as the 3+1D formalism and allows the formulation of Eq. (1.11) as an initial value problem. First, the second order Klein-Gordon equation is transformed into a set of first order equations by introducing the auxiliary variables [73]

[73]: Scheel et al. (2004), *3D simulations of linearized scalar fields in Kerr spacetime*

$$\Pi = -\alpha^{-1}(\partial_t \Psi - \beta^i \partial_i \Psi), \tag{1.18a}$$
$$\Phi_i = \partial_i \Psi. \tag{1.18b}$$

The first order evolution equations of the scalar wave equation in the 3+1D formalism are then given by [74]

[74]: Holst et al. (2004), *Optimal constraint projection for hyperbolic evolution systems*

$$\partial_t \Psi - \beta^i \partial_i \Psi = -\alpha \Pi, \tag{1.19a}$$
$$\partial_t \Pi - \beta^k \partial_k \Pi + \alpha \gamma^{ik} \partial_i \Phi_k = \alpha K \Pi + \alpha \Gamma^i \Phi_i - \gamma^{ij} \Phi_i \partial_j \alpha \tag{1.19b}$$
$$\partial_t \Phi_i - \beta^k \partial_k \Phi_i + \alpha \partial_i \Pi = -\Pi \partial_i \alpha + \Phi_j \partial_i \beta^j. \tag{1.19c}$$

This makes for a set of 5 variables $\{\Psi, \Pi, \Phi_i\}$, each of which is endowed with its own hyperbolic evolution equation. On any timeslice Σ_t, the equations are evaluated and then advanced to the next slice $\Sigma_{t+\Delta t}$ using an appropriate PDE solver as explained in Section 1.3.

Constraints

The Klein Gordon equation (1.11) is now formulated as an initial value problem that allows for evolution through different time slices. However, if one were to try to evolve Eqs. (1.19), the solution would likely blow up very quickly. In this section, I will show the root of this instability by considering the constraint evolutions. This is an essential technique in numerical relativity to formulate stable evolution equations [74] and boundary conditions [75].

[74]: Holst et al. (2004), *Optimal constraint projection for hyperbolic evolution systems*

[75]: Kidder et al. (2005), *Boundary conditions for the Einstein evolution system*

The first order reduction variables in Eq. (1.18) introduce the constraint fields [74]

$$C_i = \partial_i \Psi - \Phi_i, \tag{1.20}$$
$$C_{ij} = \partial_i \Phi_j - \partial_j \Phi_i. \tag{1.21}$$

These must vanish for any solution to the original second order Klein-Gordon equation Eq. (1.19). However, because the evolution

equations (1.19) evolve Ψ and Φ_i separately, this is not guaranteed.

A stable evolution requires that these constraints do not grow and are ideally suppressed with time. Their behavior can be studied by considering the evolution equations of the constraints themselves which can be constructed by combining Eqs. (1.19) appropriately:

$$\partial_t C_i = \beta^k \partial_k C_i + \partial_i \beta^k C_k = \mathcal{L}_\beta C_i \tag{1.22}$$

$$\partial_t C_{ij} = \beta^k \partial_k C_i + 2\partial_i \beta^k C_{kj} = \mathcal{L}_\beta C_{ij}, \tag{1.23}$$

where $\mathcal{L}_\beta$ is the Lie derivative along the shift vector. The constraints therefore evolve according to an advection equation where any initial violations are transported along the flow integral curves defined by the shift vector. Further insight into the constraint evolutions can be gained through the method of characteristics by implicitly choosing a proper time τ that fulfills:

$$\frac{dt}{d\tau} = 1 \qquad\qquad \frac{dx^k}{d\tau} = -\beta^k, \tag{1.24}$$

corresponding to an observer that moves against the shift vector. The total derivative with respect to this parameter can then be expressed as

$$\frac{dC_i}{d\tau} = \frac{\partial C_i}{\partial t}\frac{dt}{d\tau} + \frac{\partial C_i}{\partial x^k}\frac{dx^k}{d\tau} \tag{1.25}$$

$$= \frac{\partial C_i}{\partial t} - \frac{\partial C_i}{\partial x^k}\beta^k \tag{1.26}$$

$$= \partial_i \beta^k C_k, \tag{1.27}$$

where in the last line, we have used the constraint evolution equation (1.22). This is a matrix differential equation of the form $\dot{\vec{v}} = \mathbf{A}\vec{v}$, solved by a sum of exponential functions. The constraints will be exponentially suppressed if all eigenvalues of $\mathbf{A} = \partial_i \beta^k$ are negative, otherwise they will be exponentially growing. However, the spatial derivative of the shift may well have positive eigenvalues leading to uncontrolled constraint growth.

The behavior can be remedied by using the freedom of adding arbitrary factors of the constraints themselves to the evolution equations. It suffices to add the extra term $\gamma_2 \alpha C_i$ to the source term of Eq. (1.19c) which alters the constraint evolution (1.22)

according to

$$\partial_t C_i - \mathcal{L}_\beta C_i = -\gamma_2 \alpha C_i \tag{1.28}$$
$$\partial_t C_{ij} - \mathcal{L}_\beta C_{ij} = -\gamma_2 \alpha C_{ij}. \tag{1.29}$$

The derivative with respect to the proper time defined through Eqs. (1.24) then becomes

$$\frac{dC_i}{d\tau} = \partial_i \beta^k C_k - \gamma_2 \alpha C_i. \tag{1.30}$$

In matrix form, the equation is given by $\dot{\vec{v}} = (\mathbf{A} - \gamma_2 \alpha \mathbf{I})\,\vec{v}$, where $\mathbf{A} = \partial_i \beta^k$ is the original coefficient matrix. By considering the characteristic polynomial of $(\mathbf{A} - \gamma_2 \alpha \mathbf{I})$, we can immediately see that the eigenvalues of the original coefficient matrix are all subtracted by $\alpha\gamma_2$. We therefore choose $\gamma_2 > 0$ (since $\alpha > 0$ for any physical system) so that all eigenvalues of $(\mathbf{A} - \gamma_2 \alpha \mathbf{I})$ are negative and the constraints are exponentially suppressed everywhere in the domain.

The final set of evolution equations is given by (2.8) in Chapter 2 below. These contain an additional parameter γ_1 that allows control over some characteristic speeds but is usually set to 0. Finally, some terms proportional to $\gamma_1\gamma_2$ ensure that the system remains symmetric hyperbolic which is a sufficient condition for a stable evolution.

Einstein Equations

The 3+1D form of the Einstein equations are known as the ADM equations. They describe the evolution of the spatial metric γ_{ij} and the extrinsic curvature K_{ij}

$$\partial_t \gamma_{ij} = -2\alpha K_{ij} + D_i \beta_j + D_j \beta_i \tag{1.31a}$$
$$\begin{aligned}\partial_t K_{ij} = {} & \alpha(R_{ij} - 2K_{ik}K^k_j + KK_{ij}) - D_i D_j \alpha \\ & - 8\pi\alpha(S_{ij} - \frac{1}{2}\gamma_{ij}(S - \rho)) + \beta^k \partial_k K_{ij} + K_{ik}\partial_j \beta^k + K_{kj}\partial_i \beta^k,\end{aligned} \tag{1.31b}$$

where D_i is the covariant derivative compatible with γ_{ij}, $\rho = n_\alpha n_\beta T^{\alpha\beta}$ is the energy density and S_{ij} is the stress-energy-tensor projected onto the spatial hypersurface, $S_{ij} = \gamma_{i\alpha}\gamma_{j\beta}T^{\alpha\beta}$. Its trace is given by $S = \gamma^{ij}S_{ij}$.

The evolution equations are supplemented by a set of elliptic constraint equations that relate the initial metric to the extrinsic

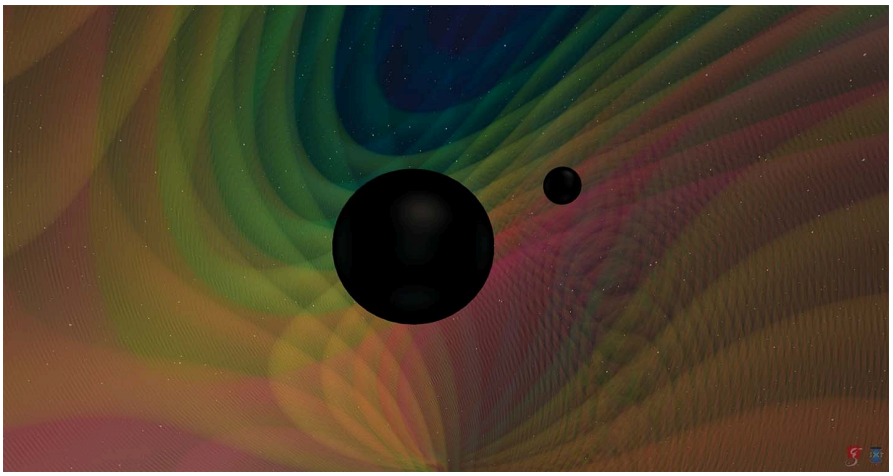

Figure 1.9: A numerical relativity simulation of a binary black hole system. Shown are the two apparent horizons on a time slice of fixed coordinate time t.
Source: Nils Vu & SXS collaboration

curvature as well as any matter content present on the manifold. They are given by the Hamiltonian constraint

$$R + K^2 - K_{ij}K^{ij} = 16\pi\rho \tag{1.32}$$

and the momentum constraint

$$D_j(K^{ij} - \gamma^{ij}K) = 8\pi S^i, \tag{1.33}$$

where $S_i = -\gamma^{ij}n^\alpha T_{\alpha j}$ is the momentum density.

The constraint equations must be satisfied on every time slice so that the data satisfies the Einstein equations. Specifying initial data for the Einstein equations is therefore significantly harder than for the scalar wave equation as these elliptic PDEs have to be solved to generate it. One of my co-author publications [76] derives and implements such an elliptic solver used to generate initial data for binary black hole evolutions.

The evolution equations (1.31) are not yet in a suitable form for numerical implementation as coordinates have to be chosen first by fixing the lapse α and shift β^i. The construction of a coordinate system appropriate for numerical evolution is not obvious as most systems will admit singularities which cause the simulation to fail. Common choices are the BSSN system [77, 78], Generalized Harmonic coordinates [79, 80] and the CCZ4 formalism [81]. An example of a BBH simulation is shown in Figure 1.9.

[76]: Vu et al. (2022), *A scalable elliptic solver with task-based parallelism for the SpECTRE numerical relativity code*

[77]: Shibata et al. (1995), *Evolution of three-dimensional gravitational waves: Harmonic slicing case*

[78]: Baumgarte et al. (1998), *On the numerical integration of Einstein's field equations*

[79]: Pretorius (2005), *Numerical relativity using a generalized harmonic decomposition*

[80]: Lindblom et al. (2006), *A New generalized harmonic evolution system*

1.3 PDE solvers

In this section, I give a brief and by no means complete overview of the most common methods used for solving hyperbolic PDEs in numerical relativity.

The Klein-Gordon equation is now cast into a form that allows the specification of initial data and exponentially suppresses constraint violations. An appropriate numerical method must now be chosen to integrate this system of partial differential equations.

1.3.1 Finite difference methods

Finite difference methods discretize the solution of the PDE onto a grid of collocation points. At each point, a stencil rule defines a set of neighboring points and coefficients used to approximate the derivative. Examples of a first, second and fourth order stencil are given by

$$\frac{df}{dx} = \frac{f(x+h) - f(x)}{h} + \mathcal{O}(h) \tag{1.34}$$

$$\frac{df}{dx} = \frac{f(x+h) - f(x-h)}{2h} + \mathcal{O}(h^2) \tag{1.35}$$

$$\frac{df}{dx} = \frac{8(f(x+h) - f(x-h)) - (f(x+2h) - f(x-2h))}{12h} + \mathcal{O}(h^4), \tag{1.36}$$

where $f(x)$ is an arbitrary function on an equidistant grid with step size h.

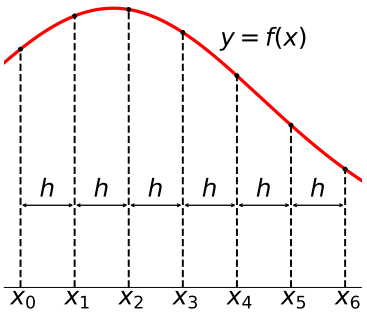

Figure 1.10: An example of a finite difference grid in one dimension.

Figure 1.11 shows how the error of these finite difference approximations scales with the number of grid points when used to compute the derivative of $f(x) = e^{\sin x}$ at $x = \pi/4$. We consider a grid of n equidistant grid points in the interval $[0, 1]$ leading to a step size of $h = 1/n$. Each finite difference method then computes the approximated derivative with the assigned step size; the error with respect to the analytical derivative is plotted on the y-axis against the number of grid points. It scales according to a power law: a finite difference method of order k will carry an error $\propto h^k$.

These rules can all be generalized to compute derivatives in several dimensions. Typically, only the spatial derivatives of the PDE will be evaluated using the finite difference method, which transforms the PDE (space and time derivatives) to an ODE (time derivatives

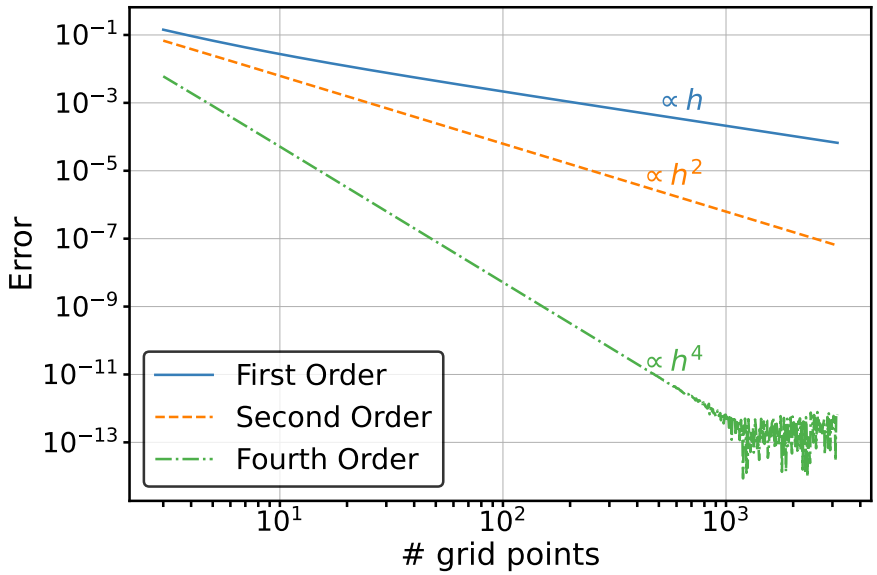

Figure 1.11: The error of computing derivative of $f(x) = e^{\sin x}$ at $x = \pi/4$ using a first, second and fourth order finite difference method.

only) for the value of the field at each grid point. The ODE can then be advanced using an arbitrary time stepper, for instance, a Runge-Kutta method. This is known as the method of lines because the ODE governing the evolution of the function will define a separate line through the time dimension at each grid point. The mesh used to compute the derivatives is typically build up of cubes and can be refined adaptively by e.g. doubling the number of grid points in regions where the derivatives are particularly large and more accuracy is required.

Finite difference methods are usually relatively easy to implement and have the big advantage of being fairly robust. The local nature of computing the derivatives also makes them a common choice for solving PDEs that can admit discontinuous shocks propagating through the domain such as arise in hydrodynamics. One popular choice to handle shocks are essentially non-oscillatory (ENO) methods which detect grid points near a discontinuity and then adaptively select stencils that avoid these points to compute the derivatives [82].

[82]: Harten et al. (1987), *Uniformly high order accurate essentially non-oscillatory schemes, III*

1.3.2 Spectral methods

Spectral methods represent the solution of the PDE as a series expansion in a global, orthogonal basis. A common choice for hyperbolic equations in 3+1 dimensions is to expand the spatial dimensions in a basis $\Psi_k(x^i)$ with unknown time dependent coefficients $a_k(t)$ [83]. In 1+1 dimension, a time dependent function

[83]: Boyd (2013), *Chebyshev and Fourier Spectral Methods: Second Revised Edition*

$f(t, x)$ is then expanded as:

$$f(t, x) = \sum_{k=0}^{N} a_k(t)\psi_k(x). \tag{1.37}$$

Common choices for the basis include Chebyshev polynomials, Legendre polynomials and spherical harmonics. The derivative of each basis function can be exactly represented by the linear combination of several other basis functions. Taking the derivative of a spectral expansion therefore boils down to a matrix multiplication with the so-called differentiation matrix. When inserted into the PDE, what remains is an ODE for the coefficients $a_k(t)$ which can be advanced using an arbitrary time stepper.

Pseudo-spectral methods transform the modal representation of a spectral method to a mesh with points distributed according to a certain quadrature. The Vandermonde matrix contains the value of each basis function ψ_k evaluated at a set of grid points ξ_i, $V_{ki} = \psi_k(\xi_i)$. A spectral expansion can then be transformed to the values of a grid by multiplying this matrix with the coefficients[4]. The choice of quadrature include equidistant points for periodic problems where a Fourier basis is used or Gauss/Gauss-Lobatto quadrature when Chebyshev or Legendre polynomials are employed. Integrals over the grid can then be computed using a quadrature rule, e.g. to recover the spectral coefficients.

4: This is rarely done with direct matrix multiplication as special properties of the Vandermonde matrix often allows for more efficient evaluations such as through a Fast Fourier Transformation.

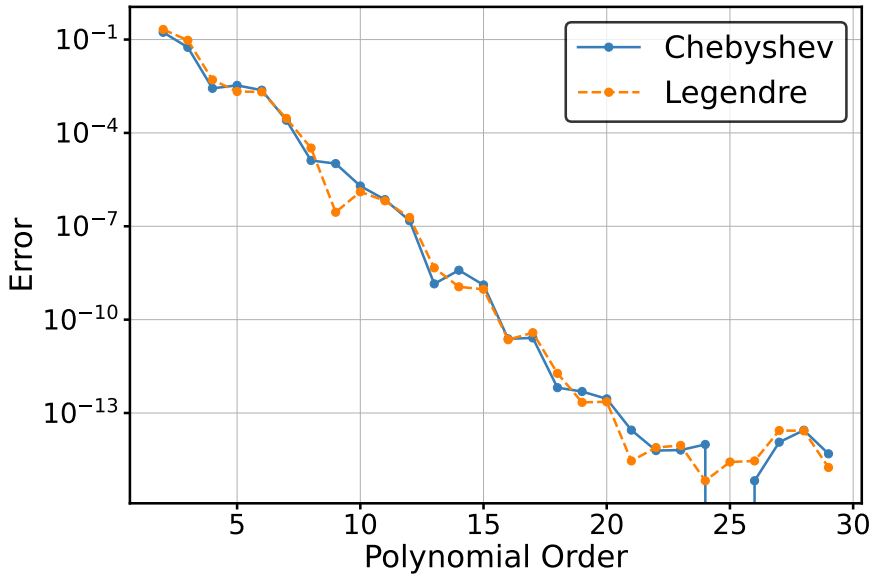

Figure 1.12: The error of computing the derivative of $f(x) = e^{\sin x}$ at $x = \pi/4$ using a spectral method with Chebyshev and Legendre polynomials.

Spectral methods have the enormous advantage that their solution converges exponentially with the polynomial order for smooth problems. Figure 1.12 shows the error of computing the derivative of $f(x) = e^{\sin x}$ at $x = \pi/4$ with a spectral method using both

Chebyshev and Legendre polynomials with Gauss quadrature. Double precision of 10^{-14} is a achieved with a polynomial of order 21, corresponding to 22 grid points for a pseudo-spectral method. This is much less than the finite difference method in Fig. 1.11 which required over 1000 points. The accuracy of the evolution can be dynamically adjusted by changing the polynomial order. While this makes spectral methods extremely effective for smooth problems, they struggle with problems that have many different regions requiring different resolutions and particularly discontinuities such as shocks. The Gibbs phenomenon causes the polynomials to oscillate around the shock and severely suppress the convergence behavior. A spectral method will have heavily reduced convergence in a broader region around the discontinuity and their global nature does not allow to increase accuracy in a small subset of the domain. An example of this is shown in Fig. 1.13. Some techniques such as limiters exist to address the issues but are not always useful.

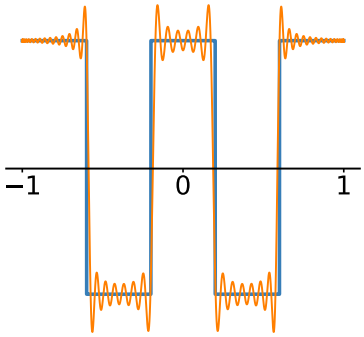

Figure 1.13: An illustration of the Gibbs phenomenon arising when discontinuous function is approximated with a Chebyshev series of polynomial order 100.

1.3.3 Discontinuous Galerkin methods

Finally, the discontinuous Galerkin (DG) scheme is a finite element method closely related to spectral methods [84]. As an example, let us consider the scalar advection equation in one dimension given by

$$\partial_t u(t,x) + v\partial_x u(t,x) = 0. \tag{1.38}$$

Unlike spectral methods, the domain is not globally represented by a series expansion but decomposed into a set of non-overlapping elements which we denote Ω^i. The solution $u(t,x)$ is then expanded into an orthogonal basis within each element

$$u^i(t,x) = \sum_{j=0}^{N} a_j^k(t)\psi_j(x) \qquad x \in \Omega^i. \tag{1.39}$$

In a nodal DG method, this expansion is then projected onto a mesh endowed with a certain quadrature analogous to a pseudo-spectral method. A weak solution to the PDE is constructed by demanding that the projection of this equation onto the expansion basis $\psi_k(x)$ vanishes within each element[5]

$$\int_{\Omega^i} \partial_t u^i(t,x)\psi_k(x)dx + v\int_{\Omega^i} \partial_x u^i(t,x)\psi_k(x)dx = 0. \tag{1.40}$$

[84]: Hesthaven et al. (2007), *Nodal Discontinuous Galerkin Methods: Algorithms, Analysis, and Applications*

5: This is known as a Galerkin projection/method, if the set of test functions onto which the expansion is projected is the same as the basis functions used to expand the solution.

The second term can be transformed using integration by parts yielding

$$\int_{\Omega^i} \partial_t u^i \psi_k dx + v \int_{\Omega^i} u^i \partial_x \psi_k dx = - \oint_{\partial\Omega^i} \hat{n} \cdot (v u^i)^* \psi_k dx, \quad (1.41)$$

where we have dropped the explicit space and time dependencies. The vector $\hat{n}$ is normal to the boundary of the DG element $\partial\Omega^i$ and reduces to ±1 in the one dimensional case. It is contracted with the term $(vu^i)^*$, known as the numerical flux. The right hand side of this equation is integrated over the boundary $\partial\Omega^i$ of the element. However, at this point the flux is given both by the element Ω^i itself and the neighboring elements $\Omega^{i\pm1}$. Different choices of numerical flux use different combinations of the two solutions to construct the surface integral. It is not always clear which numerical flux will give the most accurate results but the choice is ideally motivated by the physical properties of the PDE.

When the expansion (1.39) is inserted into the DG scheme (1.41), only integrals of the basis functions remain captured by the mass matrix

$$\mathcal{M}^i_{jk} = \int_{\Omega^i} \psi_j(x)\psi_k(x)dx \quad (1.42)$$

and the stiffness matrix

$$\mathcal{S}^i_{jk} = \int_{\Omega^i} \psi_j(x)\partial_x\psi_k(x)dx. \quad (1.43)$$

All these integrals can be pre-computed using the quadrature rule defined by the grid of each element, greatly saving computational cost.

The DG method has the big advantage that it can locally change its resolution by both changing the polynomial order within an element (p-refinement) or splitting/merging an element into smaller/larger elements (h-refinement). This gives it more flexibility for problems which have varying accuracy requirements within different parts of the domain. Additionally, there is no enforced continuity between elements so discontinuities can be resolved if they are placed on an element boundary. This is very effective for non-moving discontinuities; shocks that traverse the domain however, will cause Gibbs oscillations within an element as they do for spectral methods.

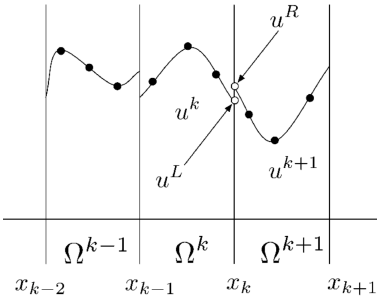

Figure 1.14: An example of a discontinuous Galerkin finite element grid in one dimension. Source: [85]

1.4 The SpECTRE numerical relativity code

This section gives an overview of SpECTRE [86] as well as some motivation that led to the most important design and infrastructure choices.

1.4.1 Moore's law

Moore's Law, originally posited by Gordon Moore in 1965 [87], observed that the number of transistors on a microchip doubles approximately every two years, resulting in a corresponding increase in computational power and a decrease in relative cost. Figure 1.15 shows this trend, where the orange triangles demonstrate the exponential growth of transistors built into a single computer chip until today.

[87]: Moore (2006), *Cramming more components onto integrated circuits, Reprinted from Electronics, volume 38, number 8, April 19, 1965, pp.114 ff.*

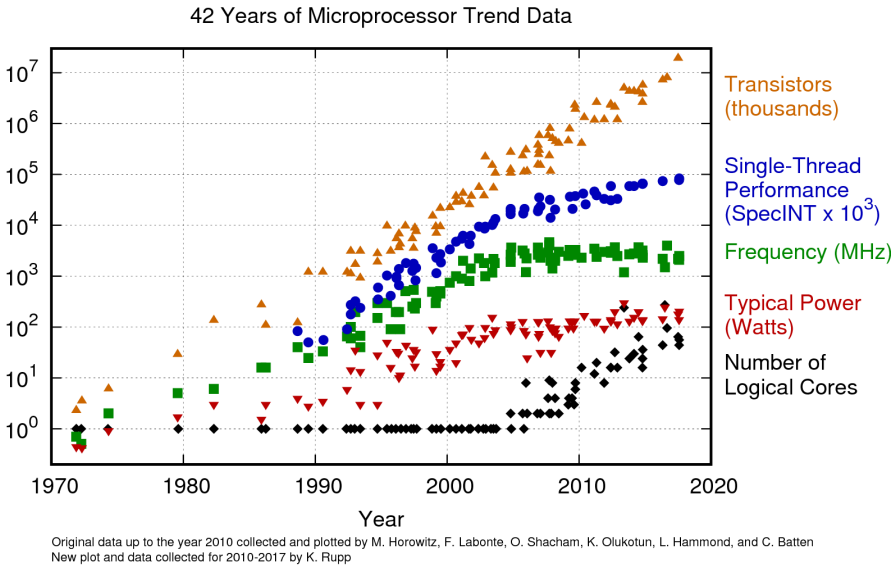

Figure 1.15: The evolution of microprocessor properties such as transistors, clocking frequency and number of cores since 1970. Source: [88]

This growth was originally driven by continually shrinking the transistor sizes and increasing the clocking speed of a single processor. Around the year 2000, transistor dimensions became so small that physical limitations of power dissipation and heat generation could not be overcome and the clocking speed stalled in the GHz regime. The green squares show how the frequency of singular CPUs increased exponentially until 2000 and has remained at approximately the same value since.

At this point, integrated circuits started to shift towards multi-core architectures, adding multiple processing units to a single chip to sustain the exponential performance improvements. The black squares show the number of logical cores within a chip starting

to grow exponentially in the early 2000s. Modern HPC systems, as used for the results of this thesis often have 100 cores within a single chip. While these architectures have sustained the growth in the theoretically achievable performance of an integrated circuit, not all algorithms are equally suitable for parallel architectures.

1.4.2 The Spectral Einstein Code (SpEC)

The spectral Einstein code [89, 90] (SpEC) is a code used for generating gravitational waveforms by solving the Einstein field equations with a pseudo-spectral method. For smooth problems such as binary black holes, the spectral method achieves exponential convergence which has allowed it to produce highly accurate and long waveforms with great computational efficiency, particularly compared to finite difference codes. Today, SpEC has been used to produce the largest and most accurate waveform catalogues [91] in existence which are used e.g. for the calibration of EOB models as well the creation of surrogate models [92, 93].

[89]: Boyle et al. (2007), *Testing the accuracy and stability of spectral methods in numerical relativity*
[90]: Mroue et al. (2013), *Catalog of 174 Binary Black Hole Simulations for Gravitational Wave Astronomy*

[91]: Boyle et al. (2019), *The SXS Collaboration catalog of binary black hole simulations*
[92]: Islam et al. (2022), *Surrogate model for gravitational wave signals from nonspinning, comparable-to large-mass-ratio black hole binaries built on black hole perturbation theory waveforms calibrated to numerical relativity*
[93]: Yoo et al. (2023), *Numerical relativity surrogate model with memory effects and post-Newtonian hybridization*

However, the pseudo-spectral method has some limitations: firstly, it is unsuitable for problems in General Relativity that admit shocks such as binary neutron stars. This can be partially remedied by evolving the equations of general relativistic hydrodynamics on a separate grid using a shock-capturing finite difference method [94, 95]. However, this is not fully self-consistent and loses a lot of the speed due to lack of spectral convergence.

Secondly, the global nature of the method means it is limited in its usage of increasingly parallel computing systems. SpEC partially addresses this issue by dividing its global domain into smaller sub-domains which can be evolved on separate computational cores and communicate over boundary conditions. However, most simulations today can not make full use of modern computational nodes with over $\sim$ 100 cores.

[94]: Foucart et al. (2019), *Gravitational waveforms from spectral Einstein code simulations: Neutron star-neutron star and low-mass black hole-neutron star binaries*
[95]: Foucart et al. (2019), *Numerical simulations of neutron star-black hole binaries in the near-equal-mass regime*

1.4.3 SpECTRE

These limitations motivated the development of a new code, SpECTRE [86] which is also used to generate the results for this thesis. It employs a DG method to solve both elliptic and hyperbolic PDEs. DG methods are naturally suitable for parallel computing systems as the domain is split up into many local elements, which can be freely distributed on the computational cores assigned to the

[86]: Deppe et al. (2024), *SpECTRE*

simulation. Each time step, neighboring elements exchange their boundary data to compute the numerical flux which minimizes inter-nodal communication and avoids any global synchronization points. This is further optimized through the use of the task-based parallelism platform Charm++ [96], which allows elements to be dynamically migrated across different cores to reduce the idle time and maximize the parallel efficiency of the evolution.

[96]: Kale et al. (2021), *UIUC-PPL/charm: Charm++ version 7.0.0*

SpECTRE is also able to resolve shocks via the *subcell method* [97]. This algorithm is able to detect when a DG element does not achieve adequate convergence due to the presence of a discontinuity in the cell. When this occurs, the solution is projected onto a finite difference grid and a shock capturing scheme is used to correctly resolve the discontinuity. Many problems in physics, particularly hydrodynamics will be smooth almost everywhere with the exception of some shocks occurring at rare occasions. Using this hybrid DG-FD method, the evolution is able to retain exponential convergence for the majority of the domain and use the far less efficient finite-difference method only where necessary [98].

[97]: Deppe et al. (2022), *A high-order shock capturing discontinuous Galerkin–finite difference hybrid method for GRMHD*

[98]: Deppe et al. (2024), *Binary neutron star mergers using a discontinuous Galerkin-finite difference hybrid method*

1.5 Simulating intermediate mass ratio black holes

Here I briefly describe the difficulties involved in simulating intermediate mass ratio binary black holes as well as the current state of simulations.

In the last few sections, I explained how the waveforms created by numerical relativity are crucial for the detection and interpretation of gravitational wave signals. Here, I motivate the need for numerical simulations of IMRI systems for future detectors and the difficulties they currently encounter.

Accurate theoretical modeling of such systems is essential for detector operation and data analysis but no methods are currently able to describe such high mass ratio binaries within the required errors. A promising approach for EMRIs is the gravitational self-force explained in Section 1.2. However, it remains unclear whether this method will be able to produce accurate waveforms for IMRIs, where the larger mass ratio will induce higher errors in the expansion.

The problem of generating IMRI template banks becomes even more difficult due to the non-vanishing eccentricity of the binary.

Current template banks have until recently been neglecting this effect [99] due to orbital circularization: for binary black holes of similar mass, the emission of gravitational waves near the periastron causes the system to circularize [100]. While there have been efforts to detect remnant eccentricity in current data [28, 101], the detections themselves do not rely on theoretical modeling of eccentric waveforms. IMRIs, however, are expected to emit gravitational waves in the detector band with significant orbital eccentricity because the circularization effect becomes suppressed with smaller mass ratios. This adds an extra dimension to the parameter space that needs to be covered by waveforms.

[99]: Abbott et al. (2019), *Search for Eccentric Binary Black Hole Mergers with Advanced LIGO and Advanced Virgo during their First and Second Observing Runs*

[100]: Peters et al. (1963), *Gravitational radiation from point masses in a Keplerian orbit*

[28]: Bonino et al. (2023), *Inferring eccentricity evolution from observations of coalescing binary black holes*

[101]: Romero-Shaw et al. (2022), *Four Eccentric Mergers Increase the Evidence that LIGO–Virgo–KAGRA's Binary Black Holes Form Dynamically*

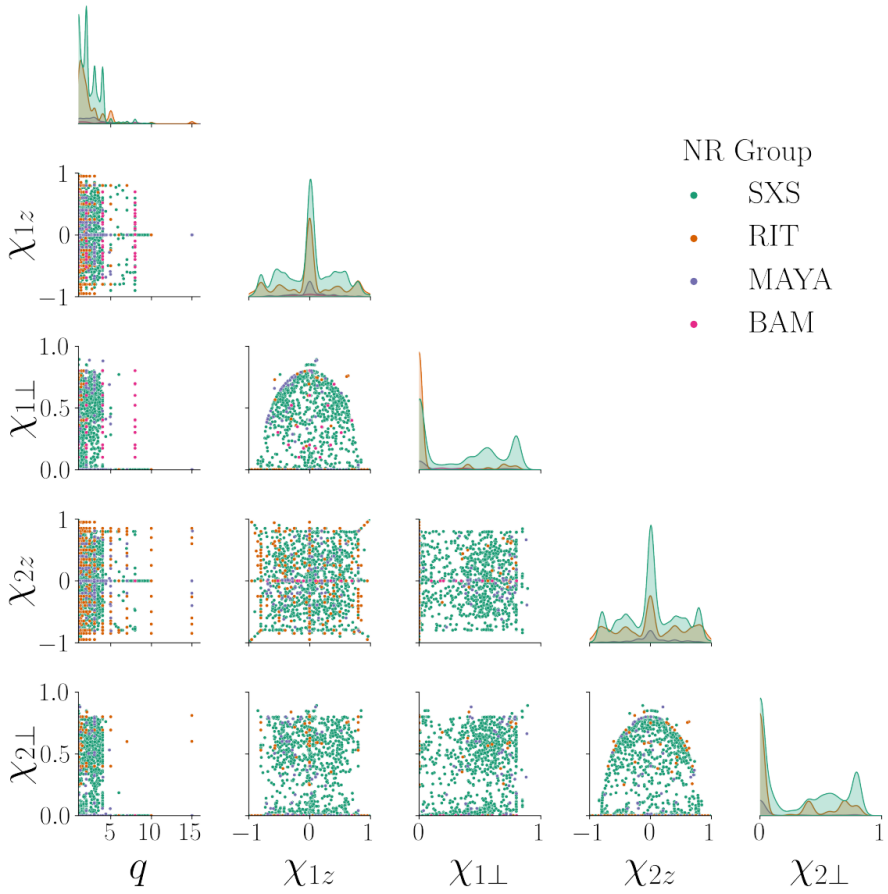

Figure 1.16: The distribution of numerical relativity simulations available from different groups in the parameter space of effective spin χ and mass ratio q.
Source: [51]

For the later stages of the inspiral, numerical relativity remains a great candidate for generating these signals. However, few simulations exist for systems with small mass ratios. Figure 1.16 shows the latest distribution of gravitational waveforms in terms of effective spin χ and the mass ratio[6] q. While the parameter space for waveforms with mass ratio $q < 5$ ($q > 0.2$) is covered fairly densely, waveforms for BBH systems with larger mass ratios are sparse.

6: This plot uses the convention of a mass ratio $q > 1$ which is the inverse of the definition used in this thesis.

The reason for this is mostly related to the Courant-Friedrichs-Lewy (CFL) condition which places an upper limit on the time step

that may be employed to advance the solution. When employing an explicit time-stepping scheme, the CFL condition requires that the time step Δt be sufficiently small relative to the spatial grid spacing Δx

$$\Delta t \leq \Delta x / \lambda_{max}, \tag{1.44}$$

where λ_{max} is the maximum wave/characteristic speed of the PDE. If this condition is violated, the solution will typically blow up exponentially.

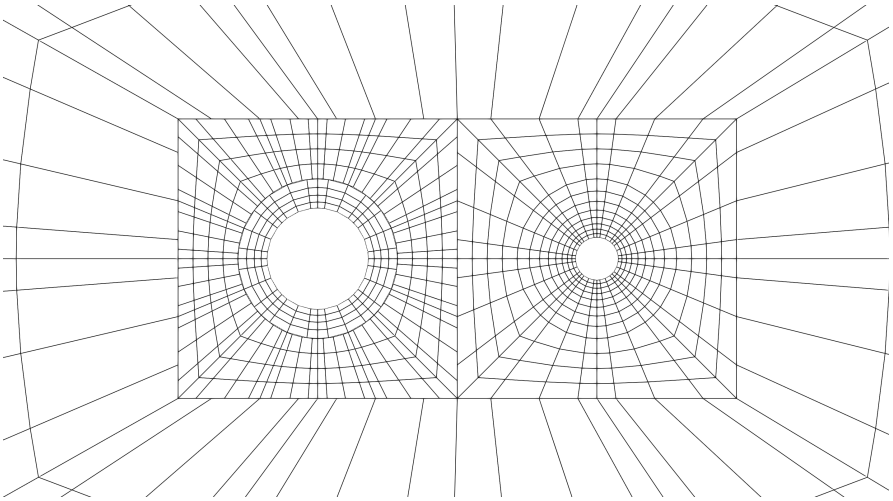

Figure 1.17: A binary black hole domain showing the much tighter grid spacing near the smaller black hole on the right than around the larger black hole on the left.

This effect is particularly punishing for binary black holes of small mass ratios because of the scale disparity in the computational domain. As the size of a black hole's event horizon decreases with its mass, the distance between grid points Δx next to the smaller black hole will be tighter than the grid points next to the larger black hole by a factor of q. An example of such a grid with mass ratio $q \approx 0.3$ can be seen in Figure 1.17. The maximum time step permitted by the CFL-condition then scales about linearly with the mass ratio. Simulating a BBH with $q = 0.1$ for a fixed amount of orbits is then ten times as expensive to simulate as an equal mass binary and IMRIs with $q < 0.01$ become entirely impossible.

In this thesis, I try to tackle this problem by excising a much larger sphere around the smaller black hole and employing a perturbative solution inside this worldtube. This method was first initialized by [1] for a scalar toy problem in 1+1D dimensions. In Chapter 2, I continue this work by generalizing the method to 3+1 dimensions using SpECTRE. In Chapter 3, I add the back-reaction of the scalar field to the charge's orbit and explore the accuracy of this method for quasi-circular orbits. Highly eccentric orbits and hyperbolic encounters are analyzed in Chapter 4. In the final Chapter 5, I summarize this work and give a brief outlook on the gravitational case.

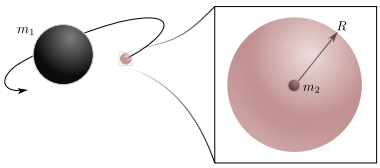

Figure 1.18: A sketch of the worldtube excision method.
Source: [1]

[1]: Dhesi et al. (2021), *Worldtube excision method for intermediate-mass-ratio inspirals: Scalar-field toy model*

Worldtube excision method: scalar-field model in 3+1D

2

This chapter is based on my lead-author publication [102]. It describes the worldtube excision method used for simulating a scalar charge on circular geodesics in Schwarzschild spacetime. My contributions to this work include the derivation and implementation of the matching algorithm. I also produced and analyzed all results.

2.1 Introduction

Inspiraling binary black holes (BBHs) are the most numerous source of gravitational wave signals detected by the LIGO and Virgo observatories [20, 103–105]. The mass ratio is one of the most important characteristics of these binaries, and observations so far [105–109] predominantly find mass ratios close to unity. However, GW190814 and GW200210_092254 have mass ratios $q \equiv m_2/m_1 \sim 0.11$ [20, 43], and GW191219_163120—where the secondary's mass suggests it is a neutron star—is estimated to have $q \sim 0.04$ [20].

It is likely that upcoming observing runs by ground-based detectors will continue to record binaries with small mass-ratios. Future ground-based detectors like the Einstein Telescope [39] and Cosmic Explorer [40], featuring an improved low-frequency sensitivity, will be able to detect the capture of stellar-mass black holes (BHs) by intermediate-mass BHs, with mass-ratios down to $q \sim 10^{-3}$ [38]. Moreover, space-borne detectors, like the LISA observatory [44, 110], will be sensitive to binaries with mass ratios in the entire range from $q \sim 1$ to extreme mass-ratio inspirals with $q \sim 10^{-5}$ [38, 111–113].

In anticipation of this remarkable expansion in observational reach, it is important to develop accurate theoretical waveform templates that reliably cover the entire relevant range of mass ratios. Standard Numerical Relativity (NR) methods [114] work well for mass ratios in the range $0.1 \lesssim q \leq 1$ (see *e.g.* [91]). However, simulations become progressively less tractable at smaller q, and few numerical simulations have been performed at $q < 0.1$ so far. The root cause is a problematic scaling of the required simulation time with q. Fundamentally, one expects the required simulation time to grow in proportion to q^{-2}, where one factor of q^{-1} is associated

[20]: Abbott et al. (2023), *GWTC-3: Compact Binary Coalescences Observed by LIGO and Virgo during the Second Part of the Third Observing Run*

[43]: Abbott et al. (2020), *GW190814: Gravitational Waves from the Coalescence of a 23 Solar Mass Black Hole with a 2.6 Solar Mass Compact Object*

[20]: Abbott et al. (2023), *GWTC-3: Compact Binary Coalescences Observed by LIGO and Virgo during the Second Part of the Third Observing Run*

[39]: Maggiore et al. (2020), *Science Case for the Einstein Telescope*

[40]: Evans et al. (2021), *A Horizon Study for Cosmic Explorer: Science, Observatories, and Community*

[38]: Jani et al. (2019), *Detectability of Intermediate-Mass Black Holes in Multiband Gravitational Wave Astronomy*

[44]: Amaro-Seoane et al. (2017), *Laser Interferometer Space Antenna*

[110]: Seoane et al. (2013), *The Gravitational Universe*

[114]: Baumgarte et al. (2010), *Numerical Relativity: Solving Einstein's Equations on the Computer*

with the number of in-band orbital cycles, and the second factor q^{-1} comes from the Courant-Friedrich-Lewy (CFL) stability limit on the time step of the numerical simulation, arising from the requirement to resolve the smaller black hole. The state of the art in small-q NR is represented by the recent simulations performed at Rochester Institute of Technology of the last 13 orbital cycles prior to merger of a black-hole binary system with $q = 1/128$ [115, 116]. Head-on simulations, where the needed evolution time is orders of magnitudes shorter than for inspirals, are possible at even smaller mass-ratios [117, 118]. While these simulations represent an important proof of concept, their computational cost is extremely high, and it is presently impossible to explore the full parameter space including spin and eccentricity.

Binaries with extreme mass-ratios, say $q \lesssim 10^{-4}$, corresponding to a compact object orbiting a massive black hole in a galactic nucleus, can be modeled with a perturbative expansion in q. This "gravitational self-force" (GSF) approach [63, 64] incorporates order-by-order in q the small deviations of the motion of the small body away from the geodesic motion that applies for test-bodies. The GSF approach is the only method for modeling extreme-mass-ratio inspirals, and development is ongoing towards waveform models suitable for signal identification and interpretation with LISA [65, 66, 119–122]. With NR being well-suited to comparable masses and the GSF approach to extreme mass-ratios, the question arises of how to model the intermediate mass-ratio regime. For simple binary systems (of nonspinning black holes in quasi-circular or eccentric inspirals) NR simulations suggest [123, 124] that GSF calculations may be sufficiently accurate even at mass-ratios reaching the NR regime. "Post-adiabatic" GSF waveforms [66] for non-spinning, quasi-circular binaries have shown those predictions were somewhat over-optimistic in the $q > 0.1$ range [125], but they have borne out the prediction for smaller mass ratios $\lesssim 0.1$. However, it remains unclear whether the two methods, separately applied, can achieve reliable waveform models of intermediate-mass-ratio inspirals over the full astrophysically relevant parameter space.

In this chapter, we continue the work of [1] to develop a new approach to the simulation of intermediate-mass-ratio systems, combining NR techniques with black hole perturbation theory. The general idea is to excise a large region around the smaller black hole. Inside this region—a "worldtube" in spacetime—an approximate analytical solution is prescribed for the spacetime metric, arising from the perturbation theory of compact objects

[115]: Lousto et al. (2020), *Exploring the Small Mass Ratio Binary Black Hole Merger via Zeno's Dichotomy Approach*

[116]: Rosato et al. (2021), *Adapted gauge to small mass ratio binary black hole evolutions*

[117]: Sperhake et al. (2011), *Extreme black hole simulations: collisions of unequal mass black holes and the point particle limit*

[118]: Lousto et al. (2023), *Study of the intermediate mass ratio black hole binary merger up to 1000:1 with numerical relativity*

[63]: Barack et al. (2019), *Self-force and radiation reaction in general relativity*

[64]: Pound et al. (2022), *Black Hole Perturbation Theory and Gravitational Self-Force*

[123]: Meent et al. (2020), *Intermediate mass-ratio black hole binaries: Applicability of small mass-ratio perturbation theory*

[124]: Ramos-Buades et al. (2022), *Eccentric binary black holes: Comparing numerical relativity and small mass-ratio perturbation theory*

[66]: Wardell et al. (2021), *Gravitational waveforms for compact binaries from second-order self-force theory*

[125]: Albertini et al. (2022), *Comparing second-order gravitational self-force, numerical relativity, and effective one body waveforms from inspiralling, quasicircular, and nonspinning black hole binaries*

[1]: Dhesi et al. (2021), *Worldtube excision method for intermediate-mass-ratio inspirals: Scalar-field toy model*

in a tidal environment. An NR simulation is set up for the binary, in which the worldtube's interior is excised from the numerical domain, and replaced with the analytical solution. At each time step of the numerical evolution, the numerical solution (outside the worldtube) and analytical solution inside are matched across the worldtube's boundary, in a process that fixes a priori unknown tidal coefficients in the analytical solution, gauge degrees of freedom, and also provides boundary conditions to the NR evolution. The intended effect of this construction is to partially alleviate the scale disparity that thwarts the efficiency of the numerical evolution at small q: The smallest length scales on the numerical domain is now that of the worldtube-radius R, rather than the scale m_2 of the smaller body. As a result, the CFL limit is expected to increase by a factor $R/m_2 \gg 1$, with a comparable gain in computational efficiency.

In Ref. [1], as also in the present work, we consider a linear scalar-field toy model where the small black hole is replaced with a pointlike scalar charge moving on a circular geodesic around a Schwarzschild black hole. Instead of tackling the full Einstein's equations, one solves the less complicated massless linear Klein-Gordon equation for a scalar field. Our previous work [1] decomposed the scalar field into spherical harmonics and solved the resulting 1+1-dimensional (1+1D) partial differential equation for each mode separately. Such a modal decomposition will not be possible in the fully nonlinear BBH case. As a step towards the BBH case, in this chapter, we derive and implement a generalized matching scheme in full 3+1D. Our implementation is publicly accessible as part of the SpECTRE platform [86], a new general-relativistic code developed by the SXS collaboration, which employs a nodal discontinuous Galerkin method with task-based parallelism. The input file for the simulations presented in this chapter is given as supplemental material. (An evolution of the scalar field equation in 3+1D with a point source was performed in [126] using a different method.)

[1]: Dhesi et al. (2021), *Worldtube excision method for intermediate-mass-ratio inspirals: Scalar-field toy model*

[86]: Deppe et al. (2024), *SpECTRE*

[126]: Vega et al. (2009), *Self-force with (3 + 1) codes: A primer for numerical relativists*

The chapter is organized as follows. In Section 2.2 we describe our scalar-field model, and formulate it as an initial-boundary evolution problem suitable for implementation on SpECTRE. Section 2.3 describes the construction of the approximate analytical solution inside the worldtube. In Section 2.4, we show how the unknown parameters of this local solution can be continuously determined from the evolution data on the worldtube boundary, using a set of ordinary differential equations (in time) derived from the Klein-Gordon equations. The fully specified solution inside

the worldtube is then used to formulate boundary conditions for the evolution system. We present the results of our simulations in Section 2.5, and demonstrate a good agreement with both analytical solutions in limiting cases, and numerical results from other simulations. We explore the convergence of our numerical solutions with worldtube size, and show that its rate matches our theoretical expectations. Finally, in Section 2.6, we summarize our findings and discuss the next steps in our program. We use geometrized units throughout the text with $G = c = 1$.

2.2 Numerical field evolution outside the worldtube

We place a pointlike particle with scalar charge q on a fixed, geodesic circular orbit around a Schwarzschild black hole of mass M. The evolution of the scalar field Ψ is governed by the massless Klein-Gordon equation,

$$g^{\mu\nu}\nabla_\mu\nabla_\nu\Psi = -4\pi q \int \frac{\delta^4(x^\alpha - x_p^\alpha(\tau))}{\sqrt{-g}} d\tau. \tag{2.1}$$

Here $g^{\mu\nu}$ is the inverse Schwarzschild metric, and ∇_μ is the covariant derivative compatible with it. $x_p^\alpha(\tau)$ is the particle's geodesic worldline parameterized in terms of proper time τ. In Kerr-Schild coordinates $x^\alpha = (t, x^i)$, parametrized by coordinate time t, the worldline with orbital radius r_p and angular velocity $\omega = (M/r_p^3)^{1/2}$ is given by

$$x_p^\alpha(t) = \Big(t,\ r_p\cos(\omega t),\ r_p\sin(\omega t),\ 0\Big), \tag{2.2}$$

where we have fixed the orbital plane and phase without loss of generality.

We excise the interior of a sphere with constant Kerr-Schild radius $R = \sqrt{\delta_{ij}(x^i - x_p^i)(x^j - x_p^j)}$, centered on the particle's position, from the numerical domain. We refer to this excision region as the worldtube and elaborate in Sec. 2.4 how boundary conditions are provided to the evolution domain.

Outside the worldtube, the numerical evolution of the scalar-field variable $\Psi^{\mathcal{N}}$ ('$\mathcal{N}$' for 'numerical', to contrast with the analytical solution inside the worldtube, to be introduced below) is governed

by the source-free Klein-Gordon equation on the fixed background spacetime:

$$g^{\mu\nu}\nabla_\mu\nabla_\nu\Psi^{\mathcal{N}} = 0. \tag{2.3}$$

The background spacetime is given in the usual 3+1 split,

$$ds^2 = -\alpha^2 dt^2 + \gamma_{ij}(dx^i + \beta^i dt)(dx^j + \beta^j dt), \tag{2.4}$$

where α is the lapse, β^i is the shift and γ_{ij} is the spatial metric on t = const. hypersurfaces. The background spacetime of our simulations is a single Schwarzschild black hole in Kerr-Schild coordinates.

The Klein-Gordon equation is transformed into the standard first-order form by introducing the auxiliary variables [73]

[73]: Scheel et al. (2004), *3D simulations of linearized scalar fields in Kerr spacetime*

$$\Pi = -\alpha^{-1}(\partial_t\Psi^{\mathcal{N}} - \beta^i\partial_i\Psi^{\mathcal{N}}), \tag{2.5a}$$

$$\Phi_i = \partial_i\Psi^{\mathcal{N}}. \tag{2.5b}$$

This introduces two constraint fields [74],

[74]: Holst et al. (2004), *Optimal constraint projection for hyperbolic evolution systems*

$$C_i = \partial_i\Psi^{\mathcal{N}} - \Phi_i, \tag{2.6}$$

$$C_{ij} = \partial_i\Phi_j - \partial_j\Phi_i, \tag{2.7}$$

which must vanish for any solution to the original, second-order evolution equation. Following [127], we write the first-order evolution equations for the vacuum Klein-Gordon equation (2.3) as

[127]: Lindblom et al. (2006), *A new generalized harmonic evolution system*

$$\partial_t\Psi^{\mathcal{N}} - (1+\gamma_1)\beta^i\partial_i\Psi^{\mathcal{N}} = -\alpha\Pi - \gamma_1\beta^i\Phi_i, \tag{2.8a}$$

$$\partial_t\Pi - \beta^k\partial_k\Pi + \alpha\gamma^{ik}\partial_i\Phi_k - \gamma_1\gamma_2\beta^i\partial_i\Psi^{\mathcal{N}} = \alpha K\Pi + \alpha\Gamma^i\Phi_i - \gamma^{ij}\Phi_i\partial_j\alpha - \gamma_1\gamma_2\beta^i\Phi_i, \tag{2.8b}$$

$$\partial_t\Phi_i - \beta^k\partial_k\Phi_i + \alpha\partial_i\Pi - \gamma_2\alpha\partial_i\Psi^{\mathcal{N}} = -\Pi\partial_i\alpha + \Phi_j\partial_i\beta^j - \gamma_2\alpha\Phi_i. \tag{2.8c}$$

The lapse α, shift β^i, spatial metric γ_{ij}, inverse spatial metric γ^{ij}, trace of the extrinsic curvature $K := \gamma^{ij}K_{ij}$ and trace of the spatial Christoffel symbol $\Gamma^i := \gamma^{jk}\Gamma^i_{jk}$ appearing in Eqs. (2.8) depend only on the background Schwarzschild spacetime. Explicitly, they

read as follows in Kerr-Schild coordinates:

$$\alpha = \left(1 + \frac{2M}{r}\right)^{-1/2}, \tag{2.9a}$$

$$\beta^i = \frac{2M\alpha^2}{r^2} x^i, \tag{2.9b}$$

$$\gamma_{ij} = \delta_{ij} + \frac{2M}{r^3} x^k x^l \delta_{ik}\delta_{jl}, \tag{2.9c}$$

$$\gamma^{ij} = \delta^{ij} - \frac{2M\alpha^2}{r^3} x^i x^j, \tag{2.9d}$$

$$K = \frac{2M\alpha^3}{r^2}\left(1 + \frac{3M}{r}\right), \tag{2.9e}$$

$$\Gamma^i = \frac{8M^2 + 3Mr}{(2Mr + 3r^2)^2} x^i, \tag{2.9f}$$

where $r = \sqrt{\delta_{ij} x^i x^k}$ is the areal radius from the central black hole. The variables γ_1 and γ_2 appearing in Eqs. (2.8) are constraint damping parameters. Compared to the first-order reduction presented in [74], the additional term $\gamma_1\gamma_2\beta^i C_i$ in Eq. (2.8b) ensures that the system is symmetric hyperbolic for any values of γ_1 and γ_2 [127]. For γ_2, we found that a central Gaussian profile $\gamma_2 = Ae^{-(\sigma r)^2} + c$ with $A = 10$, $\sigma = 10^{-1}/M$ and $c = 10^{-4}$ results in a long-term stable evolution for all tested systems. We choose $\gamma_1 = 0$ throughout.

[74]: Holst et al. (2004), *Optimal constraint projection for hyperbolic evolution systems*

[127]: Lindblom et al. (2006), *A new generalized harmonic evolution system*

The evolution equations (2.8) are in the general symmetric hyperbolic form

$$\partial_t \psi^a + A^{ia}{}_b \partial_i \psi^b = F^a, \tag{2.10}$$

with $\psi^a := (\Psi, \Pi, \Phi_i)$ representing the set of first-order variables, enumerated by the indices a and b. For the imposition of boundary conditions at a boundary with normal co-vector $\hat{n}_i$, we solve the (left) eigenvalue problem

$$e^{\hat{a}}{}_a \, \hat{n}_i A^{ia}{}_b = v_{(\hat{a})} e^{\hat{a}}{}_b \tag{2.11}$$

for the eigenvalues $v_{(\hat{a})}$ and eigenvectors $e^{\hat{a}}{}_b$, enumerated by the index $\hat{a}$. The $v_{(\hat{a})}$ are known as the characteristic speeds, and the parentheses indicate that there is no implicit sum convention on the right hand side of Eq. (2.11). The co-vector $\hat{n}_i$ is normalized with respect to the three metric, i.e. $\gamma^{ij}\hat{n}_i\hat{n}_j = 1$, and we define $\hat{n}^i = \gamma^{ij}\hat{n}_j$. The characteristic fields $\psi^{\hat{a}}$ are obtained by projecting the evolved variables ψ^a onto the set of eigenvectors $e^{\hat{a}}{}_a$:

$$\psi^{\hat{a}} = e^{\hat{a}}{}_a \, \psi^a. \tag{2.12}$$

For the evolution system (2.8), the characteristic fields are $\psi^{\hat{a}} = (Z^1, Z_i^2, U^+, U^-)$ with

$$Z^1 = \Psi^{\mathcal{N}}, \tag{2.13a}$$
$$Z_i^2 = P_i^k \Phi_k, \tag{2.13b}$$
$$U^\pm = \Pi \pm \hat{n}^i \Phi_i - \gamma_2 \Psi^{\mathcal{N}}. \tag{2.13c}$$

Here, $P_i^k = \delta_i^k - \hat{n}^k \hat{n}_i$ denotes the projection operator orthogonal to $\hat{n}^i$, so that Z_i^2 carries only two degrees of freedom. The corresponding characteristic speeds are $v_{Z^1} = -\hat{n}_i \beta^i (1 + \gamma_1)$, $v_{Z^2} = -\hat{n}_i \beta^i$ and $v_{U^\pm} = -\hat{n}_i \beta^i \pm \alpha$. We note that the fields $U^\pm$ reduce to the known physical retarded/advanced derivatives $\partial_t \Psi \pm \partial_r \Psi$ in flat space with $\gamma_2 = 0$. The other characteristic fields result from the reduction of the PDE system to first order.

Boundary conditions must be specified at the external boundaries of the domain for each characteristic field, if and only if it is flowing into the domain, specifically those with negative characteristic speeds. There are three external boundaries in our domain: one excision sphere within the central black hole, one excision sphere around the scalar charge (the surface of the worldtube), and the outer boundary.

At the black hole excision sphere, all characteristic fields are flowing out of the computational domain into the excised domain, so no boundary conditions need to be applied. For the outer boundary and at the worldtube boundary, the fields Z^1, Z_i^2 may require boundary conditions, while U^- always requires ones and U^+ never requires ones.

Boundary conditions for the physical characteristic field U^- at the outer boundary are derived from the second-order Bayliss-Turkel radiation condition [128]. These boundary conditions are applied with the method of Bjorhus [129]. At the worldtube boundary, the local solution inside the worldtube is used to provide boundary conditions for U^-, as explained in detail in Section 2.4.

[128]: Bayliss et al. (1980), *Radiation boundary conditions for wave-like equations*

[129]: Bjørhus (1995), *The ODE Formulation of Hyperbolic PDEs Discretized by the Spectral Collocation Method*

Boundary conditions for Z^1 and Z_i^2 can be derived by requiring that there are no constraint violations flowing into the domain [75], as described in Appendix 2.7. These constraint-preserving boundary conditions are applied with the method of Bjorhus [129] at the worldtube boundary and at the outer boundary; see Eq. (2.68).

[75]: Kidder et al. (2005), *Boundary conditions for the Einstein evolution system*

The evolution equations (2.8) are solved with SpECTRE [86], which employs a nodal discontinuous Galerkin (DG) scheme

[86]: Deppe et al. (2024), *SpECTRE*

in 3+1 dimensions. The domain is built up of several hundred DG elements, each endowed with a tensor product of Legendre polynomials using Gauss-Lobatto quadrature. The elements are deformed from unit cubes to fit the domain structure using a series of smooth maps as illustrated in Fig. 2.1. Discontinuous Galerkin methods require a choice of numerical flux that dictates how fields are evolved on element boundaries where they are multiply defined [84]. Here we employ an upwind flux.

[84]: Hesthaven et al. (2007), *Nodal Discontinuous Galerkin Methods: Algorithms, Analysis, and Applications*

SpECTRE uses dual coordinate frames [130] to solve the evolution equations. The components of the tensors in the evolution Eqs. (2.8) are constructed in Kerr-Schild coordinates x^i. We refer to these as the *inertial* frame because the coordinates are not rotating with respect to the asymptotic frame at spatial infinity. The evolution equations for the inertial components are solved as functions of co-rotating coordinates $(\bar{t}, x^{\bar{i}}) = (\bar{t}, \bar{x}, \bar{y}, \bar{z})$ given by the transformation

[130]: Scheel et al. (2006), *Solving Einstein's equations with dual coordinate frames*

$$\bar{t} = t, \tag{2.14a}$$
$$\bar{x} = x\cos(\omega t) + y\sin(\omega t), \tag{2.14b}$$
$$\bar{y} = -x\sin(\omega t) + y\cos(\omega t), \tag{2.14c}$$
$$\bar{z} = z. \tag{2.14d}$$

Tensor components in this frame we denote with a bar, as in $g_{\bar{\alpha}\bar{\beta}}$. For more demanding situations (e.g. binary black hole simulations), the transformation $x^i \to x^{\bar{i}}$ can take a much more complicated form [131, 132]. The grid points of the DG domain, as well as the particle position $x^{\bar{i}}_p = (r_p, 0, 0)$ are constant in space in these coordinates, which we will refer to as *grid* coordinates. The internal worldtube solution is evolved in the grid frame directly, which considerably simplifies the formulation of the matching scheme in Sec. 2.4.

[131]: Hemberger et al. (2013), *Dynamical Excision Boundaries in Spectral Evolutions of Binary Black Hole Spacetimes*

[132]: Scheel et al. (2015), *Improved methods for simulating nearly extremal binary black holes*

A Dormand-Prince time stepper is used to advance the solution of the numerical fields with a global time step. We apply a weak exponential filter to the evolution fields after every time step to ensure stability of the evolution.

The code is parallelized using the heterogeneous task-based parallelism framework Charm++ [96]. The inclusion of the worldtube does not adversely impact the parallel efficiency, as its computational cost is negligible compared to even a single DG element evaluation, and no additional communication between cores is introduced.

[96]: Kale et al. (2021), *UIUC-PPL/charm: Charm++ version 7.0.0*

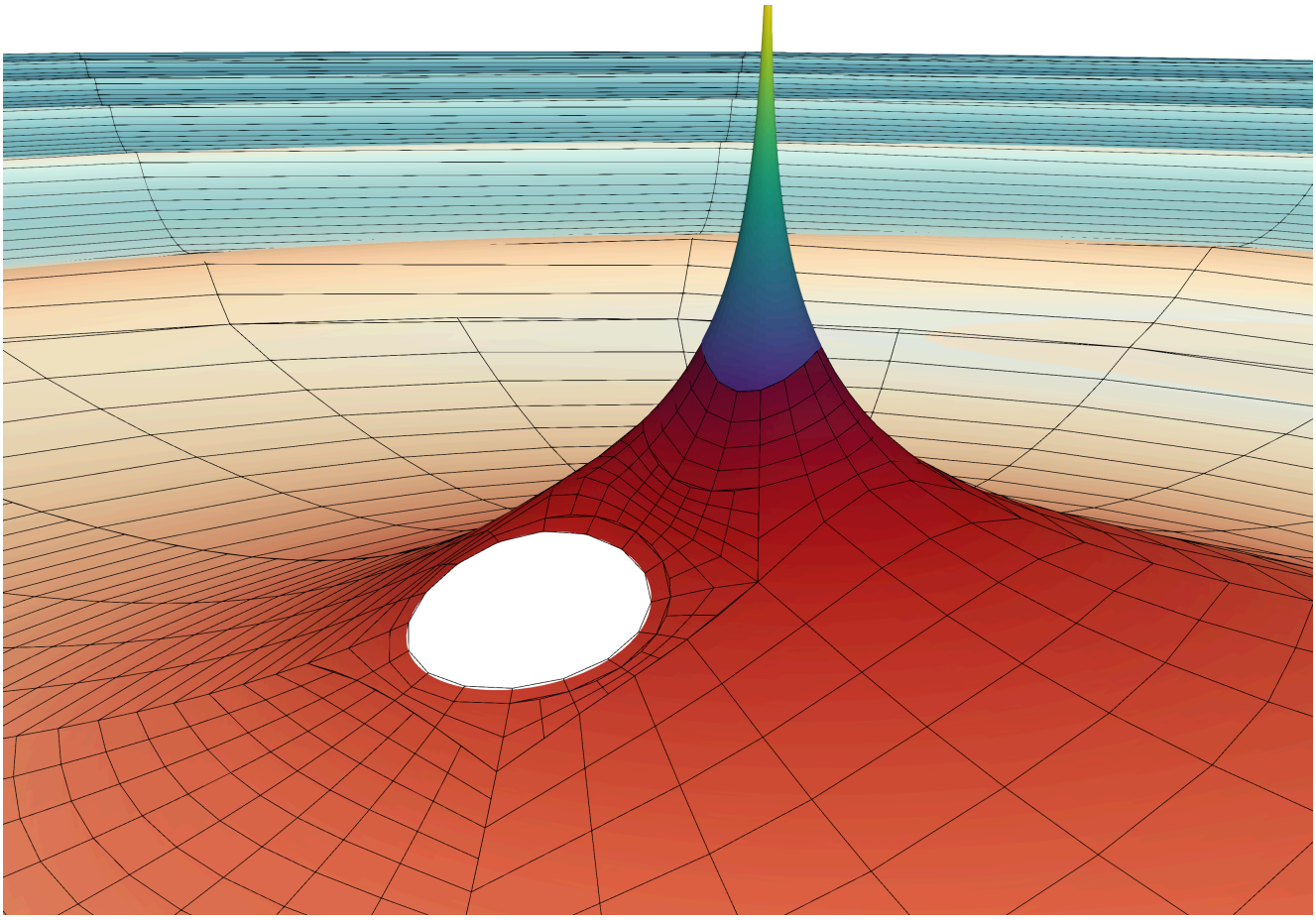

Figure 2.1: Illustration of the computational domain: Shown is the equatorial plane, with height-deformation proportional to the value of the scalar field. The grid lines correspond to the DG-element boundaries of the 3-D numerical evolution. The central blue/green peak represents the region inside the worldtube, where the approximate solution is dominated by the singularity of the scalar field at the point-charge. Left of the peak an excision region is cut out within the horizon of the central black hole. A zoomed-out view of the entire domain is shown in Figure 2.2.

2.3 Approximate solution inside the worldtube

Inside the worldtube, the scalar field is given by an analytical expansion in powers of coordinate distance from the particle's worldline x_p. We use $\Psi^{\mathcal{A}}$ to denote this analytical solution, and we use a formal parameter $\epsilon = 1$ to count powers of the separation between the worldline and the field point.

As in Ref. [1], we split the field $\Psi^{\mathcal{A}}$ into a puncture field $\Psi^{\mathcal{P}}$ and a regular field $\Psi^{\mathcal{R}}$:

$$\Psi^{\mathcal{A}} = \Psi^{\mathcal{P}} + \Psi^{\mathcal{R}}. \tag{2.15}$$

$\Psi^{\mathcal{P}}$ is an approximate particular solution to the inhomogeneous equation (3.1), and it will be fully determined in advance; $\Psi^{\mathcal{R}}$ is an approximate smooth solution to the homogeneous equation,

[1]: Dhesi et al. (2021), *Worldtube excision method for intermediate-mass-ratio inspirals: Scalar-field toy model*

and it will be determined dynamically through matching $\Psi^{\mathcal{A}}$ to $\Psi^{\mathcal{N}}$ at the worldtube boundary.

We express both $\Psi^{\mathcal{P}}$ and $\Psi^{\mathcal{R}}$ in terms of the coordinate distance $\Delta x^\alpha := x^\alpha - \tilde{x}^\alpha$, where $\tilde{x}^\alpha$ is a reference point on x_p. For a given field point x^α at coordinate time t, we let $\tilde{x}^\alpha := x_p^\alpha(t)$ be the point on x_p at the same value of t, such that $\Delta t = 0$. Tensors evaluated at $\tilde{x}^\alpha$ are written with a tilde, as in $\tilde{g}_{\mu\nu}$. To facilitate matching $\Psi^{\mathcal{A}}$ to $\Psi^{\mathcal{N}}$, we ultimately express both $\Psi^{\mathcal{P}}$ and $\Psi^{\mathcal{R}}$ in the co-rotating grid coordinates $(t, x^{\bar{i}})$ introduced in Eq. (2.14), but most of this section applies in both inertial and co-rotating coordinates.

Unlike in Ref. [1], for $\Psi^{\mathcal{P}}$ we use an approximation to the Detweiler-Whiting singular field [133]; this choice ensures that we can calculate the scalar self-force directly from the regular field $\Psi^{\mathcal{R}}$. Covariant expansions of the Detweiler-Whiting singular field are readily available to high order in ϵ; see [134, 135], for example, with [136] deriving the scalar singular field to the highest order in the literature, $\mathcal{O}(\epsilon^4)$. These covariant expressions contain several ingredients. First among them is Synge's world function $\sigma(x, \tilde{x})$ [137], which is equal to half the squared geodesic distance between x and $\tilde{x}$. Its gradient, $\tilde{\sigma}_\alpha := \tilde{\nabla}_\alpha \sigma(x, \tilde{x})$, is a directed measure of distance from $\tilde{x}$ to x. The projection of $\tilde{\sigma}_\alpha$ tangent to the worldline has magnitude

$$\varrho := \tilde{\sigma}_\alpha \tilde{u}^\alpha, \tag{2.16}$$

and the projection normal to the worldline has magnitude

$$s := \sqrt{(\tilde{g}^{\alpha\beta} + \tilde{u}^\alpha \tilde{u}^\beta)\tilde{\sigma}_\alpha \tilde{\sigma}_\beta}\,, \tag{2.17}$$

where $\tilde{u}^\alpha$ is the particle's four-velocity at time t. In terms of these quantities, the covariant expansion of $\Psi^{\mathcal{P}}$ through order ϵ^2 is given by [135, 136]

$$\begin{aligned}\Psi^{\mathcal{P}} = q\Bigg\{&\frac{1}{\epsilon s} + \frac{\epsilon}{6s^3}(\varrho^2 - s^2)\tilde{C}_{u\sigma u\sigma} \\ &+ \frac{\epsilon^2}{24 s^3}\left[(\varrho^2 - 3s^2)\varrho \tilde{C}_{u\sigma u\sigma|u} - (\varrho^2 - s^2)\tilde{C}_{u\sigma u\sigma|\sigma}\right] \\ &+ \mathcal{O}(\epsilon^3)\Bigg\}.\end{aligned} \tag{2.18}$$

Here

$$\tilde{C}_{u\sigma u\sigma} := \tilde{C}_{\alpha\beta\mu\nu}\tilde{u}^\alpha \tilde{\sigma}^\beta \tilde{u}^\mu \tilde{\sigma}^\nu, \tag{2.19}$$

$$\tilde{C}_{u\sigma u\sigma|\sigma} := \tilde{\nabla}_\gamma \tilde{C}_{\alpha\beta\mu\nu}\tilde{u}^\alpha \tilde{\sigma}^\beta \tilde{u}^\mu \tilde{\sigma}^\nu \tilde{\sigma}^\gamma \tag{2.20}$$

[1]: Dhesi et al. (2021), *Worldtube excision method for intermediate-mass-ratio inspirals: Scalar-field toy model*

[133]: Detweiler et al. (2003), *Self-force via a Green's functsion decomposition*

[134]: Haas et al. (2006), *Mode-sum regularization of the scalar self-force: Formulation in terms of a tetrad decomposition of the singular field*

[135]: Wardell et al. (2012), *A Generic effective source for scalar self-force calculations*

[136]: Heffernan et al. (2012), *High-order expansions of the Detweiler-Whiting singular field in Schwarzschild spacetime*

[137]: Synge (1960), *Relativity: The General theory*

are contractions of the Weyl tensor $C_{\alpha\beta\mu\nu}$ and its derivative evaluated at the reference point $\tilde{x}$ on the particle's worldline.

We now express the covariant expansion (2.18) in terms of Kerr-Schild coordinates. To achieve this we follow the method in [135], which begins from an expansion of $\sigma(x, \tilde{x})$ in powers of Δx^α,

[135]: Wardell et al. (2012), *A Generic effective source for scalar self-force calculations*

$$\begin{aligned}\sigma = \frac{1}{2}\tilde{g}_{\alpha\beta}\Delta x^\alpha \Delta x^\beta + \tilde{A}_{\alpha\beta\gamma}\Delta x^\alpha \Delta x^\beta \Delta x^\gamma \\ + \tilde{B}_{\alpha\beta\gamma\delta}\Delta x^\alpha \Delta x^\beta \Delta x^\gamma \Delta x^\delta \\ + \tilde{C}_{\alpha\beta\gamma\delta\rho}\Delta x^\alpha \Delta x^\beta \Delta x^\gamma \Delta x^\delta \Delta x^\rho + \ldots\end{aligned} \tag{2.21}$$

Differentiating this with respect to $\tilde{x}^\alpha$, we obtain

$$\begin{aligned}\tilde{\sigma}_\alpha = -\tilde{g}_{\alpha\beta}\Delta x^\beta + (\frac{1}{2}\tilde{g}_{\beta\gamma,\alpha} - 3\tilde{A}_{\alpha\beta\gamma})\Delta x^\beta \Delta x^\gamma \\ + (\tilde{A}_{\beta\gamma\delta,\alpha} - 4\tilde{B}_{\alpha\beta\gamma\delta})\Delta x^\beta \Delta x^\gamma \Delta x^\delta \\ + (\tilde{B}_{\beta\gamma\delta\rho,\alpha} - 5\tilde{C}_{\alpha\beta\gamma\delta\rho})\Delta x^\beta \Delta x^\gamma \Delta x^\delta \Delta x^\rho + \ldots\end{aligned} \tag{2.22}$$

We then use the identity $2\sigma = \tilde{\sigma}_\alpha \tilde{\sigma}^\alpha$ to recursively determine the coefficients $\tilde{A}_{\alpha\beta\gamma}$, $\tilde{B}_{\alpha\beta\gamma\delta}$, $\tilde{C}_{\alpha\beta\gamma\delta\rho}$ and so on. This yields, for example, $\tilde{A}_{\alpha\beta\gamma} = \frac{1}{4}\tilde{g}_{(\alpha\beta,\gamma)}$. We now contract $\tilde{\sigma}_\alpha$ with the four-velocity, metric and Weyl tensor to get the coordinate expressions for ϱ, s, $\tilde{C}_{u\sigma u\sigma}$, and $\tilde{C}_{u\sigma u\sigma|\sigma}$ as per their definitions (3.30), (3.31), (2.19), and (2.20). Our final expression for $\Psi^{\mathcal{P}}$ is obtained by substituting all of these results into Eq. (2.18) and re-expanding in powers of Δx^α.

We write the result in the style of [138]:

[138]: Barack et al. (2002), *Regularization parameters for the self-force in Schwarzschild space-time. 1. Scalar case*

$$\Psi^{\mathcal{P}} = q\left[\frac{1}{\epsilon s_1} + \frac{\mathrm{P}_3(\Delta x^\alpha)}{s_1^3} + \frac{\epsilon \mathrm{P}_6(\Delta x^\alpha)}{s_1^5} + \frac{\epsilon^2 \mathrm{P}_9(\Delta x^\alpha)}{s_1^7} + \mathcal{O}(\epsilon^3)\right]. \tag{2.23}$$

Here $s_1 = \sqrt{(\tilde{g}_{\alpha\beta} + \tilde{u}_\alpha \tilde{u}_\beta)\Delta x^\alpha \Delta x^\beta}$ is the leading coordinate approximation to s, and $\mathrm{P}_n(\Delta x^\alpha)$ is a polynomial in Δx^α of homogeneous order n.

The form (2.23) is valid in any coordinate system. In the co-rotating grid coordinates, the reference point on x_p is $\tilde{x}^{\bar{\alpha}} = x_p^{\bar{\alpha}}(t) = (t, r_p, 0, 0)$, and the coordinate separation $\Delta x^{\bar{\imath}} := x^{\bar{\imath}} - x_p^{\bar{\imath}}(t)$ is $\Delta x = \bar{x} - r_p$, $\Delta y = \bar{y}$, and $\Delta z = \bar{z}$. The distance s_1 then reduces

to

$$(s_1)^2 = \left(1 + \frac{2M}{r_p}\right)\Delta x^2 + \Delta y^2 + \Delta z^2 + (\tilde{u}^t)^2\left(\frac{2M\Delta x}{r_p} + r_p\omega\Delta y\right)^2, \quad (2.24)$$

where $\tilde{u}^t = (1 - 3M/r_p)^{-1/2}$. The polynomials $\mathrm{P}_3(\Delta x^\alpha)$, $\mathrm{P}_6(\Delta x^\alpha)$, and $\mathrm{P}_9(\Delta x^\alpha)$ are too long to be included here. Instead we have made them available online as Mathematica code *.

We now turn to the regular field $\Psi^{\mathcal{R}}$. Because it approximates a smooth homogeneous solution, we can write it as a Taylor series around $\tilde{x}^\alpha$. In the grid coordinates, such an expansion reads

$$\Psi^{\mathcal{R}}(t, x^{\bar{\imath}}) = \Psi^{\mathcal{R}}_0(t) + \epsilon\Psi^{\mathcal{R}}_{\bar{\imath}}(t)\Delta x^{\bar{\imath}} + \epsilon^2\Psi^{\mathcal{R}}_{\bar{\imath}\bar{\jmath}}(t)\Delta x^{\bar{\imath}}\Delta x^{\bar{\jmath}} + \mathcal{O}(\epsilon^3), \quad (2.25)$$

with the notation $\Psi^{\mathcal{R}}_0(t) := \Psi^{\mathcal{R}}(t, x^{\bar{\imath}}_p)$, $\Psi^{\mathcal{R}}_{\bar{\imath}}(t) := \partial_{\bar{\imath}}\Psi^{\mathcal{R}}(t, x^{\bar{\jmath}}_p)$, $\Psi^{\mathcal{R}}_{\bar{\imath}\bar{\jmath}}(t) := \frac{1}{2}\partial_{\bar{\imath}}\partial_{\bar{\jmath}}\Psi^{\mathcal{R}}(t, x^{\bar{k}}_p)$, and so on. The coefficients $\Psi^{\mathcal{R}}_{\bar{\imath}_1\ldots\bar{\imath}_k}$ in this series contain the full freedom in the approximate solution $\Psi^{\mathcal{A}}$. However, not all of these coefficients are independent; the field equation imposes relationships between them. As shown in Ref. [139], once the field equation is enforced, only the trace-free piece of each $\Psi^{\mathcal{R}}_{\bar{\imath}_1\ldots\bar{\imath}_k}$ is left undetermined. An nth-order approximate solution $\Psi^{\mathcal{R}}$ contains $\sum_{k=0}^{n}(2k+1) = (n+1)^2$ of these undetermined functions. All other functions of t in $\Psi^{\mathcal{R}}$ are related to these by ordinary differential equations (ODEs) that result from the field equations. In the next section we show how all the functions $\Psi^{\mathcal{R}}_{\bar{\imath}_1\ldots\bar{\imath}_k}(t)$ can be determined through the combination of (i) matching $\Psi^{\mathcal{R}}$ to $\Psi^{\mathcal{N}}$ and (ii) solving the ODEs in t that follow from the field equation.

[139]: Pound (2012), *Nonlinear gravitational self-force. I. Field outside a small body*

2.4 Matching method

The idea behind the matching method is straightforward. We numerically solve the scalar wave equation on a Schwarzschild background, excising the worldtube containing the scalar charge from the numerical domain. Inside the worldtube, the solution is given by the analytical approximation $\Psi^{\mathcal{A}} = \Psi^{\mathcal{P}} + \Psi^{\mathcal{R}}$ described above. Outside the worldtube we have the numerical field $\Psi^{\mathcal{N}}$. We

* https://github.com/nikwit/Puncture-Field-KS-Coords

demand

$$\Psi^{\mathcal{N}} \overset{\Gamma}{=} \Psi^{\mathcal{P}} + \Psi^{\mathcal{R}}, \tag{2.26}$$

where $\overset{\Gamma}{=}$ henceforth represents an equality that holds on the (2+1D) worldtube's boundary Γ. We will show that this matching condition, together with the scalar wave equation, fully determine the regular field $\Psi^{\mathcal{R}}$ inside the worldtube. This solution, in turn, provides boundary conditions for the evolution of the numerical field, specifically for U^-.

We formulate the matching scheme in the co-moving grid coordinates $x^{\bar{i}}$ introduced in Eq. (2.14). The Euclidean distance to the particle is defined as $\rho := \sqrt{\delta_{\bar{i}\bar{j}}\Delta x^{\bar{i}}\Delta x^{\bar{j}}} = \sqrt{\delta_{ij}\Delta x^i \Delta x^j}$. The boundary of the worldtube is located at $\rho = R$, with normal vector $n^{\bar{i}} := \Delta x^{\bar{i}}/\rho$. We note that $n^{\bar{i}}$ is normalized with respect to $\delta_{\bar{i}\bar{j}}$, whereas $\hat{n}^i$ in Sec. 2.2 is normalized with respect to the 3-metric γ_{ij}.

We now introduce the details of our matching scheme for order $n = 0$, 1 and 2, which are the expansion orders implemented numerically in this work. The matching scheme for an expansion of arbitrary order n is given in Appendix 2.8. We start by re-writing the Taylor expansion in Eq. (2.25) in terms of the quantities ρ and $n^{\bar{i}}$, and we introduce an analogous expansion for the time derivative of the regular field:

$$\Psi^{\mathcal{R}}(t, x^{\bar{i}}) = \Psi^{\mathcal{R}}_0(t) + \rho\Psi^{\mathcal{R}}_{\bar{i}}(t)n^{\bar{i}} + \rho^2\Psi^{\mathcal{R}}_{\bar{i}\bar{j}}(t)n^{\bar{i}}n^{\bar{j}} + \mathcal{O}(\rho^3), \tag{2.27a}$$

$$\dot{\Psi}^{\mathcal{R}}(t, x^{\bar{i}}) = \dot{\Psi}^{\mathcal{R}}_0(t) + \rho\dot{\Psi}^{\mathcal{R}}_{\bar{i}}(t)n^{\bar{i}} + \rho^2\dot{\Psi}^{\mathcal{R}}_{\bar{i}\bar{j}}(t)n^{\bar{i}}n^{\bar{j}} + \mathcal{O}(\rho^3), \tag{2.27b}$$

where we now drop the order-counting parameter $\epsilon = 1$. The set of coefficients $\left\{\Psi^{\mathcal{R}}_0(t), \Psi^{\mathcal{R}}_{\bar{i}}(t), \Psi^{\mathcal{R}}_{\bar{i}\bar{j}}(t)\right\}$ have one, three and six independent components, respectively, for a total of ten. We will show that all of these can be uniquely determined at each time step from (i) the numerical field $\Psi^{\mathcal{N}}(t, x^{\bar{i}})$ at the worldtube boundary, and (ii) the Klein-Gordon equation (2.3).

2.4.1 Worldtube boundary data

At each time step t_s we enforce the continuity condition

$$\Psi^{\mathcal{R}}(t_s, x^{\bar{i}}) \overset{\Gamma}{=} \Psi^{\mathcal{N}}(t_s, x^{\bar{i}}) - \Psi^{\mathcal{P}}(t_s, x^{\bar{i}}), \tag{2.28}$$

both for the field itself and its time derivative. In the following section we will omit explicit expressions which enforce continuity

between the time derivative of the regular field $\dot{\Psi}^{\mathcal{R}}(t, x^{\bar{i}})$ and the numerical field $\partial_t \Psi^{\mathcal{N}}(t, x^{\bar{i}})$ because they are completely analogous to the expressions for the fields themselves. We will utilize symmetric trace-free (STF) tensors, indicated with angular brackets, e.g. $A^{\langle k_1 \ldots k_l \rangle}$.

Note that $A^{\langle k_1 \cdots k_l \rangle} B_{k_1 \cdots k_l} = A^{k_1 \cdots k_l} B_{\langle k_1 \cdots k_l \rangle} = A^{\langle k_1 \cdots k_l \rangle} B_{\langle k_1 \cdots k_l \rangle}$; more details about STF tensors are given in Appendix 2.8. Transforming Eq. (2.27a) to a STF basis using (2.80) yields, at order $n = 2$,

$$\Psi^{\mathcal{R}}(t_s, x^{\bar{i}}) = \Psi^{\mathcal{R}}_0(t_s) + \frac{1}{3}\rho^2 \delta^{\bar{i}\bar{j}} \Psi^{\mathcal{R}}_{\bar{i}\bar{j}} + \rho \Psi^{\mathcal{R}}_{\langle \bar{i} \rangle} n^{\langle \bar{i} \rangle} + \rho^2 \Psi^{\mathcal{R}}_{\langle \bar{i}\bar{j} \rangle} n^{\langle \bar{i}} n^{\bar{j} \rangle}, \quad (2.29)$$

with $n^{\langle \bar{i} \rangle} = n^{\bar{i}}$ and $n^{\langle \bar{i}} n^{\bar{j} \rangle} = n^{\bar{i}} n^{\bar{j}} - \frac{1}{3}\delta^{\bar{i}\bar{j}}$. Equation (2.29) will be used on the left-hand side in Eq. (2.28).

The right-hand side of Eq. (2.28) is obtained by evaluating the puncture field of Eq. (2.23) and its time derivative at the coordinates of the DG collocation points on the worldtube surface, and subtracting them pointwise from the corresponding values of $\Psi^{\mathcal{N}}(t_s, x^{\bar{i}})$ and $\partial_t \Psi^{\mathcal{N}}(t_s, x^{\bar{i}})$. This expression is then projected numerically onto the set of spherical harmonics defined on the worldtube Γ with constant radius ρ,

$$\Psi^{\mathcal{N}}(t_s, x^{\bar{i}}) - \Psi^{\mathcal{P}}(t_s, x^{\bar{i}}) \overset{\Gamma}{=} \sum_{l=0}^{n=2} \sum_{m=-l}^{l} a^{\mathcal{N},\mathcal{R}}_{lm}(t_s) Y_{lm}(n^{\bar{i}}), \quad (2.30)$$

where

$$a^{\mathcal{N},\mathcal{R}}_{lm}(t_s) = \oint_{\Gamma} \left[\Psi^{\mathcal{N}}(t_s, x^{\bar{i}}) - \Psi^{\mathcal{P}}(t_s, x^{\bar{i}}) \right] Y^*_{lm}(n^{\bar{i}}) d\Omega \quad (2.31)$$

are the spherical harmonic coefficients of the *numerical, regular* field $\Psi^{\mathcal{N}}(t_s, x^{\bar{i}}) - \Psi^{\mathcal{P}}(t_s, x^{\bar{i}})$ and $d\Omega$ is the area element of the flat-space unit 2-sphere. In practice we use real-valued spherical harmonics and evaluate the integral with the Gauss-Lobatto quadrature used by the DG method.

Both the spherical harmonics Y_{lm} and the STF normal vector $n^{\langle \bar{k}_1} \cdots n^{\bar{k}_l \rangle}$ provide an orthogonal basis for functions on a sphere. They can be transformed into each other using Eqs. (2.82),

$$\sum_{l=0}^{n=2} \sum_{m=-l}^{l} a^{\mathcal{N},\mathcal{R}}_{lm}(t_s) Y_{lm}(n^{\bar{i}}) = \Psi^{\mathcal{N},\mathcal{R}}_{\langle 0 \rangle}(t_s) + \Psi^{\mathcal{N},\mathcal{R}}_{\langle \bar{i} \rangle}(t_s) n^{\langle \bar{i} \rangle} + \Psi^{\mathcal{N},\mathcal{R}}_{\langle \bar{i}\bar{j} \rangle}(t_s) n^{\langle \bar{i}} n^{\bar{j} \rangle}. \quad (2.32)$$

We have thus expressed both sides of the continuity condition (2.28) in a basis of STF normal vectors, using Eqs. (2.29) and (2.32). Orthogonality of the STF basis allows us to match order by order in the STF expansion:

$$\Psi^{\mathcal{N},\mathcal{R}}_{\langle 0\rangle}(t_s) = \Psi^{\mathcal{R}}_{0}(t_s) + \frac{1}{3}\rho^2\delta^{\bar{i}\bar{j}}\Psi^{\mathcal{R}}_{\bar{i}\bar{j}}(t_s), \tag{2.33a}$$

$$\Psi^{\mathcal{N},\mathcal{R}}_{\langle \bar{i}\rangle}(t_s) = \rho\Psi^{\mathcal{R}}_{\bar{i}}(t_s), \tag{2.33b}$$

$$\Psi^{\mathcal{N},\mathcal{R}}_{\langle \bar{i}\bar{j}\rangle}(t_s) = \rho^2\Psi^{\mathcal{R}}_{\langle \bar{i}\bar{j}\rangle}(t_s). \tag{2.33c}$$

We emphasise that Eqs. (2.33) contain two distinct sets of coefficients: The $\Psi^{\mathcal{N},\mathcal{R}}$ on the left-hand-sides are expansion coefficients on the surface Γ, whereas the $\Psi^{\mathcal{R}}$ on the right-hand-side are the Taylor expansion coefficients of the solution in the interior, Eq. (2.27a). The continuity conditions for a field expanded to arbitrary order are given in Eq. (2.87). For expansion orders $n = 0$ or $n = 1$ the second term in Eq. (2.33a) falls away. The regular field inside the worldtube is then fully determined by the continuity condition and can directly be used to provide boundary conditions for the future evolution. In one dimension, this is equivalent to a linear polynomial in an interval being fully determined by its two endpoints.

For $n = 2$, Eqs. (2.33) provide only 9 equations for the 10 coefficients of $\Psi^{\mathcal{R}}(t_s, x^{\bar{i}})$ because the monopole of the regular numerical field $\Psi^{\mathcal{N},\mathcal{R}}_{\langle 0\rangle}$ in Eq. (2.33a) contributes to both the zeroth-order coefficient $\Psi^{\mathcal{R}}_{0}$ and the trace of the second-order coefficient, $\delta^{\bar{i}\bar{j}}\Psi^{\mathcal{R}}_{\bar{i}\bar{j}}$. More generally, for arbitrary order, the STF expansion on the worldtube, Eq. (2.87), provides only the trace-free components of $\Psi^{\mathcal{N},\mathcal{R}}$, so that boundary-matching determines only the trace-free parts of the expansion $\Psi^{\mathcal{R}}(t_s, x^{\bar{i}})$ but not its traces. Therefore, for expansions of order $n \geq 2$, additional equations are needed to fully determine the regular field inside the worldtube. These are provided by a series expansion of the Klein-Gordon equation, as we describe below in Sec. 2.4.2.

The coefficients of the regular field's time derivative are determined completely analogously, with the continuity condition

$$\partial_t\Psi^{\mathcal{R}}(t_s, x^i) \overset{\Gamma}{=} \partial_t\Psi^{\mathcal{N}}(t_s, x^i) - \partial_t\Psi^{\mathcal{P}}(t_s, x^i). \tag{2.34}$$

$\partial_t\Psi^{\mathcal{N}}(t_s, x^i)$ is evaluated using its evolution equation (2.8a) and then transformed into the co-moving grid frame by adding the advective term $v^i_g\partial_i\Psi^{\mathcal{N}}$, where v^i_g is the instantaneous local grid velocity. The matching conditions for the time derivative of the

regular field $\dot{\Psi}^R(t_s)$ are then just the time derivative of the matching conditions for $\Psi^R(t_s)$, Eqs. (2.33).

2.4.2 Klein-Gordon equation

We rewrite the Klein-Gordon equation (2.3) in grid coordinates

$$0 = g^{\bar{\mu}\bar{\nu}}\partial_{\bar{\mu}}\partial_{\bar{\nu}}\Psi^{\mathcal{R}} - \Gamma^{\bar{\rho}}\partial_{\bar{\rho}}\Psi^{\mathcal{R}}, \tag{2.35}$$

where $\Gamma^{\bar{\rho}} := g^{\bar{\mu}\bar{\nu}}\Gamma^{\bar{\rho}}_{\bar{\mu}\bar{\nu}}$. The metric quantities $g^{\mu\nu}$ and Γ^{μ} are expanded in the grid coordinates $x^{\bar{\imath}}$ to the same order n as the regular field at each time step t_s. For $n = 2$ these expansions read

$$\begin{aligned} g^{\bar{\mu}\bar{\nu}}(t_s, x^{\bar{\imath}}) &= g_0^{\bar{\mu}\bar{\nu}}(t_s) + g_{\bar{\imath}}^{\bar{\mu}\bar{\nu}}(t_s)\Delta x^{\bar{\imath}} \\ &\quad + g_{\bar{\imath}\bar{\jmath}}^{\bar{\mu}\bar{\nu}}(t_s)\Delta x^{\bar{\imath}}\Delta x^{\bar{\jmath}} + \mathcal{O}(\rho^3), \qquad (2.36) \\ \Gamma^{\bar{\mu}}(t_s, x^{\bar{\imath}}) &= \Gamma_0^{\bar{\mu}}(t_s) + \Gamma_{\bar{\imath}}^{\bar{\mu}}(t_s)\Delta x^{\bar{\imath}} \\ &\quad + \Gamma_{\bar{\imath}\bar{\jmath}}^{\bar{\mu}}(t_s)\Delta x^{\bar{\imath}}\Delta x^{\bar{\jmath}} + \mathcal{O}(\rho^3). \qquad (2.37) \end{aligned}$$

The expansion coefficients are given by $g_0^{\bar{\mu}\bar{\nu}} := g^{\bar{\mu}\bar{\nu}}(t_s, x_p^{\bar{\imath}})$, $g_{\bar{\imath}}^{\bar{\mu}\bar{\nu}} := \partial_{\bar{\imath}} g^{\bar{\mu}\bar{\nu}}(t_s, x_p^{\bar{\jmath}})$, and $g_{\bar{\imath}\bar{\jmath}}^{\bar{\mu}\bar{\nu}}(t_s) := \frac{1}{2}\partial_{\bar{\imath}}\partial_{\bar{\jmath}} g^{\bar{\mu}\bar{\nu}}(t_s, x_p^{\bar{k}})$, and similarly for $\Gamma_0^{\bar{\mu}}$, $\Gamma_{\bar{\imath}}^{\bar{\mu}}$, and $\Gamma_{\bar{\imath}\bar{\jmath}}^{\bar{\mu}}$. Due to the spherical symmetry of the Schwarzschild spacetime, and our circular-orbit setup, these expansion coefficients are in fact independent of t_s.

We now expand the Klein-Gordon equation in powers of ρ by inserting the expansions for $\Psi^{\mathcal{R}}$, $g^{\mu\nu}$ and Γ^{μ} from Eqs. (2.27a), (2.36) and (2.37), respectively, into Eq. (2.35). The $O(\rho^0)$ piece of the equation reads

$$\begin{aligned} &g_0^{tt}\ddot{\Psi}_0^{\mathcal{R}}(t_s) + 2g_0^{t\bar{\imath}}\dot{\Psi}_{\bar{\imath}}^{\mathcal{R}}(t_s) + 2g_0^{\bar{\imath}\bar{\jmath}}\Psi_{\bar{\imath}\bar{\jmath}}^{\mathcal{R}}(t_s) \\ &\qquad - \Gamma_0^t\dot{\Psi}_0^{\mathcal{R}}(t_s) - \Gamma_0^{\bar{\imath}}\Psi_{\bar{\imath}}^{\mathcal{R}}(t_s) = 0. \end{aligned} \tag{2.38}$$

This ODE provides an additional, independent relation between the expansion coefficients $\Psi_0^{\mathcal{R}}$, $\Psi_{\bar{\imath}}^{\mathcal{R}}$ and $\Psi_{\bar{\imath}\bar{\jmath}}^{\mathcal{R}}$, which enables us to determine the remaining, trace degree of freedom of the regular field at $n = 2$. Specifically, combining Eq. (2.38) with the continuity

conditions (2.33), and using $\Psi^{\mathcal{R}}_{\bar{i}\bar{j}} = \Psi^{\mathcal{R}}_{\langle\bar{i}\bar{j}\rangle} + \frac{1}{3}\delta^{\bar{l}\bar{k}}\Psi^{\mathcal{R}}_{\bar{l}\bar{k}}\delta_{\bar{i}\bar{j}}$, we obtain

$$g_0^{tt}\ddot{\Psi}^{\mathcal{R}}_0(t_s) + 2g_0^{t\bar{i}}\dot{\Psi}^{\mathcal{N},\mathcal{R}}_{\bar{i}}(t_s) + 2g_0^{\bar{i}\bar{j}}\Psi^{\mathcal{N},\mathcal{R}}_{\langle\bar{i}\bar{j}\rangle}(t_s) + \frac{2\delta_{\bar{i}\bar{j}}g_0^{\bar{i}\bar{j}}}{\rho^2}\left(\Psi^{\mathcal{N},\mathcal{R}}_0(t_s) - \Psi^{\mathcal{R}}_0(t_s)\right) - \Gamma^0_0\dot{\Psi}^{\mathcal{R}}_0(t_s) - \Gamma^{\bar{i}}_0\Psi^{\mathcal{N},\mathcal{R}}_{\bar{i}}(t_s) = 0. \quad (2.39)$$

We reduce this ODE to first order and use a Dormand-Prince time stepper to advance the zeroth-order coefficient $\Psi^{\mathcal{R}}_0$ and its time derivative to the next time step t_{s+1}, taking the same global time step as the DG evolution. Together with the continuity conditions (2.33) at time step t_{s+1}, this completely determines all components of the second-order expansion of $\Psi^{\mathcal{R}}(t, x^{\bar{i}})$ in Eq. (2.27a) at t_{s+1}.

The coefficients of the numerical, regular field $\Psi^{\mathcal{N},\mathcal{R}}_{\langle\bar{k}_0\cdots\bar{k}_l\rangle}$ are updated each sub-step. As initial conditions of the ODE (2.39) we take $\Psi^{\mathcal{R}}_0(t_0) = \dot{\Psi}^{\mathcal{R}}_0(t_0) = 0$.

In Appendix 2.8 we formulate the generalization of this method to an arbitrary order n, and in particular we derive the generalized form of the ODE on Γ.

2.4.3 Boundary conditions for $\Psi^{\mathcal{N}}$

Once the expansion of the regular field has been fully determined, it can be used to provide boundary conditions to the DG elements neighboring the worldtube. DG methods commonly formulate boundary conditions between elements using the numerical flux, and these conditions are applied to each of the characteristic fields defined in Eqs. (2.13). We use the internal solution $\Psi^{\mathcal{A}}$ of the worldtube to provide boundary conditions for the characteristic field U^- as if the interior of the worldtube were simply another DG element. From the definition of U^- in Eq. (2.13c) and the definitions in Eq. (3.9), we obtain the boundary condition

$$U^-(t_s) \overset{\Gamma}{=} -\alpha^{-1}\partial_t\Psi^{\mathcal{A}}(t_s) + \left(\beta^{\bar{i}} - \hat{n}^{\bar{i}}\right)\partial_{\bar{i}}\Psi^{\mathcal{A}}(t_s) - \gamma_2\Psi^{\mathcal{A}}(t_s). \quad (2.40)$$

The analytical solution $\Psi^{\mathcal{A}}(t_s)$ was defined in Eq. (2.15) as the sum of the regular field $\Psi^{\mathcal{R}}$ and the puncture field $\Psi^{\mathcal{P}}$, both of which are now fully determined. The time and spatial derivative are simply obtained from $\partial_t\Psi^{\mathcal{A}}(t_s) = \partial_t\Psi^{\mathcal{N}}(t_s) + \partial_t\Psi^{\mathcal{P}}(t_s)$ and $\partial_{\bar{i}}\Psi^{\mathcal{A}}(t_s) = \partial_{\bar{i}}\Psi^{\mathcal{N}}(t_s) + \partial_{\bar{i}}\Psi^{\mathcal{P}}(t_s)$. The fields $\Psi^{\mathcal{R}}(t_s)$ and $\partial_t\Psi^{\mathcal{R}}(t_s)$

are given by Eq. (2.27) and its time derivative. The derivative normal to the worldtube boundary is similarly obtained by taking the appropriate spatial derivative of $\Psi^{\mathcal{R}}$ in Eq. (2.27a) analytically. The expression for the puncture field $\Psi^{\mathcal{P}}(t_s)$ is given in Eq. (2.25), and its time and normal derivative are computed analytically. We evaluate all of these expressions at the grid coordinates $x^{\bar{I}}$ of all DG grid points that lie on element faces abutting the worldtube to formulate pointwise boundary conditions. The value of $U^-(t_s)$ at the boundary is used to apply a correction to the time derivative of the evolution equations using the upwind flux [84].

[84]: Hesthaven et al. (2007), *Nodal Discontinuous Galerkin Methods: Algorithms, Analysis, and Applications*

We initially tried to provide boundary conditions in the above fashion for all characteristic fields entering the numerical domain, including Z^1 and Z^2_i. However, we found that this caused substantial constraint violations entering the numerical domain at the worldtube boundary. Instead, we use constraint-preserving boundary conditions for Z^1 and Z^2_i as described in Appendix 2.7.

2.4.4 Roll-on function

The initial conditions we use for the simulations are $\Psi = \partial_t \Psi = 0$ for both the DG fields outside the worldtube and the regular field inside it. The puncture field $\Psi^{\mathcal{P}}$ added to the regular field in Eq. (2.40) initially creates a discontinuity at the worldtube boundary, due to the unphysical instantaneous appearance of the scalar charge source $t = 0$. DG methods are very inefficient at resolving discontinuities within elements, due to the Gibbs phenomenon.

To alleviate this, we multiply the puncture field $\Psi^{\mathcal{P}}$ with a roll-on function $w(t)$ that smoothly grows from 0 to 1 (up to double precision) between $t = 0$ and $t = t_{\text{end}}$. We found that this effectively stretches out the initial discontinuity and causes the fields to settle more smoothly to their final values.

We tested two different roll-on functions: $w(t) = \sin[\pi t/(2t_{\text{end}})]$ and $w(t) = \text{erf}(12t/t_{\text{end}} - 6)/2 + 1/2$, where erf is the Gaussian error function. There was little difference in the long term evolution between the two choices.

The roll-on function ensures a smooth settling of the solution corresponding to the scalar charge slowly being turned on over its first 4 orbits. We found $t_{\text{end}} = 300M$ to be a good choice for the simulations with orbital radius $r_p = 5M$.

2.4.5 Error estimates

To estimate the errors that our matching method incurs, we apply the same analysis as we did for the 1 + 1D case in [1]. The estimates follow from a Kirchhoff representation of the scalar field. We first consider the field in the numerical domain, outside the tube Γ. Call this region V. Inside V, our field $\Psi^{\mathcal{N}}$ satisfies the same homogeneous field equation as the exact solution Ψ, $g^{\mu\nu}\nabla_\mu\nabla_\nu\Psi^{\mathcal{N}} = 0$, but it inherits errors that propagate out from Γ. We introduce a retarded Green's function $G(x, x')$ satisfying

[1]: Dhesi et al. (2021), *Worldtube excision method for intermediate-mass-ratio inspirals: Scalar-field toy model*

$$\Box G(x, x') = \Box' G(x, x') = \delta^4(x, x')\,, \tag{2.41}$$

where x and x' denote any two points, primes denote quantities at x', $\Box := g^{\mu\nu}\nabla_\mu\nabla_\nu$, and $\delta^4(x, x') := \frac{\delta^4(x^\mu - x^{\mu'})}{\sqrt{-g}}$. If we now take any point $x \in V$, then the equations (2.41) and $\Box\Psi^{\mathcal{N}} = 0$ imply the identity

$$\Psi^{\mathcal{N}}(x')\delta^4(x, x') = \Psi^{\mathcal{N}}(x')\Box' G(x, x') - G(x, x')\Box'\Psi^{\mathcal{N}}(x'). \tag{2.42}$$

Integrating this equation over all $x' \in V$ and then integrating by parts, we obtain the Kirchhoff representation

$$\begin{aligned}\Psi^{\mathcal{N}}(x) &= \int_V \left[\Psi^{\mathcal{N}}(x')\Box' G(x, x') - G(x, x')\Box'\Psi^{\mathcal{N}}(x')\right] dV' \\ &= \int_{\partial V} \left[\Psi^{\mathcal{N}}(x')\nabla_{\mu'} G(x, x') - G(x, x')\nabla_{\mu'}\Psi^{\mathcal{N}}(x')\right] d\Sigma^{\mu'}.\end{aligned} \tag{2.43}$$

Here $d\Sigma^{\mu'}$ is the outward-directed surface element on ∂V. For us the relevant portion of ∂V is the tube boundary Γ, where $d\Sigma^{\mu'} = \mathcal{O}(R^2)dt\, d\Omega$. As in Eq. (2.31), here $d\Omega$ is the area element of the unit 2-sphere.

In the integral over Γ, we may replace $\Psi^{\mathcal{N}}$ with $\Psi^{\mathcal{A}}$. Our truncated expansion of $\Psi^{\mathcal{A}}$ introduces an inherent $\mathcal{O}(R^{n+1})$ error in $\Psi^{\mathcal{N}}(x')$ and $\mathcal{O}(R^n)$ error in $\nabla_{\mu'}\Psi^{\mathcal{N}}(x')$ on the worldtube. Equation (2.43) implies that the $\mathcal{O}(R^n)$ error in $\nabla_{\mu'}\Psi^{\mathcal{N}}(x')$ dominates. Accounting for the $\mathcal{O}(R^2)$ surface element, we see that this creates an $\mathcal{O}(R^{n+2})$ error in $\Psi^{\mathcal{N}}(x)$.

An important takeaway from this analysis is that the error in the numerical domain is suppressed by the small spatial size of Γ. As a consequence, the error converges two orders faster than the analogous error in the 1 + 1D problem in [1].

However, we note that this analysis applies only at a fixed location

x outside the worldtube. At a point *on* the worldtube boundary Γ, the errors in $\Psi^{\mathcal{N}}$ are inherently $\mathcal{O}(R^{n+1})$, and the errors in $\nabla_\mu \Psi^{\mathcal{N}}$ are inherently $\mathcal{O}(R^n)$. There is no suppression due to the small spatial size of the worldtube in this case. The same is true of the errors at a point outside the worldtube if we consider a point x that is at a fixed multiple of R away from the worldline rather than at a fixed physical location.

We also note that in applications, we require outputs other than $\Psi^{\mathcal{N}}$: the regular field on the particle's worldline and the self-force, for example. The omitted terms in our expansion (2.25) scale with a power of distance from the worldline, which might make us expect that we incur no error in $\Psi^{\mathcal{R}}(x_p)$ and $\partial_\mu \Psi^{\mathcal{R}}(x_p)$ (and therefore in the self-force). However, we can see this is incorrect by referring again to a Kirchhoff representation of the field. Our method enforces the field equation (3.1) on $\Psi^{\mathcal{A}}$ up to an error $\sim R^{n-1}$ (two derivatives of the truncation error in $\Psi^{\mathcal{A}}$). If we momentarily ignore that error term in the field equation, and if we consider V to be the interior of Γ and repeat the steps that led to Eq. (2.43), then we obtain the Kirchhoff representation

$$\Psi^{\mathcal{A}}(x) = -4\pi q \int_\gamma G(x, x_p(\tau)) d\tau + \int_\Gamma \Big[\Psi^{\mathcal{A}}(x') \nabla_{\mu'} G(x, x') - G(x, x') \nabla_{\mu'} \Psi^{\mathcal{A}}(x') \Big] d\Sigma^{\mu'} . \quad (2.44)$$

If we now take x to be a point x_p on the worldline and consider the integral over Γ, then we have $G(x, x') \sim 1/R$ and $\nabla_{\mu'} G(x, x') \sim 1/R^2$. We can combine this with $d\Sigma^{\mu'} \sim R^2$ and with the errors $\mathcal{O}(R^{n+1})$ in $\Psi^{\mathcal{A}}(x')$ and $\mathcal{O}(R^n)$ in $\nabla_{\mu'} \Psi^{\mathcal{A}}(x')$ to deduce that the error in $\Psi^{\mathcal{A}}(x_p)$ is $\mathcal{O}(R^{n+1})$. If we take a derivative of Eq. (2.44), we find that the error in $\partial_\mu \Psi^{\mathcal{A}}(x_p)$ is $\mathcal{O}(R^n)$. These error estimates apply immediately to $\Psi^{\mathcal{R}}(x_p)$ as well.

It is also straightforward to see that these estimates are not altered by the $\mathcal{O}(R^{n-1})$ error in the field equation, which we neglected in deriving Eq. (2.44). That error contributes an error $\sim \int R^{n-1} G(x_p, x') dV' \sim R^{n+1}$ to $\Psi^{\mathcal{R}}(x_p)$, consistent with the error from the boundary integral.

In summary, we expect that for an nth-order analytical approximation, our method introduces the following errors:

$$\text{Error in } \Psi^{\mathcal{N}}(x): \quad \mathcal{O}(R^{n+2}), \quad (2.45)$$

$$\text{Error in } \Psi^{\mathcal{R}}(x_p): \quad \mathcal{O}(R^{n+1}), \quad (2.46)$$

$$\text{Error in } \partial_\alpha \Psi^{\mathcal{R}}(x_p): \quad \mathcal{O}(R^n), \quad (2.47)$$

where x is a point outside Γ and x_p is a point on the particle's worldline. Our numerical results in the next section will bear out these predictions. The error in $\partial_\alpha \Psi^{\mathcal{R}}(x_p)$, and hence in the self-force, will be particularly relevant when we allow the system to evolve (as opposed to keeping the particle on a fixed geodesic orbit). We defer discussion of this to the Conclusion.

Finally, before proceeding, we note that our error estimate for $\partial_\alpha \Psi^{\mathcal{R}}(x_p)$ might be too pessimistic in some instances. Specifically, time-antisymmetric components, linked to the dissipative pieces of the self-force, might converge more rapidly with R. This is because these components arise from the radiative piece of the field, equal to half the retarded solution minus half the advanced solution [140]. For these pieces of the field, we can replace the Green's function G in Eq. (2.44) with its radiative piece, $G^{\rm Rad} = \frac{1}{2}(G^{\rm Ret} - G^{\rm Adv})$. $G^{\rm Rad}$ is smooth when its two arguments coincide (because singularities cancel between $G^{\rm Ret}$ and $G^{\rm Adv}$), meaning it does not introduce the negative powers of R that $G^{\rm Ret}$ introduces in Eq. (2.44). We therefore might expect that errors scale with a higher power of R in the dissipative components of $\partial_\alpha \Psi^{\mathcal{R}}(x_p)$. That could be extremely beneficial in practice because dissipative effects dominate over conservative ones on the long timescale of an inspiral [141], and dissipative effects must therefore be computed with higher accuracy. However, our numerical experiments in the next section do not entirely bear out this expectation of more rapid convergence, and we leave further investigation of it to future work.

[140]: Mino (2003), *Perturbative approach to an orbital evolution around a supermassive black hole*

[141]: Hinderer et al. (2008), *Two timescale analysis of extreme mass ratio inspirals in Kerr. I. Orbital Motion*

2.5 Results

We use a central black hole of mass M for the simulations. The excision sphere inside the black hole has radius $1.9M$. The outer boundary is placed at $400M$. We use a CFL safety factor of 0.4. The scalar charge is placed on a circular orbit with radius $r_p = 5M$ with angular velocity $\omega = M^{1/2} r_p^{-3/2} \approx 0.09 M^{-1}$.

The expansion terms of the puncture field converge more quickly with larger orbital radii of the scalar charge. The truncation error of the puncture field and hence of the worldtube solution is therefore particularly large at the relatively small orbital radius of $r_p = 5M$ used in our simulations. This ensures that the scheme is tested in an extreme region, comparable to binary black holes close to merger. Because the error due to the worldtube is comparatively

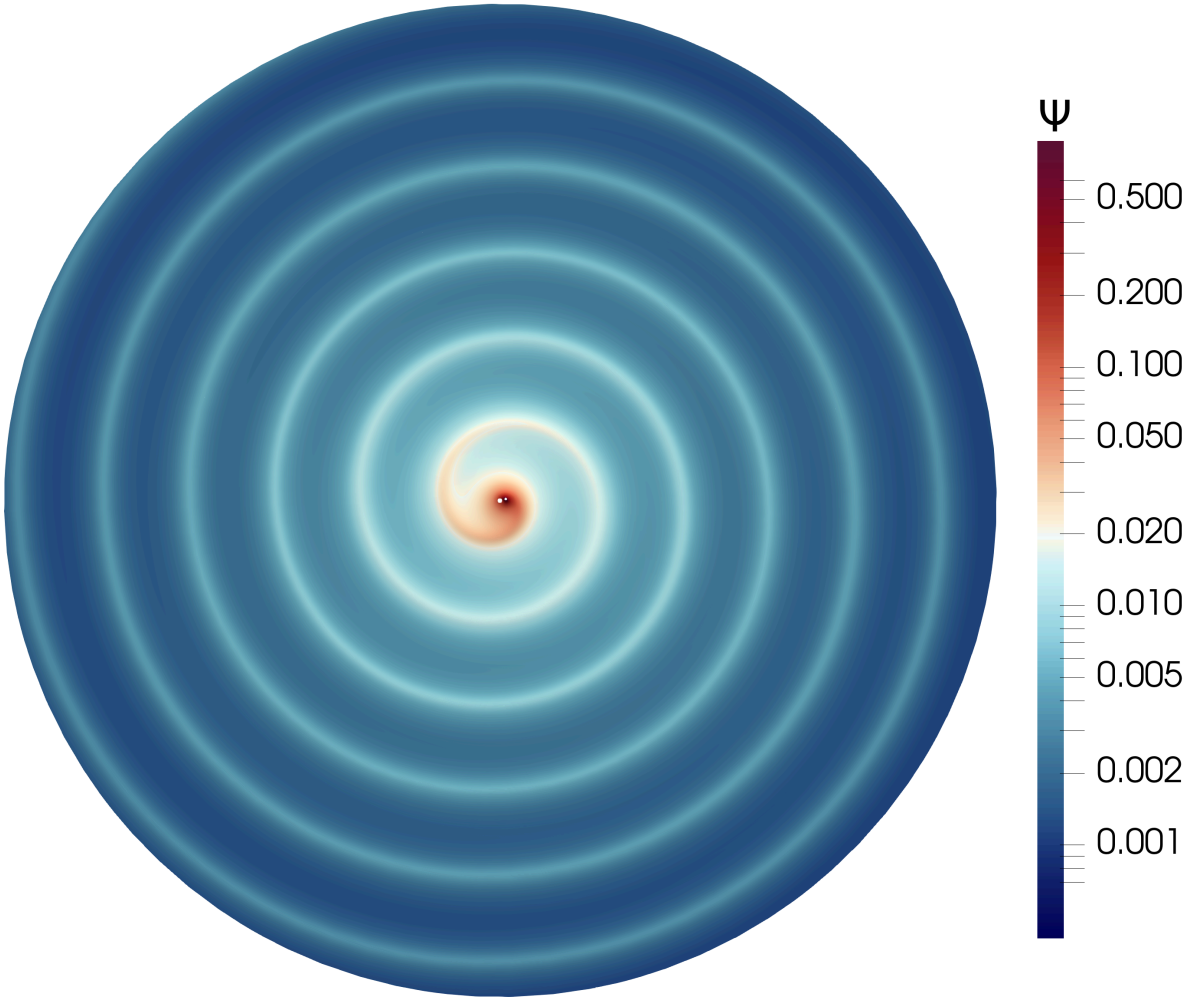

Figure 2.2: The equatorial plane of the domain, depicting the steady-state solution of the scalar field $\Psi^{\mathcal{N}}$. The scalar charge creates an outward propagating spiral as it orbits the central black hole. Figure 2.1 shows a tilted perspective zoomed into the center of the same plane with the spiral arms visible in the background.

large for a small r_p, it can be resolved with a lower resolution in the numerical domain, lowering the computational cost of the simulations.

We have implemented the worldtube scheme with the local solution expanded to orders $n = 0$, 1 and 2. The radius of the worldtube was varied between $0.2M$ and $1.6M$. The simulations were run until the field had settled to its steady state solution over the entire domain, which took between $3000M$ and $7000M$, depending on the magnitude of the settled error. Figure 2.2 shows a cut through the equatorial plane of the computational domain.

Figure 2.3 plots the steady state solution along two lines cut through the domain at late, constant Kerr-Schild times t: one along the co-moving x-axis connecting the central black hole center and the scalar charge and one along the z-axis normal to the charge's orbital plane. The undulations of the scalar field on the x-axis

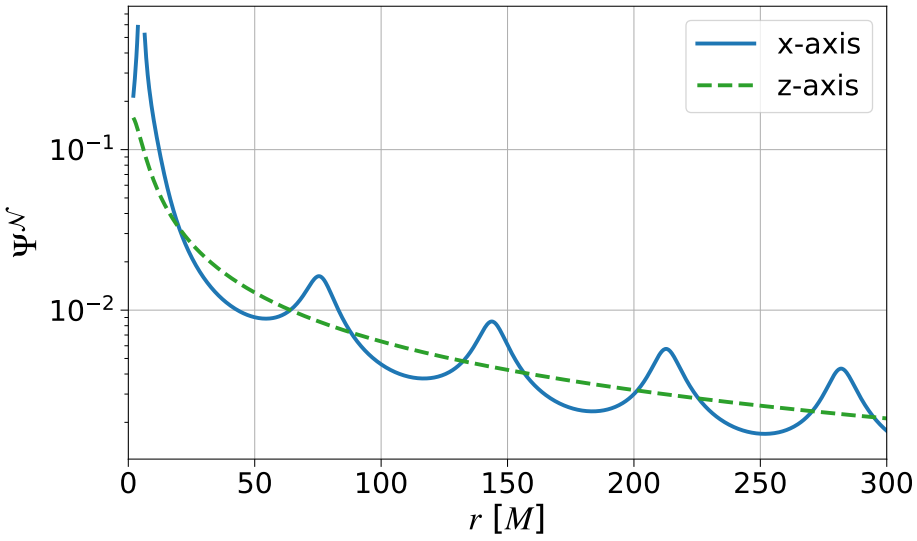

Figure 2.3: The steady-state solution of the scalar field $\Psi^{\mathcal{N}}$ along the co-moving x-axis and z-axis of the domain.

correspond to the arms of the spiral in Fig. 2.2. The missing part of the 'x-axis' line corresponds to the worldtube; the field increases strongly near the worldtube, because of the scalar charge contained at the center of the worldtube.

We verify the validity and convergence of our simulations in three different ways: First, in Sec. 2.5.1, we compare the value of the regular field $\Psi^{\mathcal{R}}$ and its spatial derivative $\partial_{\bar{i}}\Psi^{\mathcal{R}}$ at the position of the charge to published numerical results obtained using frequency-domain self-force methods. Second, in Sec. 2.5.2 we compare with the known axially symmetric analytical solution along the z-axis, given below in Eq. (2.54). Finally, we perform an internal convergence test along the co-moving x-axis in Sec. 2.5.3. For each simulation in the following sections, the resolution of the DG domain was increased until it no longer affected the steady-state solution. This guaranteed that the error measured was due to the worldtube, not the numerical evolution.

2.5.1 Regular field $\Psi^{\mathcal{R}}$ at the charge's position

The value of the regular field for a scalar charge in a circular geodesic orbit in Schwarzschild spacetime has been calculated in self-force literature. We compare the regular field of our simulations with the results of [142], who quote the value $\Psi^{\mathcal{R}}_{\text{ref}}(0) = -0.01023418q/M$ for a circular orbit with radius $5M$.

[142]: Diaz-Rivera et al. (2004), *Scalar field self-force effects on orbits about a Schwarzschild black hole*

For expansion orders $n = 0$ and $n = 1$, the regular field at the charge position is given directly by the monopole of the numerical field $\Psi^{\mathcal{N},\mathcal{R}}_{\langle 0\rangle}(t_s)$ in Eq. (2.33a) (the second term on the right-hand

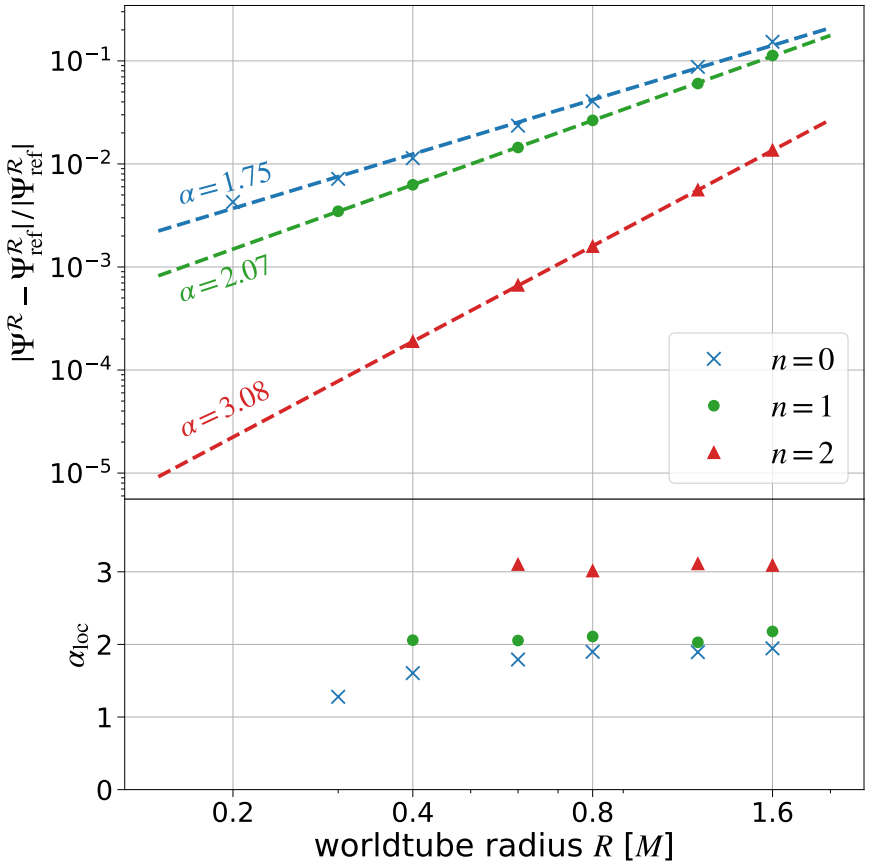

Figure 2.4: *Top panel:* The relative error of the regular field at the position of the charge compared to the value computed in [142]. Each cross represents the settled error at the final simulation time. The dashed lines are best fits for the relation $\varepsilon \propto R^{\alpha}$. *Bottom panel:* The local convergence order between simulations of neighboring worldtube radii.

side is absent for $n = 0, 1$). For $n = 2$, it is determined by solving the ODE (2.39) inside the worldtube.

The relative error $\varepsilon = |\Psi^{\mathcal{R}}(0) - \Psi^{\mathcal{R}}_{\rm ref}(0)|/|\Psi^{\mathcal{R}}_{\rm ref}(0)|$, where $\Psi^{\mathcal{R}}(0)$ is the final value of the regular field at the scalar charge, is shown in the top panel of Fig. (2.4), with each marker representing a simulation. The dashed lines show fits of the data, for each expansion order n, to a relation of the form $\varepsilon \propto R^{\alpha}$, where R (recall) is the worldtube radius. The bottom panel displays the local convergence order, defined through

$$\alpha_{{\rm loc},i} = \frac{\log(\varepsilon_i) - \log(\varepsilon_{i-1})}{\log(R_i) - \log(R_{i-1})}, \tag{2.48}$$

where R_i are the worldtube radii in our sample, and ε_i are the corresponding errors. We find that the error always decreases with smaller worldtube radius or higher order n of the local solution as expected. Equation (2.46) indicated a convergence order inside the worldtube of $\alpha = n + 1$ at sufficiently small worldtube radii. For $n = 1$ and 2 we find that this prediction is confirmed quite well, with global convergence orders measured as ~ 2.07 and ~ 3.08, respectively, and local convergence order

uniformly close to this value. At $n = 0$ we measure a global convergence order of ~ 1.72 and a local convergence order that appears to decrease with the worldtube radius. This suggests that for $n = 0$ the scheme is not fully in the convergent regime for the values of R we consider; rather, there are still significant contributions from higher-order terms. At smaller worldtube radii R, these higher-order-in-R contributions become less significant and the local convergence rate approaches the expected value of 1.

We also compare the gradient of $\Psi^{\mathcal{R}}$ at the position of the particle, which enters the expression for the self-force acting on the particle due to back-reaction from the scalar field. The value of the radial derivative is given in [142] as $\partial_{r_s}\Psi^{\mathcal{R}}_{\text{ref}}(0) = 0.0004149937q/M^2$ using Schwarzschild coordinates $(t_s, r_s, \theta_s, \varphi_s)$. We are not aware of any works which report the angular derivative of the scalar field at $r_p = 5M$. Instead, it was computed for us to be $\partial_{\varphi_s}\Psi^{\mathcal{R}}_{\text{ref}}(0) = -0.01009125769q/M^2$ using the frequency domain code of [143]. The coordinate transformation from Kerr-Schild time t to Schwarzschild time t_s is given by

[142]: Diaz-Rivera et al. (2004), *Scalar field self-force effects on orbits about a Schwarzschild black hole*

[143]: Macedo et al. (2022), *Hyperboloidal method for frequency-domain self-force calculations*

$$t_s = t + 2M \ln\left(\frac{r}{2M} - 1\right), \tag{2.49}$$

which makes the conversion between $\partial_{r_s}\Psi^{\mathcal{R}}$ and the Kerr–Schild radial derivative $\partial_r\Psi^{\mathcal{R}}$

$$\begin{aligned}\partial_{r_s} &= \partial_r + \frac{2M}{2M-r}\partial_t \\ &= \partial_r + \frac{2M}{2M-r}(\partial_{\bar{t}} + \frac{\partial x^{\bar{\imath}}}{\partial t}\partial_{\bar{\imath}}),\end{aligned} \tag{2.50}$$

where in the second line we have transformed into the co-moving coordinate frame given in Eqs. (2.14). The reference values of the regular field's gradient at the particle's position are then given by

$$\partial_r\Psi^{\mathcal{R}}_{\text{ref}}(0) = \partial_{\bar{x}}\Psi^{\mathcal{R}}_{\text{ref}}(0) = \partial_{r_s}\Psi^{\mathcal{R}}_{\text{ref}}(0) - \frac{2M\omega}{2M-r_p}\partial_{\varphi_s}\Psi^{\mathcal{R}}_{\text{ref}}(0), \tag{2.51}$$

$$\partial_\varphi\Psi^{\mathcal{R}}_{\text{ref}}(0) = r_p\partial_{\bar{y}}\Psi^{\mathcal{R}}_{\text{ref}}(0) = \partial_{\varphi_s}\Psi^{\mathcal{R}}_{\text{ref}}(0), \tag{2.52}$$

which we use to compare to our simulation values.

Figure 2.5 compares the radial and azimuthal derivative of $\Psi^{\mathcal{R}}$ obtained by our worldtube evolutions against these reference values. Shown are the differences from the reference values for orders $n = 1$ and 2, with power-law fits $\propto R^{\alpha}$. At zeroth order, the

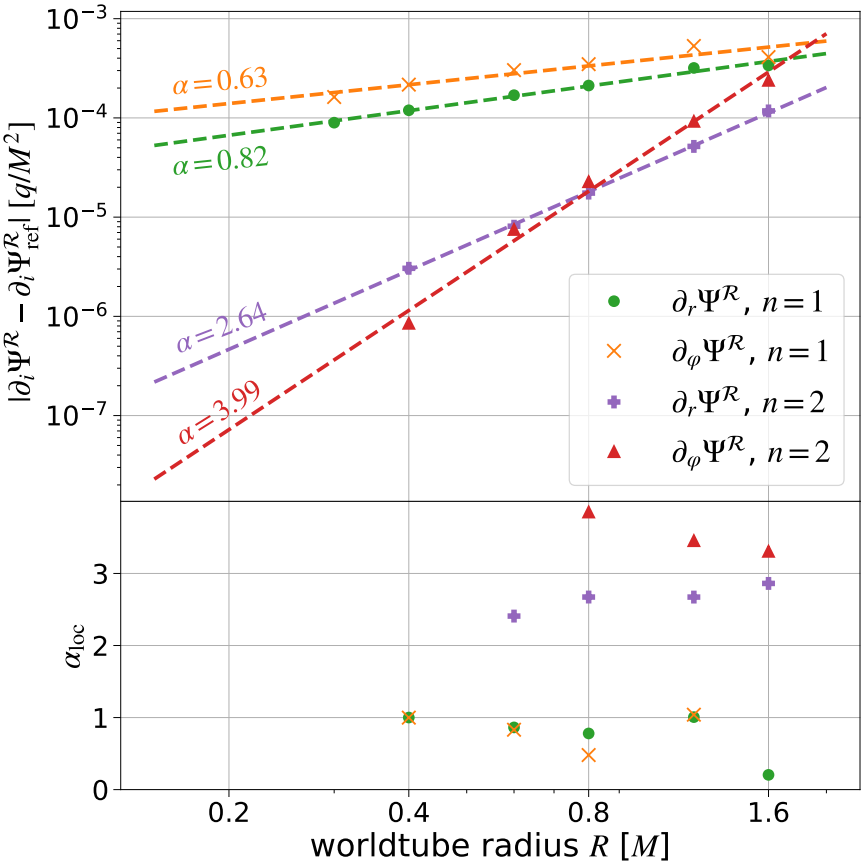

Figure 2.5: *Top panel:* The absolute difference between the radial and angular derivatives of the regular field at the position of the particle and the reference values of Eqs. (2.51) and (2.52). Each cross represents the final value of a simulation. The dashed lines are best fits to the power-law relation $\propto R^\alpha$. *Bottom panel:* The local convergence order between the simulations of adjacent worldtube radii as defined in Eq. (3.75). The simulations at order $n = 1$ show a convergence order consistent with the predicted rate $\alpha = 1$. The $n = 2$ simulations show a higher convergence rate likely due to dominant higher order terms. Some anomalies are not visible.

regular field is constant across the worldtube so the derivatives can not be computed. The lower panel of Fig. 2.5 plots the local convergence order $\alpha_{\rm loc}$ defined in (3.75).

We argued in Eq. (2.47) that the error of the regular field's derivatives at the particle position should scale with the worldtube radius as $\propto R^n$. For $n = 1$, this behavior is confirmed by the local convergence $\alpha_{\rm loc}$ of our simulations with the exception of worldtube radius $R = 1.6M$, which is anomalously lower than expected and skews the global convergence order. For $n = 2$, the radial derivative $\partial_r\Psi^{\mathcal{R}}$ (linked to the conservative, time-symmetric piece of the self-force) shows a local convergence that approaches the expected order of R^2 at smaller worldtube radii. This suggests that the error is just entering the regime where the $\mathcal{O}(R^n)$ contribution becomes dominant. For the angular derivative $\partial_\varphi\Psi^{\mathcal{R}}$ (linked to the dissipative, time-antisymmetric piece of the self-force), the local convergence order is larger than 3 for all simulations. This could indicate that the error is still dominated by higher-order contributions at the sampled worldtube radii. Alternatively, it could indicate that dissipative quantities converge more rapidly with R than conservative one, as suggested in Sec. 2.4.5; however, the results for $n = 1$ do not support that proposal, showing the same

convergence rate for $\partial_\varphi \Psi^{\mathcal{R}}$ as for $\partial_r \Psi^{\mathcal{R}}$. We stress that in any case, the convergence is at least as rapid as predicted in Eq. (2.47).

2.5.2 Solution along the z-axis

The spherical symmetry of the Schwarzschild background allows for the Klein-Gordon Eq. (2.3) to be decomposed into separately evolving spherical harmonic modes $\Psi_{lm}(r,t)$, where the spherical harmonic decomposition is centered on the black hole (different to the spherical harmonics introduced in Eq. (2.30), which are centered on the worldtube). On the polar axis ($x = y = 0$) all modes vanish except the axially symmetric ones, i.e. those with $m = 0$. These modes are also static and admit simple analytical solutions [1]. Along the polar axis these solutions read

[1]: Dhesi et al. (2021), *Worldtube excision method for intermediate-mass-ratio inspirals: Scalar-field toy model*

$$\begin{aligned}\Psi_{l0}(z) =& \frac{4\pi\sqrt{1-3M/r_p}}{M} Y_{l0}(n^x)\times \\ &\Big(Q_l(r_p/M-1)P_l(z/M-1)\Theta(r_p-z) \\ &\quad + Q_l(z/M-1)P_l(r_p/M-1)\Theta(z-r_p)\Big),\end{aligned} \tag{2.53}$$

where P_l and Q_l are Legendre functions of the first and second kind, respectively, n^x is the normal vector pointing in the direction of the x coordinate axis, and Θ is the Heaviside function. The full solution along the z-axis is then given by

$$\Psi_z(z) = q\sum_{l=0}^{\infty} \Psi_{l0}(z) Y_{l0}(n^z), \tag{2.54}$$

where n^z is normal vector pointing in the coordinate z direction. The expansion (2.54) converges exponentially in l everywhere except in the neighborhood of $z = r_p$, where the convergence is too slow to yield good results in practice. We therefore ignore this region and cut it out of plots when comparing with the analytical solution Ψ_z.

Figure 2.6 shows the relative error $|\Psi^{\mathcal{N}} - \Psi_z|/\Psi_z$ between our numerical worldtube solutions $\Psi^{\mathcal{N}}$ and Eq. (2.54), computed at late evolution time, after $\Psi^{\mathcal{N}}$ has settled into its steady state. The error is fairly constant along the axis. It is immediately clear that smaller R and higher n lead to improved agreement.

To investigate convergence with worldtube radius, we define the

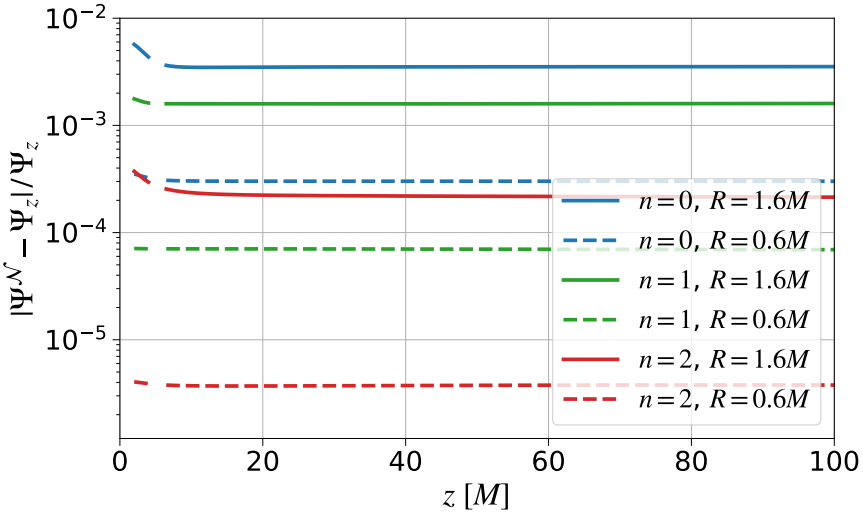

Figure 2.6: The relative error of the scalar field Ψ along the z-axis compared to the analytical solution Ψ_z given by Eq. (2.54). We show two simulations with worldtube radii $1.6M$ and $0.6M$ for each order, 0, 1 and 2. The error decreases with higher order or smaller worldtube radius, as expected. A small region is cut out around $z = r_p = 5M$, where Eq. (2.54) converges too slowly to be calculated to sufficient accuracy in practice.

L_1-norm

$$\|f(x)\| := \int_{10M}^{100M} |f(x)| dx, \tag{2.55}$$

which we use to integrate the relative error shown in Fig. 2.6 between $z = 10M$ and $z = 100M$ for each simulation. Using this norm, the top panel of Fig. 2.7 plots the relative differences between the analytical solution Eq. (2.54) and numerical solutions $\Psi^{\mathcal{N}}$ using various R and n and evaluated at late time in steady state. Each symbol represents the integrated, relative error of a simulation's final value. Also plotted is a best fit of the error convergence $\propto R^{\alpha}$, where R is the worldtube radius and α is the global convergence order. The lower panel of Fig. 2.7 shows the local convergence order α_{loc} as defined in Eq. (3.75).

As explained in Section 2.4.5, we expect the convergence order $\alpha = n + 2$ in the volume outside the worldtube. At order $n = 2$, the global convergence order is best fit to $\alpha = 4.07$ which matches the predicted error. Order 1 has a fitted global convergence order of 3.14 and a local convergence order close to this value across the worldtube radii sampled. For the zeroth-order expansion, a global value of 2.33 is calculated, but the local order consistently decreases with smaller worldtube radii, which suggests that the error might still get contributions from higher-order terms at the larger worldtube radii, similar to the zeroth-order expansion in Fig. 2.4.

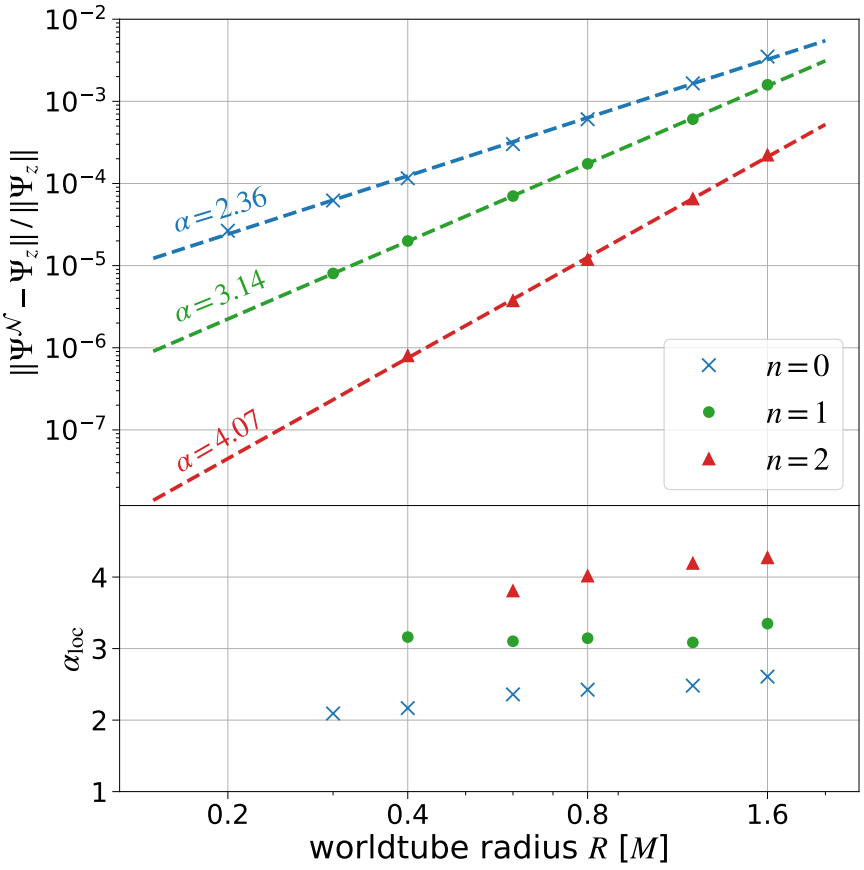

Figure 2.7: *Top panel:* The relative difference between the numerical, retarded field $\Psi^{\mathcal{N}}$ along the z-axis and the analytical solution Ψ_z given in Eq. (2.54), integrated between $z = 10M$ and $z = 100M$ using the L_1-norm of Eq. (2.55). Each cross represents the final value of a simulation. The straight lines are a best fit to the power-law relation $\varepsilon \propto R^{\alpha}$. *Bottom panel:* The local convergence order between the simulations of adjacent worldtube radii as defined in Eq. (3.75). The simulations with $n = 1$ and $n = 2$ show a constant convergence order consistent with the predicted rate $\alpha = n + 2$. The $n = 0$ simulations show a higher convergence rate at larger worldtube radii but approach the expected value at smaller radii.

2.5.3 Solution along the x-axis

The tests of our method so far compared to previously known data, either at the position of the charge or on the z-axis. We now evaluate the convergence with worldtube radius in the volume, at locations where no analytic solution is available. To this end, we evaluate our numerical solutions $\Psi^{\mathcal{N}}$ along the co-rotating $\bar{x}$-axis, which passes through the center of the Schwarzschild black hole and the point charge. The settled field along this axis is shown as the blue curve in Figure 2.3. The simulation with $n = 2$ and $R = 0.4M$ is used as a reference solution, denoted Ψ_{ref}, since it has the lowest error inside the worldtube and along the z-axis, as demonstrated above.

Figure 2.8 shows the relative difference with respect to the reference solution between $x = 1.9M$ and $x = 100M$ for two sample simulations at each order. The field along the x-axis has more features as it lies in the orbital plane of the charge. The error along the x-axis is therefore not quite as smooth as along the z-axis; for instance at $x \approx 80M$ some features are apparent, which coincide to a wave-crest in $\Psi^{\mathcal{N}}$ (see Fig. 2.3). The error decreases with both a higher expansion order n and a decreasing worldtube radius R

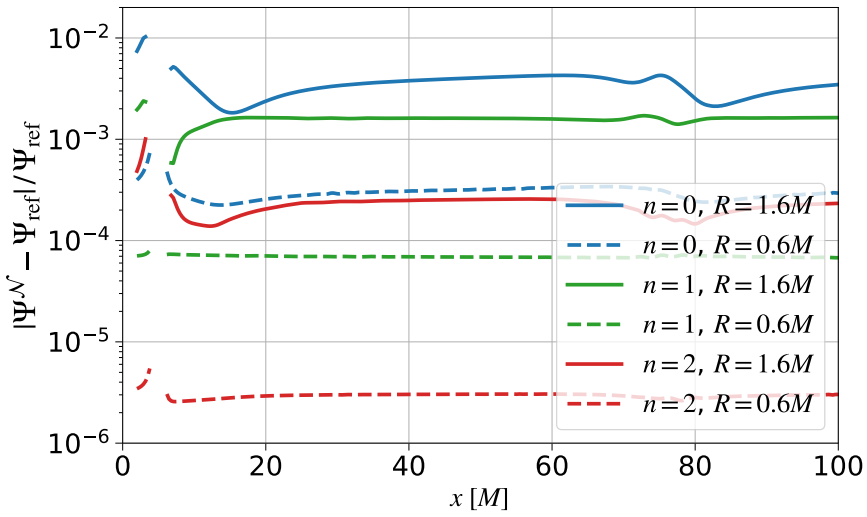

Figure 2.8: The relative error along the x-axis between $x = 10M$ and $x = 100M$ for two sample simulations of each order. The worldtube is centered at $x = 5M$ and cut out from the plots.

as is expected.

To quantify the convergence with respect to R we compute the norm Eq. (2.55) integrated along the co-moving x-axis, $\|\Psi^{\mathcal{N}}(x) - \Psi_{\rm ref}(x)\|$. This difference, normalized, is plotted in Fig. 2.9, where each marker represents an individual simulation. The straight lines show power law fits $\propto R^{\alpha}$. In the bottom panel we show the local convergence order $\alpha_{\rm loc}$ as defined in Eq. (3.75). The convergence rates in worldtube radius R are close to the expectation from Eq. (2.45), $\alpha = n + 2$, with global convergence order α equal to 2.25, 3.18, 4.29 for orders 0, 1 and 2, respectively. For $n = 0$, the local convergence order $\alpha_{\rm loc}$ is steadily decreasing with the worldtube radius R towards the expected value of $\alpha = 2$, which suggests it is just entering the convergent regime here. The local convergence rate of the $n = 2$ simulations appears to jump slightly at the smallest worldtube radius sampled, which we attribute to numerical error.

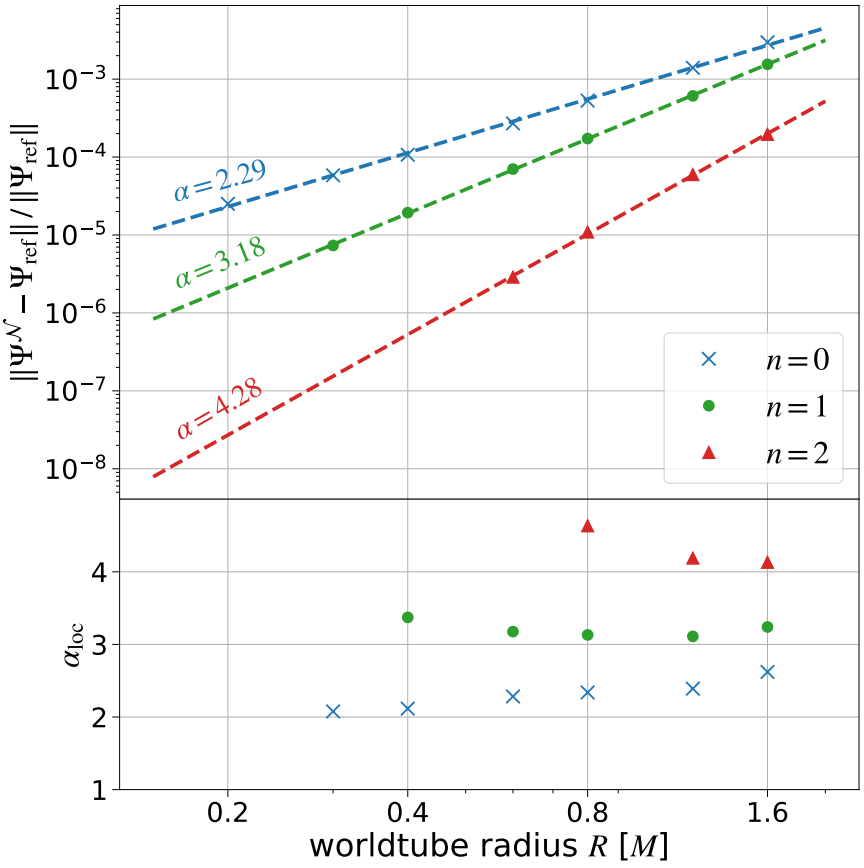

Figure 2.9: *Top panel:* The relative error ε integrated along the comoving x-axis compared to a reference solution $\Psi_{\rm ref}$ with $n = 2$ and $R = 0.4M$. Each cross represents a simulation, and the straight lines are a best fit of the relation $\varepsilon \propto R^{\alpha}$. *Bottom panel:* The local convergence order as defined in Eq. (3.75). At first and second order, the simulations reproduce the expected convergence order of $\alpha = n + 2$. At zeroth order, the local convergence approaches the expected order for smaller worldtube radii, likely indicating that the error still has contributions from higher-order terms in this regime.

2.6 Conclusions

In this chapter we continue the work of [1] and explore a novel approach to simulating high mass-ratio binary black holes. A large region (worldtube) is excised from the numerical domain around the smaller black hole, to alleviate the limiting CFL condition due to small grid spacing in this region. The solution inside the worldtube is represented by a perturbative approximation that is determined by the numerical solution on the boundary and in turn provides boundary conditions to the numerical evolution.

We test this method using the toy problem of a scalar charge in circular orbit around a central black hole. The simulations are carried out in 3+1D using SpECTRE, the new discontinuous Galerkin code developed by the SXS collaboration. In order to develop algorithms that generalize to the full GR problem, we do not decompose our solution into spherical harmonics as is the usual approach. We split the solution near the scalar charge into a puncture field, which is fully determined as a local expansion in Sec. 2.3, and a regular field, which is a smooth Taylor series with undetermined coefficients. The expansion coefficients in the regular field are determined by (i) the numerical solution on the

[1]: Dhesi et al. (2021), *Worldtube excision method for intermediate-mass-ratio inspirals: Scalar-field toy model*

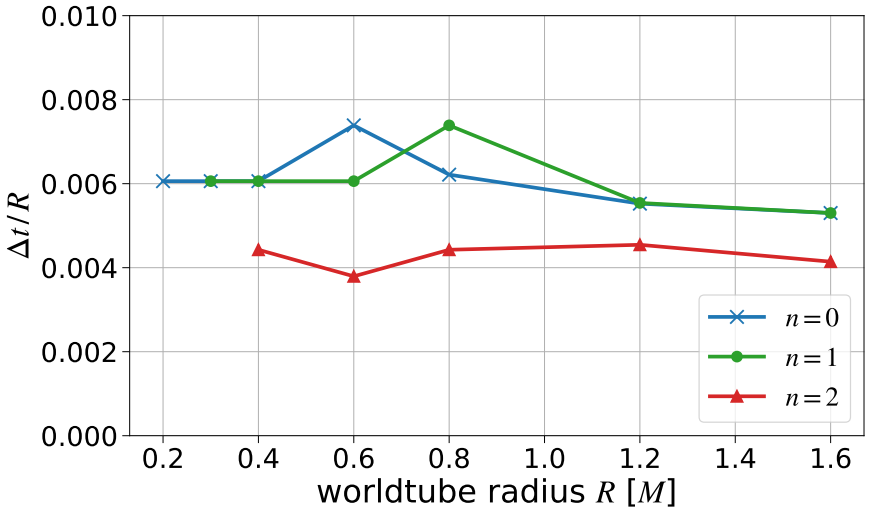

Figure 2.10: Time steps Δt of the worldtube simulations presented here.

worldtube boundary and (ii) the scalar wave equation as described in Sec. 2.4. Our puncture is constructed from the Detweiler-Whiting singular field, allowing us to calculate the scalar self-force from our regular field.

We implement the described matching scheme for orders $n = 0, 1$ and 2 and perform numerical simulations for a circular orbit of radius $r_p = 5M$ for a variety of worldtube radii. In Sec. 2.4.5 we make a theoretical argument for how the error introduced by the excision should converge with the excision radius in- and outside the worldtube. We confirm these results in Sec. 2.5 and show that the scheme solves the scalar wave equation with high accuracy even at relatively large worldtube radii. We further validate our method by comparing against known values of the Detweiler-Whiting regular field and its first derivatives on the particle's worldline.

The ultimate goal of the worldtube method is to speed up BBH simulations at large mass-ratios by alleviating the CFL condition. Figure 2.10 considers the time steps sizes Δt taken by our primary simulations. Plotted is $\Delta t/R$ vs the worldtube radius R. Note that the resolutions of our simulations were adjusted such that for each simulation, numerical truncation error is subdominant compared to the worldtube error, resulting in differences in Δt for simulations with different expansion orders at the same worldtube radius. Nevertheless, it is apparent that for fixed order, the time step is roughly proportional to the worldtube radius. Therefore, the promise that larger worldtube radii allow larger time steps $\propto R$ indeed holds. Ideally, the worldtube error should be comparable to or somewhat smaller than the NR error. Our results show that this can be achieved by either decreasing the worldtube radius or by increasing the expansion order. The former, of course, would lead

to a smaller grid-spacing and a more significant CFL condition, whereas the latter has no noticeable performance cost. We have discussed the next steps towards tackling BBH simulations using the worldtube method in [1].

[1]: Dhesi et al. (2021), *Worldtube excision method for intermediate-mass-ratio inspirals: Scalar-field toy model*

Before tackling the full BBH problem, our next step will be to include the back-reaction of the scalar field onto the charged particle [144]. In the present work we have computed the first derivatives of the Detweiler-Whiting regular field, from which we can construct the scalar self-force, but we have so far ignored the effect of that force. Once it is accounted for, the equations of motion for the scalar charge q of bare mass μ_0 are given by [145]

[144]: Diener et al. (2012), *Self-Consistent Orbital Evolution of a Particle around a Schwarzschild Black Hole*

[145]: Quinn (2000), *Axiomatic approach to radiation reaction of scalar point particles in curved spacetime*

$$u^\beta \nabla_\beta (\mu u_\alpha) = q \partial_\alpha \Psi^{\mathcal{R}}, \tag{2.56}$$

$$\mu = -q\Psi^{\mathcal{R}} + \mu_0. \tag{2.57}$$

Allowing the particle's trajectory to evolve dynamically in this way is an important step toward the full gravity problem which we explore in the next chapter.

2.7 Appendix: Constraint-preserving boundary conditions

The domain features two boundaries which require boundary conditions on the characteristic fields flowing into the domain: the worldtube boundary and the outer boundary. For the fields Z^1 and Z^2_i (arising from reduction to first-order form), we use constraint-preserving boundary conditions which are formulated analogously to [75] and applied using the Bjorhus condition. We begin by rewriting Eq. (2.6) in terms of the characteristic fields with respect to a boundary with normal vector $\hat{n}^i$,

[75]: Kidder et al. (2005), *Boundary conditions for the Einstein evolution system*

$$C_i = \partial_i \Psi - \Phi_i \tag{2.58}$$

$$= \partial_i Z^1 - \frac{1}{2}(U^+ - U^-)\hat{n}_i - Z^2_i. \tag{2.59}$$

The normal component of this constraint is given by

$$\hat{n}^i C_i = \hat{n}^i \partial_i Z^1 - \frac{1}{2}(U^+ - U^-) - \hat{n}^i Z^2_i. \tag{2.60}$$

Vanishing of the constraints implies in particular that the normal component vanishes, $\hat{n}^i C_i = 0$, we interpret as a boundary

condition on Z^i:

$$(\hat{n}^i \partial_i Z^1)_{BC} = \frac{1}{2}(U^+ - U^-) + \hat{n}^i Z^2_i. \tag{2.61}$$

Applying the same procedure to Eq. (2.7) yields

$$\hat{n}^i C_{ij} = \hat{n}^i \partial_i Z^2_j + \frac{1}{2}\hat{n}^i \hat{n}_j \, \partial_i (U^+ - U^-) - \frac{1}{2}\partial_j \, (U^+ - U^-) - \hat{n}^i \partial_j Z^2_i \tag{2.62}$$

and

$$(\hat{n}^i \partial_i \, Z^2_j)_{BC} = -\frac{1}{2}\hat{n}^i \hat{n}_j \, \partial_i (U^+ - U^-) + \frac{1}{2}\partial_j \, (U^+ + U^-) + \hat{n}^i \partial_j Z^2_i. \tag{2.63}$$

In order to implement Eqs. (2.61) and (2.63), we return to the evolution equations in first order form,

$$\partial_t \psi^\alpha + A^{i\alpha}_\beta \partial_i \psi^\beta = F^\alpha. \tag{2.64}$$

Projecting onto the characteristic fields, one finds

$$e^{\hat{a}}{}_a (\partial_t \psi^a + A^{ia}_b \partial_i \psi^b) = e^{\hat{a}}{}_a F^a, \tag{2.65}$$

$$\partial_t \psi^{\hat{a}} + e^{\hat{a}}{}_a A^{ia}_b (P^k_i + \hat{n}^k \hat{n}_i) \partial_k \psi^b = e^{\hat{a}}{}_a F^a, \tag{2.66}$$

$$\partial_t \psi^{\hat{a}} + v_{(\hat{a})} \hat{n}^k \partial_k \psi^{\hat{a}} + e^{\hat{a}}{}_a A^{ia}_b P^k_i \partial_k \psi^b = e^{\hat{a}}{}_a F^a. \tag{2.67}$$

Boundary conditions are now applied by modifying the term $v_{(\hat{a})} \hat{n}^k \partial_k \psi^{\hat{a}}$: Iff $v_{(\hat{a})} < 0$ at a grid-point on the boundary, then the following modified evolution equation is used at that grid-point:

$$d_t \psi^{\hat{a}} = D_t \psi^{\hat{a}} + v_{(\hat{a})} \left(\hat{n}^i \partial_i \psi^{\hat{a}} - (\hat{n}^i \partial_i \psi^{\hat{a}})_{BC} \right). \tag{2.68}$$

Here

$$D_t \psi^{\hat{a}} \equiv -e^{\hat{a}}{}_a A^{ia}_b \partial_i \psi^b + e^{\hat{a}}{}_a F^a \tag{2.69}$$

represents the volume time-derivative of the characteristic fields. In other words, the time-derivative arising from the volume equations is corrected with a term that ensures the desired boundary condition. Summing Eqs. (2.60) and (2.61) yields

$$\hat{n}^i \partial_i Z^1 - (\hat{n}^i \partial_i Z^1)_{BC} = \hat{n}^i C_i. \tag{2.70}$$

Analogously, combining Eqs. (2.62) and (2.63) results in

$$\hat{n}^i \partial_i Z^2_j - (\hat{n}^i \partial_i Z^2_j)_{BC} = \hat{n}^i C_{ij}. \tag{2.71}$$

Finally, we insert this into the Bjorhus condition (2.68) to obtain

$$d_t Z^1 = D_t Z^1 + v_{Z^1} \hat{n}^i C_i, \tag{2.72}$$
$$d_t Z^2_i = D_t Z^2_i + v_{Z^2} \hat{n}^i C_{ij}, \tag{2.73}$$

where boundary corrections are only imposed when the corresponding characteristic speeds are negative.

2.8 Appendix: Matching method at arbitrary order

The main text in Sec. 2.4 develops our matching scheme up to order $n = 2$. Here we show how this can be generalized to arbitrary order n.

First, we introduce some notation and useful identities. We make use of multi-index notation according to [6] where a capital index L stands for a collection of l indices,

[6]: Poisson et al. (2014), *Gravity: Newtonian, Post-Newtonian, Relativistic*

$$A_L = A_{k_1 k_2 \cdots k_l}. \tag{2.74}$$

The tensor product of l coordinate vectors or l normal vectors is abbreviated as

$$x^L = x^{k_1} x^{k_2} \cdots n^{k_l}, \tag{2.75}$$
$$n^L = n^{k_1} n^{k_2} \cdots n^{k_l}, \tag{2.76}$$

and the tensor product of l Kronecker symbols is written as

$$\delta^{2L} = \delta^{k_1 k_2} \delta^{k_3 k_4} \cdots \delta^{k_{2l-1} k_{2l}}. \tag{2.77}$$

Symmetric, trace-free (STF) tensors are written with angular brackets around the indices. The combination of l STF normal vectors is defined as [146]

[146]: Thorne (1980), *Multipole expansions of gravitational radiation*

$$n^{\langle L \rangle} = n^{\langle k_1} \cdots n^{k_l \rangle} = \sum_{k=0}^{\lfloor l/2 \rfloor} \tilde{c}^{\,l}_k \delta^{(2K} n^{L-2K)}, \tag{2.78}$$

where

$$\tilde{c}^{\,l}_k = (-1)^k \frac{l!(2l-2k-1)!!}{(2l-1)!!(l-2k)!(2k)!!}. \tag{2.79}$$

The parentheses in Eq. (2.78) indicate indices to be symmetrized and $\lfloor l/2 \rfloor$ is the largest integer less than or equal to $l/2$. The inverse expression is given by [147]

[147]: Blanchet et al. (1986), *Radiative gravitational fields in general relativity. I - General structure of the field outside the source*

$$n^L = n^{k_1} \cdots n^{k_l} = \sum_{k=0}^{\lfloor l/2 \rfloor} c_k^l \delta^{(2K} n^{\langle L-2K \rangle)} \tag{2.80}$$

with

$$c_k^l = \frac{l!(2l-4k+1)!!}{(2l-2k+1)!!(l-2k)!(2k)!!}. \tag{2.81}$$

The $n^{\langle L \rangle}$ provide an orthogonal basis for functions on a sphere, and each $n^{\langle L \rangle}$ is an eigenfunction of the Laplacian $\nabla^2 := \delta^{ab}\partial_a\partial_b$, satisfying $\nabla^2 n^{\langle L \rangle} = -\frac{\ell(\ell+1)}{\rho^2} n^{\langle L \rangle}$. For a fixed l, the STF tensors $n^{\langle L \rangle}$ span the same functions as the set of spherical harmonics $Y_{lm}(\theta, \phi)$ of rank l. This can be seen by expressing the normal vector as $n^i = (\sin\theta\cos\phi,\ \sin\theta\sin\phi,\ \cos\theta)$, leading to [6]

[6]: Poisson et al. (2014), *Gravity: Newtonian, Post-Newtonian, Relativistic*

$$Y_{lm} = \mathcal{Y}_{lm}^{*\langle L \rangle} n_{\langle L \rangle}, \tag{2.82a}$$

$$n^{\langle L \rangle} = N_l \sum_{m=-l}^{l} \mathcal{Y}_{lm}^{\langle L \rangle} Y_{lm}, \tag{2.82b}$$

where

$$\mathcal{Y}_{lm}^{\langle L \rangle} := \frac{1}{N_l} \int_{S^2} n^{\langle L \rangle} Y_{lm}^* d\Omega, \tag{2.82c}$$

$$N_l := \frac{4\pi l!}{(2l+1)!!}. \tag{2.82d}$$

We start by expanding the regular scalar field $\Psi^{\mathcal{R}}(t, x^i)$ and its time derivative in a power series around the charge's position to arbitrary order n as shown in Eq. (2.83). We will show that all free components of the expansion can be uniquely determined at each time step from (i) numerical data from the worldtube boundary and (ii) the Klein-Gordon equation (2.3).

2.8.1 Worldtube boundary data

We carry the Taylor expansion of the regular field given in Eq. (2.25) to nth order and give an analogous expansion for the time deriva-

tive

$$\Psi^{\mathcal{R}}(t,x^{\bar{i}}) = \sum_{l=0}^{n} \Psi^{\mathcal{R}}_{\bar{k}_1\cdots\bar{k}_n}(t)x^{\bar{k}_1}\cdots x^{\bar{k}_n} + \mathcal{O}(\rho^{n+1}), \tag{2.83a}$$

$$\partial_t\Psi^{\mathcal{R}}(t,x^{\bar{i}}) = \sum_{l=0}^{n} \dot{\Psi}^{\mathcal{R}}_{\bar{k}_1\cdots\bar{k}_n}(t)x^{\bar{k}_1}\cdots x^{\bar{k}_n} + \mathcal{O}(\rho^{n+1}), \tag{2.83b}$$

which has $\frac{1}{2}\sum_{i=0}^{n}(i+2)(i+1) = \frac{1}{6}(n+3)(n+2)(n+1)$ components.

The continuity condition at the worldtube boundary is given by Eq. (2.28). Both sides of this equation can be expressed in a basis of STF normal vectors. The regular field $\Psi^{\mathcal{R}}(t_s,x^{\bar{i}})$ on the left is transformed using Eq. (2.80) to give

$$\Psi^{\mathcal{R}}(t_s,x^{i}) = \sum_{l=0}^{n}\rho^l\Psi^{\mathcal{R}}_{\bar{L}}(t_s)\sum_{k=0}^{\lfloor l/2\rfloor} c_k^l\delta^{(2\bar{K}}n^{\langle\bar{L}-2\bar{K}\rangle)} \tag{2.84}$$

$$= \sum_{l=0}^{n}\sum_{k=0}^{\lfloor l/2\rfloor}\rho^l c_k^l\Psi^{\mathcal{R}}_{\bar{L}-2\bar{K}\bar{i}_1\bar{i}_1\cdots\bar{i}_k\bar{i}_k}(t_s)n^{\langle\bar{L}-2\bar{K}\rangle}. \tag{2.85}$$

As in Sec. 2.4, the right-hand side of Eq. (2.28) is calculated by projecting the numerical, regular field onto spherical harmonics up to order n to obtain the coefficients $a_{lm}^{\mathcal{N},\mathcal{R}}$. This expansion is then transformed to STF normal vectors using Eq. (2.82a),

$$\sum_{l=0}^{n}\Psi^{\mathcal{N},\mathcal{R}}_{\langle\bar{L}\rangle}(t_s)n^{\langle\bar{L}\rangle} = \sum_{l=0}^{n}\sum_{m=-l}^{l}a_{lm}(t_s)Y_{lm}(x^{\bar{i}}). \tag{2.86}$$

The orthogonality of the STF normal vectors allows us to match Eqs. (2.85) and (2.86) order by order, yielding a system of algebraic equations:

$$\Psi^{\mathcal{N},\mathcal{R}}_{\langle\bar{L}\rangle}(t_s) = \sum_{k=0}^{\lfloor\frac{n-l}{2}\rfloor}\rho^{l+2k}c_k^{l+2k}\Psi^{\mathcal{R}}_{\bar{L}\bar{i}_1\bar{i}_1\cdots\bar{i}_k\bar{i}_k}(t_s), \quad 0\le l\le n. \tag{2.87}$$

Each tensor component in the set $\left\{\Psi^{\mathcal{N},\mathcal{R}}_{\langle\bar{L}\rangle}\right\}_l$ with $0\le l\le n$ fixes one degree of freedom of the Taylor coefficients $\left\{\Psi^{\mathcal{R}}_{\bar{L}}\right\}_l$ for a total of $(n+1)^2$ equations. The matching equations for the time derivative coefficients $\left\{\dot{\Psi}^{\mathcal{R}}_{\bar{L}}\right\}_l$ are derived completely analogously.

2.8.2 Klein-Gordon equation

The remaining components of $\left\{\Psi^{\mathcal{R}}_{\bar{L}}\right\}_l$ are fixed by the Klein-Gordon equation (2.35). The metric quantities $g^{\mu\nu}$ and Γ^{μ} are expanded to the same order n as the regular field in the grid frame $x^{\bar{\imath}}$,

$$g^{\bar{\mu}\bar{\nu}}(t_s, x^{\bar{\imath}}) = \sum_{l=0}^{n} g^{\bar{\mu}\bar{\nu}}_{\bar{L}}\, x^{\bar{L}} + \mathcal{O}(\rho^{n+1}), \tag{2.88}$$

$$\Gamma^{\bar{\mu}}(t_s, x^{\bar{\imath}}) = \sum_{l=0}^{n} \Gamma^{\bar{\mu}}_{\bar{L}}\, x^{\bar{L}} + \mathcal{O}(\rho^{n+1}), \tag{2.89}$$

where the expansion coefficients are given by

$$g^{\bar{\mu}\bar{\nu}}_{\bar{L}} := \frac{1}{l!}\partial_{\bar{L}} g^{\bar{\mu}\bar{\nu}}(t_s, x^{\bar{\imath}}_p), \tag{2.90}$$

$$\Gamma^{\bar{\mu}}_{\bar{L}} := \frac{1}{l!}\partial_{\bar{L}} \Gamma^{\bar{\mu}}(t_s, x^{\bar{\imath}}_p). \tag{2.91}$$

Here, recall, $x^{\bar{\imath}}_p = (r_p, 0, 0)$. Substituting these expansions into the Klein-Gordon equation, we obtain

$$\begin{aligned} 0 = &\left(\sum_{l=0}^{n} g^{\bar{\mu}\bar{\nu}}_{\bar{L}} x^{\bar{L}}\right) \partial_{\bar{\mu}}\partial_{\bar{\nu}} \left(\sum_{l=0}^{n} \Psi^{\mathcal{R}}_{\bar{L}} x^{\bar{L}}\right) \\ &+ \left(\sum_{l=0}^{n} \Gamma^{\bar{\mu}}_{\bar{L}} x^{\bar{L}}\right) \partial_{\bar{\mu}} \left(\sum_{l=0}^{n} \Psi^{\mathcal{R}}_{\bar{L}} x^{\bar{L}}\right). \end{aligned} \tag{2.92}$$

We now split the partial derivative into its time part ∂_t and spatial part $\partial_{\bar{\imath}}$ and solve order by order in ρ. The kth-order equation reads

$$\begin{aligned} 0 = \sum_{l=0}^{k} \Big(& g^{tt}_{\bar{K}-\bar{L}} \ddot{\Psi}^{\mathcal{R}}_{\bar{L}} + 2(l+1) g^{t\bar{\imath}}_{\bar{K}-\bar{L}} \dot{\Psi}^{\mathcal{R}}_{\bar{L}\bar{\imath}} \\ & + (l+2)(l+1) g^{\bar{\imath}\bar{\jmath}}_{\bar{K}-\bar{L}} \Psi^{\mathcal{R}}_{\bar{L}\bar{\imath}\bar{\jmath}} - \Gamma^{t}_{\bar{K}-\bar{L}} \dot{\Psi}^{\mathcal{R}}_{\bar{L}} \\ & - (l+1) \Gamma^{\bar{\imath}}_{\bar{K}-\bar{L}} \Psi^{\mathcal{R}}_{\bar{L}\bar{\imath}} \Big) \qquad 0 \le k \le n-2, \end{aligned} \tag{2.93}$$

where we have made use of the identity $\partial_{\bar{\imath}} a_{\bar{L}}(t) x^{\bar{L}} = l a_{\bar{L}-1\bar{\imath}}(t) x^{\bar{L}-1}$ for $a_{\bar{L}}$ completely symmetric $a_{(\bar{L})} = a_{\bar{L}}$. The set of equations (2.93) fixes $\frac{1}{6}(n+1)n(n-1)$ components of $\Psi^{\mathcal{R}}$ which, when combined with equations Eq. (2.87), fixes all components of the expansion (2.83).

Worldtube excision method: self-consistent evolution in a scalar-charge model

3

This chapter is based on my lead-author publication [148]. It describes the addition of a self-consistent evolution algorithm to a scalar charge and analyzes quasi-circular inspirals.
My contributions to this work include the derivation and implementation of the iterative method to evolve the particle's motion as well as the algorithm to adjust the DG grid accordingly. I also produced and analyzed all results.

3.1 Introduction

Inspiraling binary black holes (BBHs) will remain prime targets for gravitational-wave searches as we approach the era of third-generation instruments and LISA (the Laser Interferometer Space Antenna). Precision modelling of BBH signals over the full parameter space of expected sources remains a high priority task [51]. Unique difficulties are posed in the intermediate mass-ratios regime, where Numerical Relativity (NR) simulations become less efficient while perturbative methods may not be adequate. This work continues the program initiated in Dhesi *et al.* [1] (henceforth *Paper I*) aimed at developing a synergistic approach to the problem, combining NR techniques with methods in black hole perturbation theory. The general idea is to alleviate the scale disparity that hampers NR simulations by excising a large region around the smaller black hole (BH), inside which an approximate analytical solution is used, representing a tidally perturbed BH geometry. The smallest lengthscale on the numerical domain is now that of the excised sphere (a "worldtube" in spacetime), rather than the scale of the smaller body. As a result, the Courant-Friedrich-Lewy (CFL) stability limit on the timestep of the numerical simulation is relaxed, with a commensurate gain in computational efficiency.

[51]: Afshordi et al. (2023), *Waveform Modelling for the Laser Interferometer Space Antenna*

[1]: Dhesi et al. (2021), *Worldtube excision method for intermediate-mass-ratio inspirals: Scalar-field toy model*

Paper I laid out the basic framework and tested it in a simple scalar-field model in 1+1 dimensions. In this toy model, reviewed further below, the smaller BH is replaced with a point particle endowed with scalar charge, which sources a (massless) scalar field, assumed to satisfy the Klein-Gordon equation on the fixed geometry of the large object, taken to be a Schwarzschild black hole. The scalar charge in Paper I was taken to move on a fixed circular geodesic

orbit around the BH, with both gravitational and scalar-field back-reaction forces ignored. Paper I was focused on exploring various techniques for matching the numerical field outside the excision worldtube to the analytically prescribed solution inside it. It also investigated and quantified the scaling of the model error with the worldtube size, using two independent numerical implementation schemes.

The previous chapter applied the worldtube idea in full 3+1 dimensions, still working with a scalar-field toy model and a fixed circular geodesic source. The problem was reformulated as an initial-boundary evolution problem suitable for implementation on the SpECTRE platform [86], and a completely new implementation code was developed. The paper detailed the construction of a suitable approximate analytical solution inside the worldtube, and devised a procedure for fixing remaining, *a priori* unknown degrees of freedom using dynamical matching to the external numerical solution across the worldtube's boundary. The convergence of the numerical solutions with worldtube size was quantified and shown to agree with theoretical expectations. Detailed comparisons were made with analytical solutions in limiting cases, and with numerical results from other simulations, showing a reassuring agreement.

[86]: Deppe et al. (2024), *SpECTRE*

In the current work we make a crucial step towards the physical BBH problem by relaxing the condition that the scalar charge is moving on a fixed geodesic orbit, and instead allowing the orbit to evolve radiatively, solving the sourced field equation in a self-consistent manner. This requires substantial adaptations in both formulation and code infrastructure. The analytical model inside the worldtube must be generalised to allow for the source's acceleration as it moves in its inspiral trajectory around the large BH. The architecture of the numerical domain must be significantly modified, too. In particular, our evolution code employs a discontinuous Galerkin (DG) scheme with several hundred DG elements that are deformed to fit the domain structure using a series of smooth coordinate maps, and these must now become time-dependent.

We begin in Sec. 3.2 with a general summary of the worldtube method. Section 3.3 details our numerical method, including the construction of time-dependent coordinate maps for generic orbits, and the procedure for matching numerical data to the analytical solution across the worldtube's boundary. In Sec. 3.4 we give a generalized approximate analytical model for the field inside the worldtube, allowing for source acceleration. Section

3.5 describes in detail the procedure employed to perform a self-consistent evolution of the sourced field equations, coupled to the particle's equation of motion. Since, at each timestep, the analytical field inside the worldtube depends on the particle's acceleration, which itself is determined from the field that we are attempting to calculate, the acceleration equations take an implicit form. We describe an iterative scheme developed to deal with this problem.

Section 3.6 contains a sample of illustrative results from our numerical simulations. We show examples of inspiral orbits and emitted scalar-field waveforms, tracking the evolution all through the inspiral, plunge and ringdown phases. We use invariant diagnostics–the adiabaticity parameter and total orbital phase—to perform quantitative tests against accurate perturbative calculations in the adiabatic approximation, showing excellent agreement. We show, furthermore, how our simulations resolve post-adiabatic information. We explore in detail the scaling of numerical error with worldtube size and with the number of iterations of the acceleration equation, in both cases confirming the expected convergence. Section 2.6 summarizes our results and discusses forthcoming steps in our program.

To the best of our knowledge, our work is the first to report a fully self-consistent evolution in the scalar-field model. Previously, Diener *et al*. [149] have studied the radiative evolution of orbits in the same model, using an alternative method—the so called "effective source" approach (whose relation to our worldtube method is discussed in Sec. III.C of Paper I). However, in that work it was found that, in order to achieve a numerically stable evolution, certain terms (involving time derivatives of the acceleration) had to be ignored in the equations that couple the particle's equation of motion to the local analytical approximation. For that reason, we were unable to perform a detailed comparison to our results.

[149]: Diener et al. (2012), *Self-consistent orbital evolution of a particle around a Schwarzschild black hole*

The rest of this introduction reviews the scalar-field toy model employed in this work. Throughout the chapter we use geometrized units, with $G = c = 1$. We use Latin indices to denote spatial tensor components and Greek indices for spacetime components.

3.1.1 Scalar-field toy model

We consider a Schwarzschild BH of mass M orbited by a pointlike particle carrying a scalar charge q and mass $\mu \ll M$. The particle

sources a (test) scalar field Ψ, assumed to be governed by the massless Klein-Gordon equation

$$g^{\mu\nu}\nabla_\mu\nabla_\nu\Psi = -4\pi q \int \frac{\delta^4(x^\alpha - x_p^\alpha(\tau))}{\sqrt{-g}} d\tau, \tag{3.1}$$

and subject to the usual retarded boundary conditions at null infinity and on the event horizon. In Eq. (3.1), $g^{\mu\nu}$ is the inverse Schwarzschild metric and ∇_μ is the covariant derivative compatible with it. $x_p^\alpha(\tau)$ describes the particle's worldline, parameterized in terms of proper time τ. The worldline itself satisfies the equation of motion

$$u^\beta\nabla_\beta(\mu u_\alpha) = q\nabla_\alpha\Psi^{\mathcal{R}}, \tag{3.2}$$

where $u^\alpha := \frac{dx_p^\alpha}{d\tau}$ is the tangent four-velocity, and $\Psi^{\mathcal{R}}$ is the Detweiler-Whiting regular piece of Ψ ('R field') at the position of the particle. On the left-hand side here is the covariant derivative of the particle's four-momentum along the orbit, and the right-hand side represents the back-reaction force from the particle's own scalar field, known as self-force. Equations (3.1) and (3.2), together with a prescription for constructing $\Psi^{\mathcal{R}}$ out of Ψ, form a closed coupled set of "self-consistent" evolution equations, whose solution we aim to obtain. This solution is uniquely determined once initial conditions are given in the form of x^α and u^α at an initial time, together with initial data for Ψ.

It is useful to split Eq. (3.2) into its components orthogonal and tangent to u^α, respectively given by

$$u^\beta\nabla_\beta(u_\alpha) = \frac{q}{\mu}(\delta_\alpha^\beta + u^\beta u_\alpha)\nabla_\beta\Psi^{\mathcal{R}}, \tag{3.3}$$

$$\frac{d\mu}{d\tau} = -qu^\alpha\nabla_\alpha\Psi^{\mathcal{R}}. \tag{3.4}$$

The first equation describes the self-acceleration of the scalar charge on the Schwarzschild background due to the scalar-field back reaction. The second equation can be immediately integrated to yield

$$\mu = \mu_0 - q\Psi^{\mathcal{R}}, \tag{3.5}$$

which describes the evolution of the particle's mass over time due to exchange of energy with the ambient scalar field.

From Eq. (3.3) and the fact that $\nabla_\beta\Psi^{\mathcal{R}} \propto q/M^2$, we see that the magnitude of the self-acceleration is controlled by the dimensionless

parameter

$$\epsilon := \frac{q^2}{\mu_0 M}, \tag{3.6}$$

which plays the role of the (small) mass ratio in the analogous BBH problem. We assume $\epsilon \ll 1$, in order to ensure that the orbital evolution is slow during the inspiral, as in the BBH case. In practice, μ changes by a few percent at most during the systems studied here, so the distinction between μ and μ_0 in Eq. (3.6) is subdominant. In this work we also completely neglect the *gravitational* back-reaction on the particle's motion.

3.2 Summary of worldtube method

In the previous chapter, we developed a technique for solving the field equation (3.1) with a source corresponding to a scalar charge on a fixed, circular geodesic orbit. Much of the infrastructure of Paper I carries over to our present work, so we start with a summary of that infrastructure.

We describe the trajectory of the scalar charge using $x_p^i(t)$ in Kerr-Schild (KS) coordinates t, x^i associated with the BH. For the Schwarzschild black hole considered here, the horizon is at $r = 2M$ where the radius in KS coordinates is given by

$$r = \left(\delta_{ij} x^i x^j\right)^{1/2}. \tag{3.7}$$

A KS coordinate sphere, centered on $x_p^i(t)$, is excised from the computational domain. We refer to the spacetime boundary of the excised region as *the worldtube*, denoted by Γ. By construction, the scalar charge is always at the center of the spherical excision sphere. Outside the worldtube, we solve the homogeneous Klein-Gordon equation

$$g^{\mu\nu}\nabla_\mu\nabla_\nu\Psi^{\mathcal{N}} = 0, \tag{3.8}$$

with 3+1 dimensional numerical relativity methods. The superscript $\mathcal{N}$ denotes this numerical solution (as distinguished from the fields $\Psi^{\mathcal{P}}$ and $\Psi^{\mathcal{R}}$ defined below). To facilitate numerical implementation, Eq. (3.8) is reduced to first order in space and time by introducing the following auxiliary variables [150]:

$$\Pi = -\alpha^{-1}(\partial_t\Psi^{\mathcal{N}} - \beta^i\partial_i\Psi^{\mathcal{N}}), \tag{3.9a}$$

$$\Phi_i = \partial_i\Psi^{\mathcal{N}}, \tag{3.9b}$$

[150]: Scheel et al. (2004), *3-D simulations of linearized scalar fields in Kerr space-time*

where α and β^i are, respectively, the lapse function and shift vector of the background metric. They are solved using SpECTRE [86] in 3+1 dimensions using a nodal discontinuous Galerkin (DG) scheme.

[86]: Deppe et al. (2024), *SpECTRE*

In the vicinity of the charge, an approximate particular solution to the inhomogeneous equation (3.1) is given by the puncture field $\Psi^{\mathcal{P}}$. It is constructed as an approximation to the Detweiler-Whiting singular field [133] and expressed as a power series in coordinate distance from $x_p^i(t)$. In Chapter 2, we derived $\Psi^{\mathcal{P}}$ for circular geodesic orbits; here, in Section 3.4, we extend it to generic, accelerated equatorial orbits.

[133]: Detweiler et al. (2003), *Self-force via a Green's functsion decomposition*

The residual field $\Psi^{\mathcal{R}} = \Psi - \Psi^{\mathcal{P}}$ approximately solves the homogeneous Klein-Gordon equation in the worldtube's interior. Our perturbative approximation of the interior solution consists of expanding $\Psi^{\mathcal{R}}$ and its time derivative as a Taylor Series truncated at order n. For $n = 1$, these read

$$\Psi^{\mathcal{R}}(t, x^i) = \Psi_0^{\mathcal{R}}(t) + \Psi_i^{\mathcal{R}}(t)\rho n^i + \mathcal{O}(\rho^2), \tag{3.10}$$

$$\partial_t \Psi^{\mathcal{R}}(t, x^i) = (\partial_t \Psi^{\mathcal{R}})_0(t) + (\partial_t \Psi^{\mathcal{R}})_i(t)\rho n^i + \mathcal{O}(\rho^2). \tag{3.11}$$

Different to the previous chapter, we write this expansion in *inertial* KS coordinates x^i. We define the displacement to the particle as $\Delta x^i := x^i - x_p^i$, the KS spatial distance by $\rho := \sqrt{\delta_{ij}\Delta x^i \Delta x^j}$ and normal vector through $n^i := \Delta x^i/\rho$. The boundary of the worldtube is located at $\rho = R$ (for some constant R). Because Eq. (3.11) expands the inertial time-derivative around a time-dependent expansion point $x_p^i(t)$, the coefficients on the right-hand side of Eq. (3.11) are not the time-derivatives of the coefficients in Eq. (3.10), i.e. $d\Psi_0^{\mathcal{R}}/dt \neq (\partial_t \Psi^{\mathcal{R}})_0$.

The essence of the worldtube scheme lies in determining the unknown expansion coefficients in Eqs. (3.10) and (3.11) dynamically during the evolution. Most of the coefficients are determined from a continuity condition at the worldtube's boundary Γ, which matches the exterior solution $\Psi^{\mathcal{N}}$ to the interior, residual solution $\Psi^{\mathcal{R}}$ at each time step:

$$\Psi^{\mathcal{R}} \overset{\Gamma}{=} \Psi^{\mathcal{N}} - \Psi^{\mathcal{P}}, \tag{3.12}$$

$$\partial_t \Psi^{\mathcal{R}} \overset{\Gamma}{=} \partial_t \Psi^{\mathcal{N}} - \partial_t \Psi^{\mathcal{P}}. \tag{3.13}$$

This matching is done mode by mode in a multipole expansion. For expansion orders $n > 1$, to fully determine all coefficients one must additionally use further constraints coming from the

requirement that $\Psi^{\mathcal{R}}$ solves the vacuum Klein-Gordon equations. As described in the previous chapter, one arrives at ODEs in time, to be solved along with the evolution equation.

Once fully determined, the expansions (3.10) and (3.11) are used to provide boundary conditions to the DG evolution at the worldtube boundary as described in the previous chapter.

The errors of various quantities in the simulation are expected to scale with the worldtube radius R according to a power law. In Chapter 2, we derived the following predictions:

$$\text{Error in } \Psi^{\mathcal{N}}(x^i): \quad \mathcal{O}(R^{n+2}), \tag{3.14}$$

$$\text{Error in } \Psi^{\mathcal{R}}(x^i_p): \quad \mathcal{O}(R^{n+1}), \tag{3.15}$$

$$\text{Error in } \partial_\alpha \Psi^{\mathcal{R}}(x^i_p): \quad \mathcal{O}(R^{n}). \tag{3.16}$$

The validity of these scaling relations was illustrated numerically in the previous chapter for a particle on a fixed, circular geodesic orbit with radius $r_0 = 5M$.

In the next three sections we describe the extension of the above scheme to radiatively evolving orbits. This involves (i) the addition of time-dependent maps to the code, able to track the particle on generic orbits; (ii) the generalization of the puncture field to generic orbits; and (iii) the derivation of an iterative scheme to accommodate the new puncture field. We restrict ourselves to the first-order expansion case, $n = 1$.

3.3 Time-dependent maps for generic orbits

3.3.1 Coordinate frames

The computational domain is constructed by combining several hundred DG elements, each containing up to several thousand collocation points. These grid points correspond to the nodal representation of a tensor product of Legendre polynomials using Gauss-Lobatto quadrature.

The elements are deformed from unit cubes to fit the domain structure using a series of maps. An initial set of time-independent maps transforms them to the so-called grid frame which is co-moving with the grid points. It is depicted in the left panel of Figure 3.1. We denote the corresponding grid coordinates with a bar, $x^{\bar{i}}$.

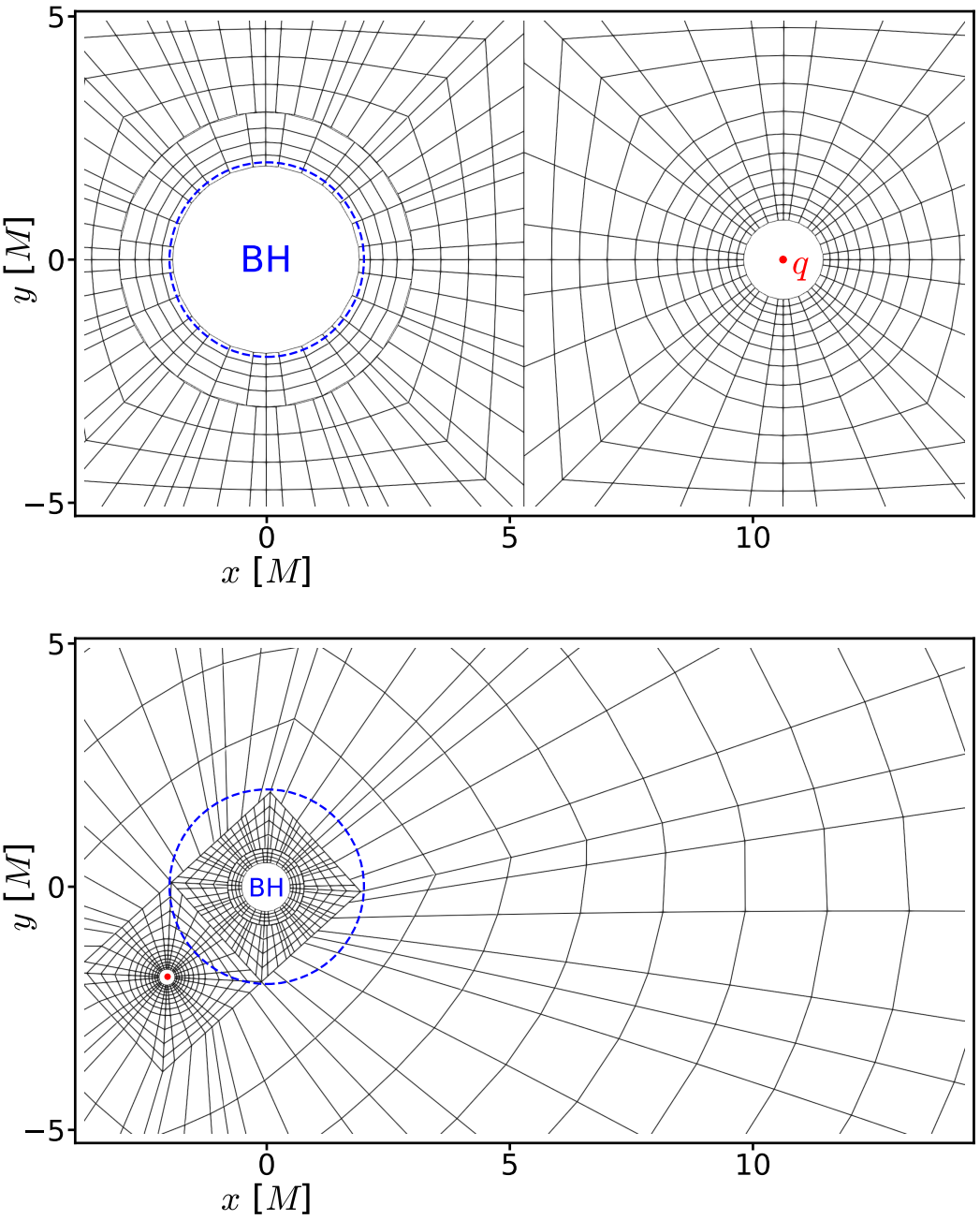

Figure 3.1: *Top:* The DG grid in the time-independent grid frame, equivalent to the inertial Kerr-Schild coordinates at the start of a simulation. On the right side is the worldtube excision sphere with the scalar charge q at its center indicated by a red dot. On the left side is the excision sphere around the central black hole. The blue ring corresponds to the event horizon at $r = 2M$. The KS coordinates are centered on the black hole, and during the evolution the grid rotates around this center. *Bottom:* The DG grid in the inertial frame at a later time of a simulation, at the same scale as on the left. The worldtube excision sphere at the bottom left is close to crossing the event horizon at $r = 2M$. A series of time-dependent functions map the collocation points from the grid frame as depicted in the top panel to the inertial frame by rotating and compressing the grid. The approximate value for the phase is $\phi \approx \frac{5\pi}{4}\pi$, for the orbital radius it is $r_p \approx 2.7M$, for the worldtube radius $R \approx 0.15M$, and the black hole excision radius is $\approx 0.5M$.

A set of time-dependent maps then transform the grid coordinates to the inertial KS coordinates x^i introduced earlier. These time-dependent maps cause the grid points to move across the spacetime background in the inertial frame, to follow the motion of the scalar point charge. The setup is motivated by BBH evolutions where control systems continually adjust time-dependent parameters in these maps to track the motion and shape of the black holes' apparent horizons [131, 132, 151].

[131]: Hemberger et al. (2013), *Dynamical Excision Boundaries in Spectral Evolutions of Binary Black Hole Spacetimes*
[132]: Scheel et al. (2015), *Improved methods for simulating nearly extremal binary black holes*
[151]: Scheel et al. (2006), *Solving Einstein's equations with dual coordinate frames*

In this work, we integrate the particle's orbit along with the DG evolution and determine the time-dependent parameters in the maps by demanding that the worldtube is centered on the scalar charge at each time step. This corresponds to the particle physically moving across the KS background with its position fixed at the excision sphere's center. Because $x^i_p(t)$ is determined directly from the ODE Eq. (3.3), this setup does not utilize control systems.

In the previous chapter, we fixed the particle's orbit to be circular. The map from grid to inertial coordinates then amounts to a global rotation with constant angular velocity. We now generalize to a series of time-dependent maps to accommodate generic, equatorial orbits with dynamically adjustable excision radii:

A rotation map controls the angular position of the particle and is applied globally to each DG element according to

$$x = \bar{x}\cos\phi(t) - \bar{y}\sin\phi(t), \tag{3.17a}$$
$$y = \bar{x}\sin\phi(t) + \bar{y}\cos\phi(t), \tag{3.17b}$$
$$z = \bar{z}, \tag{3.17c}$$

where $\phi(t)$ is the time-dependent rotation angle. The orbital velocity $\dot{\phi}(t)$ is no longer constant but tracks the particle's orbit. The rotation is always around the z-axis as we fix the particle's orbit in the xy-plane.

A compression map stretches grid points according to a time-dependent factor $\lambda(t)$ about a center $C^{\bar{i}}$. We define the coordinate distance from $C^{\bar{i}}$ in the grid frame to be $\bar{r} = \sqrt{\delta_{\bar{i}\bar{j}}(x^{\bar{i}} - C^{\bar{i}})(x^{\bar{j}} - C^{\bar{j}})}$. The compression factor falls off linearly in the radial interval $[r_{\min}, r_{\max}]$, and the compression map is given in the piecewise form as

$$x^i = \begin{cases} x^{\bar{i}} - \lambda(t)\frac{x^{\bar{i}} - C^{\bar{i}}}{r_{\min}}, & \bar{r} < r_{\min}, \\ x^{\bar{i}} - \lambda(t)\frac{r_{\max} - \bar{r}}{r_{\max} - r_{\min}}\frac{x^{\bar{i}} - C^{\bar{i}}}{\bar{r}}, & r_{\min} \le \bar{r} \le r_{\max}, \\ x^{\bar{i}}, & \bar{r} > r_{\max}. \end{cases} \tag{3.18}$$

The Jacobian of this map is discontinuous at $r_{\min}$ and $r_{\max}$. The DG method can handle this as long as these radii are placed at element boundaries. We apply three compression maps to the domain as follows:

A global compression map is centered on the central black hole with the inner radius placed at the so-called envelope $r_{\min} = r_{\text{env}}$ which is chosen several times larger than the initial separation of the two excision spheres. The outer radius $r_{\max}$ is placed at the outer boundary of the domain. The radial separation between the worldtube and the black hole in the inertial frame can then be controlled by adjusting the corresponding parameter $\lambda_r(t)$ which linearly scales the entire inner portion of the grid. The outer boundary of the domain does not change as the compression factor drops to zero at the outer boundary.

Two additional compression maps are centered on the black hole and the worldtube, respectively, with $r_{\min}$ set to the initial excision sphere radii and $r_{\max}$ placed at the spherical element boundaries surrounding them. We denote the corresponding functions of time as $\lambda_{\text{bh}}(t)$ and $\lambda_{\text{wt}}(t)$, respectively. As the compression map is spherically symmetric, the excision regions remain spherical in the inertial frame.

The combination of all four time-dependent maps allows for separate control of the angular and radial position of the worldtube through $\phi(t)$ and $\lambda_r(t)$, as well as the excision sphere radii through $\lambda_{\text{bh}}(t)$ and $\lambda_{\text{wt}}(t)$. An example of this concatenation of maps is shown in Figure 3.1. The top figure corresponds to the DG elements in the time-independent grid frame which coincides with the inertial frame the beginning of the simulation. The bottom figure shows the same grid points transformed to the inertial frame at a later time of the simulation.

At each time t, the DG elements need to be supplied with the value and derivative of the time-dependent parameters $\phi(t)$, $\lambda_r(t)$, $\lambda_{\text{bh}}(t)$ and $\lambda_{\text{wt}}(t)$ to evaluate the evolution equations at their collocation points in the inertial frame $x^{\bar{i}}(t, x^{\bar{i}})$. At these positions, we compute the metric quantities appearing in the evolution equations. The velocity is needed to transform the time derivative of the evolution equations into the co-moving grid frame as described e.g. in [151]. We now show how the values of these time-dependent parameters are determined from the orbit of the scalar charge.

[151]: Scheel et al. (2006), *Solving Einstein's equations with dual coordinate frames*

3.3.2 Particle's position

At the start of the simulation, all functions of time are set to zero, $\phi = \lambda_r = \lambda_{\rm bh} = \lambda_{\rm wt} = 0$, so that grid coordinates coincide with inertial coordinates, $x^i(x^{\bar{i}}, t = 0) = x^{\bar{i}}$. The worldtube is initially located on the positive x-axis with center at an orbital radius r_0.

In Section 3.5, we will derive an ordinary differential equation (ODE) governing the particle's motion. At each time step, we integrate the ODE to calculate the new position $x^i_p(t) = (x_p(t), y_p(t), z_p(t))$ and velocity $\dot{x}^i_p(t) = (\dot{x}_p(t), \dot{y}_p(t), \dot{z}_p(t))$ of the particle in Kerr-Schild coordinates. The time-dependent parameters are then adjusted so that the function from grid to inertial coordinates $x^i(t, x^{\bar{i}})$ maps the center of the worldtube to the current position of the particle,

$$x^i(t, x^{\bar{i}}_p) = x^i_p(t). \tag{3.19}$$

This condition is satisfied by choosing the following values:

$$\phi(t) = \arctan\left(y_p(t), x_p(t)\right), \tag{3.20}$$

$$\dot{\phi}(t) = \frac{x_p(t)\dot{y}_p(t) - y_p(t)\dot{x}_p(t)}{r^2_p(t)}, \tag{3.21}$$

$$\lambda_r(t) = r_{\rm env}\left(1 - \frac{r_p(t)}{r_0}\right), \tag{3.22}$$

$$\dot{\lambda}_r(t) = \frac{-r_{\rm env}\dot{r}_p(t)}{r_0}, \tag{3.23}$$

where we defined the orbital radius of the particle as $r_p(t) = \sqrt{\delta_{ij}x^i_p(t)x^j_p(t)}$, with radial velocity $\dot{r}_p(t) = \delta_{ij}\dot{x}^i_p(t)x^j_p(t)/r_p(t)$.

3.3.3 Radii of excision spheres

The time-dependent map parameters $\lambda_{\rm bh}(t)$ and $\lambda_{\rm wt}(t)$ merely modify the size of the excision regions around the centre of the black hole or the scalar charge, respectively, and can be chosen independently of Eq. (3.19).

Our choice for $\lambda_{\rm wt}$ is motivated by observing that the worldtube scheme is more accurate at larger r_p, since the expansion terms of the puncture field converge more quickly there. If the orbital radius decreases, the truncation error of the puncture field, and hence that of the regular field too, grow. We expect the error ε due to the worldtube to scale with r_p as [1]

[1]: Dhesi et al. (2021), *Worldtube excision method for intermediate-mass-ratio inspirals: Scalar-field toy model*

$$\varepsilon \sim r_p^{-3(n+1)/2}. \tag{3.24}$$

Recall that n is the expansion order of the scheme, fixed to $n = 1$ in this work. The error in the field and its derivatives also scale with the worldtube radius R, according to the relations (3.14)–(3.16): $\sim R^{n+1}$ for the field and $\sim R^n$ for its derivatives. We can keep the error roughly constant as the orbit evolves, by adjusting the worldtube radius R as a function of the changing orbital radius r_p. To achieve this we use the power-law relation

$$R(t) = R_0 \left(\frac{r_p(t)}{r_0} \right)^{\beta}, \tag{3.25}$$

where R_0 is the initial excision radius and the exponent β can be chosen freely. A value of $\beta = 3/2$ should ensure that the error in $\Psi^{\mathcal{R}}$ remains constant; a value of $\beta = 3$ is required to keep the error in the derivatives $\partial_i \Psi^{\mathcal{R}}$ constant. For the simulations presented in this work we choose $\beta = 3/2$, as the larger worldtube reduces computational cost.

The excision sphere within the central black hole is assigned an initial radius of $R_0 = 1.99$ M. It is then shrunk using Eq. (3.25) with $\beta = 1$. The dynamic shrinking of both excision spheres allows the worldtube to approach and ultimately to pass through the black hole horizon with the grid remaining well-behaved; see the bottom panel of Figure 3.1 for the configuration shortly before the particle passes through the horizon.

Care has to be taken in determining the actual functions of time $\lambda_{\rm bh}(t)$ and $\lambda_{\rm wt}(t)$ to match the desired excision sphere radii $R(t)$, as the global compression map governed by $\lambda_r(t)$ has already affected the radii. The appropriate choice to attain an excision sphere radius of $R_{\rm bh/wt}(t)$ is

$$\lambda_{\rm bh/wt}(t) = R_0 + \frac{R_{\rm bh/wt}(t) r_{\rm env}}{\lambda_r(t) - r_{\rm env}}, \tag{3.26}$$

$$\dot{\lambda}_{\rm bh/wt}(t) = \frac{r_{\rm env}}{\lambda_r(t) - r_{\rm env}} \left(\dot{R}_{\rm bh/wt}(t) + \frac{R_{\rm bh/wt}(t) \dot{\lambda}_r(t)}{r_{\rm env} - \lambda_r(t)} \right), \tag{3.27}$$

where $R_0 = R_{\rm bh/wt}(r_0)$ is the excision sphere radius at the start of the simulation.

3.4 Puncture field

Local expansions of the Detweiler-Whiting singular field for a scalar charge are well developed [134–136]. These have primarily focused on the case of a charge moving on a geodesic, but Refs. [152, 153], for example, considered the case of an accelerated source particle.

Here we start from the results of Ref. [152]. That reference provided punctures for gravitational perturbations $h_{\alpha\beta}$ produced by an accelerated point mass μ, but we can readily extract the puncture for our scalar field by noting that the trace of the linear metric perturbation, $h := g^{\alpha\beta}h_{\alpha\beta}$, satisfies the same Klein-Gordon equation (3.1) as the scalar field, $g^{\mu\nu}\nabla_\mu\nabla_\nu h = -16\pi\mu\int \frac{\delta^4(x^\alpha - x_p^\alpha(\tau))}{\sqrt{-g}}d\tau$, with the replacement $q \leftrightarrow 4\mu$. Therefore we have $\Psi^{\mathcal{P}} = \frac{q}{4\mu}h^{\mathcal{P}}$.

The resulting puncture takes the form

$$\Psi^{\mathcal{P}} = \Psi^{\mathcal{P}}_{\rm geo} + \Psi^{\mathcal{P}}_{\rm acc}, \tag{3.28}$$

where $\Psi^{\mathcal{P}}_{\rm geo}$ is the puncture for a particle on a geodesic, and $\Psi^{\mathcal{P}}_{\rm acc}$ is the correction due to the particle's acceleration. The first term is given by

$$\Psi^{\mathcal{P}}_{\rm geo} = \frac{q}{\lambda s} + \frac{q\lambda}{6s^3}(\varrho^2 - s^2)C_{u\sigma u\sigma} + \mathcal{O}(\lambda^2). \tag{3.29}$$

Here we have introduced a number of auxiliary quantities. $\lambda := 1$ is used to count powers of distance to the particle. s, ϱ, and $C_{u\sigma u\sigma}$ are defined from Synge's world function $\sigma(x,\tilde{x})$ and its derivative $\tilde{\sigma}_\alpha := \tilde{\nabla}_\alpha\sigma(x,\tilde{x})$ [137], where we use a tilde to label quantities evaluated on the particle at time t, as in $\tilde{x}^\alpha := (t, x_p^i(t))$. $\sigma(x,\tilde{x})$ is equal to half the squared geodesic distance between x^α and $\tilde{x}^\alpha$, and its gradient $\tilde{\sigma}_\alpha$ is a directed measure of distance from $\tilde{x}^\alpha$ to x^α. In terms of these, we have defined

$$\varrho := \tilde{\sigma}_\alpha u^\alpha, \tag{3.30}$$

$$s := \sqrt{(\tilde{g}^{\alpha\beta} + u^\alpha u^\beta)\tilde{\sigma}_\alpha\tilde{\sigma}_\beta}\,, \tag{3.31}$$

$$C_{u\sigma u\sigma} := \tilde{C}_{\alpha\beta\mu\nu}u^\alpha\tilde{\sigma}^\beta u^\mu\tilde{\sigma}^\nu, \tag{3.32}$$

where $\tilde{C}_{\alpha\beta\mu\nu}$ is the Weyl tensor at $\tilde{x}^\alpha$. Written in an analogous

[134]: Haas et al. (2006), *Mode-sum regularization of the scalar self-force: Formulation in terms of a tetrad decomposition of the singular field*
[135]: Wardell et al. (2012), *A Generic effective source for scalar self-force calculations*
[136]: Heffernan et al. (2012), *High-order expansions of the Detweiler-Whiting singular field in Schwarzschild spacetime*
[152]: Pound et al. (2014), *Practical, covariant puncture for second-order self-force calculations*
[153]: Heffernan et al. (2018), *Accelerated motion and the self-force in Schwarzschild spacetime*

[137]: Synge (1960), *Relativity: The General theory*

form, the correction to Eq. (3.29) due to acceleration reads

$$\Psi^{\mathcal{P}}_{\rm acc} = \frac{\lambda^0 f^\alpha \sigma_\alpha \left(s^2-\varrho^2\right)}{2s^3} + \lambda\Bigg\{\frac{f^\alpha \sigma_\alpha \left(s^2-\varrho^2\right)}{2s^3} - \frac{\varrho D_u f^\alpha \sigma_\alpha \left(\varrho^2-3s^2\right)}{6s^3} - \frac{f_\alpha f^\alpha \left(\varrho^2+s^2\right)}{s}\Bigg\} + \mathcal{O}(\lambda^2), \quad (3.33)$$

where f^α is the self-force per unit mass, given by the right-hand side of Eq. (3.3), and $D_u f^\alpha := u^\beta \nabla_\beta f^\alpha$ is its covariant derivative along the worldline. Explicitly,

$$f^\alpha = \frac{q}{\mu}\left(\tilde{g}^{\alpha\beta} + u^\alpha u^\beta\right)\partial_\beta\, \Psi^{\mathcal{R}}\big|_{x_p^i}\,, \quad (3.34)$$

$$u^\beta \nabla_\beta f^\alpha = \frac{q}{\mu}\left(\dot{f}^\alpha u^0 + \tilde{\Gamma}^\alpha_{\beta\gamma} u^\beta f^\gamma\right). \quad (3.35)$$

In all expressions, it is understood that the four-velocity u^α and self-force per unit mass f^α are evaluated on the worldline at time t. We note that the acceleration terms $\Psi^{\mathcal{P}}_{\rm acc}$ depend on the self-force per unit mass f^α at $\mathcal{O}(\lambda^0)$ and also start to depend on the derivatives $\partial_\beta f^\alpha$ at $\mathcal{O}(\lambda^1)$.

Starting from the above covariant expansions, we re-expand all quantities in powers of the Kerr-Schild coordinate distance from the particle, $\Delta x^i := x^i - x_p^i(t)$. Although we use all terms through order λ in our numerics, here for brevity we only present the order-λ^{-1} and -λ^0 terms. Our results for those terms are the following:

$$\begin{aligned}\Psi^{\mathcal{P}}_{\rm geo} = \frac{q}{\lambda s_0} + \frac{\lambda^0 qM}{2r_p^8 s_0^3}\Bigg\{ & r_p^3 x_p^i \Delta x_p^i x_p^k x_p^l \Delta x^m \Delta x^n \left(3\delta_{km}\delta_{ln} - 2\delta_{kl}\delta_{mn}\right) \\ & + \left(u^0\right)^2\left(r_p^3 \dot{x}_p^i \Delta x^i + 2M r_p x_p^i \Delta x^i + 2M \dot{x}_p^i x_p^i x_p^j \Delta x^j\right) \\ & \times\Big[2r_p x_p^a x_p^b \Delta x^k \Delta x^l \left(2\delta_{ak}\delta_{bl} - \delta_{ab}\delta_{kl}\right) \\ & + \dot{x}_p^a \Delta x_p^a x_p^k x_p^l \Delta x^m \Delta x^n \left(3\delta_{km}\delta_{ln} - 2\delta_{kl}\delta_{mn}\right)\Big]\Bigg\} + \mathcal{O}(\lambda)\end{aligned} \quad (3.36)$$

for the geodesic piece and

$$\Psi^{\mathcal{P}}_{\rm acc} = \frac{\lambda^0 q}{2r_p^9 s_0^3}\Bigg\{ \left(u^0\right)^2\Big[2Mr_p x_p^i \Delta x_p^i + 2Mx^i \dot{x}_p^i x_p^j \Delta x^j + r_p^3 \dot{x}_p^i \Delta x^i\Big]^2 \\ \times\Big[2Mf^t r_p x_p^i \Delta x^i + f^i\left(r_p^3 \Delta x^i + 2Mx_p^i x_p^j \Delta x^j\right)\Big] \\ -2Mf^t r_p^7 s_0^2 x_p^i \Delta x^i \\ -r_p^6 s_0^2 f^i\left(r_p^3 \Delta x^i + 2Mx_p^i x_p^j \Delta x^j\right)\Bigg\} + \mathcal{O}(\lambda) \tag{3.37}$$

for the correction due to acceleration. Here we have introduced the convention that two repeated upper indices are summed over with a Kronecker delta, i.e. $x^i y^i := x^i y^j \delta_{ij}$. We have also introduced $u^0 := dt/d\tau$, given by

$$\left(u^0\right)^2 = \frac{r_p^3}{r_p^3\left(\dot{x}_p^i \dot{x}_p^i - 1\right) - 2Mr_p^2 - 4Mr_p x_p^i \dot{x}_p^i - 2M\left(x_p^i \dot{x}_p^i\right)^2}, \tag{3.38}$$

and the leading-order term in the coordinate expansion of Eq. (3.31), given by

$$s_0^2 = \Delta x^i \Delta x^i + \frac{2M\left(\Delta x^i x_p^i\right)^2}{r_p^3} \\ + \frac{\left(u^0\right)^2\left(r_p^3 \Delta x^i \dot{x}_p^i + 2Mr_p \Delta x^i x_p^i + 2M\Delta x^i x_p^i \dot{x}_p^j x_p^j\right)^2}{r_p^6}. \tag{3.39}$$

3.5 Self consistent evolution

The motion of a scalar charge subject to the scalar self-force is governed by Eq. (3.3). In coordinate form, the spatial components are given by

$$(u^0)^2 \ddot{x}_p^i = \frac{q}{\mu}(g^{i\alpha} - \dot{x}_p^i g^{0\alpha})\partial_\alpha \Psi^{\mathcal{R}} - (\Gamma^i_{\beta\gamma} - \dot{x}_p^i \Gamma^0_{\beta\gamma})u^\beta u^\gamma, \tag{3.40}$$

where $\Gamma^\alpha_{\beta\gamma}$ are the Christoffel symbols of the second kind and $u^i = \dot{x}_p^i u^0$. The first term on the right-hand side represents the covariant acceleration due to the scalar self-force, and the second

term describes the coordinate acceleration of the background geodesic.

The metric and Christoffel symbols are known a priori as the particle is evolved on a fixed Schwarzschild background in Kerr-Schild coordinates. The relevant expressions can be found e.g. in [154].

[154]: Visser (2007), *The Kerr spacetime: A Brief introduction*

3.5.1 Iterative Scheme

The particle's self-acceleration is driven by spatial and time derivatives of the regular field $\Psi^{\mathcal{R}}$, as described in Eqs. (3.3) or (3.40). Inside the worldtube, the regular field is represented by a Taylor expansion, the coefficients of which are determined from continuity conditions on $\Psi^{\mathcal{R}}$ and its time derivative on the worldtube boundary, Eqs. (3.12) and (3.13). These conditions involve the puncture field $\Psi^{\mathcal{P}}$ and its time derivative, which themselves, however, depend on the particle's self-acceleration and its derivatives; recall Eq. (3.37). The acceleration equation (3.40) is therefore an *implicit* equation for $\ddot{x}^i_p$.

To deal with this problem, we construct an iterative scheme. For the ease of the reader, we first define the scheme using just the geodesic component of the puncture field, $\Psi^{\mathcal{P}} = \Psi^{\mathcal{P}}_{\text{geo}}$ and elaborate how the acceleration terms $\Psi^{\mathcal{P}}_{\text{acc}}$ are included in the next section. The geodesic puncture field $\Psi^{\mathcal{P}}_{\text{geo}}$, as given in Eq. (3.36), only depends on the particle's position and velocity but its time derivative $\partial_t \Psi^{\mathcal{P}}_{\text{geo}}$ depends on the particle's acceleration.

Let $\ddot{x}^i_{p(k)}$ be this acceleration during the k-th iteration of this scheme. From this, we compute the corresponding value for the geodesic puncture field by evaluating Eq. (3.36) and its time derivative

$$\Psi^{\mathcal{P}}_{(k)} = \Psi^{\mathcal{P}}_{\text{geo}}(x^i_p, \dot{x}^i_p), \tag{3.41}$$

$$\partial_t \Psi^{\mathcal{P}}_{(k)} = \partial_t \Psi^{\mathcal{P}}_{\text{geo}}(x^i_p, \dot{x}^i_p, \ddot{x}^i_p = \ddot{x}^i_{p(k)}). \tag{3.42}$$

This allows us to calculate iteration k for the Taylor expansions of the regular field $\Psi^{\mathcal{R}}_{(k)}$ and its time derivative $\partial_t \Psi^{\mathcal{R}}_{(k)}$ using the continuity condition (3.12) and (3.13)

$$\Psi^{\mathcal{R}}_{(k)}(t, x^i) \overset{\Gamma}{=} \Psi^{\mathcal{N}}(t, x^i) - \Psi^{\mathcal{P}}_{(k)}(t, x^i), \tag{3.43}$$

$$\partial_t \Psi^{\mathcal{R}}_{(k)}(t, x^i) \overset{\Gamma}{=} \partial_t \Psi^{\mathcal{N}}(t, x^i) - \partial_t \Psi^{\mathcal{P}}_{(k)}(t, x^i). \tag{3.44}$$

The regular field then yields an updated guess for the acceleration through Eq. (3.40)

$$\ddot{x}^i_{p(k+1)} = \ddot{x}^i(\partial_\alpha \Psi^{\mathcal{R}}_{(k)}). \tag{3.45}$$

The updated acceleration can be re-inserted into Eq. (3.41) and the iteration procedure can in principle be repeated an arbitrary number of times. The convergence of this scheme is explored in Section 3.6.4.

We initialize this iterative procedure with the geodesic acceleration $\ddot{x}^i_{(0)} = \ddot{x}^i_{\text{geo}}$ as given by the second term in Eq. (3.40). This choice conveniently separates the first iterations by order in ϵ: the values from the 0-th iteration $\ddot{x}^i_{p(0)}$, $\partial_t \Psi^{\mathcal{P}}_{(0)}$ and $\partial_t \Psi^{\mathcal{R}}_{(0)}$ are all computed for a geodesic orbit and are accurate up to order ϵ^0. The first iteration of the acceleration $\ddot{x}^i_{p(1)}$ is then accurate up to order ϵ^1, as is the resulting derivative of the puncture field $\partial_t \Psi^{\mathcal{P}}_{(1)}$.

3.5.2 Evaluation of acceleration terms

The acceleration terms of the puncture field $\Psi^{\mathcal{P}}_{\text{acc}}$ directly depend on the particle's acceleration $\ddot{x}^i_p$ captured by the self-acceleration f^α and its derivatives, see Eq. (3.37). We now explain how this contribution, and its required derivatives, are evaluated at the kth iteration step, given the particle's current position and velocity as well as $\Psi^{\mathcal{R}}_{(k-1)}(t, x^i)$ and $\partial_t \Psi^{\mathcal{R}}_{(k-1)}(t, x^i)$.

We denote the partial derivative of a field $h(t, x^i)$ evaluated at the position of the particle x^i_p:

$$\left.\frac{\partial h}{\partial x^\alpha}\right|_{x^i_p}(t) = \frac{\partial h}{\partial x^\alpha}(t, x^i = x^i_p(t)). \tag{3.46}$$

We label with a tilde fields evaluated along the path of the particle, $\tilde{f}(t) = f(t, x^i = x^i_p(t))$. We also introduce the total time derivative operator d_t to take time derivatives of fields evaluated at the position of the particle. It acts on an arbitrary field $\tilde{h}$ as

$$d_t \tilde{h} = \left.\frac{\partial h}{\partial t}\right|_{x^i_p} + \dot{x}^i_p \left.\frac{\partial h}{\partial x^i}\right|_{x^i_p}. \tag{3.47}$$

The second total time derivative is given by

$$d_t^2 \tilde{h} = \left.\frac{\partial^2 h}{\partial t^2}\right|_{x_p^i} + 2\dot{x}_p^i \left.\frac{\partial^2 h}{\partial t \partial x^i}\right|_{x_p^i} + \dot{x}_p^i \dot{x}_p^j \left.\frac{\partial^2 h}{\partial x^i \partial x^j}\right|_{x_p^i} + \ddot{x}_p^i \left.\frac{\partial h}{\partial x^i}\right|_{x_p^i} . \tag{3.48}$$

For $n = 1$, the acceleration terms Eq. (3.37) depend on $f^\alpha(t)$ and its first covariant derivative along the orbit, $(u^\beta \nabla_\beta f^\alpha)(t)$. We also require $\partial_t \Psi^{\mathcal{P}}_{\text{acc}}$, which involves the time derivative of these two quantities. These expressions, in turn, require the calculation of the first and second time derivatives of the four velocity, $\dot{u}^\alpha$ and $\ddot{u}^\alpha$, as well as various partial derivatives of the regular field evaluated at the position of the particle. Here we give explicit expressions for all these necessary input quantities.

The first two time derivatives of the self-force are given by

$$\dot{f}^\alpha = \frac{q}{\mu}\Big[\left(d_t(\tilde{g}^{\alpha\beta}) + \dot{u}^\alpha u^\beta + u^\alpha \dot{u}^\beta\right) \partial_\beta \Psi^{\mathcal{R}}|_{x_p^i} + \left(\tilde{g}^{\alpha\beta} + u^\alpha u^\beta\right) d_t(\partial_\beta \Psi^{\mathcal{R}}|_{x_p^i}) \Big], \tag{3.49a}$$

$$\begin{aligned} \ddot{f}^\alpha = \frac{q}{\mu}\Big[& \left(d_t^2(\tilde{g}^{\alpha\beta}) + \ddot{u}^\alpha u^\beta + 2\dot{u}^\alpha \dot{u}^\beta + u^\alpha \ddot{u}^\beta\right) \partial_\beta \Psi^{\mathcal{R}}|_{x_p^i} \\ & + 2\left(d_t(\tilde{g}^{\alpha\beta}) + \dot{u}^\alpha u^\beta + u^\alpha \dot{u}^\beta\right) d_t(\partial_\beta \Psi^{\mathcal{R}}|_{x_p^i}) \\ & + \left(\tilde{g}^{\alpha\beta} + u^\alpha u^\beta\right) d_t^2(\partial_\beta \Psi^{\mathcal{R}}|_{x_p^i}) \Big]. \end{aligned} \tag{3.49b}$$

The derivative of $u^\beta \nabla_\beta f^\alpha$ is given by

$$\begin{aligned} \frac{d}{dt}(u^\beta \nabla_\beta f^\alpha) = {} & \ddot{f}^\alpha u^0 + \dot{f}^\alpha \dot{u}^0 \\ & + d_t \tilde{\Gamma}^\alpha_{\beta\gamma} u^\beta f^\gamma + \tilde{\Gamma}^\alpha_{\beta\gamma} \dot{u}^\beta f^\gamma + \tilde{\Gamma}^\alpha_{\beta\gamma} u^\beta \dot{f}^\gamma . \end{aligned} \tag{3.50}$$

The quantities $\partial_i g^{\alpha\beta}$, $\partial_i \partial_j g^{\alpha\beta}$ and $\partial_i \Gamma^\alpha_{\beta\gamma}$, which are required for the total time derivatives of the metric and Christoffel symbols, are calculated analytically. We do not give the expressions here for brevity.

The first derivative of the four velocity is given directly by the evolution equation (3.3), and the second time derivative can be

obtained from its derivative:

$$\dot{u}^\alpha = \frac{1}{u^0}\left(\frac{q}{\mu}\tilde{g}^{\alpha\beta}\partial_\beta\Psi^{\mathcal{R}}|_{x_p^i} - \tilde{\Gamma}^\alpha_{\beta\gamma}u^\beta u^\gamma\right), \tag{3.51a}$$

$$\begin{aligned}\ddot{u}^\alpha = \frac{1}{u^0}\Bigg(&\frac{q}{\mu}d_t\tilde{g}^{\alpha\beta}\partial_\beta\Psi^{\mathcal{R}}|_{x_p^i} + \frac{q}{\mu}\tilde{g}^{\alpha\beta}d_t(\partial_\beta\Psi^{\mathcal{R}}|_{x_p^i}) \\ &- d_t\tilde{\Gamma}^\alpha_{\beta\gamma}u^\beta u^\gamma - 2\tilde{\Gamma}^\alpha_{\beta\gamma}\dot{u}^\beta u^\gamma - \dot{u}^0\dot{u}^\alpha\Bigg).\end{aligned} \tag{3.51b}$$

Some of the required derivatives of the regular field $\Psi^{\mathcal{R}}$ can be obtained directly from the Taylor expansions (3.10),

$$\partial_i\Psi^{\mathcal{R}}|_{x_p^i} = \Psi^{\mathcal{R}}_i(t), \tag{3.52}$$

$$\partial_t\Psi^{\mathcal{R}}|_{x_p^i} = (\partial_t\Psi^{\mathcal{R}})_0(t), \tag{3.53}$$

$$\partial_t\partial_i\Psi^{\mathcal{R}}|_{x_p^i} = (\partial_t\Psi^{\mathcal{R}})_i(t). \tag{3.54}$$

Higher derivatives, however, are not obtainable directly in this manner. We make use of the fact that we can take arbitrarily high spatial derivatives of the regular field and its time derivative by taking spatial derivatives of their expansions. For expansion order $n = 1$, this implies that all second and higher spatial derivatives of the regular field and its time derivative can be consistently set to zero. This leaves the higher time derivatives $\partial_t^2\Psi^{\mathcal{R}}|_{x_p^i}$, $\partial_t^3\Psi^R|_{x_p^i}$ and $\partial_t^2\partial_i\Psi^{\mathcal{R}}|_{x_p^i}$ to be determined. We obtain these by taking derivatives of the vacuum scalar wave equation which the regular field satisfies. As they express the second time derivative in terms of spatial derivatives, we can consistently express all second time derivatives in terms of spatial derivatives yielding

$$\partial_t^2\Psi^{\mathcal{R}} = \frac{1}{g^{tt}}\Big(-2g^{ti}\partial_t\partial_i\Psi^{\mathcal{R}} + \Gamma^t\partial_t\Psi^{\mathcal{R}} + \Gamma^i\partial_i\Psi^{\mathcal{R}}\Big), \tag{3.55}$$

$$\begin{aligned}\partial_t^2\partial_i\Psi^{\mathcal{R}} = \frac{1}{g^{tt}}\Big(&2\partial_i g^{tj}\partial_t\partial_j\Psi^{\mathcal{R}} - \partial_i\Gamma^t\partial_t\Psi^{\mathcal{R}} \\ &- \Gamma^t\partial_t\partial_i\Psi^{\mathcal{R}} - \partial_i\Gamma^j\partial_j\Psi^{\mathcal{R}} - \partial_i g^{tt}\partial_t^2\Psi^{\mathcal{R}}\Big).\end{aligned} \tag{3.56}$$

The time derivative of Eq. (3.55), yields the final necessary term

$$\partial_t^3\Psi^R = \frac{1}{g^{tt}}\left(2g^{ti}\partial_t^2\partial_i\Psi^{\mathcal{R}} - \Gamma^t\partial_t^2\Psi^R - \Gamma^i\partial_t\partial_i\Psi^{\mathcal{R}}\right). \tag{3.57}$$

At this point, we have prescribed all quantities necessary for evaluating the acceleration term $\Psi^{\mathcal{P}}_{\text{acc}}$ and its time derivative in terms of the expansion coefficients of $\Psi^{\mathcal{R}}$ and $\partial_t\Psi^{\mathcal{R}}$, the current position and velocity of the particle, and background quantities. This allows

for $\Psi^{\mathcal{P}}_{\rm acc}$ to be included in the iterative scheme consistently. We construct the kth iteration of the puncture field from an acceleration $\ddot{x}^i_{p(k)}$ as

$$\Psi^{\mathcal{P}}_{(k)} = \Psi^{\mathcal{P}}_{\rm geo}\left(x^i_p, \dot{x}^i_p\right) + \Psi^{\mathcal{P}}_{\rm acc}\left(x^i_p, \dot{x}^i_p, \ddot{x}^i_{p(k)}, \partial_\alpha \Psi^{\mathcal{R}}_{(k-1)}|_{x^i_p}\right), \tag{3.58}$$

$$\partial_t \Psi^{\mathcal{P}}_{(k)} = \partial_t \Psi^{\mathcal{P}}_{\rm geo}\left(x^i_p, \dot{x}^i_p, \ddot{x}^i_{p(k)}\right) + \partial_t \Psi^{\mathcal{P}}_{\rm acc}\left(x^i_p, \dot{x}^i_p, \ddot{x}^i_{p(k)}, \partial_\alpha \Psi^{\mathcal{R}}_{(k-1)}|_{x^i_p}\right). \tag{3.59}$$

Recall that the scheme is initialized with the geodesic acceleration $\ddot{x}^i_{p(0)} = \ddot{x}^i_{\rm geo}$ so the zeroth iteration of the puncture field is given by its geodesic component $\Psi^{\mathcal{P}}_{(0)} = \Psi^{\mathcal{P}}_{\rm geo}$ and $\partial_t \Psi^{\mathcal{P}}_{(0)} = \partial_t \Psi^{\mathcal{P}}_{\rm geo}$. The acceleration terms $\Psi^{\mathcal{P}}_{\rm acc}$ only start to contribute to the particle's acceleration at the second iteration $\ddot{x}^i_{p(2)}$. At this point, $\ddot{x}^i_p$ includes terms of $\mathcal{O}(\epsilon^2)$ and we must use in Eq. (3.40) the dynamical mass $\mu(t)$ as obtained in Eq. (3.5), rather than the rest mass μ_0.

The acceleration terms can cause the simulation to grow unstable during a self-consistent evolution. We find this happens only for relatively large ϵ ($\gtrsim 0.1$) and far into the inspiral, usually when the scalar charge is near the horizon of the central black hole. The instabilities do not occur when the acceleration terms are not included in the evolution. We are unsure what the underlying cause is, but it does not affect the regions of parameter space we probe in Sec. 3.6. It might be a consequence of the coupled system (the Klein-Gordon equation coupled to the particle's equation of motion) being effectively higher than second-order in time, meaning the instability could be similar in nature to the well-known problem of runaway solutions in the equation of motion of an accelerated charged particle in electromagnetism [155, 156]; our iterative procedure is similar to an iterative reduction-of-order approximation in that context [157]. If the instability is a pathology of the original system of equations (3.1) and (3.2) in this way, then it can be understood as a failing of the point-particle approximation [158, 159].

Spectre employs a task-based parallelism design where the worldtube and the DG elements are assigned to different cores of a computational cluster. At each iteration, the DG elements neighboring the worldtube evaluate the puncture field $\Psi^{\mathcal{P}}_{(k)}$, integrate it over the worldtube boundary and send the result to the worldtube. It uses this data to compute the next iteration of the acceleration,

[155]: Dirac (1938), *Classical theory of radiating electrons*
[156]: Spohn (2000), *The Critical manifold of the Lorentz-Dirac equation*
[157]: Ekman et al. (2021), *Reduction of order, resummation, and radiation reaction*
[158]: Rohrlich (n.d.), *Dynamics of a charged particle*
[159]: Gralla et al. (2009), *A Rigorous Derivation of Electromagnetic Self-force*

$\ddot{x}^i_{p(k+1)}$, and the self-force per unit-mass f^α and its derivatives, which it then sends back to the neighboring elements. Each iteration therefore introduces a synchronization point between the worldtube and adjacent DG elements where computational cores are idly waiting for the results of another core. We find that in our simulations each iteration does increase runtime by $15-20$ per cent compared to the evolution with one iteration.

3.5.3 Evolving the orbit

Given the position $x^i_p(t_s)$ and velocity $\dot{x}^i_p(t_s)$ of the particle, as well as data for the evolved fields $\Psi^{\mathcal{N}}(t_s, x^i)$, $\Pi(t_s, x^i)$ and $\Phi_i(t_s, x^i)$ at time step t_s, we can evaluate time derivatives of the evolved fields using Eq. (3.8) and compute the acceleration $\ddot{x}^i_p(t_s)$ with Eq. (3.40). Both the PDEs for the fields and the ODEs of the trajectory are advanced with the same time stepper and step.

The evaluation of the evolution equations requires for the DG method to know both the position and velocity of the collocation points at the corresponding time step as discussed in Section 3.3. These are set by the new position $x^i_p(t_{s+1})$ and velocity $\dot{x}^i_p(t_{s+1})$ of the particle through the time-dependent parameters $\lambda_r(t_{s+1})$ and $\phi(t_{s+1})$ and their derivatives, by demanding that the center of the worldtube is mapped onto the new position of the worldtube through Eqs. (3.20). The parameters controlling the excision sphere radii $\lambda_{\rm wt}(t_{s+1})$ and $\lambda_{\rm bh}(t_{s+1})$ are fixed by the condition (3.26). These fully determine the global map from grid to inertial Kerr-Schild coordinates $x^i(t_{s+1}, x^{\bar{i}})$ and its time derivative at the new time step t_{s+1} and therefore the position and velocity of each grid point. Both the evolved variables and the orbit can now be advanced to the next time step t_{s+2} and the procedure repeated. When using multi-step methods, all variables are updated each substep.

3.6 Results

For the results presented here, we excise a sphere with initial radius $R_0 = 1.99M$ from the center of our domain. The excision will at all times be contained within the event horizon of the Schwarzschild black hole of fixed mass M. The particle with charge q and mass μ is initially placed at an orbital radius r_0 and the worldtube is centered on it. The outer boundary of the domain is placed at

$r = 500M$. The left side of Fig. 3.1 shows a cut through the inner part of the domain at the start of the simulation.

The DG evolution of the scalar field $\Psi^{\mathcal{N}}$ is carried out in a manner very similar to the circular orbit case of the previous chapter. We employ a multi-step fourth-order Runge-Kutta method [160] and the orbital parameters are advanced along with the evolved variables at each substep. A weak exponential filter is employed on all the evolved variables at each time step. The resolution of the DG grid is always set so that its error is subdominant to the error introduced by the worldtube. For simplicity, we always choose the charge and mass to be equal: $q = \mu_0 = \epsilon M$. This is no restriction, since only the ratio $q^2/(\mu_0 M)$ is relevant for the evolution of the system.

[160]: Owren et al. (1992), *Derivation of Efficient, Continuous, Explicit Runge–Kutta Methods*

At time $t = t_0 = 0$, the regular field inside the worldtube and the evolved variables are set to zero throughout the domain, $\Psi^{\mathcal{R}}(t_0, x^i) = \Psi^{\mathcal{N}}(t_0, x^i) = \Pi(t_0, x^i) = \Phi_i(t_0, x^i) = 0$. The simulation is then evolved up to $t_1 = 1500M$ with the worldtube orbiting on a prescribed, circular geodesic exactly as in the previous chapter. During this time, $\Psi^{\mathcal{R}}$ and the evolved variables converge to a steady-state solution which acts as initial condition to the inspiral.

Starting at t_1, we include the acceleration due to the scalar self-force given by the first term in Eq. (3.40), as discussed in Section 3.5. A transition function $w(t)$ is used to continuously activate this extra term, chosen as

$$w(t) = 1 - \exp\left(-\left(\frac{t - t_1}{\sigma}\right)^4\right). \tag{3.60}$$

Here, σ is the timescale over which the scalar self-force is turned on. A short timescale will cause the orbit to have higher residual eccentricity whereas a long time scale is computationally more expensive. Quantitative results below are presented starting at $t = t_1 + 2\sigma$ where the self-force is fully active to more than one part in 10^7. The smoothness of the turn-on function also avoids a jump in the puncture field caused by the addition of the acceleration terms $\Psi^{\mathcal{P}}_{\text{acc}}$.

The back-reaction of the scalar radiation causes the charge to lose potential energy and to spiral into the central black hole on a quasi-circular orbit. Figure 3.2 depicts one of these simulations. Here, the particle was placed at an initial radius $r_0 = 10.5M$ and a comparatively large value $\epsilon = 0.08$ leads to a fast inspiral. The orbit

is only shown starting at $t = 3500M$, at which point the self-force is fully activated. The orbital radius decreases at a faster rate as the particle gets closer to the central black hole. The red dot shows the particle's position as it crosses the ISCO at $r = 6M$. At this point, it quickly plunges into the event horizon, depicted by the dashed black line.

Once the scalar charge is contained entirely within the horizon it can no longer transfer any information to future null infinity, and there starts a vacuum "ringdown" evolution, in which the scalar field $\Psi^{\mathcal{N}}$ evolves outside the BH without a source term. In practice, we choose to evolve the simulation with the scalar charge until the worldtube excision sphere is contained entirely within a radius of $r = 1.99M$. At this point, we halt the simulation and save the values of the evolved variables $\Psi^{\mathcal{N}}$, Π and Φ_i on the final timeslice $t = t_{\rm rd}$. The evolution of the scalar field is continued on a new domain which has a single central excision sphere of constant radius $r = 1.995M$. This choice places the boundary within the black hole horizon so no boundary conditions are required, and outside the worldtube so data can be supplied entirely from $\Psi^{\mathcal{N}}$. The ringdown evolution of the scalar field is then initialized at time $t_{\rm rd}$ by interpolating the evolved variables to the new grid points. The simulation is continued on the same background spacetime for a duration of $1000M$ at which point the scalar field has dissipated beyond the resolution of the grid.

Figure 3.3 shows the value of $r\Psi^{\mathcal{N}}(t, x^i)/q$ in the orbital plane evaluated at $x = 300M$. It is plotted against retarded time $t - r$ zeroed at the onset of ringdown time, corresponding to KS time $t = t_{\rm rd}$. The dominant frequency of the produced waveform matches the orbital frequency of the particle and gradually increases during the inspiral. The vertical dashed line shows the retarded time at which the particle crossed the ISCO. The waveform looks different to typical gravitational waveforms, as the scalar charge emits dominant monopole and dipole radiation causing its profile to oscillate around a positive value. The average amplitude of the waveform also slightly decreases during the final orbits, presumably because a significant part of the monopolar radiation is absorbed by the central black hole at this stage.

We define the phase $\phi_p(t)$ and angular velocity $\omega(t)$ of the particle as

$$\phi_p = \arctan(y_p, x_p), \tag{3.61}$$

$$\omega = \dot{\phi}_p. \tag{3.62}$$

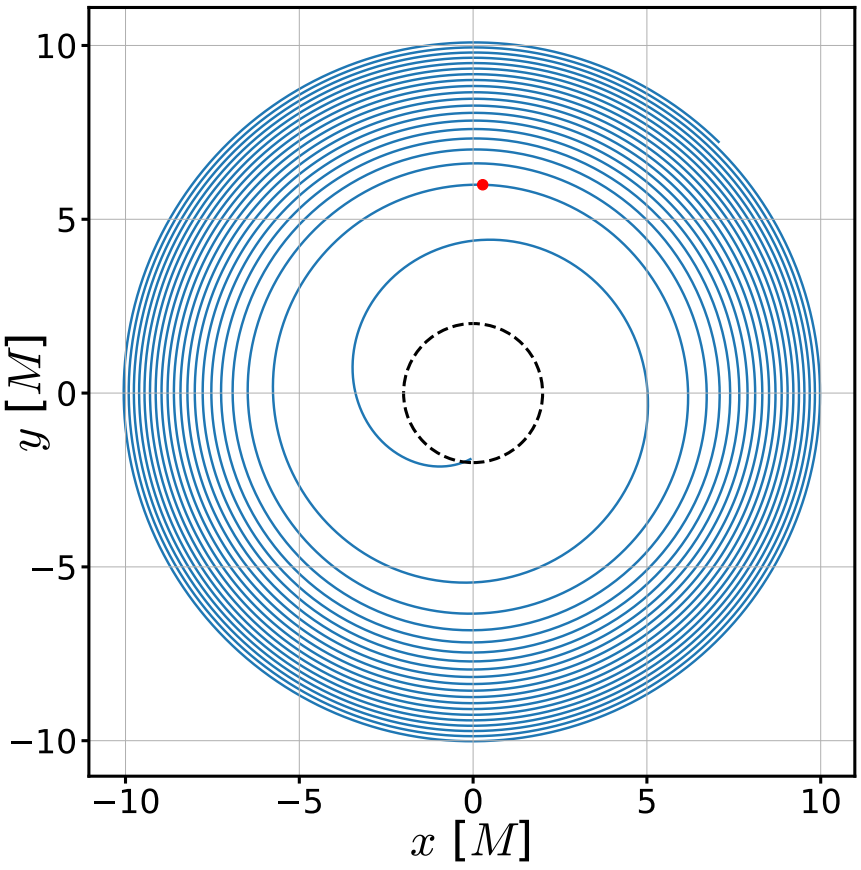

Figure 3.2: The orbit of a particle inspiralling into a central black hole under the influence of the scalar self-force. The orbit inspirals at a faster rate as the particle approaches the black hole and, after crossing the ISCO, plunges into the event horizon depicted by the dashed, black ring. The red dot shows the position of the particle as it crosses the ISCO at $r_p = 6M$. Here, $\epsilon = 0.08$ and $R_0 = 0.8M$.

The definition of the phase ϕ_p coincides with the time-dependent parameter $\phi(t)$ of the rotation map (3.17) because we demand that the worldtube excision sphere is tracking the particle through Eq. (3.20).

In general, we will compare two simulations at the same angular velocity $\omega(t)$. As the angular velocity is strictly monotonically increasing for the quasi-circular inspirals presented here, it can be mapped to the coordinate time t one-to-one. This allows us to evaluate the difference between two simulations at a common angular velocity but still plot it against the corresponding coordinate time of one of the simulations.

We also define the quantity $r_\omega = M^{1/3}\omega^{-2/3}$, which is the radius corresponding to a perfectly circular geodesic orbit with angular velocity ω. During the inspiral, the value of r_ω is typically similar to the Kerr-Schild orbital radius r_p of the particle. Comparing two simulations at the same r_ω is mathematically equivalent to comparing them at the same angular velocity ω but hopefully more intuitive to the reader.

In Sec. 3.6.1, we study the dependence of the self-force driven inspiral on the small parameter ϵ by fixing the initial worldtube

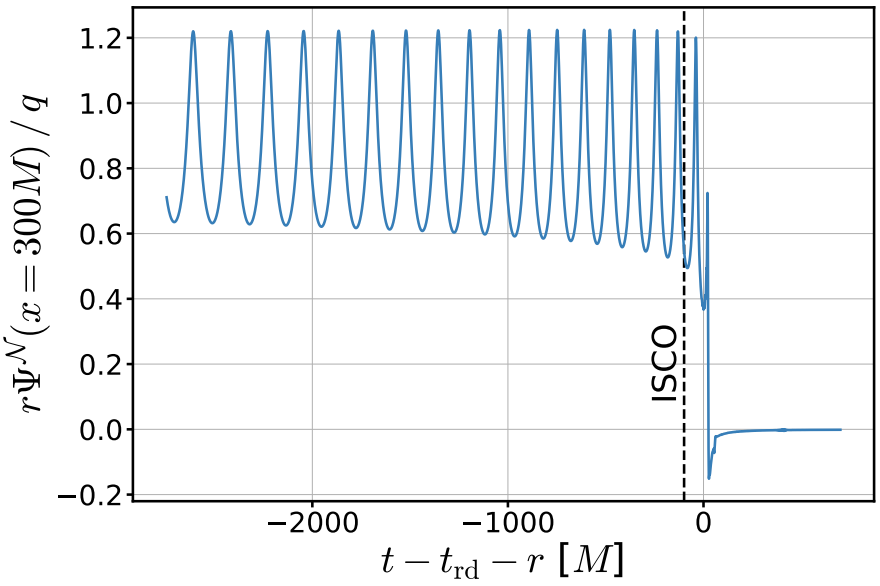

Figure 3.3: The value of the scalar field $r\Psi^{\mathcal{N}}/q$ evaluated in the orbital plane at $x = 300M$ for the same simulation as depicted in Figure 3.2. The x axis shows the retarded time $t - r$, zeroed at the ringdown time $t_{\rm rd}$. The dashed vertical black line indicates the retarded time when the charge crossed the ISCO.

radius R_0 and varying ϵ between 0.005 and 0.08. In the following Section 3.6.2, we fix $\epsilon = 0.01$ and explore the convergence with worldtube radius R_0 by varying it between $3.2M$ and $0.2M$. In Sec. 3.6.3, we repeat these simulations but do not include the acceleration terms $\Psi^{\mathcal{P}}_{\rm acc}$ to see how this affects the evolution. Finally, we explore the convergence of the iterative scheme in Sec. 3.6.4 by fixing both $\epsilon = 0.01$ and the initial worldtube radius $R_0 = 0.8M$ and iterating the acceleration $\ddot{x}^i_{p(k)}$ up to $k = 2, 3, 5$ or 7.

3.6.1 Comparison with adiabatic approximation

We explore the effect of the inspiral parameter ϵ by varying it between $\epsilon = 0.005$ and $\epsilon = 0.08$ for a total of 14 values. Two simulations are run for each value of ϵ, one with initial worldtube radius $R_0 = 0.8M$ and one with $R_0 = 0.4M$. For simulations with $\epsilon \leq 0.01$, we set an initial orbital radius $r_0 = 8M$. For larger ϵ, the inspiral can happen so quickly that the particle would cross the ISCO before the self-force is fully turned on. To remedy this, we appropriately set larger initial orbital radii up to $10.5M$ such that the self-force is fully active at latest when the particle reaches an orbital radius of $r_p = 7.8M$. The worldtube radius $R(t)$ is shrunk according to Eq. (3.25) with r_0 fixed to $8M$, even for simulations starting at larger initial separations. This leads to simulations having the same worldtube radius at the same r_p, independent of initial separation. We apply the iterative scheme derived in Secs. 3.5.1 and 3.5.2 and iterate each simulation until it does not affect the final results. The turn-on timescale is set to $\sigma = 1000M$

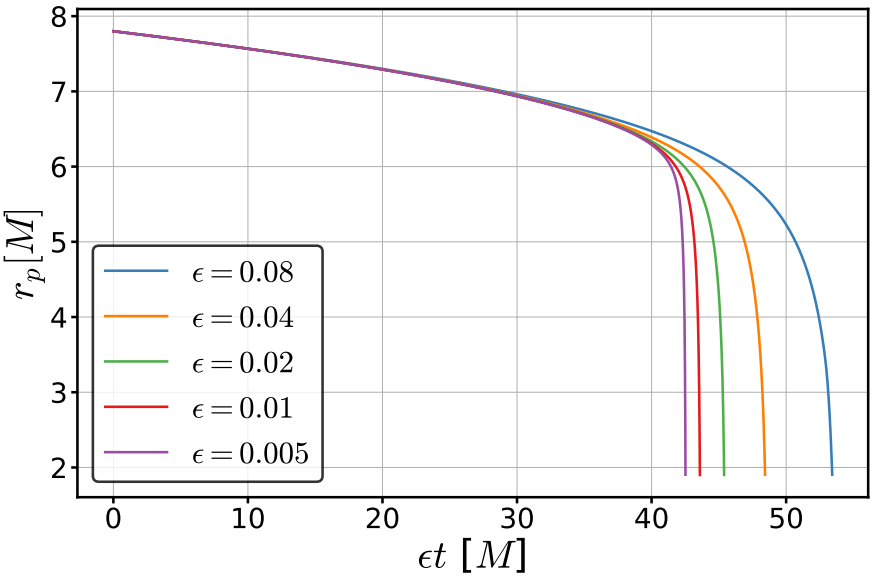

Figure 3.4: The orbital radius r_p plotted against coordinate time t multiplied by the inspiral parameter ϵ for different values of ϵ. The time was set to zero for all simulations at an orbital radius of $r_p = 7.8M$, when the scalar self-force was fully active. Initially, the radii are almost identical between simulations. Near the ISCO, they start to deviate due to non-adiabatic effects. Beyond the ISCO, the particle quickly plunges into the central black hole.

for all simulations. The puncture field includes the acceleration terms according to Eq. (3.58).

To understand the ϵ dependence of our results, we compare against a standard adiabatic approximation [63], which fixes the particle on a quasi-circular orbit with $\omega = \sqrt{M/r_p^3}$ and evolves the orbital radius according to the fluxes of energy to null infinity and down the BH horizon. Concretely, we assume a solution to Eq. (3.1) of the form

[63]: Barack et al. (2019), *Self-force and radiation reaction in general relativity*

$$\Psi = \sum_{\ell m} [\Psi_{\ell m}(r_p, r) + \mathcal{O}(\epsilon)] e^{-im\phi_p} Y_{\ell m}(\theta, \phi). \tag{3.63}$$

Substituting this expansion into the Klein-Gordon equation, using $d\phi_p/dt = \omega$ and $dr_p/dt = \mathcal{O}(\epsilon)$, discarding subleading terms, and factoring out $e^{-im\phi_p} Y_{\ell m}(\theta, \phi)$ reduces the PDE to decoupled radial ODEs for the coefficients $\Psi_{\ell m}(r_p, r)$, which we solve on a grid of r_p values using the Teukolsky package from the Black Hole Perturbation Toolkit [161]. At each value of r_p, the energy fluxes $\mathcal{F}_\infty$ and $\mathcal{F}_H$ are extracted from the solutions $\Psi_{\ell m}(r_p, r \to \infty)$ and $\Psi_{\ell m}(r_p, r \to 2M)$. In terms of these fluxes, the orbital energy $\mathcal{E}$ changes at a rate

[161]: Wardell et al. (2023), *Teukolsky (1.0.4)*

$$\frac{d\mathcal{E}}{dt} = -\mathcal{F} := -(\mathcal{F}_\infty + \mathcal{F}_H). \tag{3.64}$$

At leading order, $\mathcal{E}$ is related to the orbital radius by the geodesic relationship, $\mathcal{E} = \mu_0 \frac{1-2M/r_p}{\sqrt{1-3M/r_p}}$, which allows us to express the rate of change of r_p in terms of $\mathcal{F}$. The evolution of the orbital phase

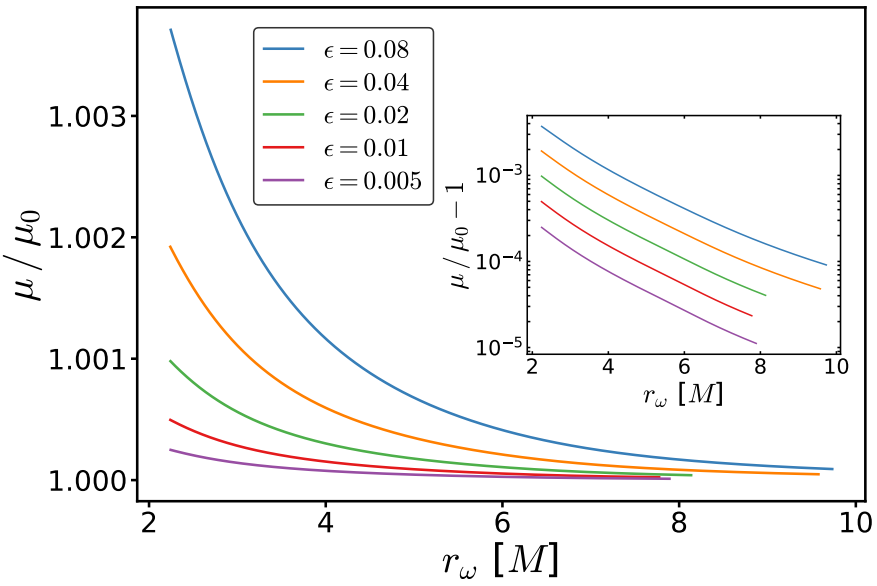

Figure 3.5: The evolution of the dynamic mass μ shown as a fraction of μ_0 for simulations with varying ϵ. The mass grows with the orbital frequency during the evolution. The inset on the right shows $\mu/\mu_0 - 1$ (plotted logarithmically), which remains proportional to ϵ throughout the simulation.

and radius are then governed by

$$\frac{d\phi_p}{dt} = \omega(r_p), \tag{3.65}$$

$$\frac{dr_p}{dt} = -\epsilon \frac{\hat{\mathscr{F}}(\hat{r}_p)}{d\hat{\mathscr{E}}/d\hat{r}_p}. \tag{3.66}$$

To express the last equation in terms of ϵ, we have introduced the normalized quantities $\hat{\mathscr{E}} := \mathscr{E}/\mu$, $\hat{\mathscr{F}} := \mathscr{F}/q^2$, and $\hat{r}_p := r_p/M$.

The solution to Eqs. (3.65) and (3.66) can be written as

$$\phi_p = \frac{\phi_0(r_p)}{\epsilon}. \tag{3.67}$$

From Eq. (3.66), we can also obtain an adiabatic approximation for the dimensionless adiabaticity parameter $\dot{\omega}/\omega^2$,

$$\frac{\dot{\omega}}{\omega^2} = \epsilon G_0(r_p), \tag{3.68}$$

where $G_0(r_p) = -\frac{d\omega/dr_p}{\omega(r_p)^2} \frac{\hat{\mathscr{F}}(\hat{r}_p)}{d\hat{\mathscr{E}}/d\hat{r}_p}$. We note that unlike the self-consistent evolution we perform in our worldtube scheme, this approximation (and its extension in the next paragraph) breaks down at the ISCO: as r_p approaches the ISCO, $d\hat{\mathscr{E}}/d\hat{r}_p$ vanishes and G_0 diverges.

It will also be useful to compare against the expected ϵ dependence beyond leading order in a two-timescale expansion. If the expansion is carried to higher order in ϵ following Refs. [162, 163],

then Eqs. (3.67) and (3.68) take the post-adiabatic form

$$\phi_p = \frac{\phi_0(r_\omega)}{\epsilon} + \phi_1(r_\omega) + \epsilon\phi_2(r_\omega) + \mathcal{O}(\epsilon^2), \tag{3.69}$$

$$\frac{\dot{\omega}}{\omega^2} = \epsilon G_0(r_\omega) + \epsilon^2 G_1(r_\omega) + \epsilon^3 G_2(r_\omega) + \mathcal{O}(\epsilon^4). \tag{3.70}$$

Here it is more useful to use the invariant orbital radius r_ω, but note that ϕ_0 and G_0 are the same functions as in the adiabatic approximation, now simply evaluated at r_ω rather than r_p.

Figure 3.4 shows the orbital radius r_p extracted from our numerical simulations for different values of ϵ plotted against coordinate time t multiplied by ϵ. Here, the worldtube radius is fixed to $R_0 = 0.8M$ and we set t to zero at an orbital radius of $r_p = 7.8M$ when the scalar self-force was fully active for all simulations. The rescaling of time by ϵ is motivated by Eq. (3.66), which shows that at adiabatic order the orbital radius is independent of ϵ when treated as a function of ϵt. Initially, our results conform to that behavior: our numerically computed orbital radii lie on top of each other, which suggests that the orbit is well described by the adiabatic approximation. The lines start to deviate near the ISCO, as non-adiabatic effects start to become significant. Once the particle passes the ISCO at $r_p = 6M$, it quickly plunges into the central black hole. The simulations shown here proceed through 69 orbits for $\epsilon = 0.005$ between $r_p = 7.8M$ and $r_p = 6M$, and through 4.8 orbits for $\epsilon = 0.08$.

Figure 3.5 shows the evolution of the dynamic mass μ given by Eq. (3.5), plotted as a fraction of μ_0. The mass grows as the particle inspirals and can increase by ≈ 0.1 per cent of μ_0. The inset on the right plots this fraction logarithmically as $\mu/\mu_0 - 1$, which can be re-written as $-\epsilon\Psi^{\mathcal{R}}/q$ using Eq. (3.5). It remains proportional to ϵ during the simulation as $\Psi^{\mathcal{R}}$ is proportional to the scalar charge q. This again conforms to the expected behavior at adiabatic order; beyond adiabatic order, we would expect order-ϵ corrections to appear in $\Psi^{\mathcal{R}}$ as a function of r_ω, but these appear to remain small even when the particle has crossed the ISCO.

Figure 3.6 plots $\dot{\omega}/\omega^2$ against r_ω. The solid lines correspond to simulations with worldtube radius $R_0 = 0.8M$. The simulations start at an initial separation between $r_0 = 8M$ and $r_0 = 10M$, depending on the value of ϵ. Outside the ISCO, the particle is on a quasi-circular orbit. The geodesic angular acceleration $\dot{\omega}$ is close to zero in this regime and the adiabaticity parameter is dominated by the scalar self-force given by the first term of Eq. (3.40). The adiabaticity parameter roughly doubles for each doubling of ϵ

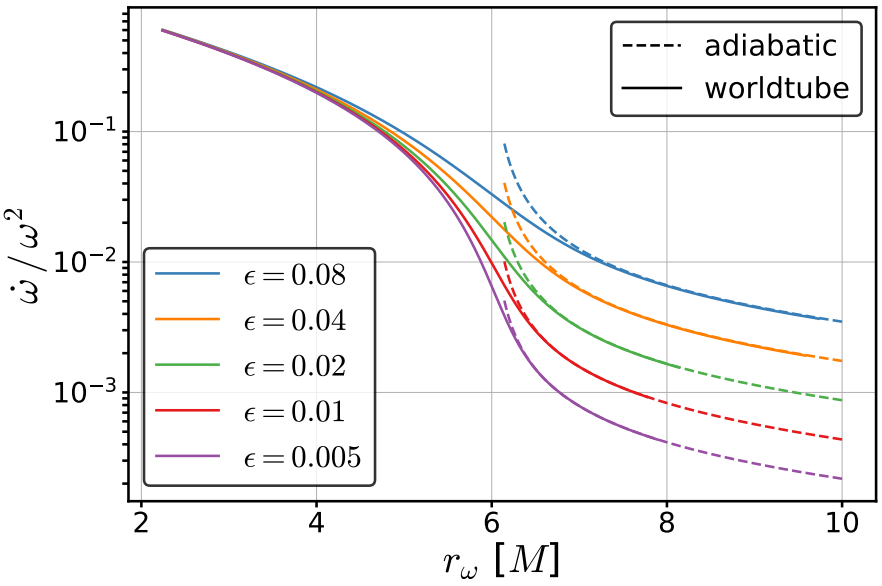

Figure 3.6: The value of the adiabaticity parameter $\dot{\omega}/\omega^2$ plotted for a circular inspiral for different values of ϵ. The solid lines correspond to a worldtube simulation with initial worldtube radius $R_0 = 0.8M$. The dashed lines correspond to the adiabatic approximation given by the first term in Eq. (3.70), which breaks down at the ISCO.

here, as predicted by Eq. (3.70). For $r_p < 6M$, the scalar charge plunges into the black hole. The geodesic angular acceleration starts to dominate over the scalar self-force in this regime so the solid lines approach a common value independent of ϵ.

The dashed lines in Fig. 3.6 show the results of the adiabatic approximation, given by the leading term in Eq. (3.70). We calculate these results starting at separation $r_p = 10M$ until their divergence at the ISCO. The adiabaticity parameter looks almost identical to the worldtube scheme and starts to deviate only near the ISCO.

We investigate the transition regime from inspiral to plunge further and define the "local convergence order" of the adiabaticity parameter

$$\alpha_{\epsilon,j}(r_\omega) = \frac{\log(Q_j(r_\omega)) - \log(Q_{j-1}(r_\omega))}{\log(\epsilon_j) - \log(\epsilon_{j-1})}, \tag{3.71}$$

where ϵ_j are the different values of the inspiral parameter that were simulated and we have denoted with $Q_j = \dot{\omega}_j/\omega_j^2$ the corresponding values of the adiabaticity parameter. The quantity α_ϵ gives the power in ϵ with which the adiabaticity parameter changes between simulations with different ϵ. We evaluate α_ϵ as a function of r_ω to investigate the different regimes inspiral, transition-to-plunge, and plunge. Figure 3.7 shows $\alpha_{\epsilon,j}$ for the same set of simulations shown in Fig. 3.6. Early in the inspiral (where r_ω is significantly larger than $r_{\rm ISCO} = 6M$), $\alpha_{\epsilon,j} \approx 1$, since in that regime $\dot{\omega}/\omega^2$ is proportional to ϵ. Deep inside the plunge (when $r_\omega \ll r_{\rm ISCO}$), the particle follows a plunge geodesic independent of ϵ, and $\alpha_{\epsilon,j}$ approaches zero. The transition regime in between is broader for larger values of ϵ. At

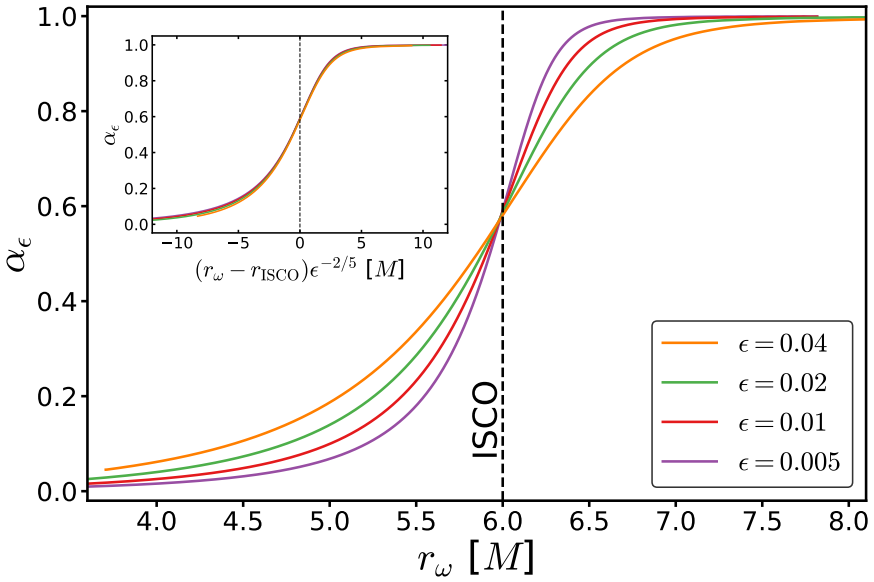

Figure 3.7: The convergence order α_ϵ of the adiabaticity parameter $\dot{\omega}/\omega^2$ between simulations of adjacent ϵ. The convergence order is close to one during the early inspiral on the right, where $\dot{\omega}/\omega^2$ is proportional to ϵ and close to zero during the final plunge on the left, where it is independent of ϵ. The width of this transition grows with larger values of ϵ. The inset on the left shows the same plot with the x-axis rescaled by a factor of $\epsilon^{-2/5}$ around $r_{\rm ISCO} = 6M$. The curves now collapse, suggesting that the width of the transition regime scales as $\epsilon^{2/5}$.

the ISCO, $\alpha_{\epsilon,j} \approx 3/5$, in line with the theoretical prediction [164]; see, for example, Eq. (25) of Ref. [125].

We expect the width of this interval in the transition regime to scale as $\epsilon^{2/5}$ [165]. To check this, we rescale the x-axis around the ISCO by a factor of $\epsilon^{-2/5}$ as shown in the inset of Fig. 3.7. Now the values of α_ϵ coincide between the different simulations and the width of the transition region appears independent of ϵ as expected.

Let us now investigate the deviations of our worldtube inspiral from the adiabatic approximation in more detail. We explore the effect of higher-order terms by considering the ϵ dependence of the orbital phase accumulated during the inspiral. We define $\phi_{\rm tot}$ as the total phase covered between the frequencies corresponding to $r_\omega^{(0)} = 7.8M$ and $r_\omega^{(1)} = 6.8M$. We consider an expansion of the form predicted by Eq. (3.69),

$$\epsilon\phi_{\rm tot} = a + b\epsilon + c\epsilon^2 + \ldots \tag{3.72}$$

Figure 3.8 shows $\epsilon\phi_{\rm tot}$ plotted for a range of ϵ using the adiabatic approximation (marked by green triangles), as well as for simulations with initial worldtube radius $R_0 = 0.8M$ (blue circles) and $R_0 = 0.4M$ (red crosses). Each marker corresponds to a separate simulation. Also plotted is a cubic fit for each worldtube size and

[164]: Compère et al. (2022), *Asymptotically matched quasi-circular inspiral and transition-to-plunge in the small mass ratio expansion*

[125]: Albertini et al. (2022), *Comparing second-order gravitational self-force, numerical relativity, and effective one body waveforms from inspiralling, quasicircular, and non-spinning black hole binaries*

[165]: Ori et al. (2000), *The Transition from inspiral to plunge for a compact body in a circular equatorial orbit around a massive, spinning black hole*

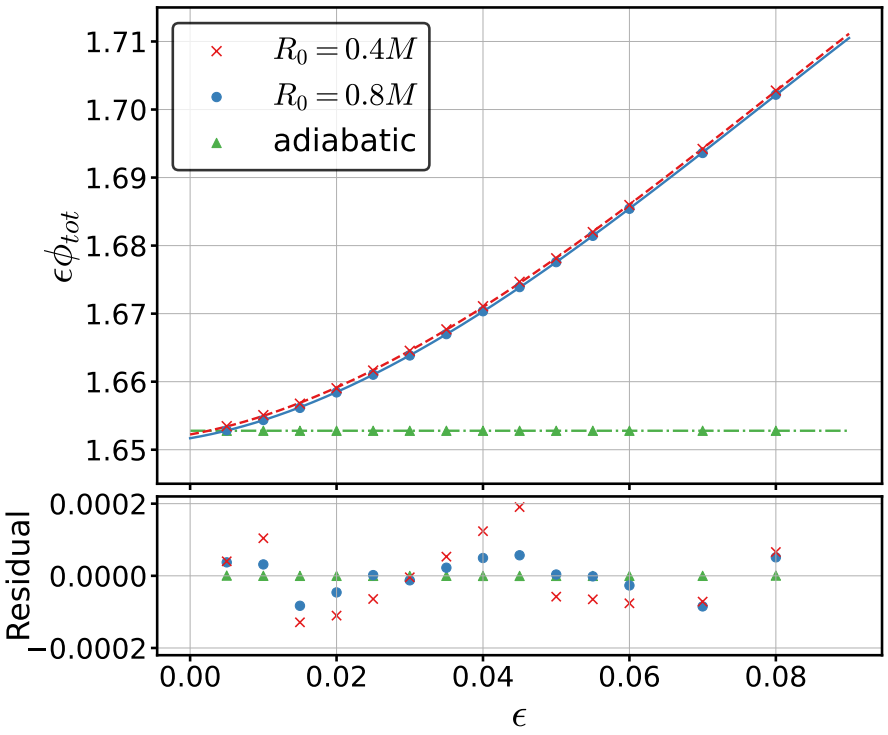

Figure 3.8: The total phase $\phi_{\rm tot}$ covered between the two angular velocities corresponding to $r_\omega^{(0)} = 7.8M$ and $r_\omega^{(1)} = 6.8M$, multiplied by ϵ. Each marker represents a separate simulation. The blue dots correspond to simulations with initial worldtube radius $R_0 = 0.8M$, the red crosses correspond to $R_0 = 0.4M$. A cubic fit is shown for each worldtube radius as well. The green triangles correspond to the adiabatic approximation which only captures the leading order term of the scalar self-force. A linear fit is shown as well.

a linear fit for the adiabatic approximation given by:

$$\begin{aligned} R_0 = 0.8M: \ \epsilon\phi_{\rm tot} &= 1.6516 + 0.184\epsilon + 8.49\epsilon^2 - 36.4\epsilon^3, \\ R_0 = 0.4M: \ \epsilon\phi_{\rm tot} &= 1.6522 + 0.195\epsilon + 8.20\epsilon^2 - 34.4\epsilon^3, \\ \text{adiabatic}: \ \epsilon\phi_{\rm tot} &= 1.6527 - 4.3\times10^{-7}\epsilon. \end{aligned}$$

The bottom panel displays the residuals of each fit.

The adiabatic approximation only resolves the leading order term in ϵ given by the constant coefficient a, whereas the worldtube simulations are sensitive to all powers of ϵ. It is therefore unclear which order polynomial should be used to fit our simulations. A higher-order polynomial will always have lower residuals but will start to overfit the data at some order. A low-order fit will absorb higher-order physical effects into the low-order coefficients, skewing their values.

We choose to fit a cubic polynomial here, as the residuals start to look more or less unstructured at this point. A brief Bayesian analysis confirmed that a cubic fit has the highest evidence of all orders. The coefficients of the fit depend on the choice of the arbitrary frequencies $r_\omega^{(0)}$ and $r_\omega^{(1)}$ between which the phase is covered. We analyze the results here for $r_\omega^{(0)} = 7.8M$ and $r_\omega^{(1)} = 6.8M$, but our general conclusions hold for all frequency intervals examined.

The coefficient a corresponds to the difference $\phi_0(r_\omega^{(1)}) - \phi_0(r_\omega^{(0)})$ predicted by the adiabatic approximation (3.67). This limit is approached by the worldtube simulations at the left side of Fig. 3.8 as ϵ approaches zero. The cubic fits in Eq. (3.73) demonstrate that the worldtube simulations extract this value with a relative error of $\sim 10^{-4}$. The smaller worldtube radius $R_0 = 0.4M$ has a lower error indicating the expected convergence with worldtube size.

The difference in the simulations with worldtube radius $R_0 = 0.8M$ and $R_0 = 0.4M$ gives an estimate of the error induced by the finite size of the worldtube. The top panel of Figure 3.8 shows that the error remains small for the range of ϵ sampled as the points of the two simulations lie almost on top of each other. This is reflected by the small difference in the linear and post-adiabatic coefficients, which suggests that our simulations are able to resolve such higher-order effects accurately. However, the exact values of the post-adiabatic coefficients are more uncertain, as our fits yield values that depend rather strongly on the polynomial order used for the fit. An accurate extraction of such coefficients would require many simulations at small ϵ and worldtube radii, which are computationally expensive and beyond the scope of this project.

3.6.2 Convergence with worldtube radius

In the previous chapter, we predicted the (global) converge rates α with worldtube radius R of the numerical field $\Psi^{\mathcal{N}}$, the regular field $\Psi^{\mathcal{R}}$ and its derivatives $\partial_i \Psi^{\mathcal{R}}$ which we have summarized in Eqs. (3.14)–(3.16). These scaling relations were confirmed for circular geodesic orbits with radius $r_0 = 5M$. The predicted rates are, however, valid for arbitrarily accelerated orbits and a correct generalization of the worldtube scheme should show the same behavior.

We investigate convergence with worldtube radius by running a set of simulations with R_0 varying between $3.2M$ and $0.2M$. As no analytical solutions or comparable codes exist to our knowledge, we choose the evolution with smallest initial worldtube radius $0.2M$ as a reference solution and compute errors with respect to it. The initial orbital radius is set to $r_0 = 8M$ for each simulation and we compute the second iteration of the acceleration $\ddot{x}^i_{p(2)}$ at each time step. The turn-on timescale is fixed to $\sigma = 500M$. The puncture field is computed with the acceleration terms according to Eq. (3.58).

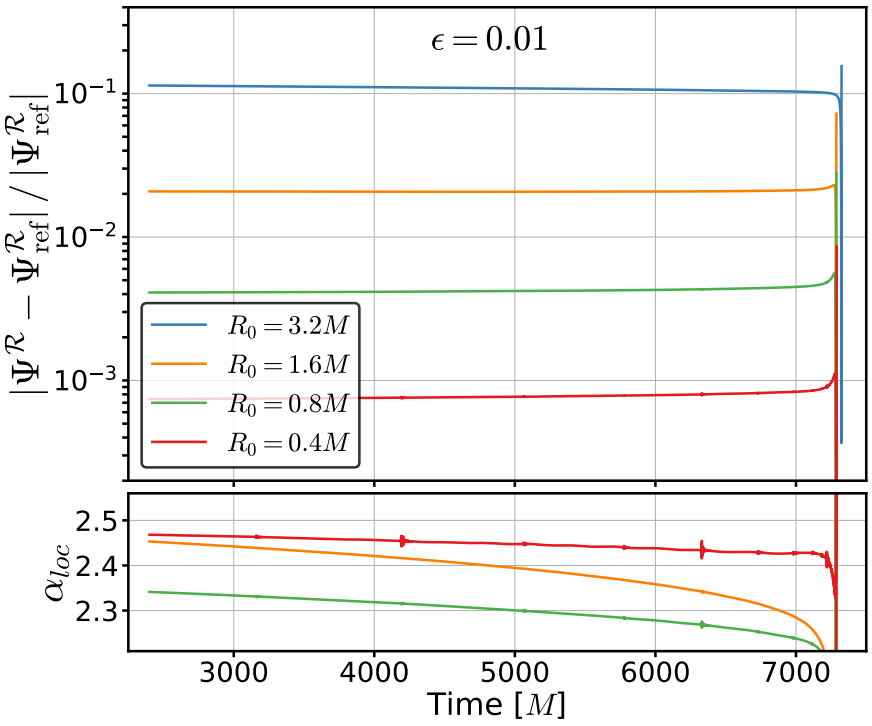

Figure 3.9: *Top panel:* The relative error of the regular field $\Psi^{\mathcal{R}}$ at the position of the charge compared to a reference solution of small worldtube radius. The error is computed for fixed angular velocities. Each line represents a simulation with different initial worldtube radius. The error remains constant during the inspiral as the worldtube is shrunk at a rate that compensates the increasing error at smaller orbital radii. *Bottom panel:* The local convergence order between simulations of neighboring worldtube radii. It continually exceeds the expected convergence rate of $\alpha = 2$.

Regular field

We denote the reference solution of the regular field at the position of the particle as $\Psi^{\mathcal{R}}_{\rm ref}(\omega)$ to emphasize that we are evaluating it as a function of the particle's angular velocity. The relative error of a simulation at angular velocity ω is defined as

$$\varepsilon(\omega) = \frac{|\Psi^{\mathcal{R}}(\omega) - \Psi^{\mathcal{R}}_{\rm ref}(\omega)|}{|\Psi^{\mathcal{R}}_{\rm ref}(\omega)|}. \tag{3.74}$$

The top panel of Fig. 3.9 shows this relative error $\varepsilon(\omega)$ plotted against the coordinate time corresponding to the angular velocity of the reference solution. For all simulations, the error of the regular field $\Psi^{\mathcal{R}}$ at the charge's position remains constant until the particle is close to the event horizon. Recall that in all simulations presented here, we shrink $R(t)$ according to the power law given by Eq. (3.25) with exponent $\beta = 3/2$. The constant error in the regular field confirms our hypothesis from Sec. 3.3.3 that this choice compensates the increase in the error of the regular field $\Psi^{\mathcal{R}}$ as the orbital radius $r_p(t)$ decreases.

The convergence rate α is no longer constant for the inspiralling orbits, as the simulations do not reach a steady-state solution. We

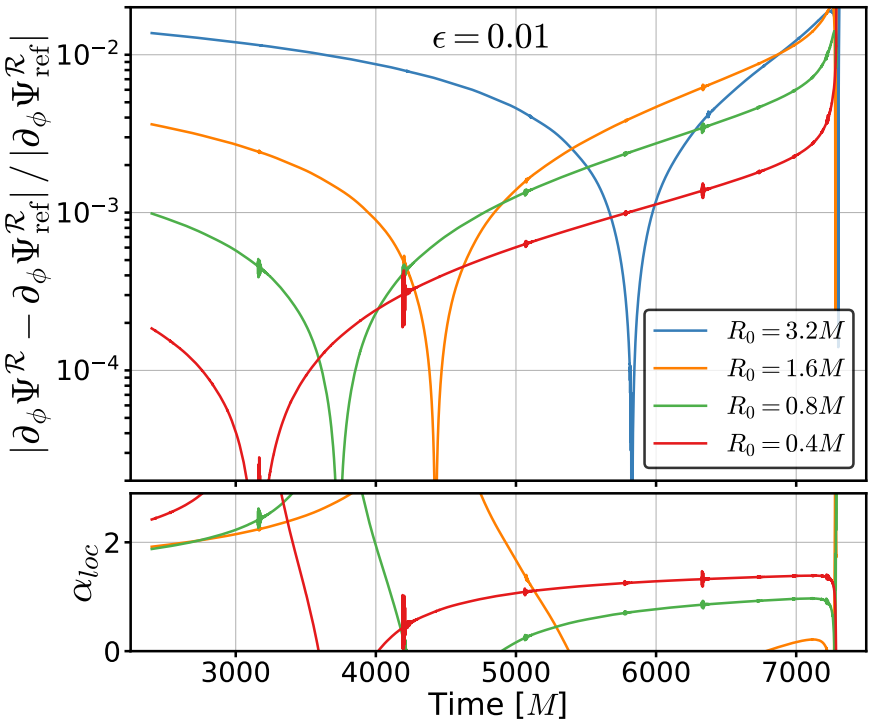

Figure 3.10: *Top panel:* The relative error of the angular derivative of the regular field $\partial_\phi \Psi^{\mathcal{R}}$ at the position of the charge compared to a reference solution of small worldtube radius. The error is computed for fixed angular velocities. *Bottom panel:* The local convergence order between simulations of neighboring worldtube radii.

introduce the local convergence order

$$\alpha_{\mathrm{loc},j}(\omega) = \frac{\log(\varepsilon_j(\omega)) - \log(\varepsilon_{j-1}(\omega))}{\log(R_{0,j}) - \log(R_{0,j-1})}, \tag{3.75}$$

where $R_{0,j}$ are the different initial worldtube radii evolved, and ε_j are the corresponding errors. The metric $\alpha_{\mathrm{loc},j}$ gives a "local" measure of α reached between simulations with worldtube radius $R_{0,j}$ and the next smaller worldtube radius $R_{0,j-1}$ and is therefore less prone to be influenced by zero-crossings or anomalies in the errors. The bottom panel of Fig. 3.10 shows $\alpha_{\mathrm{loc}}(\omega)$. The rates are continually between 2.2 and 2.5 for all worldtube radii up until the scalar charge is very close to the event horizon. This consistently exceeds the prediction $\alpha = 2$ from Eq. (3.15).

Angular derivative of regular field

Next, we show the convergence of the error in the angular derivative of the regular field at the particle's position $\partial_\phi \Psi^{\mathcal{R}}|_{x_p^i}$. This component corresponds to the dissipative part of the scalar self-force, which dominates the particle's inspiral rate. Its relative error against a reference simulation with initial worldtube radius $R_0 = 0.2M$ is depicted in the top panel of Fig. 3.10. As before, data at the same frequency are subtracted from each other at fixed

angular velocity ω but plotted against the corresponding time of the reference simulation.

All simulations show a zero crossing in this error over the course of the inspiral, appearing later for larger worldtube radii. With the exception of this crossing, the errors are consistently increasing over the course of the evolution. This is expected as the worldtube radius is shrunk according to the power law (3.25) with $\beta = 3/2$, a choice that keeps the error in the regular field $\Psi^{\mathcal{R}}$ constant. A value of $\beta = 3$ would be required to keep the error in the derivatives of the field constant.

The bottom panel displays the local convergence order α_{loc} of the relative error in $\partial_\phi \Psi^{\mathcal{R}}|_{x_p^i}$. When the scalar self-force is fully turned on at around $t = 2500M$ at an orbital radius close to $r_p \approx 8M$, the converge order is around 2 for all simulations. As the errors goes through zero crossings, the convergence jumps but, at least for the smaller worldtube radii, appears to settle to a value $\alpha_{\text{loc}} \approx 1$. We suspect that, at larger worldtube radii, higher-order terms still dominate, which causes the convergence order to be higher than predicted by Eq. (3.16). As the orbital radius decreases, the terms stop dominating and we approach the expected convergence order. The radial and time derivative of the regular field show similar behavior, but we do not include their analysis here.

Orbital phase

Lastly, we consider the error in the orbital phase ϕ_p. As the simulations are already accumulating phase differences while the self-force is being turned on, we compare phase differences at fixed angular velocity rather than time. The phase offset $\delta\phi$ and the accumulated phase error $\varepsilon(\omega)$ with respect to a reference simulation are defined as

$$\delta\phi = \phi_p(\omega_0) - \phi_{p,\text{ref}}(\omega_0) \tag{3.76}$$

$$\varepsilon(\omega) = |\phi_p(\omega) - \phi_{p,\text{ref}}(\omega) - \delta\phi|, \tag{3.77}$$

where ω_0 is an arbitrary angular velocity at which the phase difference is set to zero, $\varepsilon(\omega_0) = 0$. We choose $\omega_0 = 0.2M^{-1}$ here, which is close to the final passage through the event horizon of the particle.

The phase differences are shown in the top panel of Fig. 3.11 plotted against the coordinate time corresponding to the angular velocity of the reference simulation. The entire inspiral covered about 41 orbits

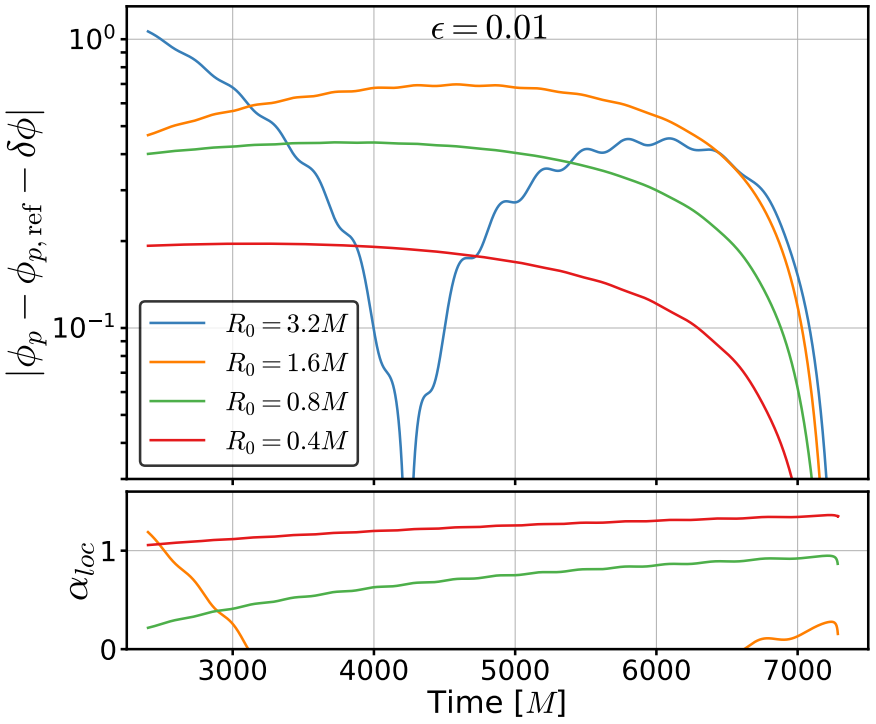

Figure 3.11: *Top panel:* The accumulated phase error of the orbit compared to a reference solution of small worldtube radius. The phase difference is set to zero at an angular velocity of $\omega_0 = 0.2M^{-1}$ corresponding to the right end of the figure. *Bottom panel:* The local convergence order between simulations of neighboring worldtube radii. The zero crossings in the error skew the convergence orders for larger worldtube radii.

while the self-force was fully turned on, during which a total phase error between 0.2 and 1 radians was accumulated. This corresponds to a relative error of $\sim 10^{-3}$. The phase error of the blue line with the largest initial worldtube radius of $R_0 = 3.2M$ shows a zero crossing in the orbit as well as signs of some residual eccentricity. The orange line with initial worldtube radius $R_0 = 1.6M$ also appears to approach a zero crossing towards the start of the simulation.

The bottom panel of Fig. 3.11 shows the local convergence order α_{loc}. We expect that the phase error is dominated by the dissipative part of the scalar self-force driven by $\partial_\phi \Psi^{\mathcal{R}}|_{x_p^i}$ and should therefore display the same convergence behavior of $\alpha = 1$. The evolution with initial worldtube radius $R_0 = 0.4M$ shown by the red line supports this with a local convergence order slightly larger than 1 for the entire inspiral. The zero crossings of the error in the other simulations make the analysis more difficult but the convergence order for the slightly larger initial worldtube size $R_0 = 0.8M$ appears to approach $\alpha_{\mathrm{loc}} \approx 1$ towards the end of the simulation.

3.6.3 Effect of acceleration terms

In the previous section, we showed that the iterative scheme derived in Sec. 3.5.1 attains at least the same convergence orders predicted in Eqs. (3.15) and (3.16) for a scalar charge inspiralling

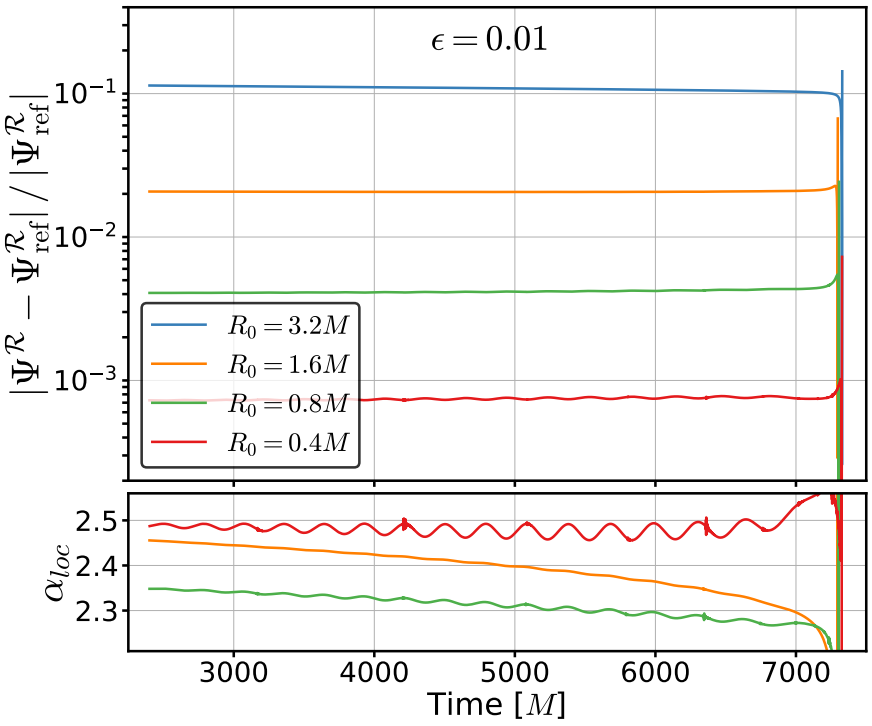

Figure 3.12: *Top panel:* The relative error of the regular field $\Psi^{\mathcal{R}}$ at the position of the charge compared to a reference solution of small worldtube radius when not including the acceleration terms in the puncture field. *Bottom panel:* The local convergence order between simulations of neighboring worldtube radii. This figure is very similar to Fig. 3.9 indicating the acceleration terms do not affect the convergence rate of $\Psi^{\mathcal{R}}$. However, they change the value to which the regular field $\Psi^{\mathcal{R}}$ converges by about 3 per cent.

under the influence of the scalar self-force. These simulations include acceleration terms in the computation of the puncture field, and we explain our method of calculating them in Sec. 3.5.2. Given the difficulties involved in including the acceleration terms, one might wonder whether they are indeed needed at the accuracies reached here. To this end, we repeat the simulations of the previous section but use Eq. (3.41) to evaluate the puncture field, i.e. we do not include the acceleration terms. Other than that, the simulations presented here are identical to those from the last section. The acceleration is calculated up to the second iteration $\ddot{x}^i_{p(2)}$ and the initial worldtube radius R_0 is varied between $3.2M$ and $0.2M$. The evolution with smallest initial worldtube radius $0.2M$ (not including acceleration terms) is again used as a reference solution to compute errors with respect to it.

Regular field

The top panel of Fig. 3.12 shows the relative error of the regular field at a fixed angular velocity as defined in Eq. (3.74). The error looks almost identical to the equivalent top panel of Fig. 3.9, which includes the acceleration terms. However, the regular field of the reference simulations $\Psi^{\mathcal{R}}_{\rm ref}$ changes by about 3 per cent throughout the evolution if these terms are included. The regular field therefore converges to a different value.

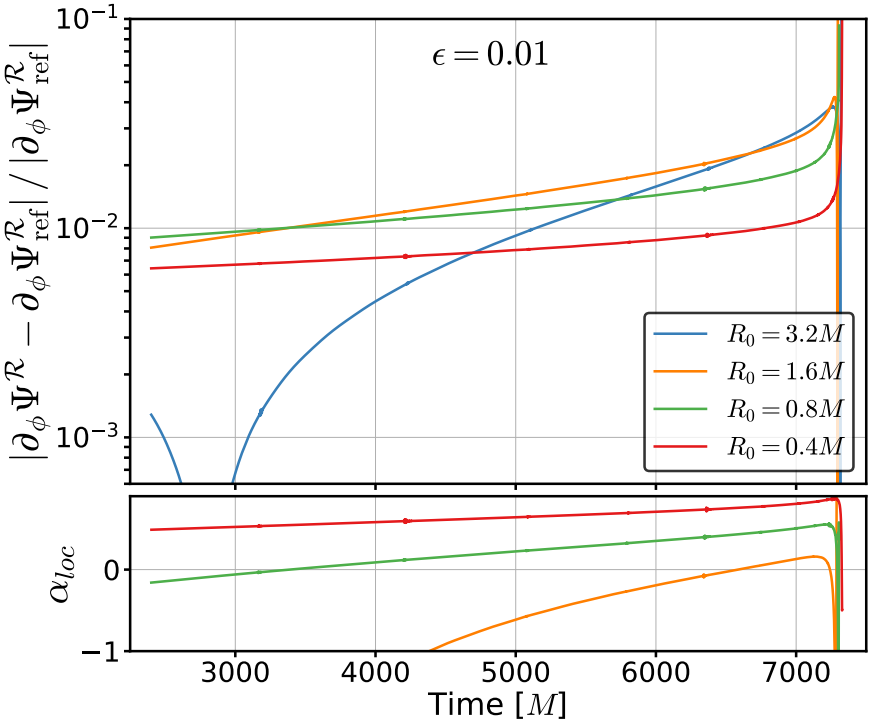

Figure 3.13: *Top panel:* The relative error of the angular derivative of the regular field $\partial_\phi \Psi^{\mathcal{R}}$ at the position of the charge compared to a reference solution of small worldtube radius. The simulations here do not include the acceleration terms. *Bottom panel:* The local convergence order between simulations of neighboring worldtube radii. The convergence rate is below the expected value of $\alpha = 1$. Figure 3.10 shows the same metric when the acceleration terms are included.

The bottom panel shows the local convergence order $\alpha_{\rm loc}(\omega)$ between simulations with adjacent worldtube radii. These naturally also look almost identical and show convergence orders between 2.2 and 2.5, which is consistent with the prediction (3.15). The only discernible effect of ignoring the acceleration terms are visible oscillations in the error and convergence rates, which suggests that the residual eccentricities between the simulations are no longer in phase. Nevertheless, we can conclude that the acceleration terms significantly change the value to which the regular field $\Psi^{\mathcal{R}}$ converges but do not have a visible effect on the convergence rate in this regime.

Angular derivative of regular field

Next, we explore the effect of the acceleration terms on the angular derivative of the regular field at the particle's position, $\partial_\phi \Psi^{\mathcal{R}}|_{x_p^i}$, which is responsible for the dissipative part of the scalar self-force. Its error is as usual defined with respect to the reference solution $\partial_\phi \Psi^{\mathcal{R}}_{\rm ref}$ as in Eq. (3.74).

The relative error with respect to coordinate time is plotted in the top panel of Fig. 3.13. It is 1-2 orders of magnitude larger compared to the corresponding top panel of Fig. 3.10, where the acceleration terms were included. The only exception is the largest worldtube radius, $R_0 = 3.2M$, which shows a zero crossing at the start of

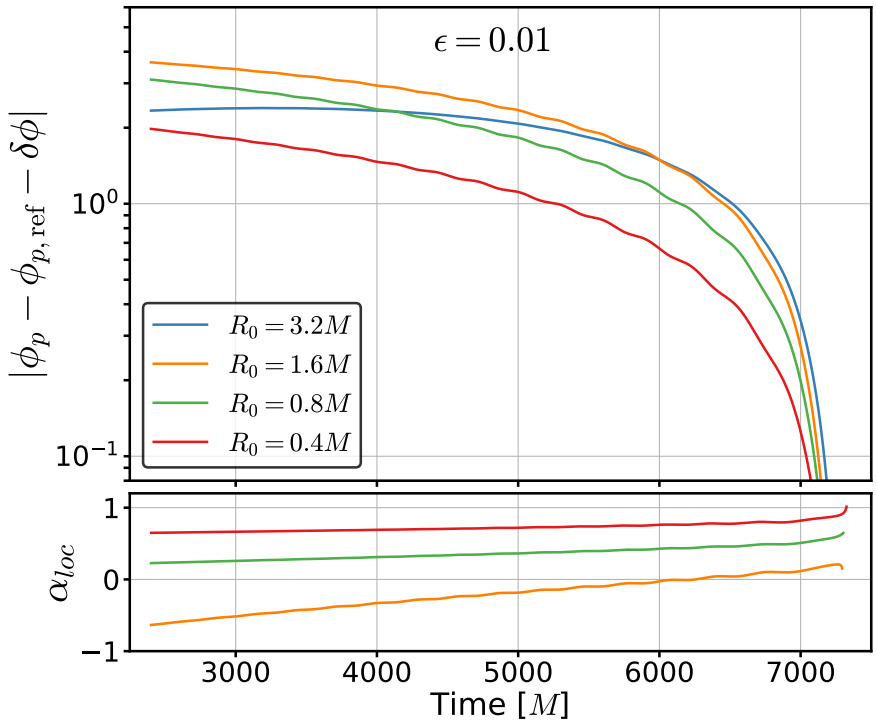

Figure 3.14: *Top panel:* The accumulated phase error of the orbit compared to a reference solution of small worldtube radius when the acceleration terms are not included. The phase difference is set to zero at an angular velocity of $\omega_0 = 0.2M^{-1}$ which, roughly corresponding to $t \approx 7100M$. *Bottom panel:* The local convergence order between simulations of neighboring worldtube radii. Figure 3.11 shows results for the same runs with acceleration terms included which have lower errors and higher convergence rates.

the simulation. For the other evolutions, decreasing the worldtube radius appears to slightly decrease the relative error in $\partial_\phi \Psi^{\mathcal{R}}|_{x_p^i}$. The local convergence rate α_{loc} depicted in the bottom panel reveals that convergence is consistently lower than the predicted rate of $\alpha = 1$.

The acceleration terms therefore appear to be essential for correctly computing the angular derivative of the regular field $\partial_\phi \Psi^{\mathcal{R}}|_{x_p^i}$. As this component drives the inspiral of the particle, we expect that the particle's orbit to be also significantly affected.

This behavior roughly conforms with our theoretical expectation. Omitting the acceleration terms amounts to neglecting a term of order ϵR^0 in the puncture and ϵR^{-1} in the derivative of the puncture, inducing errors of those orders in $\Psi^{\mathcal{R}}$ and $\partial_\alpha \Psi^{\mathcal{R}}$. Therefore, when $R \to 0$, $\Psi^{\mathcal{R}}$ will converge but have a finite error of order ϵ, while $\partial_\alpha \Psi^{\mathcal{R}}$ will actually diverge as R^{-1}; the fact that we find similar convergence for $\Psi^{\mathcal{R}}$ and slow convergence for $\partial_\alpha \Psi^{\mathcal{R}}$ (rather than divergence) is likely due to the small value of ϵ suppressing the effect.

Orbital phase

Finally, we explore how the acceleration terms affect the particle's orbital phase $\phi(t)$. We measure the effect with the accumulated

phase error ε defined in Eq. (3.76) which zeros the phase difference at an angular velocity $\omega_0 = 0.2M^{-1}$. The top panel of Fig. 3.14 shows ε plotted against coordinate time corresponding to the angular velocity of the reference simulation. When compared to the corresponding top panel of Fig. 3.11, the accumulated phase difference is about an order of magnitude higher when the acceleration terms are omitted. While a lower worldtube radius in general still reduces the total phase difference, a comparison of the bottom panels of Fig. 3.11 and 3.14 reveals that the local convergence order is consistently about half an order higher when acceleration terms are included.

3.6.4 Convergence of the iterative scheme

In Sec. 3.5.1 we presented an iterative scheme that addresses the implicit form of the particle's equation of motion (3.40) under the influence of the scalar self-force. We check the convergence with iterations by running a set of simulations with $k = 2$, 3, 5 and 7 iterations of the acceleration $\ddot{x}^i_{p(k)}$, and then use the simulation with 7 iterations as a reference solution to estimate errors. We fix the initial worldtube radius to $R_0 = 0.8M$ and the inspiral parameter to $\epsilon = 0.01$. The acceleration terms are included and the turn-on timescale is set to $\sigma = 1000M$ in these runs.

Figure 3.15 shows the relative error in the angular derivative of the regular field $\partial_\phi \Psi^{\mathcal{R}}$ at the position of the particle for 2, 3 and 5 iterations, respectively. The error is computed analogously to Eq. (3.74), which compares the value at the same orbital angular velocity ω of the orbit against the reference value $\partial_\phi \Psi^{\mathcal{R}}_{(7)}$. The simulation with 2 iterations shows a constant relative error of $\sim 10^{-5}$ until the particle is very close to the horizon. This justifies our choice of using two iterations when analyzing the convergence with worldtube radius R_0 in section 3.6.2 because the worldtube always induces an error at least an order of magnitude larger.

We expect that each additional iteration adds a correction that is a factor of ϵ smaller than the previous one. This is demonstrated by the orange line, which used 3 iterations and shows an error two order of magnitudes smaller $\sim 10^{-7}$. When using 5 iterations, the additional corrections get so small that the finite resolution of the DG grid causes the error to be fairly noisy. However, a majority of the simulation still shows an error of $\sim 10^{-11}$, which is four orders of magnitude lower than with 3 iterations, as expected. For larger ϵ, convergence with the iterations k is slower so that several

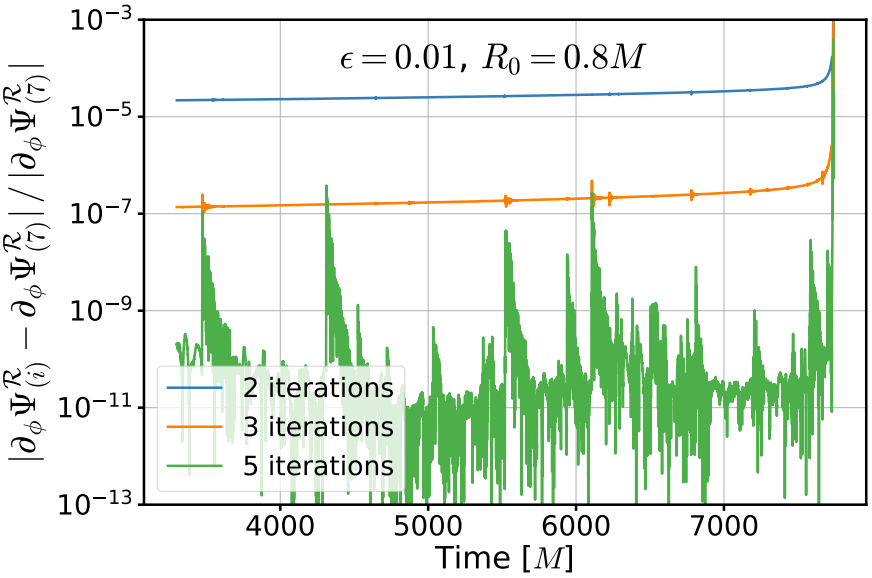

Figure 3.15: The relative error in the angular derivative of the regular field $\partial_\phi \Psi^{\mathcal{R}}$ when using different number of iterations compared to using seven iterations. The error decreases by a factor of $\epsilon = 0.01$ with each iteration, as expected. The green curve is noisy due to the finite resolution of the DG evolution.

iterations were used in Sec. 3.6.1 where ϵ was set as high as 0.08.

3.7 Conclusions and outlook

In this work, we continue to explore a new approach to simulating intermediate mass-ratio binary black holes in numerical relativity. The method works by excising a worldtube much larger than the smaller object from an evolution domain and employing a perturbative solution inside this region. The perturbative solution is calibrated from the evolution outside the excision sphere and in turn provides boundary conditions to it.

In the previous chapter, we implemented this scheme for a scalar charge on a circular geodesic orbit using SpECTRE, a numerical relativity code that employs a DG method to evolve the Klein-Gordon equation in 3+1 dimensions. Here we extend the scheme to include the effect of radiative back-reaction on the charge, known as the scalar self-force.

We construct series of time-dependent maps that allow the worldtube to track the particle's motion on generic equatorial orbits along with the rest of the grid. Then, we derive a puncture field that is valid for generically accelerated orbits. Finally, we show that the particle's acceleration under the scalar self-force is given in implicit form and construct an iterative scheme to address this issue.

The scheme is tested with a set of quasi-circular inspirals for different values of the inspiral parameter ϵ, the worldtube radius R and number of iterations k used in solving the implicit equation for the self-force. We compare the results to an adiabatic approximation and show that we not only resolve effects at leading order in ϵ but also get important contributions from higher orders. We demonstrate that the regular field at the position of the particle and its derivatives converge with the worldtube radius R at the theoretically predicted rates. At last, we show that the iterative scheme converges rapidly.

In this work, we have restricted ourselves to expansion order $n = 1$ in coordinate distance and have shown that the resulting simulations can be run with high accuracy within a day. The inclusion of second order $n = 2$, as implemented for circular orbits in the previous chapter, would greatly speed up simulations as a much larger worldtube radius can be used to achieve the same accuracy. Our previous work also indicates that the next order would increase the accuracy of the scheme by up to two orders of magnitude at the same worldtube radius. An implementation would require the derivation of the puncture field at the next order as well as adjusting the iterative scheme to include these higher-order terms. Both additions should be straightforward if tedious, and we leave them to future work.

While only quasi-circular orbits were presented in this work, our method is applicable for generic bound orbits. In the next chapter, we examine the effects of the scalar self-force on eccentric orbits and hyperbolic encounters during a self-consistent evolution.

Other avenues for future work include the extraction of multipolar energy-momentum fluxes in scalar-field radiation to infinity and down the event horizon, which would allow us to check flux balance laws. We currently find that the finite size of our Cauchy domain limits the accuracy at which these quantities can be extracted. This difficulty could be mitigated through a procedure of Cauchy-Characteristic extraction [166] or Cauchy-characteristic matching [167], in order to propagate the scalar field to null infinity.

[166]: Moxon et al. (2023), *SpECTRE Cauchy-characteristic evolution system for rapid, precise waveform extraction*

[167]: Ma et al. (2023), *Fully relativistic three-dimensional Cauchy-characteristic matching*

Self-consistent evolution on eccentric orbits and hyperbolic trajectories

4

This chapter considers the self-consistent evolution of a scalar charge in Schwarzschild spacetime on eccentric and hyperbolic trajectories.

4.1 Introduction

The dynamics of a scalar charge moving across Schwarzschild spacetime is a well-studied toy model for the fully nonlinear problem of intermediate/extreme mass-ratio inspirals. However, almost all studies only consider the geodesic evolution of the charge and ignore the effects of the scalar field's backreaction onto the particle's orbit, known as the scalar self-force [142, 168, 169]. Works that do consider this effect employ approximations such as two-timescale expansions driven by adiabatic fluxes [170, 171]. However, these methods ignore conservative effects [172] and become inaccurate for larger values of the inspiral parameter ϵ. In addition, they are not able to resolve the transition-to-plunge, plunge or ringdown regime of the evolution. To our knowledge, only one attempt at a self-consistent evolution has previously been explored in [149]; however, the code has low accuracy and omits the "acceleration terms" of the puncture field which are essential for an accurate evolution, as explored in Sec. 3.6.3.

In the previous chapter, we presented a fully self-consistent evolution algorithm based on the worldtube excision method. Here, the scheme is generalized to eccentric orbits as well as hyperbolic encounters. We find that our method is able to handle highly eccentric orbits up to $e \approx 0.9$ through plunge, merger and ringdown as well as hyperbolic encounters with large scattering angles.

The chapter is structured as follows. In Section 4.2, we explore the adjustments made to the code necessary for the evolution of non-quasi-circular orbits. Next, we present a series of eccentric orbits in Section 4.3 and explore the effect of varying the inspiral parameter ϵ. In Section 4.4, we consider a set of hyperbolic trajectories and show how the scalar self-force alters the scattering angle and can lead to the direct capture of the charge. Lastly, we summarize our results and present some future projects in Section 4.5.

[142]: Diaz-Rivera et al. (2004), *Scalar field self-force effects on orbits about a Schwarzschild black hole*

[168]: Warburton et al. (2010), *Self force on a scalar charge in Kerr spacetime: circular equatorial orbits*

[169]: Barack et al. (2022), *Self-force correction to the deflection angle in black-hole scattering: A scalar charge toy model*

[170]: Drasco et al. (2005), *Computing inspirals in Kerr in the adiabatic regime. I. The Scalar case*

[171]: Mino et al. (2008), *Two-timescale adiabatic expansion of a scalar field model*

[172]: Pound et al. (2005), *Limitations of the adiabatic approximation to the gravitational self-force*

[149]: Diener et al. (2012), *Self-consistent orbital evolution of a particle around a Schwarzschild black hole*

4.2 Methods

In Chapter 3, we developed an algorithm for the self-consistent evolution of a point charge, including the derivation of a puncture field for generic orbits and the construction of an iterative scheme that can evaluate the equation of motion (3.2) to arbitrary precision. The method was constructed with such generality that it can readily be extended to eccentric orbits and hyperbolic encounters by adjusting the computational domain and changing the prescription used to dynamically shrink the worldtube.

4.2.1 Worldtube radius adjustment

We originally argued that the worldtube radius R should grow with the orbital radius according to a power law $R(t) \propto r^{3/2}(t)$, as this keeps the error in the regular field $\Psi^{\mathcal{R}}$ constant. However, for highly eccentric orbits and scattering encounters, the variations in orbital radius can cause the worldtube radius to become prohibitively large. In addition, the simulation does not gain any speed for worldtube radii larger than $3M$ as the CFL criterion is no longer limited by the grid spacing near the worldtube. We therefore employ a smoothly broken power law that allows us to limit the growth of the excision sphere

$$R(r) = A \left(\frac{r}{r_b}\right)^{\alpha_1} \left[\frac{1}{2}\left(1 + \left(\frac{r}{r_b}\right)^{1/\Delta}\right)\right]^{(\alpha_2-\alpha_1)\Delta} . \tag{4.1}$$

This prescription ensures that the worldtube radius will grow according to a power law $R(t) \propto r^{\alpha_1}(t)$ in the region $r \ll r_b$ and according to $R(t) \propto r^{\alpha_2}(t)$ for $r \gg r_b$; the parameter Δ determines the width of the transition region with a larger value of Δ leading to a more gradual transition. We choose $\alpha_1 = 3/2$, $\alpha_2 = 0$ so that the worldtube radius asymptotically approaches a constant value. We then specify the worldtube radius at the ISCO $R_{\rm ISCO}$ and at infinity R_∞, and determine corresponding values for the amplitude A and the transition radius r_b using a numerical root search. Δ is set to 0.05 for all simulations presented here. A plot of this function is shown in Fig. 4.1.

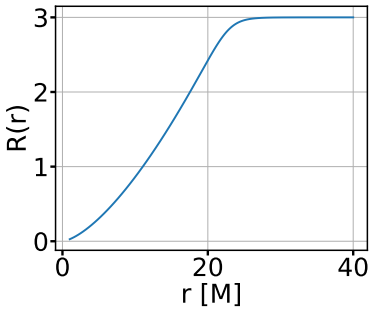

Figure 4.1: A plot of Eq. (4.1) for $R_{\rm ISCO} = 0.4M$ and $R_\infty = 3M$. The worldtube radius does not grow indefinitely but asymptotically approaches a maximum value.

4.2.2 Additional adjustments

The large variation in the orbital radius also produces a challenge for the DG domain itself. As the excision sphere always tracks the particle, the time dependent maps explored in Sec. 3.3 will stretch and compress the grid, changing the numerical resolution throughout the domain for different phases of the orbit. In particular, the grid near the worldtube will be significantly stretched at large orbital separations. We found that this does not pose problems for eccentric orbits and hyperbolic trajectories as the large worldtube radius in these regions ensures that there are no steep gradients to be resolved. The numerical error was always largest for the smallest orbital radii which we already explored in Chapter 3. Because of these considerations, the new trajectories simulated here can be accommodated by slightly adjusting the initial, fixed polynomial order in the DG elements to account for the dynamic changes in the grid spacing.

The self-consistent evolution requires several additional parameters to be set, some of which do not have obvious choices for eccentric and hyperbolic trajectories. We therefore re-run a sample of the evolutions, changing one of these parameters at a time, including the worldtube radius, the numerical resolution and the number of iterations to compute the self-force. This allows us to calculate the error induced by each of these parameters to ensure that the worldtube error always remains dominant.

4.2.3 Osculating geodesics

The Schwarzschild spacetime admits several Killing vectors. In Kerr-Schild coordinates, the time-like Killing vector reflecting the metric's time symmetry reads $\xi^\mu_t = \delta^\mu_t$ and a spacelike Killing vector is given by $\xi^\mu_\phi = (0, -y, x, 0)$, representing the rotational symmetry around the z-axis. These vectors define two constants of motion which are conserved along geodesics: the energy and angular momentum per unit mass

$$E = g_{\mu\nu} u^\mu \xi^\nu_t, \tag{4.2}$$

$$L = g_{\mu\nu} u^\mu \xi^\nu_\phi. \tag{4.3}$$

For eccentric orbits, these can be converted to an apoapsis r_a and periapsis radius r_p by considering the roots of radial Schwarzschild geodesics given by a cubic polynomial, see e.g. [173]. The radii can

[173]: Hughes (2024), *Parameterizing black hole orbits for adiabatic inspiral*

then be used to compute the semi-latus rectum and the eccentricity

$$p = \frac{2r_a r_p}{r_a + r_p}, \tag{4.4}$$

$$e = \frac{r_a - r_p}{r_a + r_p}. \tag{4.5}$$

All of these quantities are only conserved along geodesics and will evolve once the scalar self-force is turned on. However, at any point in time, we can still define a geodesic using the instantaneous position and velocity of the scalar charge. This is known as an osculating geodesic where the name indicates that it only touches the particle's worldline at this point. By defining a geodesic for every point of time, it is possible to consider the evolution of constants of geodesic motion including the energy E, the angular momentum L, the semi-latus rectum p and the eccentricity e.

For scattering trajectories, the semi-latus rectum is no longer defined. Instead, a more convenient choice of parameters are given by the velocity of the particle at infinity v_∞ and the impact parameter b. In Schwarzschild spacetime, these are related to the energy and angular momentum through (e.g. [169])

[169]: Barack et al. (2022), *Self-force correction to the deflection angle in black-hole scattering: A scalar charge toy model*

$$v_\infty^2 = 1 - E^2, \tag{4.6}$$

$$b = \frac{L}{\sqrt{E^2 - 1}}. \tag{4.7}$$

4.3 Eccentric orbits

As usual, we evolve the scalar charge for a few orbits on a geodesic orbit to build up initial data for the self-consistent evolution. The orbital time period of this geodesic is computed by numerically evaluating the integral (see e.g. [13])

[13]: Misner et al. (1973), *Gravitation*

$$T = 2\int_{r_p}^{r_a} \left((1-2/r)\sqrt{1-(1-2/r)(1+L^2/r^2)/E^2}\right)^{-1} dr. \tag{4.8}$$

In the last chapter on quasi-circular inspirals, the scalar self force was smoothly turned on over several orbits using a transition function (3.60) to avoid inducing residual eccentricity in the orbit. This is no longer necessary when considering eccentric orbits. Instead, we turn on the self-force smoothly using Eq. (3.60) during

an apoapsis passage where the self-force is expected to be insignificantly small. The parameter σ which dictates the turn-on time scale is set to $0.2T$. We found that turning on the scalar-force after four radial periods is sufficient to provide accurate initial data for the evolution; the difference from using more orbits was much lower than the error induced by the worldtube.

The top panel of Fig. 4.4 shows the orbit of a typical evolution. Here, the inspiral parameter is set to $\epsilon = 0.01$ and the initial geodesic has apoapsis $30M$ and eccentricity 0.6. The worldtube radius is set to $R_\infty = 3M$ and $R_{\rm ISCO} = 0.4M$. The particle traces out 92 orbits before it plunges into the central black hole. The periapsis distance and advance evolve continuously throughout the simulation, creating an irregular pattern.

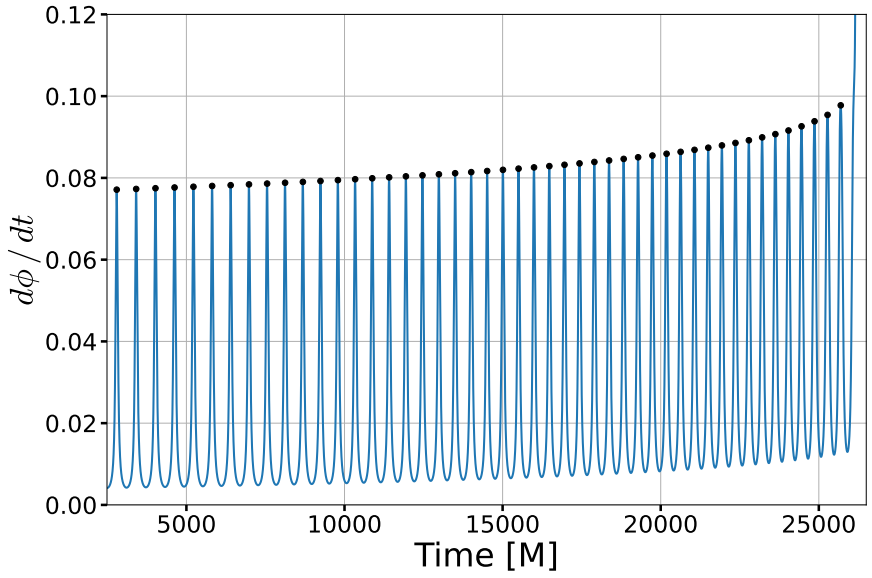

Figure 4.2: The evolution of the angular velocity $\frac{d\phi}{dt}$ for the simulation shown in Fig. 4.4. The black dots indicates the location of the periapses which occurs close to the maxima of the angular velocity.

Figure 4.2 shows the evolution of the angular velocity of the particle $\frac{d\phi}{dt}$. The quantity carries out one oscillations per orbit, approximately reaching its minimum at the apoapsis and its maximum at the periapses. The black dots indicate the location of the periapsis passages which almost coincides with the maxima of the angular velocity. Over the course of the evolution, angular velocity shows an increasing trend before it plunges.

To quantify the evolution of the periapsis advance, we define the orbit averaged radial Ω_r and angular frequency Ω_ϕ. These are computed by considering the time $T_{\rm peri}$ (given by the time period between adjacent black dots in Fig. 4.2) and phase $\phi_{\rm peri}$ covered

between adjacent periapsis passages

$$\Omega_r = \frac{2\pi}{T_{\text{peri}}}, \tag{4.9}$$

$$\Omega_\phi = \frac{\phi_{\text{peri}}}{T_{\text{peri}}}. \tag{4.10}$$

Orbital resonances are determined by the ratio of these two frequencies. Fig. 4.3 shows this ratio Ω_ϕ / Ω_r which describes the number of angular orbits covered between two periapsis passages. The initial four points, marked in orange, have a constant value of ~ 1.65 corresponding to the value of the initial geodesic. Once the self-consistent evolution begins, the periapsis distance shrinks and the particle starts a cover a larger phase with each passage. Just before the plunge, more than 5π radians are traversed each orbit.

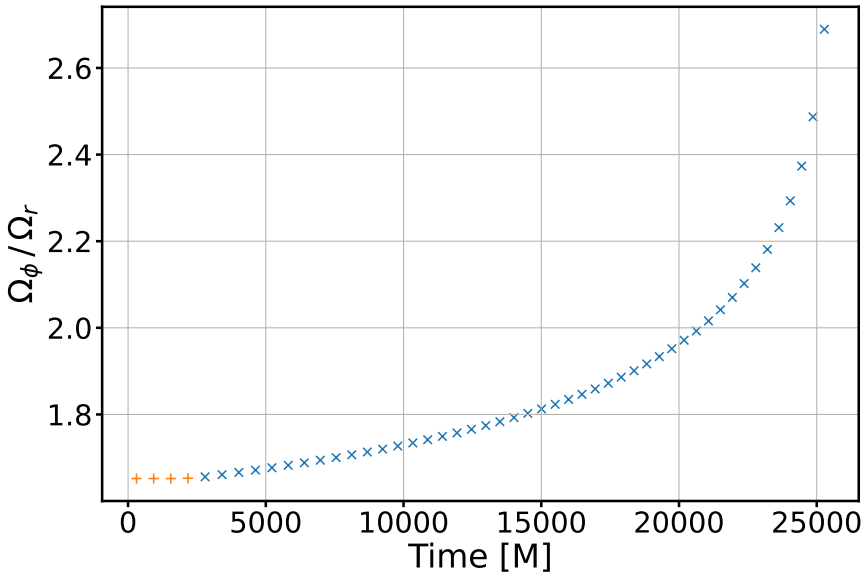

Figure 4.3: The evolution of the periapsis advance for the orbit shown in Fig. 4.4. The quantity Ω_ϕ / Ω_r corresponds to the orbit-averaged fraction of angular to radial orbits and is plotted against the orbital time. The orange markers correspond to the first four geodesic orbits. As the evolution progresses, the particle covers a larger phase between successive periapsis passages. During the final radial orbit, the charge circles the central black hole more than 2.5 times.

We analyze the waveform of the evolution by considering the decomposition of the scalar field into spherical harmonic modes, given by the expansion

$$r\Psi^{\mathcal{N}}(t, \theta, \phi)/q = \sum_{l,m} \Psi_{lm}(t) Y_{lm}(\theta, \phi) \tag{4.11}$$

at some fixed radius r. Here, $\Psi^{\mathcal{N}}$ was rescaled by the extraction radius r to offset the dominant decay of $\sim 1/r$. The orthogonality of the spherical harmonics allows for the modes $\Psi_{lm}(t)$ to be computed individually by projecting the scalar field $\Psi^{\mathcal{N}}$ onto different spherical harmonics on an extraction sphere of fixed radius r.

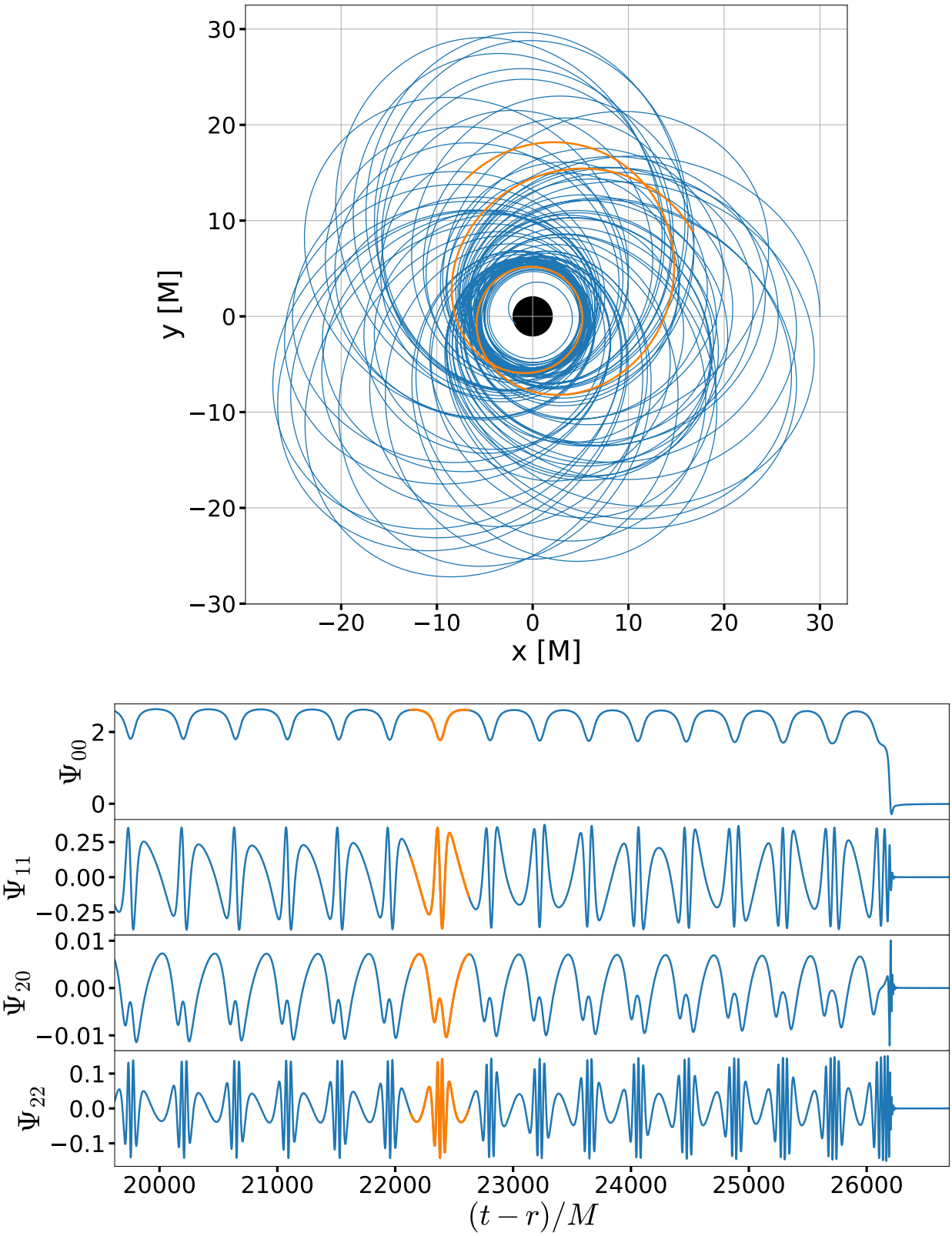

Figure 4.4: *Top Panel*: An eccentric orbit traced out by a scalar charge with inspiral parameter $\epsilon = 0.01$. The particle starts on a geodesic with apoapsis $30M$ and eccentricity 0.6. Once the scalar self-force is turned on, the apoapsis and the eccentricity decay until the particle plunges into the central black hole after $\sim 25000M$. *Bottom Panel*: The waveform produced by the final $8000M$ of this orbit extracted at $r = 450M$. Shown are the spherical harmonic modes Ψ_{00}, Ψ_{11}, Ψ_{20} and Ψ_{22} of the field $r\Psi^{\mathcal{N}}/q$. The part of the waveform highlighted in orange corresponds to the retarded time where the particle traced out the orange section of its orbit marked the top panel.

Important waveform modes during the final $\sim 8000M$ are shown in the bottom panel of Figure 4.4, plotted against the retarded time $(t - r)/M$. Shown are the spherical harmonic modes Ψ_{00}, Ψ_{11}, Ψ_{20} and Ψ_{22} of the field $r\Psi^{\mathcal{N}}/q$ where $r = 450M$ is the radius of the signal's extraction sphere. The monopole Ψ_{00} shows a single frequency around a constant value reflecting the radial motion of the particle - for a circular orbit, there would be no oscillations visible in this mode. The higher modes show more complex behavior as the orbit now has both a radial and angular frequency. With larger m, the amount of structure in the waveform mode increases as they vary more rapidly in the angular directions. Note that only modes with an even sum of $l + m$ are plotted; for odd values the modes are zero due to the equatorial symmetry of the system. The orange highlights in the modes indicate the retarded time during which the particle traced out the orange section of the orbit shown in the top panel.

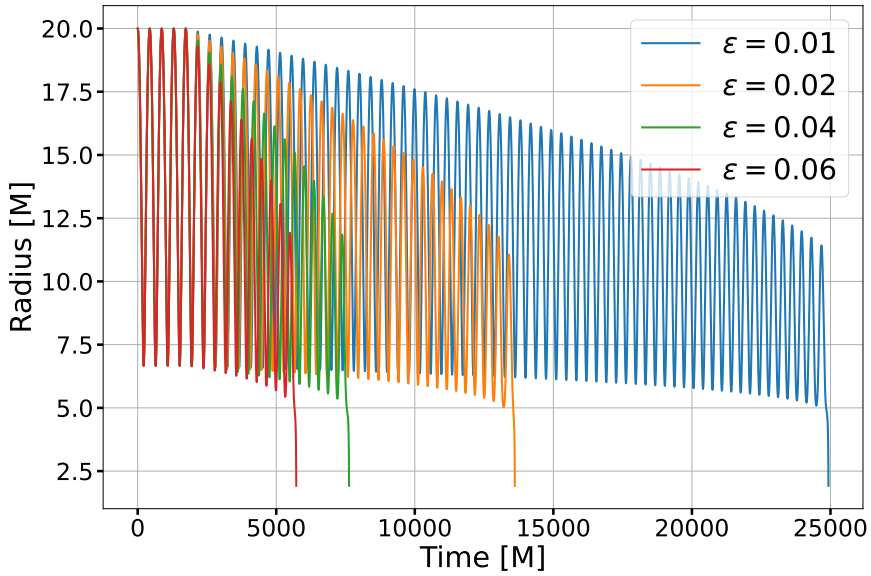

Figure 4.5: Shown is the evolution of the orbital radius of four simulations with different values of ϵ. Initially, all simulations are on the same geodesic orbit with eccentricity 0.5 and apoapsis $20M$. When the scalar force is turned on, it causes the charge to dissipate energy at a rate proportional to ϵ. As a result, the apoapsis and the eccentricity start to decay until the particle plunges into the central black hole.

Let us now discuss the dependence on the inspiral parameter ϵ. Figure 4.5 shows the evolution of the orbital radius with respect to coordinate time for a series of simulations with different values of the inspiral parameter ϵ. All simulations start on the same initial geodesic with apoapsis $20M$, periapsis $6.66M$, eccentricity of 0.5 and semi-latus rectum of $10M$. The scalar self-force is proportional to ϵ so that the particle dissipates more energy and angular momentum each orbit for larger values of ϵ. As a result, simulations with larger ϵ spiral in faster and cover fewer orbits before plunging into the central black hole.

The worldtube radius for all simulations depicted here is set to $R_\infty = 1.5M$ and $R_{\rm ISCO} = 0.2M$. We ran each simulation again

with twice these values. This allows us to use the evolutions with smaller worldtube radius as a reference solution to compute errors. The difference in the absolute phase, for instance, compared at fixed coordinate time was always around 0.01 to 0.1 radians. The error in the eccentricity defined at fixed semi-latus rectum was around 0.1 per cent for the simulations presented here. The

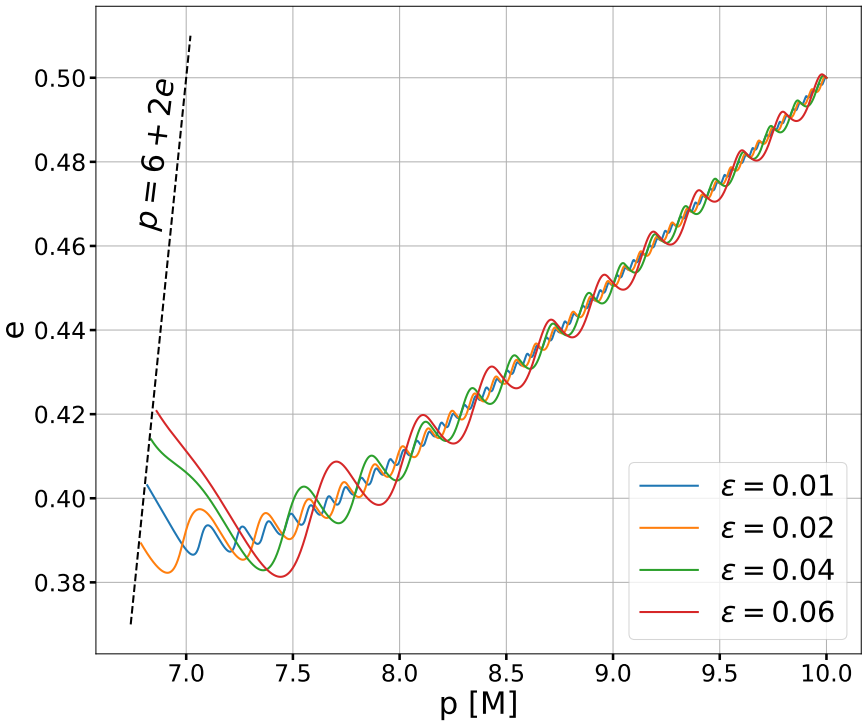

Figure 4.6: Shown is the evolution of the eccentricity and semi-latus rectum for the four orbits shown in Fig. 4.5. All simulations oscillate about approximately the same line in the pe-plane. Greater values of ϵ do fewer oscillations of a larger amplitude as they do fewer orbits each of which is altered more strongly by the scalar self-force. The black dashed line shows the separatrix $p = 2e + 6$ beyond which geodesic orbits plunge into the black hole.

evolution of the eccentricity e and the semi-latus rectum p is shown in Figure 4.6. The black dashed line shows the separatrix $p = 2e + 6$ corresponding to the last stable orbit, beyond which any geodesic plunges. The simulations with different ϵ all show the eccentricity decaying approximately along the same line with respect to the semi-latus rectum. Oscillations around this line correspond to p and e varying over a single orbit: for larger values of ϵ there are fewer oscillations with greater amplitudes as the energy dissipation each orbit is stronger. Once the particle crosses the separatrix, the semi-latus rectum p is no longer defined.

4.4 Hyperbolic encounters

Our worldtube techniques can also be applied to hyperbolic encounters of the scalar charge with a black hole, i.e. trajectories that start at infinite separation with velocity $v_\infty > 0$. A problem that arises here is the generation of initial data for the self-consistent

evolution. For bound orbits, we have simply used zero initial data, $\Psi(t_0, x^i) = \Pi(t_0, x^i) = \Phi_i(t_0, x^i) = 0$ and then evolved the system for a few geodesic orbits so the scalar field could settle to appropriate values throughout the domain. This is not possible with scattering trajectories and the evolution should ideally start with the particle at a very large distance from the central black hole so that there is sufficient time for a solution to build up in the domain. This, however, can cause problems with the numerical grid as the outer boundary has to be shifted far out requiring a larger domain size with more grid points.

Instead, we pursue a different strategy: at large distances where interactions with the black hole are small, the puncture field provides an excellent approximation to the full scalar field in the vicinity of the particle. We therefore use the zeroth order puncture field as initial conditions for the numerical domain which corresponds to Lorentz-boosted, flat spacetime solution, see Sec. 3.4. We find that this allows us to place the particle at an initial radius of $r = 200M$ on a geodesic for unbound motion with our desired asymptotic parameters. Initialization with the puncture field results in drastically reduced transients which dissipate long before the periapsis passage when compared to zero initial data. The self-consistent evolution is turned on when the particle reaches a separation of $100M$ to the black hole with the transition time $\sigma = 30M$ in Eq. (3.60). The outer boundary is placed at $1200M$.

We show some representative simulations in Figure 4.7. All these evolutions start on the same geodesic with velocity at infinity of $v_\infty = 0.1$ and impact parameter $b = 40.21M$, just above the critical value where a geodesic would plunge. The worldtube radius at infinity is set according to Eq. (4.1) with $R_\infty = 3M$ and $R_{\rm ISCO} = 0.4M$.

The black dashed line shows a geodesic orbit. The particle comes in from the right and does almost two full orbits before scattering off to infinity. When the self-consistent evolution is turned on, for the other three lines, the particle loses energy and angular momentum during the inspiral which increases the scattering angle. We define this scattering angle as

$$\delta\phi = \phi_p(t = \infty) - \phi_p(t = -\infty) - \pi \tag{4.12}$$

where ϕ_p is the phase of the orbit as defined in Eq. (3.61). The self-consistent evolution is only carried out until the particle reaches separation $r \approx 200M$ and we integrate the final state of the particle to $t = 10^{10}M$ using the geodesic equation, neglecting the scalar

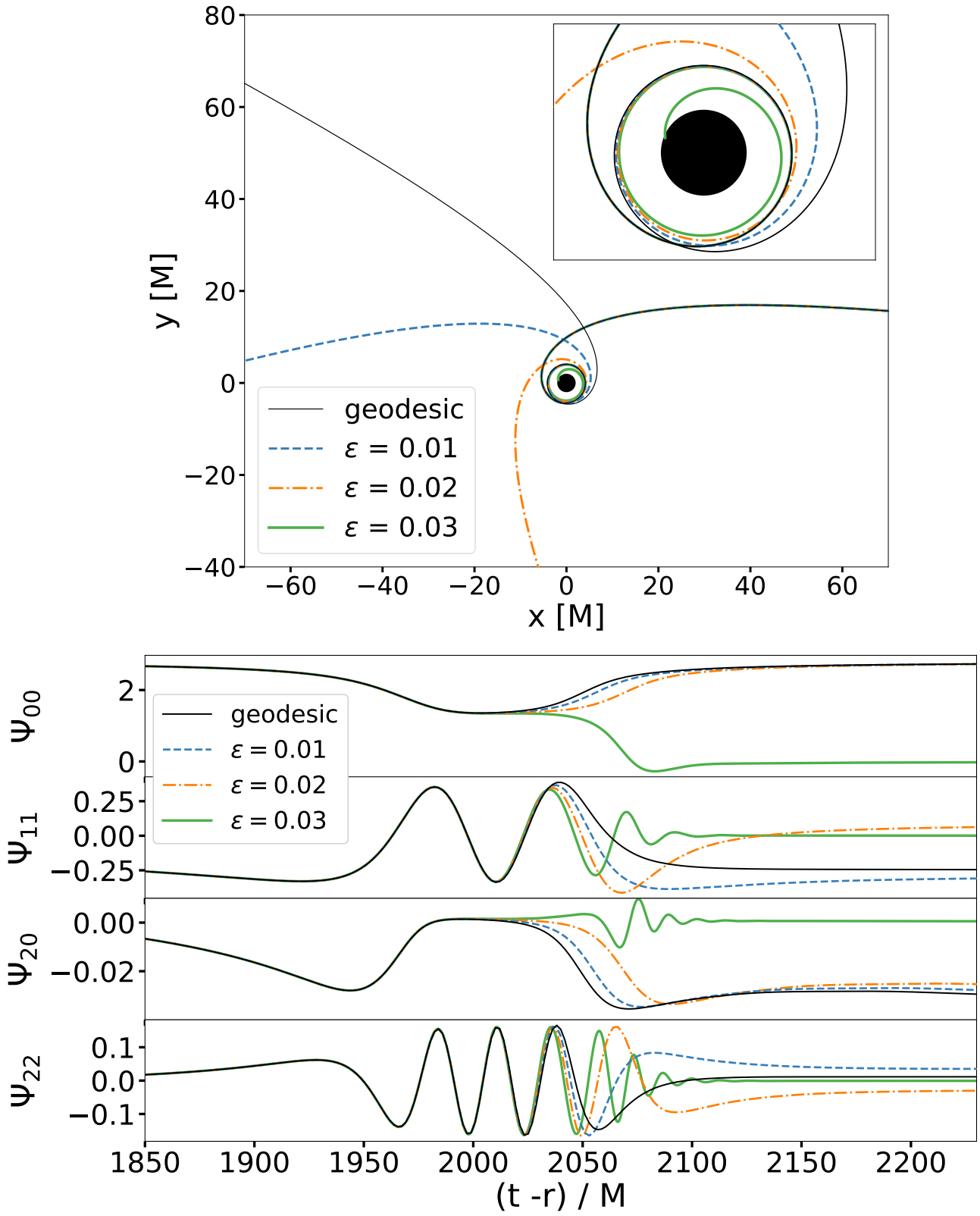

Figure 4.7: Scattering/Capture of a scalar charge around a black hole *Top Panel:* The black dashed line corresponds to a geodesic orbit with $v_\infty = 0.1$ and impact parameter $b = 40.21M$. The other lines start on the same geodesic but include the effect of the scalar self force with different values of ϵ. The simulations with $\epsilon = 0.01$ (blue, dash-dotted)and $\epsilon = 0.02$ (orange, dashed) lose energy and angular momentum as they scatter of the black hole, increasing the scattering angle. The simulation with $\epsilon = 0.03$ loses enough energy to be captured by the black hole and plunges after about 2 orbits. *Bottom Panel:* The waveform produced by the four scattering simulations extracted at $r = 950M$. Shown are four spherical harmonic modes of the field $r\Psi^{\mathcal{N}}/q$. The scalar self force visibly changes the waveform of the different modes for the scattering orbits. The direct capture shows a typical ringdown pattern before all modes decay to zero.

self-force. We checked that this does not affect the angle to double precision as long as the particle has traveled further than $\approx 100M$ from the black hole, where the self-force has effectively decayed to zero. The scattering angles are 12.29 radians for the geodesic, 13.08 radians for $\epsilon = 0.01$ and 14.85 radians for $\epsilon = 0.02$.

Particularly interesting is the simulation with $\epsilon = 0.03$ indicated by the solid green line. Here, the charge loses enough energy to be captured and plunges into the event horizon. The inset at the top right shows a zoom-in of the region around the central black hole. The four geodesics almost look identical for the first orbit but can be seen to deviate "south" of the black hole as they lose energy at different rates.

The waveforms these particles produced are depicted in the bottom panel of Figure 4.7. Again, the modes Ψ_{00}, Ψ_{11}, Ψ_{20} and Ψ_{22} defined in Eq. (4.11) are shown with the extraction sphere of the signal located at a distance of $r = 950M$. The monopole $\epsilon = 0.02$ initially has a constant value and slightly decreases during the scattering before returning to its original value. This indicates that a significant amount of this mode crosses the event horizon as the charge scatters off the black hole. For the captured orbit, the field quickly decays to zero in all modes, showing a ringdown behavior similar to the eccentric orbits. For higher modes, the different scattering angles can significantly change the amplitude of the waveform. For instance, the Ψ_{11} mode shows very different amplitudes for the simulations with $\epsilon = 0.01$ and $\epsilon = 0.02$ following the scattering event. Here, the difference in the scattering angle of the two events effectively rotates the domain, changing how the $l = 1$ mode waveform is distributed between the $m = 1$ and the $m = -1$ mode.

4.5 Conclusions

In the Chapter 3, we presented the self-consistent evolution of a scalar charge model on quasi-circular inspirals using the worldtube excision method. In this chapter, we generalized this scheme to evolve eccentric orbits and hyperbolic encounters. The majority of the methods, in particular the puncture field and the iterative scheme, were derived for generic orbits in the previous chapter and could be carried over directly.

A particular challenge arising from eccentric orbits and hyperbolic trajectories is the large variation of the orbital radius over the course

of the simulation. We showed how this could be accommodated by adapting the resolution of the numerical grid and limiting the growth of the worldtube radius by controlling it using a smoothly broken power law.

We presented an example of an eccentric orbit inspiralling for over $25000M$ of simulation time and extracted the waveform modes through inspiral, plunge, merger and ringdown. A series of eccentric orbits with varying inspiral parameter ϵ was analyzed. Moving to hyperbolic trajectories, we considered a scattering geodesic and showed how the scalar self-force increased the scattering angle of the simulation and can lead to a direct capture for sufficiently large ϵ.

To our knowledge, this presents the first work that considers the self-consistent evolution of a scalar charge for eccentric or hyperbolic trajectories. For future work, we plan to compare our model with geodesic or adiabatic methods that only capture the leading order term in ϵ. This would allow us to identify the parameter space where higher order terms are needed for an accurate evolution. For eccentric orbits, we want to compare against the code presented in [174]; for hyperbolic encounters, the geodesic code [169] would be a good candidate to compare scattering angles.

[174]: Warburton et al. (2012), *Evolution of inspiral orbits around a Schwarzschild black hole*

[169]: Barack et al. (2022), *Self-force correction to the deflection angle in black-hole scattering: A scalar charge toy model*

5 Summary and outlook

In this thesis, we presented a method that attempts to accelerate the evolution of intermediate mass ratio binary black hole simulations in numerical relativity. Classical methods are prohibitively slow as the small mass ratio introduces a scale invariance to the computational domain. The tight grid spacing next to the smaller black hole causes the time step of the evolution to become prohibitively small due to the CFL criterion, greatly increasing the computational cost. Our worldtube excision method avoids this problem by excising a large region around the smaller black hole. Inside this worldtube, a perturbative solution is employed which is calibrated from the numerical evolution data on the worldtube boundary. This solution, in turn, provides boundary conditions to the simulation. A first study of this method was presented in [1], which describes a scalar toy model in 1+1 dimensions.

[1]: Dhesi et al. (2021), *Worldtube excision method for intermediate-mass-ratio inspirals: Scalar-field toy model*

In Chapter 2, we presented an updated implementation in 3+1 dimension using the SpECTRE numerical relativity code. The code solves the evolution of a scalar charge on a circular, geodesic orbit and employs a perturbative solution up to second order in coordinate distance inside the worldtube. We demonstrated the accuracy of our scheme and showed that the error in various quantities converges with the worldtube radius as theoretically expected. The implementation readily scales to thousands of computational cores due to the parallel nature of SpECTRE.

We generalized this method to include the effect of the scalar self-force in Chapter 3. In this setup, the equation of motion is given in an implicit form. To address this, we derived an iterative algorithm that converges to the particle's acceleration with arbitrary precision at each time step. Additionally, we showed how dynamically adjusting the worldtube radius during the inspiral keeps the error in the simulation constant as the orbital radius changes. A range of quasi-circular inspirals was run with different inspiral parameters $\epsilon = q^2/(\mu M)$. A comparison with an adiabatic approximation was shown and we verified that our method correctly resolves post-adiabatic terms. Finally, we explored how the convergence rates with respect to the worldtube radius are affected by the scalar self-force. To our knowledge, this is the first implementation of a fully self-consistent inspiral under the scalar self-force.

Finally, the self-consistent evolution was extended further to include eccentric orbits and hyperbolic encounters in Chapter 4.

After a brief description of the adjustments to the code, we showed a highly eccentric inspiral that covers over 90 orbital periods. We explored the evolution of the periapsis advance and extracted different harmonic modes from the waveform. In the second part, we presented a series of hyperbolic trajectories where the scalar self force causes the particle to lose energy and angular momentum, significantly changing its scattering angle. We gave an example of how the particle can lose sufficient energy to directly plunge into the central black hole.

In this thesis, we have treated a scalar toy model where the nonlinear Einstein equations are replaced by the simpler, linear Klein-Gordon equation. Our ultimate goal is to apply the worldtube excision method to binary black holes, particularly IMRIs. Let us consider such a system consisting of a primary black hole of mass m_1 and a secondary of mass m_2 so that $m_1 \gg m_2$. In this scenario, the worldtube is excised around the secondary black hole. In the interior, a perturbative solution to the Einstein equations is given by a Schwarzschild black hole under the influence of the tidal field of the primary body. Specifically, the solution will be expanded in the ratio of the distance from the secondary s and the characteristic lengthscale of the tidal field $\mathcal{R}$. In the vicinity of the secondary, this is equivalent to an expansion in the mass ratio q. The required tidally perturbed black hole solutions have been computed up to fourth order [175, 176].

[175]: Poisson (2005), *Metric of a tidally distorted, nonrotating black hole*

[176]: Poisson et al. (2018), *Nonrotating black hole in a post-Newtonian tidal environment II*

These solutions contain several parameters which capture the physical degrees of freedom of the external tidal field and are *a priori* unknown. It should be possible to determine the values of these parameters each time step by matching it to the evolved NR fields on the worldtube boundary, analogous to the matching of the regular field in Chapter 2. Once the solution is fully determined, the worldtube can provide boundary conditions to the NR evolution. These can likely be constructed completely analogous to the ones derived for the Klein-Gordon equation in Chapter 2, by considering the characteristic fields of the Einstein equations.

A particular challenge in the gravitational case comes from the choice of coordinates. The perturbative solutions are derived in Eddington-Finkelstein coordinates employing a Regge-Wheeler gauge. While this makes the expressions very concise, this gauge is not suitable for numerical evolution and has to be transformed into a more appropriate system first.

SpEC and SpECTRE usually employ damped harmonic coordinates for binary black hole simulations [80, 177]. However, the transformation of the tidally perturbed Schwarzschild solution to this gauge has proven to be prohibitively difficult. In a series of preliminary test simulations, we found that regular harmonic coordinates are able to sustain a stable evolution of binary black hole systems until close to the final merger. For the sake of simplicity, we will therefore start our approach using harmonic coordinates even though this will likely fail near merger.

[80]: Lindblom et al. (2006), *A New generalized harmonic evolution system*
[177]: Lindblom et al. (2009), *An Improved Gauge Driver for the GH Einstein System*

The transformation of Eddington-Finkelstein to harmonic coordinates was explored in [178]. Here, the harmonic coordinate condition $\Box X^\mu = 0$, where X^μ corresponds to the coordinate "vector"[1], is expanded to the same order as the tidally perturbed Schwarzschild solution to yield the forward and backward transformation. The spacetime metric components of a tidally perturbed black hole in harmonic coordinates are then given as functions of the unknown physical parameters as well as a set of gauge parameters introduced by the transformation. Time derivatives of these parameters also enter the expressions. Our hope is that we can match each component individually to the evolved fields on the worldtube boundary by projecting them onto spherical harmonics, analogous to the scalar charge case presented in Chapter 2. This continuity condition will yield a system of algebraic-differential equations that have to be evolved along the evolution. The motion of the smaller black hole should be governed by a subset of these equations, yielding an equation of motion for the worldtube analogous to the scalar self force explored in Chapter 3.

[178]: Dhesi (2023), *Modelling black hole binaries in the intermediate-mass-ratio regime*

1: The components of X^μ correspond to the four spacetime coordinates but the object does not mathematically constitute a tensor. The harmonic coordinate condition should therefore be viewed as four independent scalar equations.

Acknowledgements

First and foremost, I want to thank my supervisor Harald Pfeiffer. Every week I would walk into his office and showcase a new way the simulations were blowing up. He would then bombard me with different ideas that struck him on where the problem lay. Over the course of my PhD, I produced hundreds of diagnostic and convergence plots based on his incredible intuition and deep understanding in and beyond numerical relativity which always pushed us in the right direction.

Secondly, I want to thank the other members of *Team Worldtube*, in particular Leor Barack and Adam Pound. Their continuous efforts and contributions were key to the success of this project. It feels like most of our weekly zoom calls were spent trying to make us numerical relativists understand the most basic perturbation theory as we tried to convey the limitations of what can be implemented in the code. That we managed to agree on a consistent notation amazes me to this day.

The time of my PhD would not have been nearly as enjoyable without my friends at the AEI. I want to thank Nils Vu for helping me ascent the cliff that is coding in SpECTRE with unwavering stoicism. I thank my office mates Raj Patil for his continuous Mathematica support and Lorenzo Speri for his fantastic Limoncello, as well as both of you for your endless good mood and optimism. I thank Oliver Long, Philip Lynch, Nihar Gupte and Benjamin Leather for many meals and drinks at the *(place formerly known as) casa de self force*, as well as Memo Lara and PJ Nee for making sure that NR remains the best part of ACR.

A big thanks also goes out to my colleagues of the SXS collaboration. In particular, I am grateful to Kyle Nelli for finding (some of the) grave bugs in my code and Nils Deppe who did the same but whose advice also stopped the simulations from blowing up after many weeks of desperation.

Finally, I thank my parents for their continuous support throughout my physics career.

Bibliography

[1] Mekhi Dhesi et al. 'Worldtube excision method for intermediate-mass-ratio inspirals: Scalar-field toy model'. In: *Phys. Rev. D* 104.12 (2021), p. 124002. DOI: 10.1103/PhysRevD.104.124002 (cited on pages vii, 30, 32, 33, 39, 40, 49, 57, 61, 63, 69, 79, 124).

[2] LIGO/VIRGO. *Observation of Gravitational Waves from a Binary Black Hole Merger*. 2016. URL: https://www.ligo.org/science/Publication-GW150914/index.php (visited on 07/02/2024) (cited on page 1).

[3] B. P. Abbott et al. 'Observation of Gravitational Waves from a Binary Black Hole Merger'. In: *Phys. Rev. Lett.* 116.6 (2016), p. 061102. DOI: 10.1103/PhysRevLett.116.061102 (cited on page 1).

[4] H. Gee. *A (Very) Short History of Life on Earth: 4.6 Billion Years in 12 Pithy Chapters*. St. Martin's Publishing Group, 2021 (cited on page 1).

[5] Sean M. Carroll. *Spacetime and Geometry: An Introduction to General Relativity*. Cambridge University Press, July 2019 (cited on page 2).

[6] Eric Poisson and Clifford M. Will. *Gravity: Newtonian, Post-Newtonian, Relativistic*. Cambridge University Press, 2014 (cited on pages 2, 65, 66).

[7] A. Einstein. 'Über den Einfluß der Schwerkraft auf die Ausbreitung des Lichtes'. In: *Annalen Phys.* 340.10 (1911), pp. 898–908. DOI: 10.1002/andp.19113401005 (cited on page 2).

[8] Albert Einstein. 'The foundation of the general theory of relativity.' In: *Annalen Phys.* 49.7 (1916). Ed. by Jong-Ping Hsu and D. Fine, pp. 769–822. DOI: 10.1002/andp.19163540702 (cited on page 3).

[9] Albert Einstein. 'Die Feldgleichungen der Gravitation'. In: *Sitzungsberichte der Königlich Preussischen Akademie der Wissenschaften* (Jan. 1915), pp. 844–847 (cited on page 3).

[10] Karl Schwarzschild. 'On the gravitational field of a mass point according to Einstein's theory'. In: *Sitzungsber. Preuss. Akad. Wiss. Berlin (Math. Phys.)* 1916 (1916), pp. 189–196 (cited on page 3).

[11] A. S. Eddington. 'A Comparison of Whitehead's and Einstein's Formulæ'. In: *Nature* 113.2832 (1924), pp. 192–192. DOI: 10.1038/113192a0 (cited on page 3).

[12] G. Lemaitre. 'The expanding universe'. In: *Annales Soc. Sci. Bruxelles A* 53 (1933), pp. 51–85. DOI: 10.1023/A:1018855621348 (cited on page 3).

[13] Charles W. Misner, K. S. Thorne, and J. A. Wheeler. *Gravitation*. San Francisco: W. H. Freeman, 1973 (cited on pages 4, 114).

[14] Roy P. Kerr. 'Gravitational field of a spinning mass as an example of algebraically special metrics'. In: *Phys. Rev. Lett.* 11 (1963), pp. 237–238. DOI: 10.1103/PhysRevLett.11.237 (cited on page 4).

[15] Albert Einstein. 'Über Gravitationswellen'. In: *Sitzungsber. Preuss. Akad. Wiss. Berlin (Math. Phys.)* 1918 (1918), pp. 154–167 (cited on page 4).

[16] Michele Maggiore. *Gravitational Waves. Vol. 1: Theory and Experiments*. Oxford University Press, 2007 (cited on pages 5, 6).

[17] Benjamin P Abbott et al. 'A guide to LIGO–Virgo detector noise and extraction of transient gravitational-wave signals'. In: *Class. Quant. Grav.* 37.5 (2020), p. 055002. DOI: 10.1088/1361-6382/ab685e (cited on page 6).

[18] Craig Cahillane and Georgia Mansell. 'Review of the Advanced LIGO Gravitational Wave Observatories Leading to Observing Run Four'. In: *Galaxies* 10.1 (2022), p. 36. DOI: 10.3390/galaxies10010036 (cited on page 6).

[19] R. Abbott et al. 'Observation of Gravitational Waves from Two Neutron Star–Black Hole Coalescences'. In: *Astrophys. J. Lett.* 915.1 (2021), p. L5. DOI: 10.3847/2041-8213/ac082e (cited on page 7).

[20] R. Abbott et al. 'GWTC-3: Compact Binary Coalescences Observed by LIGO and Virgo during the Second Part of the Third Observing Run'. In: *Phys. Rev. X* 13.4 (2023), p. 041039. DOI: 10.1103/PhysRevX.13.041039 (cited on pages 7, 9, 12, 31).

[21] R. A. Hulse and J. H. Taylor. 'Discovery of a pulsar in a binary system'. In: *Astrophys. J. Lett.* 195 (1975), pp. L51–L53. DOI: 10.1086/181708 (cited on page 7).

[22] B. P. Abbott et al. 'Tests of general relativity with GW150914'. In: *Phys. Rev. Lett.* 116.22 (2016). [Erratum: Phys.Rev.Lett. 121, 129902 (2018)], p. 221101. DOI: 10.1103/PhysRevLett.116.221101 (cited on page 8).

[23] N. V. Krishnendu and Frank Ohme. 'Testing General Relativity with Gravitational Waves: An Overview'. In: *Universe* 7.12 (2021), p. 497. DOI: 10.3390/universe7120497 (cited on page 8).

[24] R. Abbott et al. 'Population of Merging Compact Binaries Inferred Using Gravitational Waves through GWTC-3'. In: *Phys. Rev. X* 13.1 (2023), p. 011048. DOI: 10.1103/PhysRevX.13.011048 (cited on page 8).

[25] Carl L. Rodriguez et al. 'Illuminating Black Hole Binary Formation Channels with Spins in Advanced LIGO'. In: *Astrophys. J. Lett.* 832.1 (2016), p. L2. DOI: 10.3847/2041-8205/832/1/L2 (cited on page 8).

[26] Jarrod R. Hurley, Christopher A. Tout, and Onno R. Pols. 'Evolution of binary stars and the effect of tides on binary populations'. In: *Mon. Not. Roy. Astron. Soc.* 329 (2002), p. 897. DOI: 10.1046/j.1365-8711.2002.05038.x (cited on page 9).

[27] Michela Mapelli. 'Formation Channels of Single and Binary Stellar-Mass Black Holes'. In: 2021. DOI: 10.1007/978-981-15-4702-7_16-1 (cited on page 9).

[28] Alice Bonino et al. 'Inferring eccentricity evolution from observations of coalescing binary black holes'. In: *Phys. Rev. D* 107.6 (2023), p. 064024. DOI: 10.1103/PhysRevD.107.064024 (cited on pages 9, 29).

[29] Simone S. Bavera et al. 'The origin of spin in binary black holes: Predicting the distributions of the main observables of Advanced LIGO'. In: *Astron. Astrophys.* 635 (2020), A97. DOI: 10.1051/0004-6361/201936204 (cited on page 9).

[30] Andrea Antonelli et al. 'Classifying the generation and formation channels of individual LIGO-Virgo-KAGRA observations from dynamically formed binaries'. In: *Phys. Rev. D* 108.8 (2023), p. 084044. DOI: 10.1103/PhysRevD.108.084044 (cited on page 9).

[31] Kentaro Takami, Luciano Rezzolla, and Luca Baiotti. 'Constraining the Equation of State of Neutron Stars from Binary Mergers'. In: *Phys. Rev. Lett.* 113.9 (2014), p. 091104. DOI: 10.1103/PhysRevLett.113.091104 (cited on page 9).

[32] Eemeli Annala et al. 'Gravitational-wave constraints on the neutron-star-matter Equation of State'. In: *Phys. Rev. Lett.* 120.17 (2018), p. 172703. DOI: 10.1103/PhysRevLett.120.172703 (cited on page 9).

[33] Francisco Hernandez Vivanco et al. 'Measuring the neutron star equation of state with gravitational waves: The first forty binary neutron star merger observations'. In: *Phys. Rev. D* 100.10 (2019), p. 103009. DOI: 10.1103/PhysRevD.100.103009 (cited on page 9).

[34] B. P. Abbott et al. 'GW170817: Observation of Gravitational Waves from a Binary Neutron Star Inspiral'. In: *Phys. Rev. Lett.* 119.16 (2017), p. 161101. DOI: 10.1103/PhysRevLett.119.161101 (cited on page 9).

[35] B. P. Abbott et al. 'Multi-messenger Observations of a Binary Neutron Star Merger'. In: *Astrophys. J. Lett.* 848.2 (2017), p. L12. DOI: 10.3847/2041-8213/aa91c9 (cited on page 9).

[36] B. P. Abbott et al. 'A gravitational-wave standard siren measurement of the Hubble constant'. In: *Nature* 551.7678 (2017), pp. 85–88. DOI: 10.1038/nature24471 (cited on page 10).

[37] Stephen M. Feeney et al. 'Prospects for Measuring the Hubble Constant with Neutron-Star–Black-Hole Mergers'. In: *Phys. Rev. Lett.* 126.17 (2021), p. 171102. DOI: 10.1103/PhysRevLett.126.171102 (cited on page 10).

[38] Karan Jani, Deirdre Shoemaker, and Curt Cutler. 'Detectability of Intermediate-Mass Black Holes in Multiband Gravitational Wave Astronomy'. In: *Nature Astron.* 4.3 (2019), pp. 260–265. DOI: 10.1038/s41550-019-0932-7 (cited on pages 10, 11, 31).

[39] Michele Maggiore et al. 'Science Case for the Einstein Telescope'. In: *JCAP* 03 (2020), p. 050. DOI: 10.1088/1475-7516/2020/03/050 (cited on pages 10, 11, 31).

[40] Matthew Evans et al. *A Horizon Study for Cosmic Explorer: Science, Observatories, and Community*. Sept. 2021 (cited on pages 10, 31).

[41] Ingo Tews et al. 'Constraining the speed of sound inside neutron stars with chiral effective field theory interactions and observations'. In: *Astrophys. J.* 860.2 (2018), p. 149. DOI: 10.3847/1538-4357/aac267 (cited on page 11).

[42] Enis Belgacem et al. 'Cosmology and dark energy from joint gravitational wave-GRB observations'. In: *JCAP* 08 (2019), p. 015. DOI: 10.1088/1475-7516/2019/08/015 (cited on page 11).

[43] R. Abbott et al. 'GW190814: Gravitational Waves from the Coalescence of a 23 Solar Mass Black Hole with a 2.6 Solar Mass Compact Object'. In: *Astrophys. J. Lett.* 896.2 (2020), p. L44. DOI: 10.3847/2041-8213/ab960f (cited on pages 12, 31).

[44] Pau Amaro-Seoane et al. *Laser Interferometer Space Antenna*. Feb. 2017 (cited on pages 12, 31).

[45] Monica Colpi et al. 'LISA Definition Study Report'. In: (Feb. 2024) (cited on page 12).

[46] Konstantin A. Postnov and Lev R. Yungelson. 'The Evolution of Compact Binary Star Systems'. In: *Living Rev. Rel.* 17 (2014), p. 3. DOI: 10.12942/lrr-2014-3 (cited on page 12).

[47] David Merritt. *Dynamics and Evolution of Galactic Nuclei*. Vol. 23. Princeton University Press, 2013. (Visited on 07/05/2024) (cited on page 12).

[48] Xiao-Hui Fan et al. 'A Survey of z > 5.7 Quasars in the Sloan Digital Sky Survey IV: Discovery of Seven Additional Quasars'. In: *Astron. J.* 131 (2006), pp. 1203–1209. DOI: 10.1086/500296 (cited on page 12).

[49] Muhammad A. Latif and Andrea Ferrara. 'Formation of supermassive black hole seeds'. In: *Publ. Astron. Soc. Austral.* 33 (2016), e051. DOI: 10.1017/pasa.2016.41 (cited on page 12).

[50] Sebastien Clesse and Juan Garcia-Bellido. 'Massive Primordial Black Holes from Hybrid Inflation as Dark Matter and the seeds of Galaxies'. In: *Phys. Rev. D* 92.2 (2015), p. 023524. DOI: 10.1103/PhysRevD.92.023524 (cited on page 12).

[51] Niayesh Afshordi et al. 'Waveform Modelling for the Laser Interferometer Space Antenna'. In: (Nov. 2023) (cited on pages 12, 14, 29, 69).

[52] Manuel Arca-Sedda, Pau Amaro-Seoane, and Xian Chen. 'Merging stellar and intermediate-mass black holes in dense clusters: implications for LIGO, LISA, and the next generation of gravitational wave detectors'. In: *Astron. Astrophys.* 652 (2021), A54. DOI: 10.1051/0004-6361/202037785 (cited on page 12).

[53] Alberto Sesana. 'Prospects for Multiband Gravitational-Wave Astronomy after GW150914'. In: *Phys. Rev. Lett.* 116.23 (2016), p. 231102. DOI: 10.1103/PhysRevLett.116.231102 (cited on page 13).

[54] Stanislav Babak et al. 'Science with the space-based interferometer LISA. V: Extreme mass-ratio inspirals'. In: *Phys. Rev. D* 95.10 (2017), p. 103012. DOI: 10.1103/PhysRevD.95.103012 (cited on page 13).

[55] Zhen Pan and Huan Yang. 'Probing the Growth of Massive Black Holes with Black Hole-Host Galaxy Spin Correlations'. In: *Astrophys. J.* 901.2 (2020), p. 163. DOI: 10.3847/1538-4357/abb1b1 (cited on page 13).

[56] Enrico Barausse et al. 'Prospects for Fundamental Physics with LISA'. In: *Gen. Rel. Grav.* 52.8 (2020), p. 81. DOI: 10.1007/s10714-020-02691-1 (cited on page 13).

[57] A. Sesana et al. 'Linking the spin evolution of massive black holes to galaxy kinematics'. In: *Astrophys. J.* 794 (2014), p. 104. DOI: 10.1088/0004-637X/794/2/104 (cited on page 13).

[58] Thomas W. Baumgarte and Stuart L. Shapiro. *Numerical Relativity: Solving Einstein's Equations on the Computer*. Cambridge University Press, 2010 (cited on pages 14, 16).

[59] Eric Gourgoulhon. '3+1 formalism and bases of numerical relativity'. In: (Mar. 2007) (cited on pages 14, 16).

[60] Albert Einstein. 'Explanation of the Perihelion Motion of Mercury from the General Theory of Relativity'. In: *Sitzungsber. Preuss. Akad. Wiss. Berlin (Math. Phys.)* 1915 (1915), pp. 831–839 (cited on page 14).

[61] Luc Blanchet. 'Gravitational Radiation from Post-Newtonian Sources and Inspiralling Compact Binaries'. In: *Living Rev. Rel.* 17 (2014), p. 2. DOI: 10.12942/lrr-2014-2 (cited on page 14).

[62] N. E. J. Bjerrum-Bohr et al. 'The SAGEX review on scattering amplitudes Chapter 13: Post-Minkowskian expansion from scattering amplitudes'. In: *J. Phys. A* 55.44 (2022), p. 443014. DOI: 10.1088/1751-8121/ac7a78 (cited on page 14).

[63] Leor Barack and Adam Pound. 'Self-force and radiation reaction in general relativity'. In: *Rept. Prog. Phys.* 82.1 (2019), p. 016904. DOI: 10.1088/1361-6633/aae552 (cited on pages 15, 32, 94).

[64] Adam Pound and Barry Wardell. 'Black Hole Perturbation Theory and Gravitational Self-Force'. In: *Handbook of Gravitational Wave Astronomy*. Ed. by Cosimo Bambi, Stavros Katsanevas, and Konstantinos D. Kokkotas. Singapore: Springer Nature Singapore, 2022, pp. 1411–1529. DOI: 10.1007/978-981-16-4306-4_38 (cited on pages 15, 32).

[65] Adam Pound et al. 'Second-Order Self-Force Calculation of Gravitational Binding Energy in Compact Binaries'. In: *Phys. Rev. Lett.* 124.2 (2020), p. 021101. DOI: 10.1103/PhysRevLett.124.021101 (cited on pages 15, 32).

[66] Barry Wardell et al. 'Gravitational waveforms for compact binaries from second-order self-force theory'. In: (Dec. 2021) (cited on pages 15, 32).

[67] Ollie Burke et al. 'Accuracy Requirements: Assessing the Importance of First Post-Adiabatic Terms for Small-Mass-Ratio Binaries'. In: (Oct. 2023) (cited on page 15).

[68] A. Buonanno and T. Damour. 'Effective one-body approach to general relativistic two-body dynamics'. In: *Phys. Rev. D* 59 (1999), p. 084006. DOI: 10.1103/PhysRevD.59.084006 (cited on page 15).

[69] Alessandra Buonanno and Thibault Damour. 'Transition from inspiral to plunge in binary black hole coalescences'. In: *Phys. Rev. D* 62 (2000), p. 064015. DOI: 10.1103/PhysRevD.62.064015 (cited on page 15).

[70] Thibault Damour and Alessandro Nagar. 'The Effective One Body description of the Two-Body problem'. In: *Fundam. Theor. Phys.* 162 (2011). Ed. by Luc Blanchet, Alessandro Spallicci, and Bernard Whiting, pp. 211–252. DOI: 10.1007/978-90-481-3015-3_7 (cited on page 15).

[71] Mohammed Khalil et al. 'Energetics and scattering of gravitational two-body systems at fourth post-Minkowskian order'. In: *Phys. Rev. D* 106.2 (2022), p. 024042. DOI: 10.1103/PhysRevD.106.024042 (cited on page 15).

[72] Maarten van de Meent et al. 'Enhancing the SEOBNRv5 effective-one-body waveform model with second-order gravitational self-force fluxes'. In: *Phys. Rev. D* 108.12 (2023), p. 124038. DOI: 10.1103/PhysRevD.108.124038 (cited on page 15).

[73] Mark A. Scheel et al. '3D simulations of linearized scalar fields in Kerr spacetime'. In: *Physical Review D* 69.10 (2004). DOI: 10.1103/physrevd.69.104006 (cited on pages 17, 35).

[74] Michael Holst et al. 'Optimal constraint projection for hyperbolic evolution systems'. In: *Physical Review D* 70.8 (2004). DOI: 10.1103/physrevd.70.084017 (cited on pages 17, 35, 36).

[75] Lawrence E. Kidder et al. 'Boundary conditions for the Einstein evolution system'. In: *Phys. Rev. D* 71 (2005), p. 064020. DOI: 10.1103/PhysRevD.71.064020 (cited on pages 17, 37, 63).

[76] Nils L. Vu et al. 'A scalable elliptic solver with task-based parallelism for the SpECTRE numerical relativity code'. In: *Phys. Rev. D* 105.8 (2022), p. 084027. DOI: 10.1103/PhysRevD.105.084027 (cited on page 20).

[77] Masaru Shibata and Takashi Nakamura. 'Evolution of three-dimensional gravitational waves: Harmonic slicing case'. In: *Phys. Rev. D* 52 (1995), pp. 5428–5444. DOI: 10.1103/PhysRevD.52.5428 (cited on page 20).

[78] Thomas W. Baumgarte and Stuart L. Shapiro. 'On the numerical integration of Einstein's field equations'. In: *Phys. Rev. D* 59 (1998), p. 024007. DOI: 10.1103/PhysRevD.59.024007 (cited on page 20).

[79] Frans Pretorius. 'Numerical relativity using a generalized harmonic decomposition'. In: *Class. Quant. Grav.* 22 (2005), pp. 425–452. DOI: 10.1088/0264-9381/22/2/014 (cited on page 20).

[80] Lee Lindblom et al. 'A New generalized harmonic evolution system'. In: *Class. Quant. Grav.* 23 (2006), S447–S462. DOI: 10.1088/0264-9381/23/16/S09 (cited on pages 20, 126).

[81] Daniela Alic et al. 'Conformal and covariant formulation of the Z4 system with constraint-violation damping'. In: *Phys. Rev. D* 85 (2012), p. 064040. DOI: 10.1103/PhysRevD.85.064040 (cited on page 20).

[82] Ami Harten et al. 'Uniformly high order accurate essentially non-oscillatory schemes, III'. In: *Journal of Computational Physics* 71.2 (1987), pp. 231–303. DOI: https://doi.org/10.1016/0021-9991(87)90031-3 (cited on page 22).

[83] J.P. Boyd. *Chebyshev and Fourier Spectral Methods: Second Revised Edition*. Dover Books on Mathematics. Dover Publications, 2013 (cited on page 22).

[84] Jan Hesthaven and Tim Warburton. 'Nodal Discontinuous Galerkin Methods: Algorithms, Analysis, and Applications'. In: vol. 54. Springer New York, NY, Dec. 2007. DOI: 10.1007/978-0-387-72067-8 (cited on pages 24, 38, 48).

[85] Víctor J. Llorente et al. 'Comparison of the ENATE approach and discontinuous Galerkin spectral element method in 1D nonlinear transport equations'. In: *Computer Assisted Mechanics and Engineering Sciences* 23 (2017), pp. 133–146 (cited on page 25).

[86] Nils Deppe et al. *SpECTRE*. Version 2024.06.18. June 2024. DOI: 10.5281/zenodo.12098412 (cited on pages 26, 27, 33, 37, 70, 74).

[87] Gordon E. Moore. 'Cramming more components onto integrated circuits, Reprinted from Electronics, volume 38, number 8, April 19, 1965, pp.114 ff.' In: *IEEE Solid-State Circuits Society Newsletter* 11.3 (2006), pp. 33–35. DOI: 10.1109/N-SSC.2006.4785860 (cited on page 26).

[88] Karl Rupp. *42 Years of Microprocessor Trend Data*. 2018. URL: https://www.karlrupp.net/2018/02/42-years-of-microprocessor-trend-data/ (visited on 06/13/2024) (cited on page 26).

[89] Michael Boyle et al. 'Testing the accuracy and stability of spectral methods in numerical relativity'. In: *Phys. Rev. D* 75 (2007), p. 024006. DOI: 10.1103/PhysRevD.75.024006 (cited on page 27).

[90] Abdul H. Mroue et al. 'Catalog of 174 Binary Black Hole Simulations for Gravitational Wave Astronomy'. In: *Phys. Rev. Lett.* 111.24 (2013), p. 241104. DOI: 10.1103/PhysRevLett.111.241104 (cited on page 27).

[91] Michael Boyle et al. 'The SXS Collaboration catalog of binary black hole simulations'. In: *Class. Quant. Grav.* 36.19 (2019), p. 195006. DOI: 10.1088/1361-6382/ab34e2 (cited on pages 27, 31).

[92] Tousif Islam et al. 'Surrogate model for gravitational wave signals from nonspinning, comparable-to large-mass-ratio black hole binaries built on black hole perturbation theory waveforms calibrated to numerical relativity'. In: *Phys. Rev. D* 106.10 (2022), p. 104025. DOI: 10.1103/PhysRevD.106.104025 (cited on page 27).

[93] Jooheon Yoo et al. 'Numerical relativity surrogate model with memory effects and post-Newtonian hybridization'. In: *Phys. Rev. D* 108.6 (2023), p. 064027. DOI: 10.1103/PhysRevD.108.064027 (cited on page 27).

[94] Francois Foucart et al. 'Gravitational waveforms from spectral Einstein code simulations: Neutron star-neutron star and low-mass black hole-neutron star binaries'. In: *Phys. Rev. D* 99.4 (2019), p. 044008. DOI: 10.1103/PhysRevD.99.044008 (cited on page 27).

[95] F. Foucart et al. 'Numerical simulations of neutron star-black hole binaries in the near-equal-mass regime'. In: *Phys. Rev. D* 99.10 (2019), p. 103025. DOI: 10.1103/PhysRevD.99.103025 (cited on page 27).

[96] Laxmikant Kale et al. *UIUC-PPL/charm: Charm++ version 7.0.0*. Version v7.0.0. Oct. 2021. DOI: 10.5281/zenodo.5597907 (cited on pages 28, 38).

[97] Nils Deppe et al. 'A high-order shock capturing discontinuous Galerkin–finite difference hybrid method for GRMHD'. In: *Class. Quant. Grav.* 39.19 (2022), p. 195001. DOI: 10.1088/1361-6382/ac8864 (cited on page 28).

[98] Nils Deppe et al. 'Binary neutron star mergers using a discontinuous Galerkin-finite difference hybrid method'. In: (June 2024) (cited on page 28).

[99] B. P. Abbott et al. 'Search for Eccentric Binary Black Hole Mergers with Advanced LIGO and Advanced Virgo during their First and Second Observing Runs'. In: *Astrophys. J.* 883.2 (2019), p. 149. DOI: 10.3847/1538-4357/ab3c2d (cited on page 29).

[100] P. C. Peters and J. Mathews. 'Gravitational radiation from point masses in a Keplerian orbit'. In: *Phys. Rev.* 131 (1963), pp. 435–439. DOI: 10.1103/PhysRev.131.435 (cited on page 29).

[101] Isobel M. Romero-Shaw, Paul D. Lasky, and Eric Thrane. 'Four Eccentric Mergers Increase the Evidence that LIGO–Virgo–KAGRA's Binary Black Holes Form Dynamically'. In: *Astrophys. J.* 940.2 (2022), p. 171. DOI: 10.3847/1538-4357/ac9798 (cited on page 29).

[102] Nikolas A. Wittek et al. 'Worldtube excision method for intermediate-mass-ratio inspirals: Scalar-field model in 3+1 dimensions'. In: *Phys. Rev. D* 108.2 (2023), p. 024041. DOI: 10.1103/PhysRevD.108.024041 (cited on page 31).

[103] B. P. Abbott et al. 'Binary Black Hole Mergers in the first Advanced LIGO Observing Run'. In: *Phys. Rev. X* 6.4 (2016). [Erratum: Phys.Rev.X 8, 039903 (2018)], p. 041015. DOI: 10.1103/PhysRevX.6.041015 (cited on page 31).

[104] B. P. Abbott et al. 'GWTC-1: A Gravitational-Wave Transient Catalog of Compact Binary Mergers Observed by LIGO and Virgo during the First and Second Observing Runs'. In: *Phys. Rev. X* 9.3 (2019), p. 031040. DOI: 10.1103/PhysRevX.9.031040 (cited on page 31).

[105] R. Abbott et al. 'GWTC-2: Compact Binary Coalescences Observed by LIGO and Virgo During the First Half of the Third Observing Run'. In: *Phys. Rev. X* 11 (2021), p. 021053. DOI: 10.1103/PhysRevX.11.021053 (cited on page 31).

[106] B. P. Abbott et al. 'Binary Black Hole Population Properties Inferred from the First and Second Observing Runs of Advanced LIGO and Advanced Virgo'. In: *Astrophys. J. Lett.* 882.2 (2019), p. L24. DOI: 10.3847/2041-8213/ab3800 (cited on page 31).

[107] Tejaswi Venumadhav et al. 'New binary black hole mergers in the second observing run of Advanced LIGO and Advanced Virgo'. In: *Phys. Rev. D* 101.8 (2020), p. 083030. DOI: 10.1103/PhysRevD.101.083030 (cited on page 31).

[108] Alexander H. Nitz et al. *4-OGC: Catalog of gravitational waves from compact-binary mergers*. Dec. 2021 (cited on page 31).

[109] R. Abbott et al. *The population of merging compact binaries inferred using gravitational waves through GWTC-3*. Nov. 2021 (cited on page 31).

[110] Pau Amaro Seoane et al. *The Gravitational Universe*. May 2013 (cited on page 31).

[111] Michael L. Katz et al. 'Probing Massive Black Hole Binary Populations with LISA'. In: *Mon. Not. Roy. Astron. Soc.* 491.2 (2020), pp. 2301–2317. DOI: 10.1093/mnras/stz3102 (cited on page 31).

[112] Jonathan R. Gair et al. 'Constraining properties of the black hole population using LISA'. In: *Class. Quant. Grav.* 28 (2011). Ed. by William Trischuk, p. 094018. DOI: 10.1088/0264-9381/28/9/094018 (cited on page 31).

[113] Marta Volonteri et al. 'Black hole mergers from dwarf to massive galaxies with the NewHorizon and Horizon-AGN simulations'. In: *Mon. Not. Roy. Astron. Soc.* 498.2 (2020), pp. 2219–2238. DOI: 10.1093/mnras/staa2384 (cited on page 31).

[114] Thomas W. Baumgarte and Stuart L. Shapiro. *Numerical Relativity: Solving Einstein's Equations on the Computer*. Cambridge: Cambridge University Press, 2010 (cited on page 31).

[115] Carlos O. Lousto and James Healy. 'Exploring the Small Mass Ratio Binary Black Hole Merger via Zeno's Dichotomy Approach'. In: *Phys. Rev. Lett.* 125.19 (2020), p. 191102. DOI: 10.1103/PhysRevLett.125.191102 (cited on page 32).

[116] Nicole Rosato, James Healy, and Carlos O. Lousto. 'Adapted gauge to small mass ratio binary black hole evolutions'. In: *Phys. Rev. D* 103.10 (2021), p. 104068. DOI: 10.1103/PhysRevD.103.104068 (cited on page 32).

[117] Ulrich Sperhake et al. 'Extreme black hole simulations: collisions of unequal mass black holes and the point particle limit'. In: *Phys. Rev. D* 84 (2011), p. 084038. DOI: 10.1103/PhysRevD.84.084038 (cited on page 32).

[118] Carlos O. Lousto and James Healy. 'Study of the intermediate mass ratio black hole binary merger up to 1000:1 with numerical relativity'. In: *Class. Quant. Grav.* 40.9 (2023), 09LT01. DOI: 10.1088/1361-6382/acc7ef (cited on page 32).

[119] Maarten van de Meent. 'Gravitational self-force on generic bound geodesics in Kerr spacetime'. In: *Phys. Rev. D* 97.10 (2018), p. 104033. DOI: 10.1103/PhysRevD.97.104033 (cited on page 32).

[120] Alvin J. K. Chua et al. 'Rapid generation of fully relativistic extreme-mass-ratio-inspiral waveform templates for LISA data analysis'. In: *Phys. Rev. Lett.* 126.5 (2021), p. 051102. DOI: 10.1103/PhysRevLett.126.051102 (cited on page 32).

[121] Scott A. Hughes et al. 'Adiabatic waveforms for extreme mass-ratio inspirals via multivoice decomposition in time and frequency'. In: *Phys. Rev. D* 103.10 (2021), p. 104014. DOI: 10.1103/PhysRevD.103.104014 (cited on page 32).

[122] Niels Warburton et al. 'Gravitational-Wave Energy Flux for Compact Binaries through Second Order in the Mass Ratio'. In: *Phys. Rev. Lett.* 127.15 (2021), p. 151102. DOI: 10.1103/PhysRevLett.127.151102 (cited on page 32).

[123] Maarten van de Meent and Harald P. Pfeiffer. 'Intermediate mass-ratio black hole binaries: Applicability of small mass-ratio perturbation theory'. In: *Phys. Rev. Lett.* 125.18 (2020), p. 181101. DOI: 10.1103/PhysRevLett.125.181101 (cited on page 32).

[124] Antoni Ramos-Buades et al. 'Eccentric binary black holes: Comparing numerical relativity and small mass-ratio perturbation theory'. In: *Phys. Rev. D* 106.12 (2022), p. 124040. DOI: 10.1103/PhysRevD.106.124040 (cited on page 32).

[125] Angelica Albertini et al. 'Comparing second-order gravitational self-force, numerical relativity, and effective one body waveforms from inspiralling, quasicircular, and nonspinning black hole binaries'. In: *Phys. Rev. D* 106.8 (2022), p. 084061. DOI: 10.1103/PhysRevD.106.084061 (cited on pages 32, 98).

[126] Ian Vega et al. 'Self-force with (3 + 1) codes: A primer for numerical relativists'. In: *Phys. Rev. D* 80 (8 Oct. 2009), p. 084021. DOI: 10.1103/PhysRevD.80.084021 (cited on page 33).

[127] Lee Lindblom et al. 'A new generalized harmonic evolution system'. In: *Classical and Quantum Gravity* 23.16 (2006), S447. DOI: 10.1088/0264-9381/23/16/S09 (cited on pages 35, 36).

[128] Alvin Bayliss and Eli Turkel. 'Radiation boundary conditions for wave-like equations'. In: *Communications on Pure and Applied Mathematics* 33.6 (1980), pp. 707–725. DOI: https://doi.org/10.1002/cpa.3160330603 (cited on page 37).

[129] Morten Bjørhus. 'The ODE Formulation of Hyperbolic PDEs Discretized by the Spectral Collocation Method'. In: *SIAM Journal on Scientific Computing* 16.3 (1995), pp. 542–557. DOI: 10.1137/0916035 (cited on page 37).

[130] Mark A. Scheel et al. 'Solving Einstein's equations with dual coordinate frames'. In: *Physical Review D* 74.10 (2006). DOI: 10.1103/physrevd.74.104006 (cited on page 38).

[131] Daniel A. Hemberger et al. 'Dynamical Excision Boundaries in Spectral Evolutions of Binary Black Hole Spacetimes'. In: *Class. Quant. Grav.* 30 (2013), p. 115001. DOI: 10.1088/0264-9381/30/11/115001 (cited on pages 38, 77).

[132] Mark A. Scheel et al. 'Improved methods for simulating nearly extremal binary black holes'. In: *Class. Quant. Grav.* 32.10 (2015), p. 105009. DOI: 10.1088/0264-9381/32/10/105009 (cited on pages 38, 77).

[133] Steven L. Detweiler and Bernard F. Whiting. 'Selfforce via a Green's functsion decomposition'. In: *Phys. Rev. D* 67 (2003), p. 024025. DOI: 10.1103/PhysRevD.67.024025 (cited on pages 40, 74).

[134] Roland Haas and Eric Poisson. 'Mode-sum regularization of the scalar self-force: Formulation in terms of a tetrad decomposition of the singular field'. In: *Phys. Rev. D* 74 (2006), p. 044009. DOI: 10.1103/PhysRevD.74.044009 (cited on pages 40, 81).

[135] Barry Wardell et al. 'A Generic effective source for scalar self-force calculations'. In: *Phys. Rev. D* 85 (2012), p. 104044. DOI: 10.1103/PhysRevD.85.104044 (cited on pages 40, 41, 81).

[136] Anna Heffernan, Adrian Ottewill, and Barry Wardell. 'High-order expansions of the Detweiler-Whiting singular field in Schwarzschild spacetime'. In: *Phys. Rev. D* 86 (2012), p. 104023. DOI: 10.1103/PhysRevD.86.104023 (cited on pages 40, 81).

[137] J. L. Synge. *Relativity: The General theory*. North-Holland Publishing Company, 1960 (cited on pages 40, 81).

[138] Leor Barack and Amos Ori. 'Regularization parameters for the self-force in Schwarzschild space-time. 1. Scalar case'. In: *Phys. Rev. D* 66 (2002), p. 084022. DOI: 10.1103/PhysRevD.66.084022 (cited on page 41).

[139] Adam Pound. 'Nonlinear gravitational self-force. I. Field outside a small body'. In: *Phys. Rev. D* 86 (2012), p. 084019. DOI: 10.1103/PhysRevD.86.084019 (cited on page 42).

[140] Yasushi Mino. 'Perturbative approach to an orbital evolution around a supermassive black hole'. In: *Phys. Rev. D* 67 (2003), p. 084027. DOI: 10.1103/PhysRevD.67.084027 (cited on page 51).

[141] Tanja Hinderer and Eanna E. Flanagan. 'Two timescale analysis of extreme mass ratio inspirals in Kerr. I. Orbital Motion'. In: *Phys. Rev. D* 78 (2008), p. 064028. DOI: 10.1103/PhysRevD.78.064028 (cited on page 51).

[142] Luz Diaz-Rivera et al. 'Scalar field self-force effects on orbits about a Schwarzschild black hole'. In: *Physical Review D* 70.12 (2004). DOI: 10.1103/physrevd.70.124018 (cited on pages 53–55, 111).

[143] Rodrigo Panosso Macedo et al. 'Hyperboloidal method for frequency-domain self-force calculations'. In: *Physical Review D* 105.10 (2022). DOI: 10.1103/physrevd.105.104033 (cited on page 55).

[144] Peter Diener et al. 'Self-Consistent Orbital Evolution of a Particle around a Schwarzschild Black Hole'. In: *Physical Review Letters* 108.19 (2012). DOI: 10.1103/physrevlett.108.191102 (cited on page 63).

[145] Theodore C. Quinn. 'Axiomatic approach to radiation reaction of scalar point particles in curved spacetime'. In: *Physical Review D* 62.6 (2000). DOI: 10.1103/physrevd.62.064029 (cited on page 63).

[146] Kip S. Thorne. 'Multipole expansions of gravitational radiation'. In: *Rev. Mod. Phys.* 52 (2 Apr. 1980), pp. 299–339. DOI: 10.1103/RevModPhys.52.299 (cited on page 65).

[147] L. Blanchet and T. Damour. 'Radiative gravitational fields in general relativity. I - General structure of the field outside the source'. In: *Philosophical Transactions of the Royal Society of London Series A* 320.1555 (Dec. 1986), pp. 379–430. DOI: 10.1098/rsta.1986.0125 (cited on page 66).

[148] Nikolas A. Wittek et al. 'Worldtube excision method for intermediate-mass-ratio inspirals: self-consistent evolution in a scalar-charge model'. In: (Mar. 2024) (cited on page 69).

[149] Peter Diener et al. 'Self-consistent orbital evolution of a particle around a Schwarzschild black hole'. In: *Phys. Rev. Lett.* 108 (2012), p. 191102. DOI: 10.1103/PhysRevLett.108.191102 (cited on pages 71, 111).

[150] Mark A. Scheel et al. '3-D simulations of linearized scalar fields in Kerr space-time'. In: *Phys. Rev. D* 69 (2004), p. 104006. DOI: 10.1103/PhysRevD.69.104006 (cited on page 73).

[151] Mark A. Scheel et al. 'Solving Einstein's equations with dual coordinate frames'. In: *Phys. Rev. D* 74 (2006), p. 104006. DOI: 10.1103/PhysRevD.74.104006 (cited on pages 77, 78).

[152] Adam Pound and Jeremy Miller. 'Practical, covariant puncture for second-order self-force calculations'. In: *Phys. Rev. D* 89.10 (2014), p. 104020. DOI: 10.1103/PhysRevD.89.104020 (cited on page 81).

[153] Anna Heffernan et al. 'Accelerated motion and the self-force in Schwarzschild spacetime'. In: *Class. Quant. Grav.* 35.19 (2018), p. 194001. DOI: 10.1088/1361-6382/aad420 (cited on page 81).

[154] Matt Visser. 'The Kerr spacetime: A Brief introduction'. In: *Kerr Fest: Black Holes in Astrophysics, General Relativity and Quantum Gravity*. June 2007 (cited on page 84).

[155] Paul A. M. Dirac. 'Classical theory of radiating electrons'. In: *Proc. Roy. Soc. Lond. A* 167 (1938), pp. 148–169. DOI: 10.1098/rspa.1938.0124 (cited on page 88).

[156] Herbert Spohn. 'The Critical manifold of the Lorentz-Dirac equation'. In: *EPL* 50 (2000), pp. 287–292. DOI: 10.1209/epl/i2000-00268-x (cited on page 88).

[157] Robin Ekman, Tom Heinzl, and Anton Ilderton. 'Reduction of order, resummation, and radiation reaction'. In: *Phys. Rev. D* 104.3 (2021), p. 036002. DOI: 10.1103/PhysRevD.104.036002 (cited on page 88).

[158] Fritz Rohrlich. 'Dynamics of a charged particle'. In: *Physical Review E* () (cited on page 88).

[159] Samuel E. Gralla, Abraham I. Harte, and Robert M. Wald. 'A Rigorous Derivation of Electromagnetic Self-force'. In: *Phys. Rev. D* 80 (2009), p. 024031. DOI: 10.1103/PhysRevD.80.024031 (cited on page 88).

[160] Brynjulf Owren and Marino Zennaro. 'Derivation of Efficient, Continuous, Explicit Runge–Kutta Methods'. In: *SIAM Journal on Scientific and Statistical Computing* 13.6 (1992), pp. 1488–1501. DOI: 10.1137/0913084 (cited on page 90).

[161] B. Wardell et al. *Teukolsky (1.0.4)*. 2023. DOI: https://doi.org/10.5281/zenodo.10040501 (cited on page 94).

[162] Jeremy Miller and Adam Pound. 'Two-timescale evolution of extreme-mass-ratio inspirals: waveform generation scheme for quasicircular orbits in Schwarzschild spacetime'. In: *Phys. Rev. D* 103.6 (2021), p. 064048. DOI: 10.1103/PhysRevD.103.064048 (cited on page 95).

[163] Jeremy Miller et al. 'Worldtube puncture scheme for first- and second-order self-force calculations in the Fourier domain'. In: (Dec. 2023) (cited on page 95).

[164] Geoffrey Compère and Lorenzo Küchler. 'Asymptotically matched quasi-circular inspiral and transition-to-plunge in the small mass ratio expansion'. In: *SciPost Phys.* 13.2 (2022), p. 043. DOI: 10.21468/SciPostPhys.13.2.043 (cited on page 98).

[165] Amos Ori and Kip S. Thorne. 'The Transition from inspiral to plunge for a compact body in a circular equatorial orbit around a massive, spinning black hole'. In: *Phys. Rev. D* 62 (2000), p. 124022. DOI: 10.1103/PhysRevD.62.124022 (cited on page 98).

[166] Jordan Moxon et al. 'SpECTRE Cauchy-characteristic evolution system for rapid, precise waveform extraction'. In: *Phys. Rev. D* 107.6 (2023), p. 064013. DOI: 10.1103/PhysRevD.107.064013 (cited on page 110).

[167] Sizheng Ma et al. 'Fully relativistic three-dimensional Cauchy-characteristic matching'. In: (Aug. 2023) (cited on page 110).

[168] Niels Warburton and Leor Barack. 'Self force on a scalar charge in Kerr spacetime: circular equatorial orbits'. In: *Phys. Rev. D* 81 (2010), p. 084039. DOI: 10.1103/PhysRevD.81.084039 (cited on page 111).

[169] Leor Barack and Oliver Long. 'Self-force correction to the deflection angle in black-hole scattering: A scalar charge toy model'. In: *Phys. Rev. D* 106.10 (2022), p. 104031. DOI: 10.1103/PhysRevD.106.104031 (cited on pages 111, 114, 123).

[170] Steve Drasco, Eanna E. Flanagan, and Scott A. Hughes. 'Computing inspirals in Kerr in the adiabatic regime. I. The Scalar case'. In: *Class. Quant. Grav.* 22 (2005), S801–846. DOI: 10.1088/0264-9381/22/15/011 (cited on page 111).

[171] Yasushi Mino and Richard Price. 'Two-timescale adiabatic expansion of a scalar field model'. In: *Phys. Rev. D* 77 (2008), p. 064001. DOI: 10.1103/PhysRevD.77.064001 (cited on page 111).

[172] Adam Pound, Eric Poisson, and Bernhard G. Nickel. 'Limitations of the adiabatic approximation to the gravitational self-force'. In: *Phys. Rev. D* 72 (2005), p. 124001. DOI: 10.1103/PhysRevD.72.124001 (cited on page 111).

[173] Scott A. Hughes. 'Parameterizing black hole orbits for adiabatic inspiral'. In: *Phys. Rev. D* 109.6 (2024), p. 064077. DOI: 10.1103/PhysRevD.109.064077 (cited on page 113).

[174] Niels Warburton et al. 'Evolution of inspiral orbits around a Schwarzschild black hole'. In: *Phys. Rev. D* 85 (2012), p. 061501. DOI: 10.1103/PhysRevD.85.061501 (cited on page 123).

[175] Eric Poisson. 'Metric of a tidally distorted, nonrotating black hole'. In: *Phys. Rev. Lett.* 94 (2005), p. 161103. DOI: 10.1103/PhysRevLett.94.161103 (cited on page 125).

[176] Eric Poisson and Eamonn Corrigan. 'Nonrotating black hole in a post-Newtonian tidal environment II'. In: *Phys. Rev. D* 97.12 (2018), p. 124048. DOI: 10.1103/PhysRevD.97.124048 (cited on page 125).

[177] Lee Lindblom and Bela Szilagyi. 'An Improved Gauge Driver for the GH Einstein System'. In: *Phys. Rev. D* 80 (2009), p. 084019. DOI: 10.1103/PhysRevD.80.084019 (cited on page 126).

[178] Mekhi Dhesi. 'Modelling black hole binaries in the intermediate-mass-ratio regime'. PhD thesis. University of Southampton, 2023 (cited on page 126).